CRANFIELD UNIVERSITY

SCHOOL OF MECHANICAL ENGINEERING

PhD THESIS

1994

CHRISTOPHER DUFFY

Stimulated Brillouin Scattering In Monomode Optical Fibres For Sensing And Signal Processing Applications

Supervisor: Dr RP Tatam

August, 1994

Abstract

This thesis describes research into non-linear optical effects in monomode fibres for sensing and signal processing schemes. The work is initially placed into the context of relevant fibre sensor applications for aerospace. Candidate non-linear processes are then described and Stimulated Brillouin Scattering (SBS) targeted as a suitable mechanism. The SBS process in monomode fibres is then fully described, including a theoretical assessment of the magnitude of both pump and Stokes signals with fibre length.

The project developed, firstly, an all-optical frequency shifter using SBS which generated output carriers in the 1-700MHz region, depending on fibre type and system topology. In particular, a single-fibre system was demonstrated for the first time. Limitations of the technique arose through fibre photosensitivity and non-linear dynamical effects which, respectively, increased the input pump power requirements and introduced intensity and frequency instabilities into the output signal. Both processes were investigated fully. Optical fibre and pump characteristics, and system configurations, were therefore identified which minimised their impact.

The same SBS heterodyning principles were then used to investigate single-pump sensor systems. Both 'quasi-point' and two-element, multiplexed temperature sensors were demonstrated. A linear relationship between the Stokes frequency and temperature was obtained from 5 to 55°C, determined primarily by the thermal response of the acoustic phonon velocity. The sensing resolution was typically ±2°C, limited by the non-linear dynamical effects, and the spatial resolution was determined by the pump/fibre interaction length. One unique sensing element per optical input was demonstrated. These results are then placed in the context of systems utilising alternative SBS-based strategies, other non-linear effects and fibre ring resonators.

Management elements of the project were covered by detailing both the technical and strategic motivations for undertaking the research and, by describing the issues on which a cost benefit analysis of fibre sensors for aircraft can be undertaken.

Acknowledgements

I would like to acknowledge a whole host of people, without whom, the project would have been a damn sight more difficult, if not impossible.

The overall project was supported by a British Aerospace(BAe)/SERC industrial studentship. Dr Ralph Tatam, my supervisor at Cranfield, provided essential equipment, lab space and technical input for the project. His continual enthusiasm and encouragement were a great fillip (except after Group curry evenings). My thanks also to the rest of my Total Technology committee – Professor Robin Elder (Cranfield), Dr Roy Clarke (BAe) and Dr Len Cooke (BAe). Robert Brown at Cranfield also assisted with the management aspects of the project.

Various companies loaned equipment during the study. Thanks then to *Lambda Photometrics* (Detectors), *Laser Lines* (Nd:YAG Laser) and *TecOptics* (Fabry Perot components). Professor Bob Harrison at Heriot-Watt University also advised on the non-linear dynamical aspects of the project.

I am most grateful to my ex-fellow students at Cranfield who made working in the Optics Group such a 'crack'. In particular, Bro. Hashim Atcha (my business partner) and Helen Ford provided much technical assistance both during experiments and in the fleecing of the campus quiz machine. Richard Martin also provided guidance on mathematical issues. At BAe, I'd particularly like to thank Trevor Gowan for help with the computational issues. To those who helped in other ways, especially the Room 145 boys for all the stick, thanks and good-bye! Duncan Hickman deserves a special mention for his masterful advice at the start and finish of the project.

Finally, and most importantly, I'd like to thank my wife Lyn for her love and support as well as for enduring my regular absences at Cranfield doing the experiments and in Bristol compiling this document. I hope you think it's worth it! Thanks also to Mum, Bern and Caroline for their help and love over the years.

Contents

Contents (cont)

Contents (cont)

Contents (cont)

Notation

a	Fibre Core Radius
a'	Fibre Radius (Core, Cladding Plus Outer Jacket)
A_{eff}	Effective Core Area
A, B, C	Constant Terms
$\mathcal{A}$	Amplitude
b	Constant Term
$\mathcal{B}$	Birefringence
c	Velocity of Light In Vacuum
d	Polarisation Term, Differential Notation
$D, \mathbf{D}$	Electric Displacement,**Bold Font Denotes Vector**
$\mathcal{D}$	Constant Term
$E, E(\omega), \mathbf{E}(\omega)$	Electric Field, **Bold Font Denotes Vector**
$\mathcal{E}(\omega)$	Electric Field Amplitude
exp	Exponential Function, $e^1 = 2.71828$
f	Optical Frequency
f_i	Sustained Oscillation Spacing
$f_p(z)$	General Function Of Pump Signal
$f_s(z)$	General Function Of Stokes Signal
$F, \mathbf{F}$	Force, **Bold Font Denotes Vector**
$\mathcal{F}$	Finesse
g	Earth Gravity
$g_{subscript}$	Non-Linear Mechanism Gain Factor
$G(z)$	Term In Stimulated Scattering Equations
h	Planck's Constant
i	$\sqrt{-1}$, Complex Number
$I_{p,s}(z,t)$	Intensity of Pump/Stokes Signals Along Fibre
j	Integer/Constant
$J_{p,s}(z)$	Substitution Term for Pump/Stokes Signals
$J'_{p,s}(z)$	First Order Derivative of Function $J_{p,s}(z)$
k	Wave Number
k'	Thermal Conductivity
K, K_1	Integration Constants
l	Integer
L	Fibre Length
L_{eff}	Effective Interaction Length
L_B	Fibre Beat Length
n	Refractive Index
N	Constant Term
$\mathcal{N}$	Fibre Loss, dB per km
p_r	Pressure

P	Power (Optical/Electrical)
$\mathcal{P}, \mathbf{P}$	Material Polarisation, **Bold Font Denotes Vector**
q	Constant Term
r, ϕ, z	Cylindrical Co-ordinates
r_0	Single Mode Fibre Mode Radius
r_f	Outer Fibre Radius
R	Bulk/Fibre Non-linear Figure of Merit Ratio
$\mathcal{R}$	Reflectivity
s	Spatial Co-ordinate
t, T, τ	Units of Time
$\mathcal{T}$	Temperature
v	Velocity of Light In Material
V	Normalised Waveguide Frequency
V_A	Acoustic Phonon Velocity
x, y, z	Cartesian Co-ordinates
Y	Dummy Variable
z	Direction of Light Propagation In Optical Fibre
α	Attenuation Coefficient of Fibre
β, γ	Constant Terms In Stimulated Scattering Systems
$\beta_{subscript}$	Propagation Constant
Γ	Acoustic Damping Term
δ	Difference Notation
Δ	Increment Notation, Bandwidth
ϵ_0	Permitivitty of Free Space
ϵ_r	Relative Permitivitty of Material
θ	Angle Notation
λ	Optical Wavelength
κ	Coupling Coefficient
μm	10^{-6}m
μ_0	Permeability of Free Space
ν_B	Frequency (Stokes, SBS)
π	3.1416
Φ	Phase
ρ_{12}	Elasto-optic Coefficient
ϱ_o	Material Density
σ_0	Raman Cross Section
τ_f	Fibre Twist Rate
$\chi^{(j)}$	$j^{(\mathrm{th})}$ Order Non-linear Susceptibility
ψ	Poisson's Ratio
ω	Angular Frequency
ω_0	Material Resonance Frequency
∇	Gradient Vector Operator

Figures, Plates And Tables Listing

Figures

Figures(cont)

Figures(cont)

Plates

Tables

1 Introduction

1.1 General Background

1.1.1 Technical Motivation And Context Of Study

The implementation of optical fibres and associated components into communications systems over the last two decades has accelerated the development of new fibre-based sensing techniques for many applications. Fibre sensor technology shares many of the advantages over conventional electrical and mechanical sensing techniques that optical communications possesses over electronic data transmission (eg Glomb, 1987). The small size and weight of the fibre, the intrinsic dielectric properties that ensure immunity from electromagnetic interference (EMI), coupled with the non-combustibility and neutral chemical properties of the fibre, are important characteristics in many practical situations. As a result, the replacement of many conventional electrical and mechanical based transducers by their fibre counterpart has appeared inevitable for some time (eg Miller, 1986).

British Aerospace (BAe) designs and manufactures a wide range of components and systems for both civil and military aircraft and, at the outset of this study, space instrumentation and motor vehicles. The major benefits of fibre optic systems over their conventional counterparts cited above have direct relevance for applications in these areas. On modern military and commercial aircraft, for example, the task of maintaining overall system integrity and aircraft safety is becoming increasingly complex. Sophisticated electronic hardware is replacing direct mechanical control linkages between the pilot and the remote control surfaces of the airframe. This includes computers, data transmission links and remote transducers. Both natural and man-made sources of EMI, including lightning strikes, electromagnetic pulses and high energy radio frequency emissions, can have a degrading effect on such systems. Large current pulses induced in copper wires, for example, can corrupt data in integrated control systems and lead to potentially catastrophic outcomes. Indeed, malfunctioning electrical interconnections are the root source of most avionic failures (Little, 1988). Additional electrical insulation for EMI immunity only increases both maintenance costs and weight.

Consideration of EMI problems is particularly pertinent since composite based airframes, propulsion systems and control accessories are being introduced into both the military and civil sector. The inherent degree of electromagnetic shielding afforded by metallic structures is therefore eliminated, leaving the electrical components *more* vulnerable. This necessitates higher levels of electrical insulation whilst the use of fibre optics would reduce such requirements.

With regard to the size and weight of fibre systems, it has been estimated that a Boeing 747 operator can save $\$10^5$ annually per aircraft if fuel consumption is reduced by 1% (Ruffles, 1990). Light, composite based airframes provide significant weight savings and fuel economies. Miniaturisation of any other aerospace hardware through replacement by fibre optics yields further increases in fuel economy, as well as enhancing the pay-load capacity of the carrier. Fibre data links, for example, are up to an order of magnitude lighter than equivalent, unshielded wire bundles, reducing the weight of a jet engine alone by 30lbs (Baumbick, 1988). In the military sphere, by replacing the complete propulsion and flight control systems (ie sensors plus associated databuses) in F15 fighters and transport aircraft, total weight savings of 125lb and 1500lb respectively are envisaged (Seng, 1988).

The non-inflammable and benign chemical properties of the fibre are important for systems situated in the high temperature regime of the aircraft engine or potentially explosive aircraft fuel tank. Standard fibre cable can survive comfortably within protected electronic module environments (-55°C to 125°C temperature range typically used in aircraft). Speciality fibres such as polyimide coated cables can function up to 400°C which should suffice for the majority of aerospace applications.

There is currently a major worldwide effort to implement fibre optic systems into aerospace platforms (eg Kandebo, 1993). Such systems include sensors for flight and propulsion control, the communications link from sensor head to electro-optic interface and optically controlled actuators, which modify engine and airframe control surfaces. A wide range of fibre-based databuses, with speeds ranging from 1Mb/s to 1Gb/s, will be incorporated. The term ‘fly-by-light’ has been coined to describe these technologies and includes fibre optic interconnects at the backplane of avionic modules as well as all redundancy networks.

Figure 1 illustrates a simplified ‘fly-by-light’ network for propulsion and flight control applications (Baumbick, 1985). Fibre optic waveguides link the computer of the airframe and propulsion system with their respective optical sensors and actuators which are to be optically controlled. For integrated control of the airframe and propulsion systems, the two computers are linked via fibre optics.

In these systems, an increasing number of communications channels, sensors and redundancy levels are required to satisfy more complex propulsion and flight control systems and more stringent safety requirements. The concept of several data channels sharing one fibre – multiplexing – is well es-

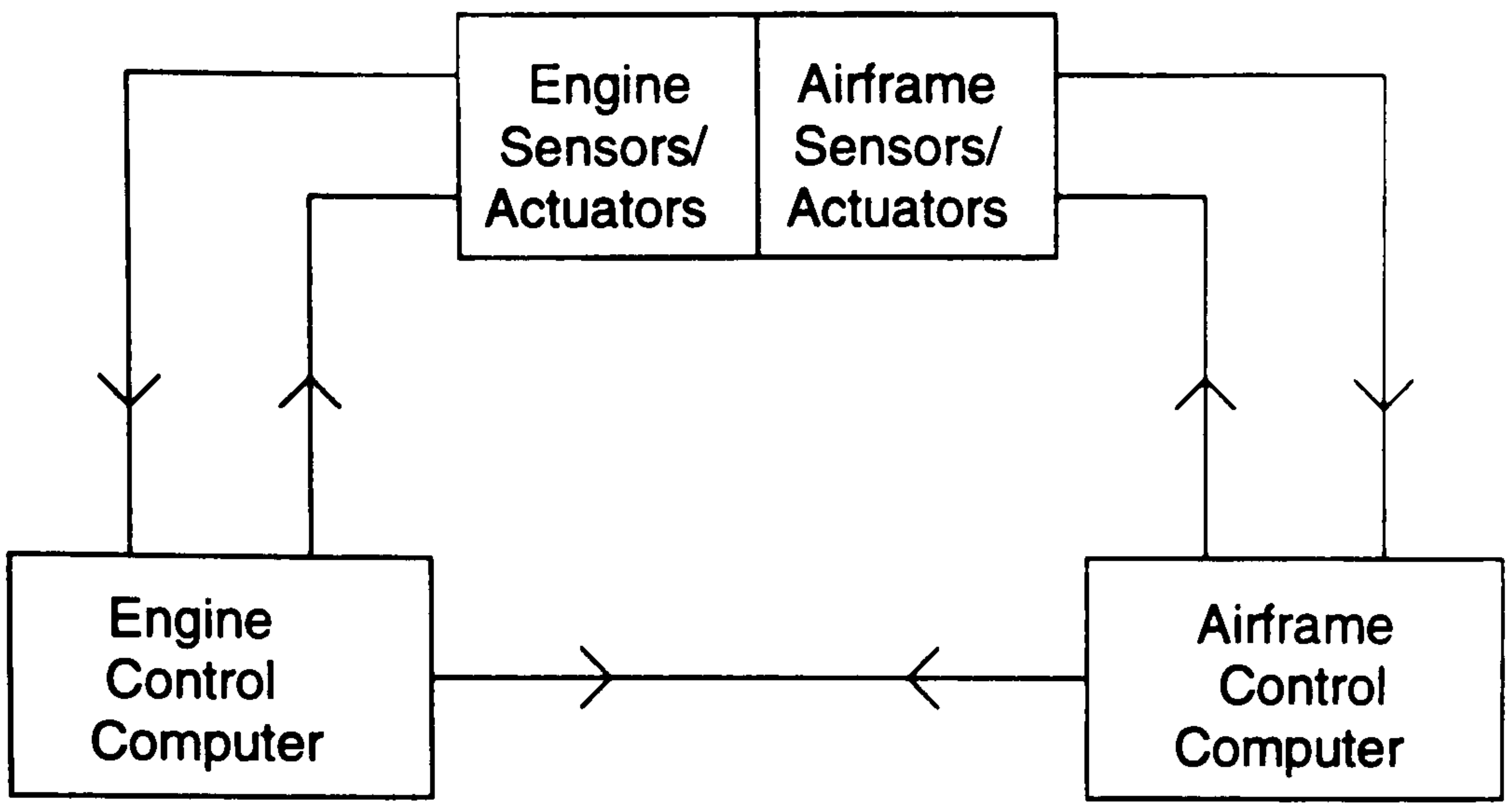

Figure 1: Simple 'Fly-By-Light' Circuit for Aircraft

tablished in communications and is an important motivation for employing optical databuses on aerospace platforms. Multiplexed sensor systems, in which several sensors share one fibre network, are advanced at the laboratory level (as discussed in section 1.2.2) and are also directly relevant to many aerospace applications. Indeed, the benefits of fibre optic sensors in flight control at the system level is often not in the performance of the sensors themselves (though passive sensing at levels exceeding electronic sensors *is* attainable and optics *do* offer certain unique sensing functions). Rather, it is the attribute of fibres to form multiplexed arrays of sensors to share one electro-optic interface that is often of most significance.

One problem (eg Glomb and Varshneya, 1988) has been the growing number of input and output parameters for the control processor. Though the processors are shrinking in size, the demands on input/output circuitry and power electronics are increasing which limits miniaturisation of the electronic enclosure. Multiplexing clearly reduces the number of wires, connectors and circuits required. *Optical* multiplexing produces even further weight reductions above that obtained by directly replacing conventional systems with fibre equivalents. The number of sensors allocated to a single interface is then limited by system fault tolerances. The interface number is set to minimise malfunction probabilities of flight control systems. A preferred multiplexing technique is still to be established. Compatibility with a large number of sensors is one important factor, for example. However, the capacity afforded by fibre optics to implement these systems are key factors drivers for continued development of the technology.

The Sowerby Research Centre (SRC) is the BAe corporate research centre and provides a research service to all the operating companies of BAe, including Military and Commercial Aircraft Divisions and, at the outset of the study, the Rover Group and BAe Space Systems. The centre contributes to the long term technology requirements of BAe. When this project was initiated in 1989, the SRC's role was to conduct medium-to-long term research in areas likely to impact on company products up to 10 years into the future. For the reasons outlined above, and particularly because of its inherent multiplexing capability, research was instigated into fibre optic technology for aerospace applications. As well as assessing the potential benefits of fibre optic systems for company products and raising awareness of the technology throughout BAe (partly described through this introduction), the research was targetted towards areas deemed relevant to the company's future requirements.

Much evidence has emerged in the last decade on exploiting the fibre optic properties described above to the wide range of applications in aerospace for sensors. Though many fibre sensors have been proposed and shown to operate effectively in the laboratory, there are comparatively few installed and functioning in the production environment. One major reason, perhaps, is the generally prohibitive unit cost of the fibre sensors in comparison with conventional transducers. Another reason is the lack of a standard suite of sensing formats compatible with signal processing systems. It has been demonstrated, for example, that a wide variety of conventional aircraft electrical sensors are addressed by a few standardised interfaces. Future fibre sensor arrays will also need to be interrogated through a limited number of interfaces and standardisation of this interface will be a major issue in introducing fibre technology for aerospace applications (Morton and Little, 1993).

Multiplexed sensor systems, in which a number of passive sensor heads share a common network and download signals of a similar format to a single, central processor, provide one possible solution. Higher levels of sophistication are provided by fully distributed sensors in which the *whole length* of fibre acts as the sensing element and the system output provides information on both measurand magnitude and distribution. This ability is unique to fibre optics. The potential benefits to aerospace platforms in terms of weight reduction, EMI immunity and all the other factors outlined above are enormous. The project was, therefore, initiated to study novel optical signal processing and sensing techniques relevant to aerospace in which

(a) the optical outputs are most compatible with conventional, well-established signal processing formats and

(b) the sensors can be configured, and optical outputs processed, to provide data on the spatial distribution of the measurand.

It is well-established, with regard to point (a), that the outputs from frequency modulated sensors can be simply and accurately converted into a digital form (Venkatesh, 1988). The digital signal processing and control circuitry that can be incorporated is capable of high precision, stability and reliability, important factors in aerospace applications. Further, such systems are immune to down-lead effects such as signal attenuation that reduces system sensitivity.

Several optical sensing techniques satisfy the requirements for spatial distribution measurement. In principle, any intrinsic process, in which the measurand modulates a property of the light within the fibre, is a function of fibre length. (Specific sensing principles are reviewed in section 1.2.) Extraction of both measurand information and its distribution is difficult, however. One major problem is the available optical power which can limit the spatial and measurand resolution, particularly in extended networks. This is compounded by the fact that the sensing principle is often based on light attenuation, thereby degrading the performance of sensing elements further along the network. Though sophisticated signal processing exists to recover much of the information, this can offset many of the advantages of utilising fibre sensors in the first instance.

Hence, in order to minimise signal processing complexity and meet the general requirements discussed above, there is a need for a sensing mechanism in which:

(a) the power of the output optical signal is maximised with respect to the optical input,

(b) the output signal can be efficiently converted to an electrical signal for post-detector processing,

(c) the output signal contains a frequency component, readily modulated by a given measurand,

(d) the output signal frequency is an absolute measure of the measurand,

(e) the output signal contains information related to fibre length.

In nonlinear optics, intense optical fields are used to induce effects in materials that cannot be predicted by the basic properties of reflection, refraction and absorption. The high power sources and low loss fibres prevalent in communications meant that nonlinear effects readily occurred in these systems. Hence, the majority of research has been aimed at either the suppression or exploitation of such effects specifically to enhance data transmission capacity. The use of the properties in either sensors or signal processing elements for sensors has been largely neglected. However, many attributes of non-linear mechanisms satisfy the requirements listed above. For example, for point (e), the interaction length between the optical pump initiating the process and the medium supporting the process, critically determines the magnitude of the effect. This will be demonstrated when the most relevant nonlinear processes for fibres are described in Chapter 2.

One nonlinear effect alone, however, satisfies all the criteria described above. This is Stimulated Brillouin Scattering (SBS), the lowest threshold process to occur for the cw, narrowband optical sources and the fibres commonly used in communications. The signal produced from the interaction is frequency downshifted with respect to the excitation source. Further, this downshift is proportional to the core refractive index and is *amplified* back towards the source. Hence, the output power is relatively high and, by modifying the optical properties of the fibre, a Frequency Modulated (FM) output can be attained. SBS therefore can be utilised in sensors in which an external measurand perturbs the fibre to modulate the signal. Alternatively, some preset modulation to the fibre core, via birefringence for example, may be used to generate signals of a known frequency. These carriers, in turn, can be exploited in sensors for signal processing purposes.

The aim of the project was therefore to explore both signal processing and sensing strategies based on SBS in monomode optical fibres, investigating fully, both the advantages to be gained and limitations imposed by, the SBS process. Though the research has not targetted any one specific application, the work has been aimed at developing new techniques which potentially satisfy future aerospace requirements (described in section 1.2.3).

1.1.2 Structure of Thesis

The general technical and strategic motivation for undertaking the research project was outlined in section 1.1.1. This is one requirement of the Cranfield University, SERC supported *Total Technology* PhD programme. Another is to place the research, though long term in nature, into the context of the company research programme, in which potential applications are to the forefront. Thus, since the study was also initiated to raise awareness of the capabilities of fibre optic sensors within BAe, a broader review of the area of fibre optic sensors was necessary than is common in such projects. Hence, the project is introduced with a synopsis of fibre optic sensor developments relevant to aerospace platforms. For fibre optic point devices, generic sensor types are described and briefly compared (1.2.1). The signal processing and electro-optic interfacing requirements of the sensors are discussed. Developments in both multiplexed and distributed topologies are then reviewed (1.2.2), before addressing specific aerospace applications, particularly for military and commercial aircraft relevant to BAe (1.2.3).

Chapter 2 considers both the theoretical and experimental characteristics of non-linear optical interactions in fibres. A general formulation for describing optical non-linearities (2.2.1) precedes a short description of fibre propagation properties (2.2.2). The basic characteristics of the most common effects in fibres are compared and contrasted (2.3) in terms of fibre properties (eg core geometry) and pump attributes (eg polarisation). Section 2.4 then concentrates on Stimulated Brillouin Scattering (SBS). The steady-state build-up of SBS in fibres was derived as part of the project and this analysis is outlined (2.4.1). This enabled direct comparison between theory and experiment. Associated Brillouin mechanisms are also briefly introduced. In order to better illustrate the theoretical analysis, the general experimental properties of SBS fibre systems are reviewed using examples mainly drawn from the literature (2.4.2). The time-dependent properties of SBS that are a feature of the outputs of many SBS fibre systems and were observed throughout the work reported here then completes the chapter (2.4.3).

The first application for SBS addressed in the study was to generate an all-optical heterodyne element for use in fibre optic sensors (Chapter 3). The work was undertaken firstly to demonstrate that FM signals could be produced compatible with the bandwidth of conventional optical detectors (ie in the kHz to GHz spectral regime) but also because an all-fibre heterodyning component is of potential benefit to many aerospace sensor applications. In addition, the work enabled a full assessment of the SBS properties of the available fibres (which represented a wide cross-section of potential sensor fibres). After a brief review of alternative in-fibre frequency shifter devices (3.2), the principles of the SBS-based approach investigated in this study are given (3.3). Six predominantly single-mode fibre types were studied and were fully characterised in terms of SBS for the cw laser sources used (Argon Ion emitting at 0.5145μm and Nd:YAG at 0.532μm) (3.4.1). A range of experimental systems are then described which successfully demonstrated the principle of the frequency shifter technique (3.4.2). These consisted of both single and dual fibre systems in which carrier signals from 8MHz to 665MHz were generated. Significantly, the first single fibre frequency shifter using SBS was demonstrated during this work. The properties of the frequency and intensity instabilities measured in the SBS output spectrum during this work were then assessed experimentally (3.5). They are then linked to the transient effects described in Chapter 2. Techniques to reduce their influence in the context of sensors and signal processing applications are reported for the first time. Throughout, the findings are compared with equivalent experimental SBS systems cited in the literature.

One significant feature exhibited by several fibre samples during the frequency shifter work, especially at the Argon Ion pump wavelengths, was fibre photosensitivity. This produced large changes in fibre attenuation in certain samples which, in turn, modulated the SBS conversion efficiency. An assessment of the photosensitive properties was undertaken and described in Chapter 4. Experiments measuring changes in fibre attenuation (4.2) and fibre polarisation (4.3) are reported. These are used to infer the optimum fibres and sources for *SBS-based* systems which suppress these processes. Comparisons are made directly with the abundant literature that exists on the subject (4.4).

Chapter 5 concentrates on specific sensing mechanisms exploiting SBS in fibres. The systems are based on both direct (5.2) and indirect (5.3) FM concepts. For *direct* modulation systems, both point (5.2.2) and two-element multiplexed topologies (5.2.3) were investigated as temperature sensors in single source systems. Dynamic range and the spatial and temperature resolutions are reported and techniques to enhance all three key properties of sensors are discussed. A detailed assessment of these sensing techniques is made (5.2.4) and it is shown, for the first time, that it is the temperature sensitivity of the acoustic phonon velocity, rather than the core refractive index, which largely modulates the Stokes signal with temperature. Alternative sensor systems based on differential modulation of the SBS carrier (5.2.2) and modulation of sustained oscillations present in the output of SBS fibre systems (5.3) are considered. Though the latter proved unsuccessful, some information was obtained on the sustained oscillation properties of optical fibres.

Potential improvements to the systems detailed in Chapters 3 and 5 are addressed in chapter 6. In particular, systems which minimise both the volume and weight of the optical components by utilising fibre ring resonators are described and assessed for signal processing and sensing applications (6.2). Alternative sensor systems based on non-linear effects in fibres are described (6.3) before the technical issues are completed with some general comments and recommendations for further research (6.4).

Another feature of the *Total Technology* programme provides the candidate with specialised management training and the opportunity to complete a management exercise linked to the scientific research. This is in addition to placing the research into the context of the company research described in this chapter. In Chapter 7, then, the practical issues on which a cost benefit analysis between fibre sensors and conventional transducers can be based are described. The discussion includes examples from both commercial and military aerospace sectors.

In Chapter 8, the principal achievements of the research are summarized and conclusions drawn.

1.2 Fibre Optic Sensor Technology Synopsis

1.2.1 Point Sensor Overview

An optical sensor or transducer consists of four basic elements as shown in Figure 2. An optical source converts electrical power into an optical signal. An optical system, located adjacent to the physical parameter to be detected (the measurand), imposes some modulation onto the optical signal. The modified signal is then reconverted to an electrical impulse and downloaded to suitable signal processing elements.

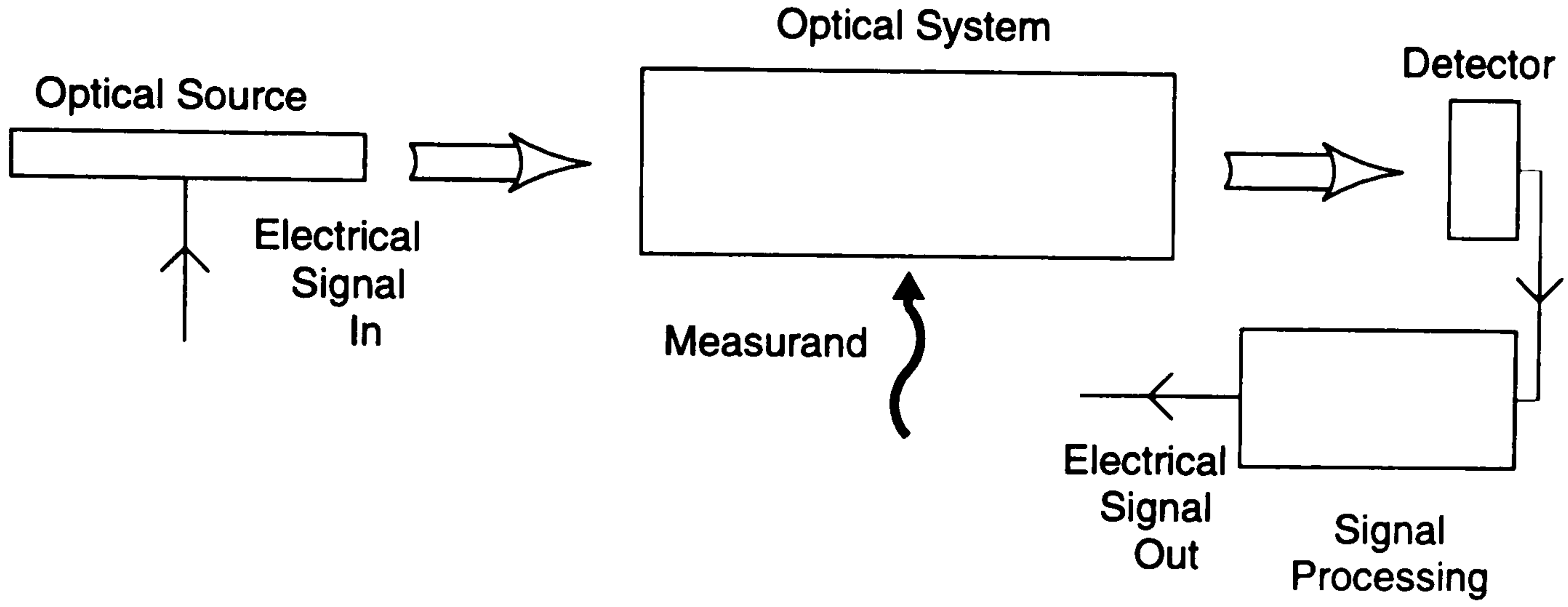

Figure 2: Basic Optical Sensor Configuration

Fibre optic sensors are generally classified into two groupings (Dakin and Culshaw, 1988). In *extrinsic* sensors, the fibre merely guides the optical signal from the source to the sensing region. The light interacts with the measurand externally to the fibre and is transmitted via fibre to the detector. The intensity of the light is usually modulated in such systems. In *intrinsic* sensors, the measurand modulates one or more properties of the light propagating within the fibre itself. No optical interfaces or additional components are necessary at the sensing region, thereby minimising insertion losses and contamination. For both sensor types, properties to modify are the intensity, wavelength (ie colour), polarisation, phase and frequency of the light. Since the photodetector responds only to intensity changes in the incident light, the optical system must be appropriately configured at the pre-detector stage to process the other parameters. In this section, the characteristics of those extrinsic and intrinsic fibre point sensors most relevant to aerospace are compared.

Extrinsic, intensity modulation sensors generally feature simple, low-cost designs for many applications. Many reflective optic based systems, for example, use a single multimode fibre to transport light from the source to the sensing head (Figure 3). The same fibre then transmits reflected light back to the detector. Displacement of the reflective membrane along the fibre axis modifies the intensity of light recoupled back into the fibre. Linear displacements of up to 1mm have been measured using this technique (Economou and Davies, 1987), employing a 0.3 Numerical Aperture (NA), 100μm core radius fibre and a silicon diaphragm sensing head.

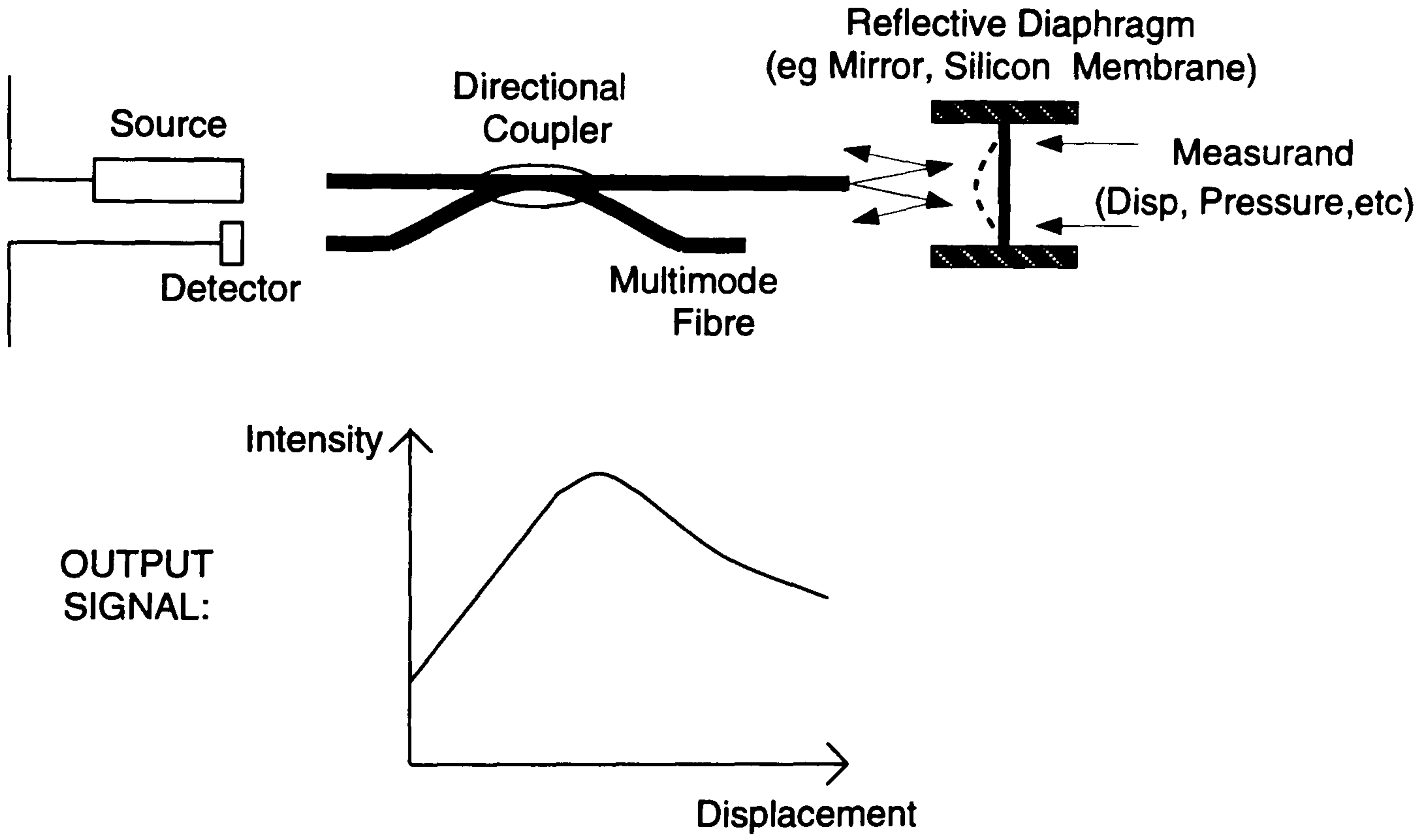

Figure 3: Extrinsic, Intensity Sensor Exploiting Reflective Optics

Many variants of this configuration exist. In all systems, the trade-off between dynamic range and sensitivity is determined by both fibre and sensor geometry. Note that silicon head devices can be adapted to sense both pressure and strain, as well as displacement.

Simple transmission based extrinsic sensors have been proposed. The displacement of transmission masks (Baumbick, 1985), bulk lenses, Moire filters or spatially varying optical density filters directly modulates the intensity coupled between input and output fibres. A pressure sensor based on displacement dependent evanescent coupling between two appropriately configured fibre cores (Spillman and MacMahon, 1980) demonstrated $5\times10^{-3}\mathring{A}$

displacement sensitivity over a 3μm dynamic range.

All the systems described have produced an analogue output and are therefore degraded by intensity drift in the source and optical system (so called 'downlead sensitivities'). Some intensity referencing is thus necessary to improve sensor performance. Two adjacent wavebands derived from one source may provide sensing and reference signals respectively. Alternatively, and to obviate the requirement of an A to D converter in the signal processing, digital encoding techniques can be employed in the sensor head. An incremental encoding device has demonstrated 10 minute rotary displacement resolution over 90° (Miller, 1986). Digital systems possess high inherent accuracy due to intensity variation immunity and are fully compatible with digital electronic processors. Analogue devices are usually simpler in design and have potentially greater resolution but only if accurate referencing is achieved. The graceful degradation in performance of analogue devices contrasts with digital fault mechanisms in which the loss of one bit of data can be catastrophic (Figueroa et al, 1991).

Many extrinsic intensity based sensors have been proposed. For example, both the total emission and spectral distribution of black-body radiation are functions of the surface temperature of the radiating source. A pyrometer transducer using sapphire collecting optics and fibre optic cable was used to monitor temperature up to 600°C (Wrigley, 1986) from gas turbine engines. Thermal modulation of the band gap in semiconductors has yielded intensity sensors showing ±0.2°C sensitivity over the 20 to 180°C range (Kajanto and Friberg, 1988). Fluorescence quenching is a common technique in analytical chemistry for trace-gas detection (Wolfbeis, 1985) and is compatible with fibre optics. A fibre may be coated with an appropriate fluorophore which simultaneously delivers the excitation pump and, since emissions occur in all directions, directs the fluorescent energy to a remote detector. Both the magnitude and spectrum of the fluorescence are functions of temperature which can be exploited in high resolution sensors (Robbins, 1986).

The scope for intrinsic intensity modulation devices is more limited due to the relative inaccessibility of the light. The presence of a chemical adjacent to the core/cladding interface can modify the evanescent field properties through localised index changes and/or the introduction of scattering centres. The intensity of the light propagating in the core is then modified, a technique that has been adapted for fuel sensing (Pitt, 1977). In microbend sensors (Figure 4), the modal distribution, and hence fibre transmission, is modified by periodic, externally applied forces arising from displacement, strain or pressure (Johnson, 1985). High resolution devices are feasible, again provided that optical references are included.

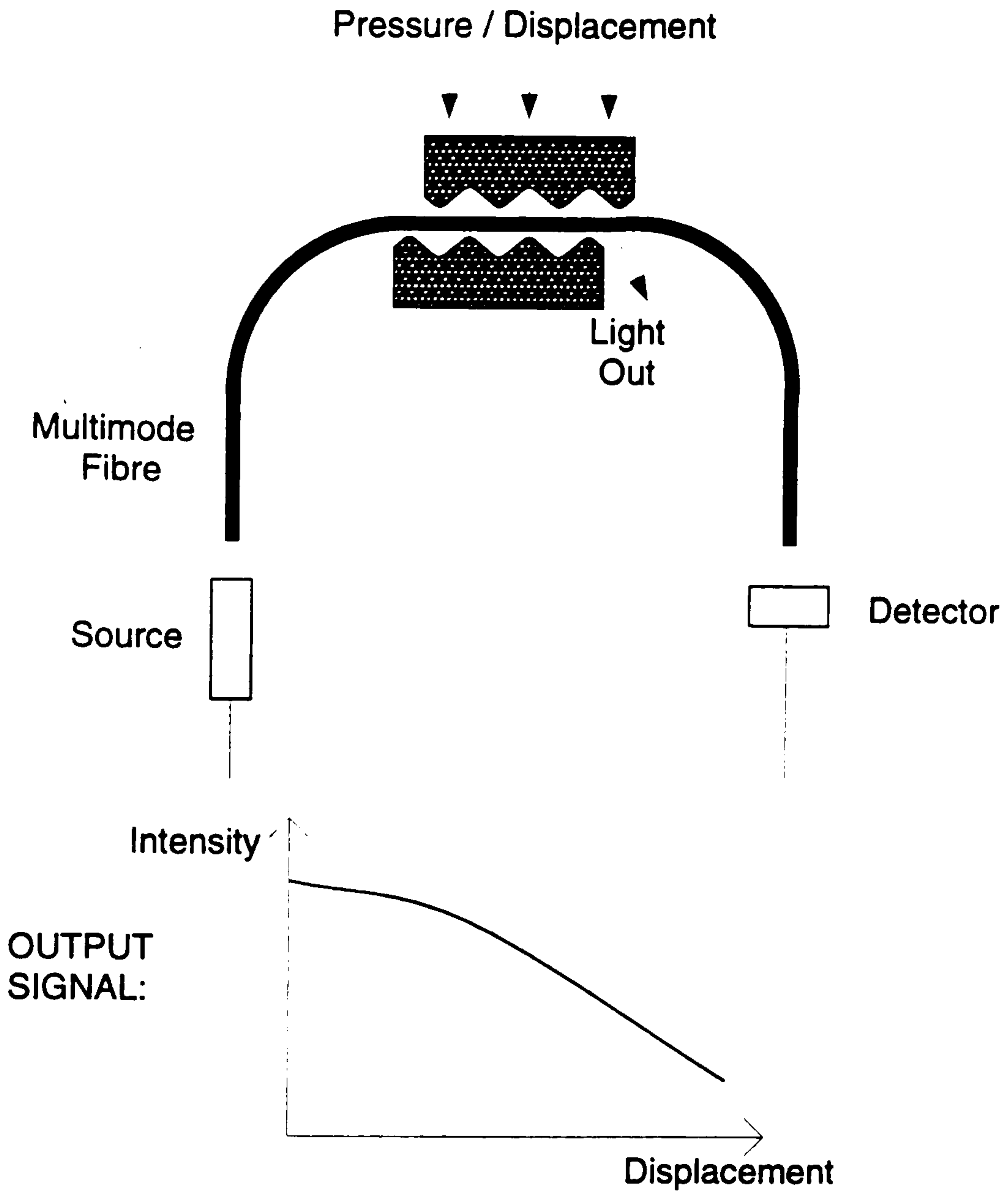

Figure 4: Fibre Microbend Sensor (after Fields et al, 1980)

Wavelength based modulators, though generally more complex than the intensity systems, contain an inherent degree of self-referencing. The measurand modulates one or more wavebands simultaneously, leaving others sensitive only to system intensity drifts. Wavelength sensors are again predominantly extrinsic, with fibres directing light from a broadband source to the sensor head and returning modulated flux to a remote spectrometer or spectral filter array. Both analogue and digital devices have been reported.

Figure 5 illustrates a displacement sensor which utilises digital and multispectral techniques (Fritsch and Beheim, 1986). Light from two broadband LED's (which produced a 100nm FWHM bandwidth spectrum) is delivered to a reflection grating using a 100μm fibre. Diffracted light then illuminates a 10-bit encoder, via a GRIN lens, consisting of alternate opaque (OFF-state) and reflective (ON-state) zones. Light reflected back into the fibre is directed to a remote spectrometer for demultiplexing. The position of the plate is determined by the binary output spectrum. High cross-talk suppression and signal to noise values (>35dB) coupled with low insertion losses (<10dB) highlight the potential of the approach. In section 1.2.3, aerospace applications for this type of sensor are outlined.

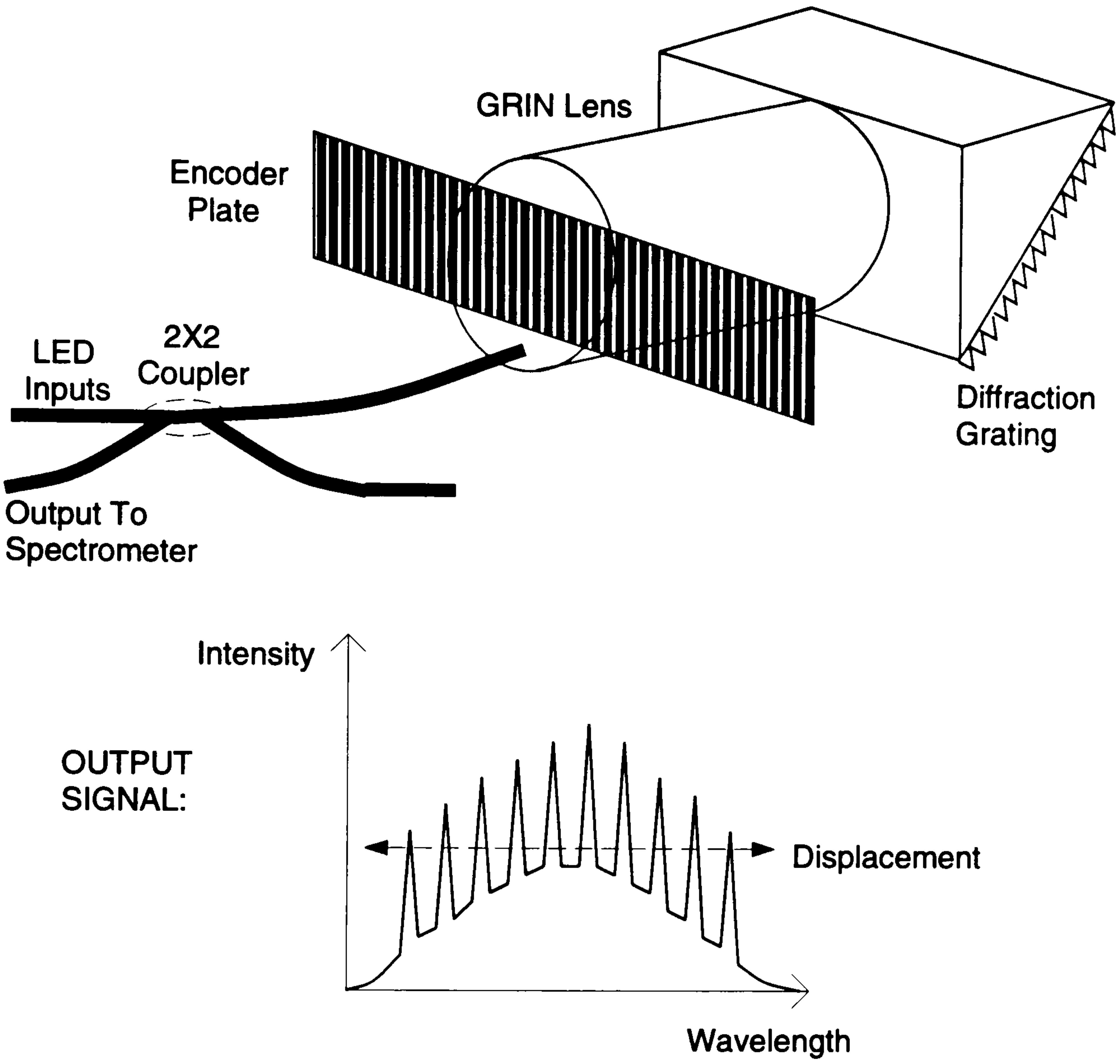

Figure 5: Digital Position Encoder Utilising Wavelength Modulation

One final extrinsic wavelength modulation technique of interest exploits the strain dependent resonant Raman spectra of polydiacetylene (PDA) crystals (Underwood, 1989). Raman spectroscopy is a well established diagnostic tool used to characterise chemical compounds. Resonance Raman scattering occurs when the exciting pump (laser) has an energy equal to or close to the absorption energy of a given molecule. Molecular excitation and subsequent emission of a signal up to 10^6 greater in intensity than the spontaneous Raman signal can occur. In crystals such as PDA, the output signal wavelength is a linear function of applied strain up to the fracture point (≈2% strain). This technique has been used to measure strain distribution within composite material structures.

An important new class of *intrinsic* wavelength modulation sensors have recently emerged based on the photorefractive properties of germanosilicate single-mode fibres (Meltz and Morey, 1991) which allow localised Bragg reflection gratings to be formed within the core. The basic mechanism is linked to the photosensitive phenomenon to be reported in Chapter 4. By modulating the temperature and/or strain adjacent to the grating, reflected spectra may be modified. Indeed, several gratings can be written along a single fibre, sensitive to different spectral regions of a single broadband source. The technique provides potentially localized and absolute measurement with a fast response time. There is much interest in developing a passive method of demultiplexing the outputs from several gratings simultaneously, that can be readily miniaturised into a sensing head and is fully compatible with fibre technology (Measures et al, 1992). Aerospace applications for these systems are detailed in section 1.2.3.

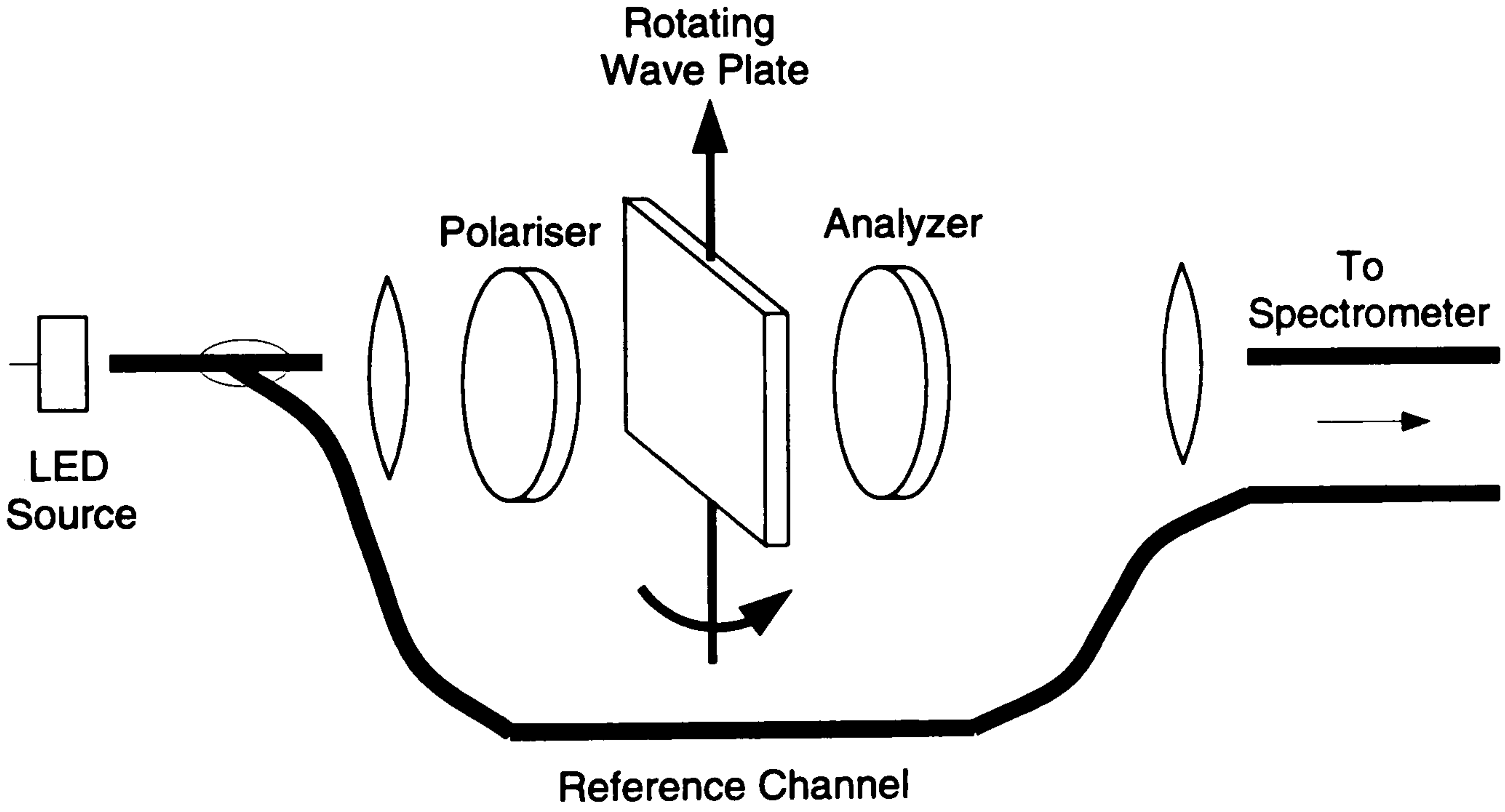

Figure 6: Extrinsic Polarisation/Spectral Modulation Technique

In extrinsic polarisation sensors, the polarisation perturbation is imposed onto the intensity or spectral characteristics of the light. The system shown in Figure 6 operates by detecting wavelength minima in the output spectrum in response to rotary displacement (Spillman and Fuhr, 1988). Light from a broadband source is polarised at 45° to the optic axis on exiting the fibre and passes through a tilted waveplate. The retardation induced by the plate is a function of wavelength so that, on passage through a second polarizer, one wavelength component of the spectrum is extinguished. The minima is shifted as the waveplate rotates and detected at a remote spectrometer. The system demonstrated 1% angular resolution over a 30° scan range and was fully referenced.

The birefringent properties of optical fibres (discussed in section 2.2.2) have been exploited for point strain, pressure and temperature measurements. Straining the fibre, for example, modulates the relative retardance between the two principal axes of birefringent fibre through both geometrical path and refractive index variations (Bock and Wolinski, 1990). This data is imposed onto an input beam polarised at 45° to the principal axes and converted to an intensity modulation by an analyzer at the fibre output. The principal disadvantages of the technique include the cross-sensitivity to other measurands and the cosinusoidal nature of the system transfer function. Optical configurations and signal processing schemes to offset these problems are considered below in the phase sensor discussion.

Phase modulation sensors possess the highest sensitivity to all measurands. Fibre interferometers are direct analogues of well established bulk optic designs as illustrated in Figure 7. In the Michelson and Mach-Zehnder interferometers, beamsplitting is achieved using 2×2 directional couplers. In the Michelson interferometer, mirrors are chemically deposited onto the fibre terminations – no mirrors are required in the Mach-Zehnder. Further advantages of the Mach-Zehnder are that feedback to the source is minimised and two anti-phase outputs are obtained, which is useful for signal processing. The Michelson, however, is a double-pass system and possesses twice the sensitivity. Further, the reference and signal arms can be placed in close proximity to maximise common mode rejection of environmental perturbations.

The Fabry-Perot system has the advantage of simplicity and can be configured to operate in either intrinsic or extrinsic modes. In the intrinsic device, the reflections from the front and back interfaces of the fibre interfere at the device output. In the extrinsic form, light from an external reflection interferes with the Fresnel reflection from the adjacent air/core interface. The differential interferometers discussed above generally require an external polarisation element to access the retardance data. Though less sensitive than the direct phase modulation counterparts, these devices possess a higher dynamic range. Sensors described in Chapter 5 are SBS analogues of direct and differential interferometers; instead of modulating the optical *phase*, the frequency of the SBS backscattered signal frequency was modulated.

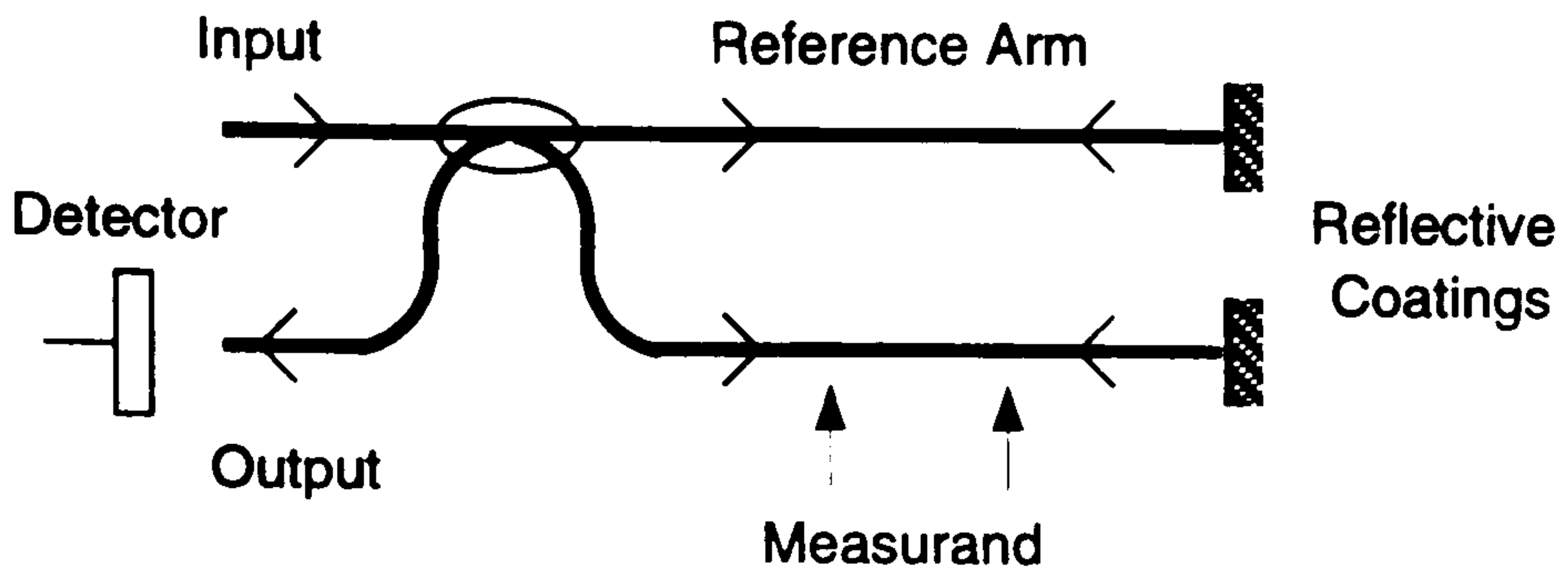

(a) Michelson Interferometer

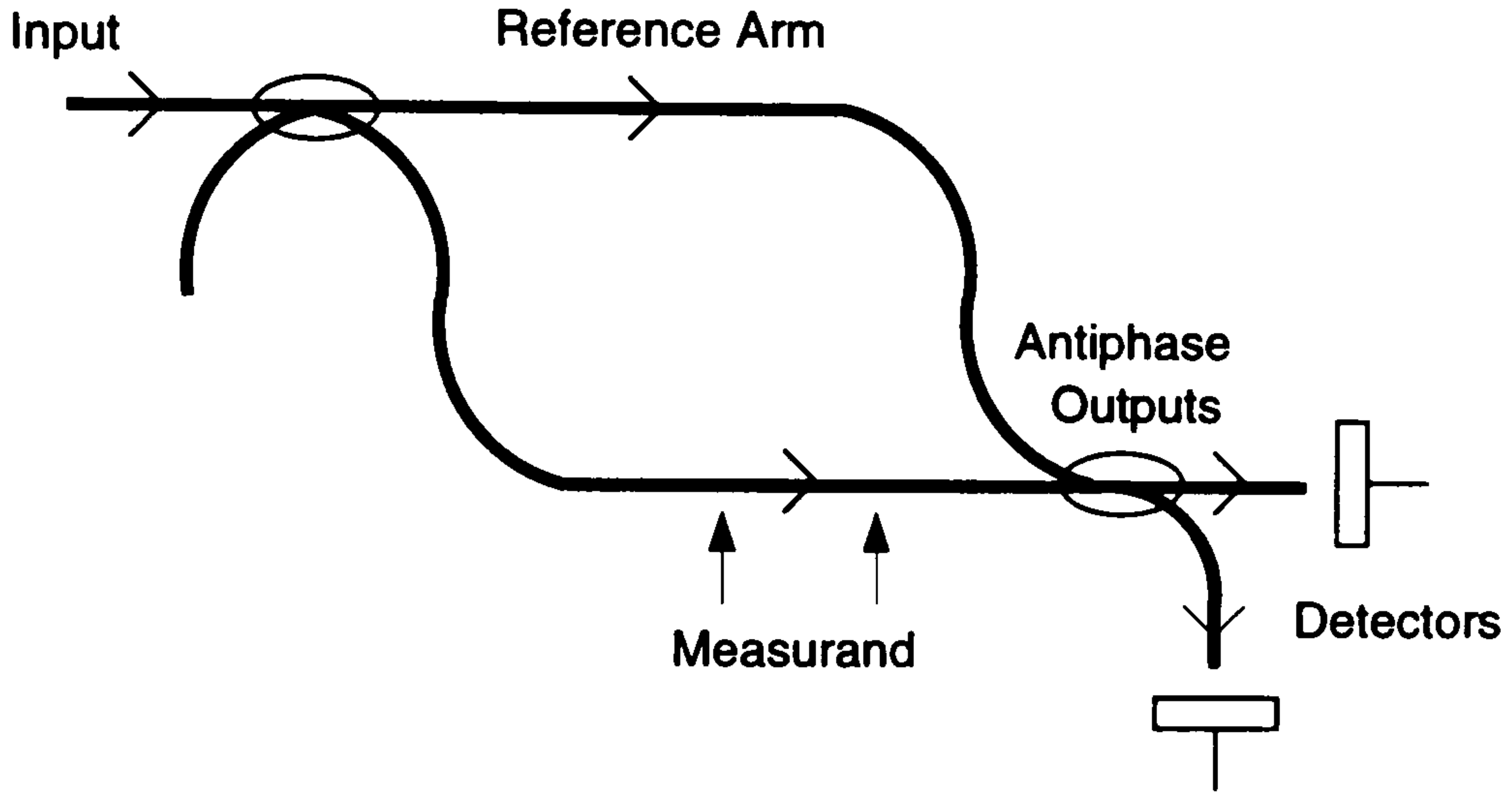

(b) Mach Zehnder Interferometer

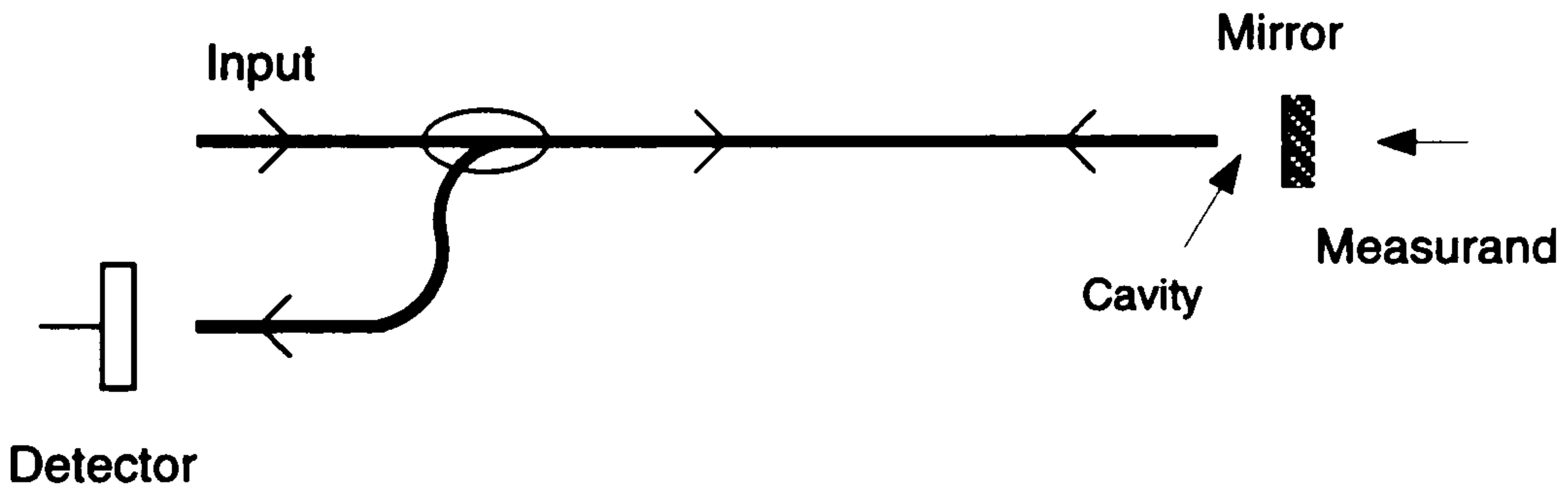

(c) Fabry Perot Interferometer

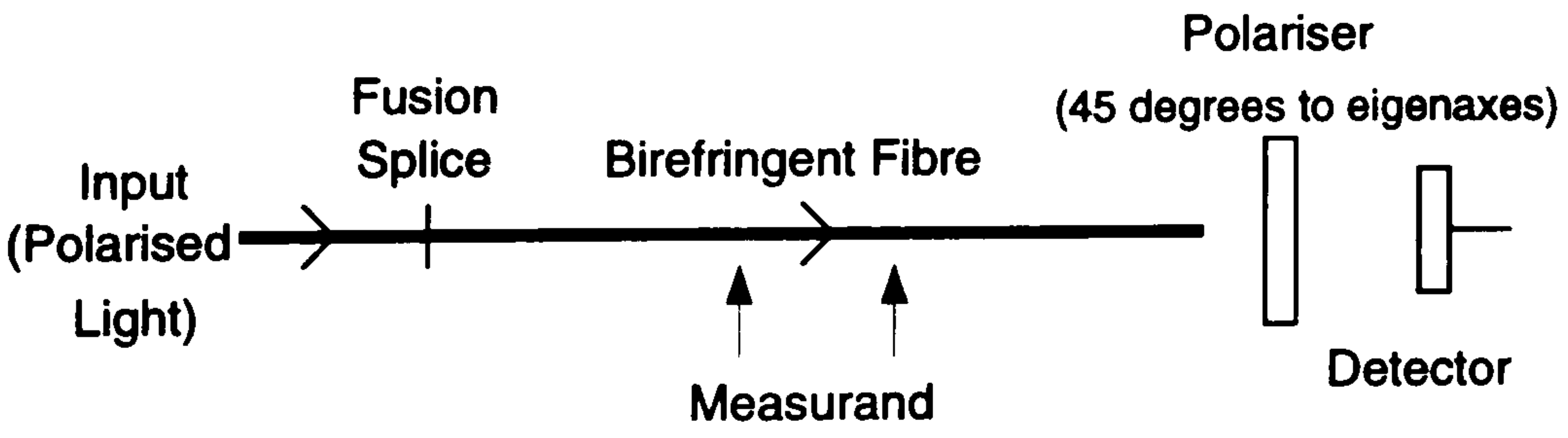

(d) Differential Interferometer

Figure 7: Fibre Optic Interferometer Configurations

Major problems associated with fibre optic interferometers are:

- the cross-sensitivity between measurands, particularly temperature,
- the cosinusoidal sensor transfer function which limits dynamic range, produces a variable device sensitivity and can cause signal fading,
- the inferring of absolute values of the measurand,
- system initialisation.

A wide variety of signal processing schemes have been proposed to overcome these problems (Jones and Jackson, 1986). In active homodyne processing, for example, the reference arm of the interferometer is phase modulated by wrapping the fibre around a piezo-electric cylinder. This is directly controlled via servo-feedback from the detector and maintains the output at quadrature. The feed-back signal is then band-pass filtered to extract the signal of interest. In passive homodyne systems, two antiphase outputs from the interferometer are arranged to vary as quadrature functions of the induced phase difference. Two output channels from a 3×3 directional coupler in conjunction with electronic filtering are often used.

Heterodyning, in which light in the reference arm is frequency shifted with respect to the sensor arm, offers a large dynamic range and the detection of fringe direction. Conventional acousto-optic Bragg cells which typically provide 40/80MHz shifts are not fully compatible with fibre optic systems due to high insertion losses and their electrical drive requirements which renders them unsuitable in harsh environments. In Chapter 3, an all-optical technique to produce a heterodyne carrier is described for use in these type of sensors. A range of pseudo-heterodyne modulation schemes have been developed in which the carrier is produced indirectly in the output of the interferometer. For example, by ramping the injection current of a laser diode with a serrodyne waveform and setting up a path imbalance in the interferometer, the output frequency and, hence, fringe pattern is continually modulated (Jackson et al, 1982). By bandpass filtering and using a phase comparator between diode driver and output modulation, the measurand is recovered.

The dynamic range of the sensor can be improved by exploiting dual wavelength, two source interferometry (Kersey and Dandridge, 1987). Stable wavelength sources are essential, though the dynamic range, inversely proportional to the wavelength difference, remains limited. Alternatively, using a broadband source, white light interferometry provides absolute measurement over a finite range and a system initialisation capability, though coupling into single mode fibres with such sources is generally more difficult.

Table 1 illustrates typical phase changes for strain and temperature (Akhavan Leilabady et al, 1985) for 0.1m bow-tie, stress birefringent fibre at 0.6328μm (3mm beat length). Both direct and differential phase sensitivities are included for comparison. The numbers do vary between fibre types.

Measurand	*Direct Interferometer*	*Differential Interferometer*
Strain	6.5×10^{6} rad m^{-1}	6.5×10^{4}rad m^{-1}
Temperature	100 rad $K^{-1}m^{-1}$	5 rad $K^{-1}m^{-1}$

Table 1 Sensitivity of Direct and Differential Interferometers To Applied Measurands

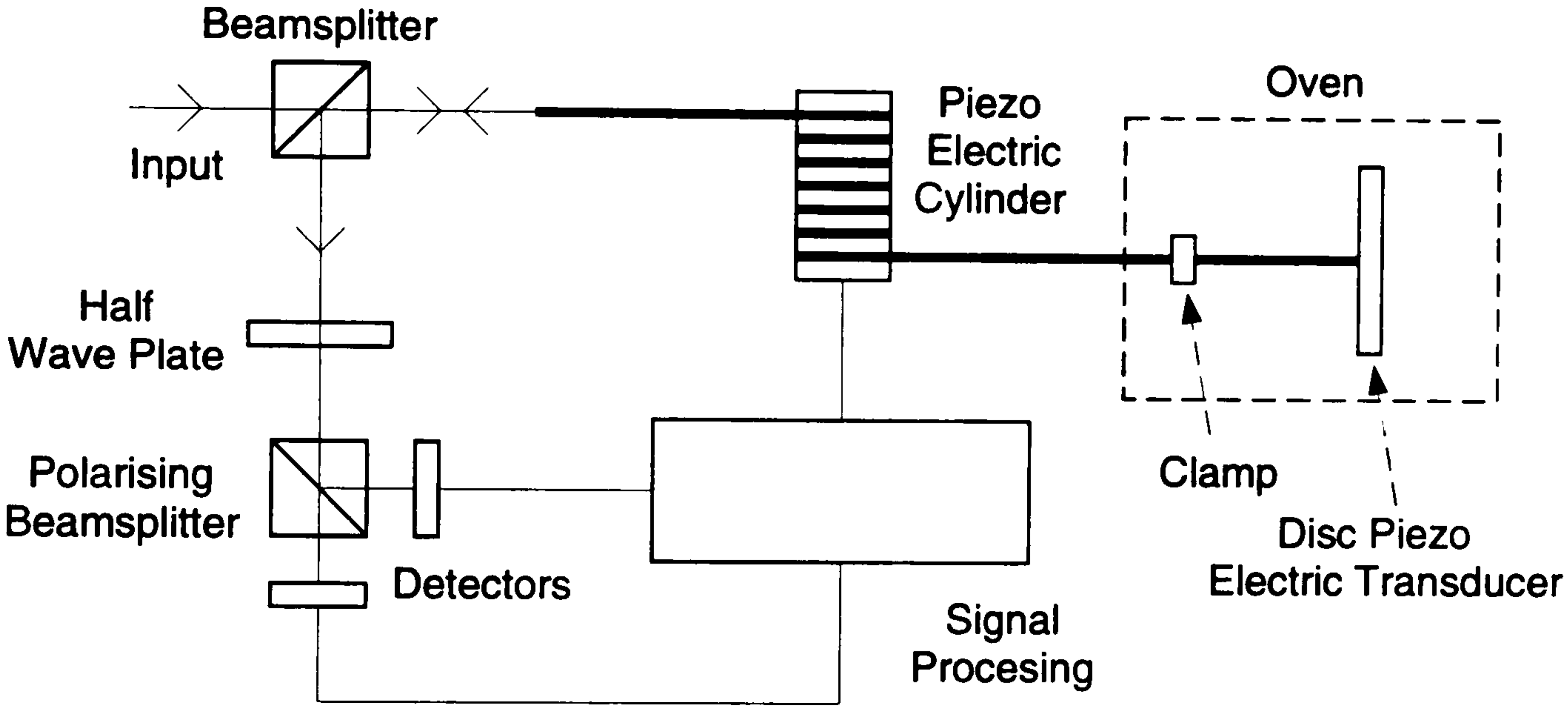

Figure 8: System for Simultaneous Measurement of Strain and Temperature

There is a big demand within aerospace (section 1.2.3) for sensors that can simultaneously sense both strain and temperature with minimal downlead sensitivity. One solution (Akhavan Leilabady et al, 1985) combines the high resolution and high dynamic range of direct and differential interferometry respectively. The system is shown in Figure 8. A length of polarisation maintaining fibre is employed as a double Fabry-Perot interferometer – each principal polarisation axis acts as a discrete cavity, the interference patterns being detected at D_1 and D_2. The differential phase change between the two axes are accessed at the signal processing stage. Measurement of absolute phase change along each axis is performed via pseudo-heterodyning with a piezoelectric cylinder scanning across a single fringe. Provided that the direct to differential phase sensitivity ratio is significantly different between the measurands, there is sufficient data to deduce both temperature and strain. More recent attempts using, for example, spatial mode interference combined with polarimetry (Vengsarkar et al, 1990) have had limited success due to the cross-sensitivity of the measurands and polarisation induced signal fade. However, all utilise the Fabry-Perot design which is the most likely interferometer to be configured in aerospace systems due to its inherent simplicity.

Two interferometric systems that have successfully bridged the gap between laboratory and real environments are the Fibre Optic Gyroscope (FOG) and the hydrophone. The FOG (Auch et al, 1987) is based on the Sagnac interferometer in which two countepropagating beams in a closed loop undergo a relative phase shift when the loop is rotated within its plane The fibre optic hydrophone (Culshaw et al, 1977) is being developed for underwater detection of acoustic waves. Though intensity and differential phase modulation schemes have been proposed for this, direct phase interferometers are most commonly used. Several research groups, notably those at Plessey in the UK and NRL in the USA have reported maritime deployment of hydrophone arrays. These techniques are discussed in the next section in the context of multiplexing.

There are relatively few physical mechanisms that directly induce small frequency shifts ($\leq$10GHz) in light, in contrast to the broadband modulation techniques discussed above for wavelength sensors. Thus, frequency modulation sensors are comparitively scarce. However, there are several important benefits to be gained by sensing in this mode. Firstly, frequency-out sensors are inherently insensitive to amplitude variations of the light and down-lead sources of drift, thereby negating the need for additional reference channels. Secondly, the outputs from the sensors can be simply digitised for signal processing and are fully compatible with phase-locked loop or phase sensitive detection circuits for additional noise suppression.

The most common frequency modulation mechanism used in sensors is the Doppler effect. The technique has been exploited for non-intrusive measurements of velocity and turbulence at remote locations (eg Ahmed et al, 1992). Monomode fibre transports coherent light to a remote probe head. Two optical beams are focussed at the measurement point, converging at different angles. Two Doppler shifted signals of different frequency are produced by a particle passing through the measurement point and transmitted via multimode fibre to a detector. Here, the signals are coherently mixed, the resultant beat frequency being proportional to particle velocity. The technique is readily adaptable to 2D flow measurements by reorientating one of the input beams. Use of fibres allows access to harsh environments such as turbomachinery compressors, with the electronically sensitive parts of the system housed remotely.

A frequency-out signal can be indirectly obtained by imposing a periodic intensity modulation onto the light. A new type of extrinsic sensors has emerged based on the optical excitation and detection of resonant vibrations in simple, micromechanical structures such as silicon cantilevers (Venkatesh, 1988). Generally, optical excitation is achieved by intensity modulating a source at the resonant frequency of the structure. By monitoring reflections from the structure from a second source (analogous to the reflective displacement sensors discussed earlier), the vibration amplitude and frequency of the structure is detected and used to monitor local measurands. The resonant frequency of the structure is a function of temperature.

In this section, the principle transduction mechanisms of fibre sensors relevant to aerospace have been described and the relative characteristics and drawbacks of each compared. No universal technique has yet emerged fully compatible with all measurands in all applications. Those which show potential for networking to a single source and signal processing unit will most likely prevail for the aerospace industry. Thus, techniques suitable for multiplexed systems are now described.

1.2.2 Multiplexed and Distributed Sensors

Multiplexing is the ability to interrogate a discrete number of passive sensors via a single fibre network. The array is controlled by a central processor which performs three principal tasks:

- To power the network
- To detect and demodulate the optical data in terms of the measurand
- To perform sensor identification

Multiplexing improves the competitiveness of fibre optic sensors by increasing the efficiency of the passive fibre link and, as discussed in section 1.1, reduces the overall size and unit cost of the system. Multiplexing techniques are classified according to the optical interrogation technique employed (Dakin, 1987). These are now briefly described, together with the principal factors influencing the choice of topology.

In spatially multiplexed systems, each sensor lies on a different fibre link. Interchannel crosstalk is inherently zero since each link is separately addressed from a single source using a scanning unit (Miller, 1986). Disadvantages of the approach are that multiple detectors are usually required, as well as the additional volume and cost of the extra fibre channels.

In Time Division Multiplexing (TDM) systems, a pulsed source addresses each sensor of the array in turn, a length of reference fibre producing the necessary time delay. A single input pulse addressing N sensors therefore produces an output stream of N pulses. A ten element Mach-Zehnder interferometric array has been demonstrated (Kersey and Dandridge, 1989). Pseudo-heterodyne processing extracted the measurand (pressure) and appropriate post-detector gating circuitry enabled sensor identification. Cross-talk was below -50dB and individual devices approached point sensor sensitivity. The power budget, particularly of pulsed sources, usually limits the number of channels in TDM systems.

In Wavelength Division Multiplexing (WDM) networks, each sensor is interrogated at a different wavelength. The input spectrum may be derived from several optical sources (generally impractical) or from a single broadband source in conjunction with wavelength splitting elements. These elements can be intrinsic (eg fibre Bragg gratings) or extrinsic. Operation is limited to a set spectral range. Interchannel crosstalk in these systems limited by the wavelength isolation of the components and is typically only -20dB. Recent developments in intrinsic polarisation based demultiplexers (Ford and Tatam, 1993) and grating devices show promise. In general, the more sensors in the system, the greater the required wavelength coverage and the more components that become necessary.

WDM was recently used in conjunction with TDM to extend the size of interferometric arrays (Kersey, 1991). Two pulsed sources at 835 and 790nm address ten and four element arrays respectively via wavelength sensitive couplers (Figure 9). The 14-pulse train at the output demonstrated -70dB cross-talk levels and ample scope for additional sensors. This hybrid approach appears to hold most promise in terms of maximising channel numbers.

The simplest manifestation of Frequency Division Multiplexing operates by modulating the light from a source at a unique frequency for each sensor in the array. The return signals are combined onto a single fibre and detected through a series of frequency selective elements. In practice, a single source Frequency Modulated Continuous Wave scheme based on heterodyne coherent mixing is used. Typically, the source frequency is ramped with a serrodyne waveform. In an unbalanced interferometer, a carrier signal is formed at the output, the frequency being proportional to the optical delay in the interferometer and source modulation rate. An array of interferometers can be arranged in series or parallel, linked by fibre delay lines. A series of carriers are then produced at the output of the array, each frequency char-

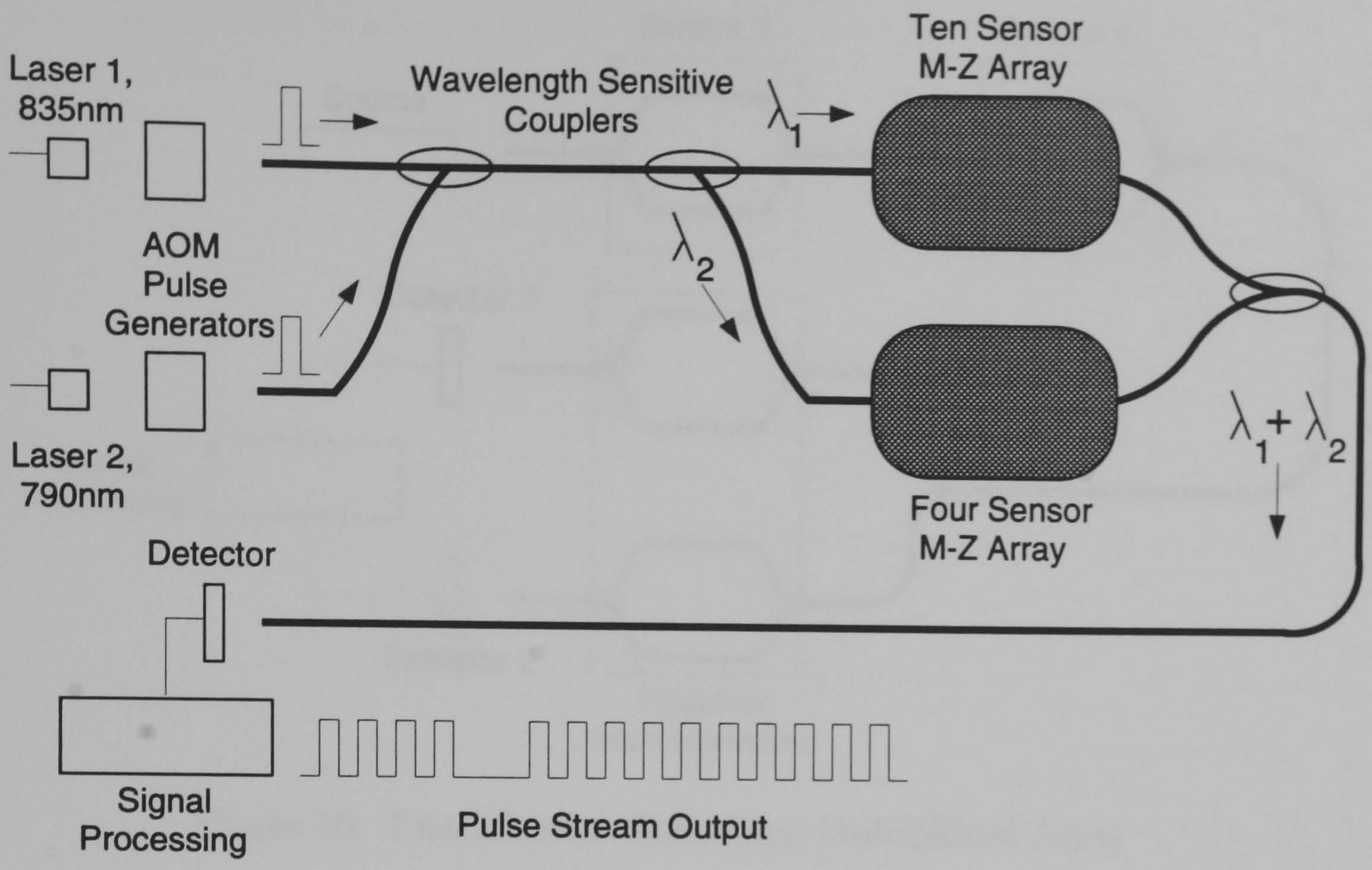

Figure 9: 14 Element Multiplexed Array Based on TDM/WDM Hybrid System

acteristic of one sensor. Changes in both frequency and phase at the output of the system are used to infer the measurand (Sakai, 1986) and no intensity referencing is required.

One final common multiplexed concept is based on temporal coherence processing and is again suitable for interferometric arrays (Brooks et al, 1985). A two element array is illustrated in Figure 10. The path difference in each sensor interferometer operates over a unique range in excess of the coherence length of the source. Prior to the detector, an equivalent number of complementary interferometers are arranged in parallel. The phase modulation from a measurand in one sensor is obtained in only one output interferometer. The system works well for small numbers of sensors. As the array is extended,however, the number of possible path lengths increases and the use of a low coherence source becomes necessary to minimise interchannel cross-talk. Practical implementation thus becomes more difficult.

Increasingly, systems are emerging which combine the techniques discussed above. For example, elements of TDM and coherence multiplexing have been demonstrated (Santos and Jackson, 1991), albeit in only a two element array, to produce two low noise, self-initialising, absolute measure-

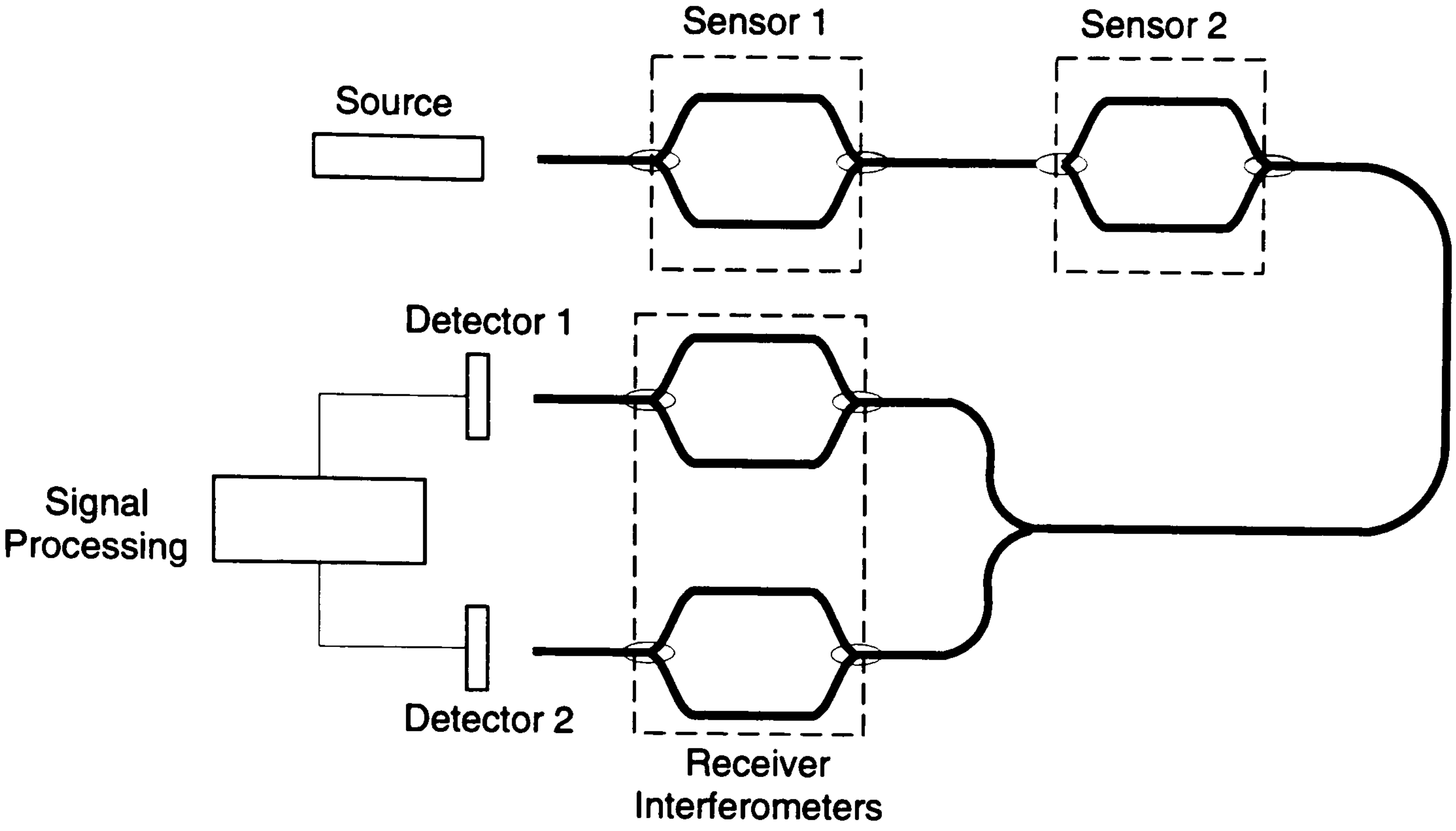

Figure 10: Two Element Coherence Multiplexed Array

ment, high sensitivity outputs. Overall, future commercial constraints will demand multiplexing, except in extreme niche applications. Formats involving some element of WDM and TDM appear most promising, though the exact topology depends on sensor number and type.

The implementation of distributed fibre technology, in which the whole fibre length acts as the sensing element so that the output provides the spatial distribution of the measurand, represents fibre optical technology operating to its fullest potential. The ability to continually monitor a measurand over a wide, flexible area has no true analogue in convential electrical-based metrology, without complex multiplexing and calibration processing. Further, the distributed *fibre* approach provides minimal interference with the operating environment. Clearly, distributed sensing is restricted to those measurands which directly affect the guiding properties of the core or cladding. Distributed sensors are classified by the manner of optical interrogation (Dakin, 1987; Giles, 1987; Rogers, 1987), as with multiplexed systems, and the most common approaches are now listed.

The majority of distributed schemes are based upon reflectometry in which discrete reflections or scattering from the fibre are used to infer the measurand. The magnitude and spatial distribution of the scatter are commonly accessed via Optical Time Domain Reflectometry (OTDR), a technique used in long haul communications networks for fault detection (Figure

11). In OTDR, a high power, short pulse of light is launched into the fibre. The Rayleigh backscatter from the pulse is continuously monitored by a receiver at the input. The backscatter is proportional to the intensity of the field at a given position along the fibre, the time of measurement relates directly to that position. Discontinuities in the power can indicate the presence of faults, such as cracks. The spatial resolution of the approach is limited by the pulse width, a 10nsec width being equivalent to a 1m sensing length.

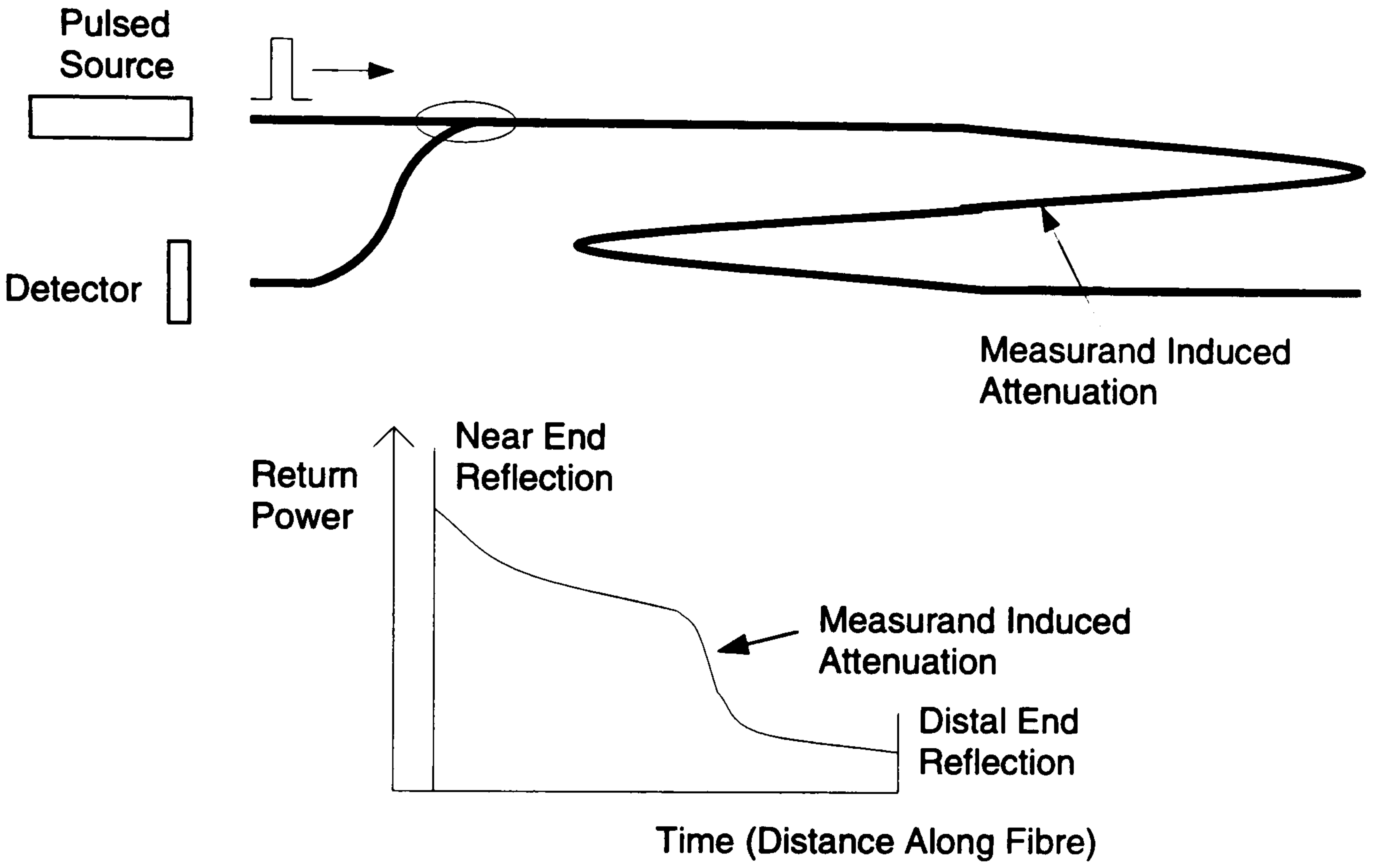

Figure 11: Optical Time Domain Reflectometry System

Since the *total* backscattered signal is approximately 30dB below the input signal - and this is distributed along the sensor length – techniques to optimise system sensitivity have been investigated. By averaging the output signals over many pulses, for example, sensor noise levels can be reduced. Alternatively, special fibres doped with neodymium to enhance thermal absorption effects at semiconductor laser wavelengths have been proposed (Farries et al, 1986). A measurement accuracy of ±2°C over a 40°C range around room temperature was demonstrated.

Polarisation Optical Time Domain Reflectometry (POTDR) monitors the polarisation properties of the scattered pulse in time with respect to the applied measurand. Rapid processing rates are necessary to measure the Stokes parameters of the light and then infer its polarisation state. Further, reciprocal effects are nulled for the double pass system. Strain sensitivities of

0.01μstrain over 0.1m are predicted. The cross-sensitivity to temperature remains a factor. Frequency derived backscatter techniques based on the POTDR principle have been recently reported (Rogers and Handerek, 1991). Frequency modulation schemes in their own right have been formulated. analogous to those proposed for multiplexing schemes, for forward scattered systems. The principle advantage is the large increase in output signal (Rogers. 1987).

One distributed approach that has attained commercial maturity exploits the spontaneous Raman spectrum present in the output of scattering systems (Dakin et al, 1985). Raman scattering involves the molecular absorption of a photon and subsequent re-emission at a lower energy (Stokes signal) or higher energy (anti-Stokes signal). Molecules must lie in an excited state to generate an anti-Stokes line, whose intensity is therefore proportional to temperature. The anti-Stokes to Stokes intensity ratio eliminates material effects such as fibre attenuation to provide a direct measure of temperature. Since the Raman signals lie a further 30dB below the Rayleigh level, a large integration time and source pulse repetition rate is necessary. The commercial system produced by *York* demonstrated a ±1°C sensitivity, with a 7.5m spatial resolution over 2km. The anti-Stokes signal may be increased by pumping in the UV and sensitivity improved by using the Rayleigh signal as reference. However, the increases in loss will limit the total sensor length.

Although one system has attained commercial maturity, several viable technologies are emerging to fulfill the distributed potential of fibre optic sensors. The sensitivity of these approaches can be further increased by amplifying the modulated optical signal. This can be achieved, in principle, by exploiting non-linear optical effects in the fibre. These ideas are developed further in Chapter 2 and specific sensors described in Chapter 5.

1.2.3 Principal Aerospace Applications

Aerospace applications for fibre optic sensors can be divided into three main categories – sensors for flight control systems, sensors for propulsion control systems and sensors for structural monitoring of advanced materials being introduced into the airframe. In this section, measurand specifications are listed for these areas, together with the environment in which the sensor must operate. Examples of current conventional transducers are given. For the reasons outlined in section 1.1.1, fibre optic sensors are likely to replace many of these sensors, and the principal contenders are described. Since 'aerospace' incorporates a wide range of mobile platforms, some generalisations have been made with regard to measurand requirements.

In *flight control* systems, the sensors provide feedback to the flight control computer on the general state of the aircraft. Early systems operated through a direct mechanical linkage between the pilot and a small number of control surfaces. As systems became more complex, electronic computers were introduced to process all the system data and generate control demands at the required rate. To maintain safety levels, a multiplicity of redundancy features became necessary with processors operating in parallel with a diversity of designs to minimise common mode failure.

Table 2 shows the principal sensing requirements and applications in flight control (Dakin and Culshaw, 1988; Figueroa et al, 1991; Miller, 1986; Todd, 1988). Approximately 50% of all the sensors monitor displacement directly and these can be modified to monitor other measurands indirectly such as pressure. Up to 90 displacement transducers (both linear and rotary) may be required in commercial fixed wing aircraft for the control of slats, sticks and pedals. This number includes some redundancy features (Gardiner and Edwards, 1987). Dynamic ranges for the sensors are application dependent, varying from 0.1 to 10cm for linear devices and between 15° and 360° for rotary systems. A 10 bit resolution over the range is a typical requirement, the response remaining linear throughout. The sensors used currently are Linear Variable Differential Transformers (LVDT's) which generate electrical outputs.

Temperature, pressure (both static and dynamic) and fuel sensors all play an important role in flight control systems. Platinum resistance thermocouples, vibrating cylinder pressure gauges and capacitative fuel level gauges respectively are typical of the devices currently employed to sense these measurands. All require some degree of electrical isolation. Overall, the sensor systems are screened from the excesses of vibration and contamination. The thermal operating range still extends from -55° to +125°C. Clearly, optical substitutes must withstand this range.

The fibre optic solutions to these problems have largely focussed on displacement sensing. A three track digital encoded intensity sensor (Miller, 1986) has demonstrated 10 minute resolution over a 90° range and has been used to monitor the throttle lever angle of a Boeing 757 in both ground and flight tests. In the US Fibre Optic Control System Integration (FOCSI) programme (Lay, 1990), a range of both linear and rotary displacement sensors using the wavelength modulation technique shown in Figure 5 have been developed. Applications include rudder pedal and leading edge flap position measurements. Interestingly, other sensors developed in the programme for temperature (eg fluorescence decay technique for external air measurements) and pressure (eg fibre microbend sensor for static pressures) are also based

Measurand	Applications	Dynamic Range	Resolution
Linear Displacement	Aircraft Landing Gear Hydraulic Spool Valves Control Surface Actuators	0.1– 10cm	4 – 12bits
Rotary Displacement	Throttle Lever Angle Speed Brake Lever Rudder Command	0-90° 0 – 360°	8 – 12bits
Temperature	External Air Temperature Skin Temperature Fluids and Gases	±60° 0 – 200°C	±1°C
Pressure	Static (Altimeter) Dynamic (Speed) Rudder/Sidestick Command Fluids and Gases	0 – 0.1MPa 0 – 1MPa	±10Pa ±100Pa
Acceleration	Airframe Fatigue Autothrottle Input	10g	±0.3g
Fuel Sensors	Flow Rate Fuel Level	Varies 0.1 – 1m	±1% ±3%
Health Monitoring	Contamination Heat Detection Smoke Detection Failure Detection		

Table 2 Principal Sensors For Flight Control Systems

on wavelength modulation. Though these approaches may not be the most accurate for the particular measurand, *all* sensors then share one common electro-optic interface (a CCD array in the FOCSI programme). This facet is important for the implementation of the technology, particularly when high quality conventional transducers are already in operation. Indeed, it is wavelength and frequency modulation systems (in conjunction with elements of TDM) which are emerging as the strongest contenders for universal sensing techniques for aerospace.

Measurand (Application)	Dynamic Range	Resolution	Local Temp
Pressure (Compressor Inlet)	0 – 250 kPa	±0.2%	≤200°C
Pressure (Compressor Outlet)	0 – 5MPa	±0.5%	≤250°C
Pressure (Burner)	0.1 – 5MPa	±1.0%	≤2000°C
Temperature (Compressor Inlet)	-70 – 200°C	±1.0°C	-70 – 200°C
Temperature (Burner Outlet)	250 – 1200°C	±0.5%	-40 – 1200°C
Temperature (Turbine Outlet)	250 – 750°C	±1.0%	-40 – 750°C
Temperature (Turbine Blade)	500 – 1000°C	±0.5%	-40 – 1000°C
Linear Disp	10 – 300mm	±1.0%	-40 – 300°C
Rotary Disp	0-60°C	±1.0%	-40 – 300°C
Angular Velocity (Turbine Blade)	1500 – 20000rpm	±3rpm	-40 – 300°C

Table 3 Gas Turbine Engine Sensor Requirements

Propulsion control sensors must withstand the harshest environment of the platform – the turbine engine. Indeed, very few conventional transducers can operate effectively within the engine. Many fibre optic devices can withstand extremely high temperatures. Table 3 shows typical sensor requirements for current turbojet/turboprop engines (Baumbick, 1985; Dakin and Culshaw, 1988; Nitka, 1988).

Temperature and pressure are the prime quantities of interest for monitoring the steady state operation of the engine. Position measurements are used to monitor and control the variable geometry of the compressor and turbine to ensure optimum operation. Speed measurements control the engine acceleration. The thermal environment varies quite dramatically from below -50°C at the point of air intake up to 2000°C at the afterburner stage. The severity is then compounded by high velocity, acoustic waves, rapid gas flow and high pressures. Not surprisingly, conventional sensors such as silica pressure gauges are located remotely from the engine, the pressure being transmitted via pneumatic tubes. Temperature sensors consist of thermocouples and LVDT's again sense displacement. Speed measurements are usually obtained via magnetic pick-up devices.

Comparatively few optical sensors have been developed for the engine. Black-body radiometric techniques for temperature (Wrigley, 1986) and optically addressed silicon microresonators (Angelides and Parsons, 1992) for both pressure and temperature have shown promise at the laboratory level. Fibre optic Laser Doppler techniques may also be used in gas-flow diagnostics. Despite this, fibre based systems still offer potential for in-flight engine monitoring.

The emergence of advanced aerospace structures employing composite materials has highlighted the need for techniques capable of monitoring the physical status of platforms in service (Measures, 1991). Composite structures are composed of layers of plastic impregnated parallel fibres. Successive levels are stacked either orthogonally or at 45°. The exact mechanical properties depend on this orientation but afford a far greater strength-to-weight ratio than conventional metallic structures. The nature of the structure does not allow for physical characterisation through measurement of one parameter on the composite surface. Since many internal imperfectations such as delamination would not be immediately detectable on the surface, a need for *embedded sensors* has arisen. Three main tasks must be addressed:

- To monitor the fabrication (curing) stage of the entire composite structure.
- To assess in-service the structural integrity of the composite by monitoring the spatial distribution of internal strains and thermal effects.
- To provide a real-time damage assessment.

Conventional electrical based sensors are widely regarded as inappropriate for these tasks. Since silica fibres possess similar mechanical properties to the composite, they can in principle be readily embedded into the structure for sensing. A single embedded fibre device may indeed execute all three tasks listed above. Measurements must be localised and yield data on measurand direction (for strain). Structural degradation must also be minimised. Further, measurements must be absolute, reproducible and linear over the dynamic range and, importantly, the sensing techniques readily adaptable for multiplexing. Two principal sensor contenders have emerged: the fibre Fabry-Perot interferometer and fibre Bragg grating sensors. These may be networked via coherence, time or wavelength multiplexing techniques. Several programmes investigating simultaneous measurement of strain and temperature in composite structures using direct and differential interferometric techniques have reported some success (Dakin and Culshaw, 1988). Much work remains, however, on overcoming down-lead sensitivities, implementing large sensor arrays, assessing the compatibility of the fibres within the composite structure and overcoming the fundamental fibre connectorisation problem between sensor array in the composite and the optical source.

For all aircraft sensors, minimum life-times of between 4,500 and 12,500 flying hours have been estimated, depending on the sensor and aircraft. The tolerable in-flight failure rate for any given aircraft sensor is no worse than 5 in 10^6 flying hours. Even so, the majority of conventional sensors contain dual and even triple redundancy levels for key areas of flight control. Reliability and safety are essential features of any emerging technology such as fibre optic sensors.

In this section, the principal applications within aerospace to which fibre sensors can be applied have been described, together with representative system performance requirements. The techniques developed in the work based on SBS have not concentrated on providing a solution for any application in particular. More, the work has aimed at developing new sensing and signal processing methods which potentially satisfy many of the operating specifications raised in this section. Before describing these methods in more detail, a description and comparison of the basic properties of nonlinear effects in fibres is given, with emphasis on SBS.

2 Nonlinear Optical Interactions In Optical Fibres

2.1 Overview of Chapter

In this chapter, the theoretical and experimental characteristics of nonlinear effects in fibres relevant to the study are described, concentrating on SBS. A brief introduction to the concept of nonlinear optics (section 2.2.1) and the waveguiding properties of optical fibres (section 2.2.2) is given initially. These aspects are combined in section 2.3, in which the principal nonlinear processes that occur in fibres, characterised in terms of nonlinear coefficients or susceptibilities, are compared and contrasted. This comparison is largely literature-based and is used to assess the impact of each mechanism on the SBS systems investigated in later chapters.

In section 2.4, the properties of SBS in optical fibres are described. The background theory that produces the SBS coupled wave equations is detailed. The solutions of these enable the variation in both pump and SBS signal with fibre length to be calculated, important in multiplexed sensor applications. Exact analytical solutions are unobtainable, though different approximations have been used in the past. These were inadequate for the present study and, as a result, a more accurate analytical representation of the solutions was obtained. The approach was validated in section 2.4.1.

The experimental properties of SBS are described in section 2.4.2, again, using the technical literature. Results showing the effect of source properties (eg wavelength and bandwidth) and fibre properties (eg dopant concentration and birefringence) on the SBS process are given. They are used to illustrate the theory developed in section 2.4.1 and enable direct comparison with the experimental systems investigated in the present work.

Sections 2.4.1 and 2.4.2 describe the steady-state properties of SBS. In section 2.4.3, the transient characteristics of SBS that have been reported are summarised. The origins of the transient effects are described in section 2.4.3. Such effects are a significant feature of the SBS systems reported in this study and are fully assessed in the appropriate experimental chapters.

2.2 Background

2.2.1 Introduction to Nonlinear Optics

In a linear dielectric material, the response of the medium electric polarisation (or dipole moment per unit volume), **P**, to an incident electric field, **E**, is given by

$$\mathbf{P} = \epsilon_0 \chi^{(1)} \mathbf{E} \qquad 2.1$$

where ϵ_0 is the permittivity and $\chi^{(1)}$, is the linear susceptibility of the medium. Thus, $\chi^{(1)}$ can be linked to the refractive index properties of the dielectric. The electric displacement of the medium, **D**, is defined as

$$\mathbf{D} = \epsilon_0 \mathbf{E} + \mathbf{P} = \epsilon_0 (1 + \chi^{(1)}) \mathbf{E} = \epsilon_0 \epsilon_r \mathbf{E} \qquad 2.2$$

where ϵ_r is the *relative* permittivity of the medium. Maxwell's wave equation for a dielectric, non-magnetic medium is then invoked (Lorrain and Corson, 1970):

$$\nabla \times \nabla \times \mathbf{E} = -\frac{1}{c^2} \frac{d^2 \mathbf{E}}{dt^2} - \mu_0 \frac{d^2 \mathbf{P}}{dt^2} \qquad 2.3$$

which rearranges in one dimension to

$$\frac{d^2 E}{dz^2} = -\frac{\epsilon_r}{c^2} \frac{d^2 E}{dt^2} \qquad 2.4$$

Since the medium refractive index, n, is defined as the quotient of c, the speed of light in vacuum, and v, the speed of light in the medium, then by combining equations 2.2 and 2.4

$$n^2 = \epsilon_r = (1 + \chi^{(1)}) \qquad 2.5$$

If $\chi^{(1)}$ is real, the electric polarisation oscillates in synchronicity with the driving field; the resultant reradiated electric field suffers a phase lag with respect to the applied field, directly proportional to n. If $\chi^{(1)}$ is complex, then

$$n = n_R + i n_I \qquad 2.6$$

and the finite n_I term implies that the medium additionally absorbs. Importantly, $\chi^{(1)}$ provides a complete description of the reflection, refraction and attenuation properties of the medium i.e. its *linear* properties.

In nonlinear media, the assumption of linearity between material response (through **P**) and the applied field **E** is no longer valid. A more general dependence is observed

$$\begin{aligned} \mathbf{P} = \textstyle\sum_j \mathbf{P}_{(j)} &= \epsilon_0 \textstyle\sum_j \chi^{(j)} \mathbf{E}^j \\ &= \epsilon_0 \left(\chi^{(1)} E^1 + \chi^{(2)} E^2 + \chi^{(3)} E^3 ...... + \chi^{(j)} E^j \right) \end{aligned} \qquad 2.7$$

where $\chi^{(n)}$ denotes the nth order susceptibility. In general terms, the response of any dielectric becomes nonlinear in the presence of intense electromagnetic fields, the result of an anharmonic motion of the bound electrons of the material. These distortions induce emissions at higher harmonics of the driving field or, in the case of multiple input fields, permits frequency mixing between the respective fields. For example, for two input beams, of frequencies ω_1 and ω_2, new components would be generated at $\omega_1 \pm \omega_2$ (sum/difference frequency generation), $2\omega_1$ and $2\omega_2$ (second harmonic generation). A similar iterative process involving terms in E^3 can then be used to formulate the resultant electric field components in $\chi^{(3)}$ and so on. In most media, only terms to $\chi^{(3)}$ are significant. The relevant effects for optical silica based fibres are discussed in section 2.3.

For a formal treatment of the physics, Maxwell's wave equation (2.3) is again invoked to include nonlinear polarisation terms:

$$\nabla \times \nabla \times \mathbf{E}(\omega_l) + \epsilon_r/c^2 \frac{d^2}{dt^2}\Big(\mathbf{E}(\omega_l)\Big) = -\mu_0 \frac{d^2}{dt^2}\Big(\mathbf{P}^{NL}(\omega_l)\Big) \qquad 2.8$$

For l fields participating in the interaction (including both incident and generated signals), a set of l coupled wave equations are formed. The waves are coupled through the nonlinear polarisation, $\mathbf{P}^{NL}(\omega_l)$, with energy being transferred between various waves, the susceptibilities acting as coupling coefficients. The number of coupled equations and, hence, new frequencies and effects produced is dependent on the number of different fields input into the system *and* the magnitude of the individual susceptibilities.

An important criterion in determining the efficiency of new frequencies generated in the nonlinear system is *phase-matching* (Shen, 1984). Conservation of both energy and momentum during the interaction requires effective matching of optical frequencies and wavenumbers respectively. The latter is known as phase matching and implies that only a discrete set of fields are generated in a medium for a given set of input fields. For example, in the $\chi^{(2)}$ sum-frequency interaction, input beams $\mathbf{E}(\omega_1)$ and $\mathbf{E}(\omega_2)$ combine to produce $\mathbf{E}(\omega_3)$ where $\omega_3 = \omega_1 + \omega_2$. Optimum conversion efficiency is obtained when $\Delta k = 0$ that is

$$\begin{aligned}\Delta k = k_1 + k_2 - k_3 &= (n_1\omega_1 + n_2\omega_2 - n_3\omega_3)/c \\ &= \Big(\omega_1(n_1 - n_3) + \omega_2(n_2 - n_3)\Big)/c\end{aligned} \qquad 2.9$$

where n_1 is the medium refractive index at ω_1, etc. For isotropic materials where $n_3 > n_1, n_2$, the phase-matched condition can never be satisfied. One solution, however, is to use birefringent materials in which input beams along the slow (or ordinary) axis can generate sum-frequency beams along the fast, extra-ordinary axis.

2.2.2 Light Propagation In Optical Fibres

A complete, formal treatise of the waveguiding properties of optical fibres requires that Maxwell's equations are rigourously applied within the cylindrical fibre geometry. A detailed analysis (see, for example, Snyder and Love, 1983) is beyond the scope of this thesis but the basic principles are now summarised. In an optical fibre, the core of radius a is raised to an index n_1, surrounded by a cladding of index n_2. To solve the waveguiding properties of the fibre, Maxwell's wave equation in cylindrical co-ordinates is used

$$\nabla^2 E = \frac{1}{r}\frac{d}{dr}\Big(r\frac{dE}{dr}\Big) + \frac{1}{r^2}\frac{d^2E}{d\phi^2} + \frac{d^2E}{dz^2} = -\frac{\epsilon_r}{c^2}\frac{d^2E}{dt^2} \qquad 2.10$$

which has a solution $E_{r,\phi,z}$ of the form

$$E_{r,\phi,z} = E_r(r)E_\phi(\phi)E_{z,t}(z,t) \qquad 2.11$$

These equations are applied to both core and cladding regions and the boundary conditions are invoked to produce exact solutions. The mathematics are rigorous but can be eased by utilising the weakly-guiding approximation (Gloge, 1971, Snyder and Love, 1983):

$$\Big(\frac{n_1 - n_2}{n_2}\Big) \ll 1 \qquad 2.12$$

which held for all fibre used in this study. It allows the electric field to be expressed in terms of transverse fields (ie in x and y only) polarised in one direction. Each transverse wave solution is associated with a set of modes designated LP_{lm}, where l and m are integers. For the lowest order mode, l=0 and the lower cut-off point for wave propagation occurs for a equal to zero. That is for a fibre of finite radius, at least one mode will always propagate. An optical fibre is characterised by V, the normalised frequency, given by

$$V = \frac{2\pi a}{\lambda}(n_1^2 - n_2^2)^{\frac{1}{2}} \qquad 2.13$$

where λ is the propagating wavelength. The condition for single mode operation within fibres is that

$$V \leq 2.405 \qquad 2.14$$

The propagating mode is the LP_{01} mode. In fact, for l=0, a set of two degenerate orthogonally polarised modes can propagate with a field distribution shown in Figure 12. For $l \geq 1$, each set of solutions comprises four modes. The field distribution and polarisation azimuth for the second lowest order mode, LP_{11}, is also illustrated in Figure 12 (Dakin and Culshaw, 1988).

During the present study, only fibres which supported LP_{01} and LP_{11} were used. Indeed, even in the latter (section 3.4), the experiment was configured such that the input light was coupled into the fundamental mode. For the LP_{01} mode, the spatial distribution of energy across the core is determined by the exact index profile across the fibre. For the step-index profile exhibited by all fibres used in the study (Figure 13), the field distribution, $\mathcal{E}(r)$, of the LP_{01} mode can be approximated by a Gaussian (Snyder and Love, 1983)

$$\mathcal{E}(r) = \mathcal{E}(0) \exp -(\frac{r}{r_0})^2 \qquad 2.15$$

where r_0 is the 1/e point of the amplitude distribution and is defined as the *mode radius.* The modal area is thus given by πr_0^2.

The value of r_0 is dependent on the fibre geometry, source wavelength and core/cladding index values. r_0 can be deduced for a given fibre/source combination by calculating the V-number of the system (equation 2.13) and then invoking the empirical relationship between r_0, V and a, the fibre radius, (Marcuse, 1978). This relationship is given by

$$\frac{r_0}{a} = A + \frac{B}{V^{\frac{3}{2}}} + \frac{C}{V^6} \text{ valid for } 1.5 < V < \infty \qquad 2.16$$

where A=0.632, B=1.478 and C=4.76. The ratio of effective mode area, A_{eff}, to core area, πa^2, is plotted in Figure 14 as a function of V.

The number of modes propagating in a fibre increases monotonically with V, and hence, wavenumber, core radius and the $(n_1^2 - n_2^2)^{\frac{1}{2}}$ term. This latter term defines the fibre *numerical aperture*, the input acceptance angle of the fibre for propagation within the core. For many moded fibre, the electric field is approximately uniformly distributed across the core and the modal area equates to the core area.

The LP_{01} mode of single mode fibre consists of two degenerate orthogonally polarised components, denoted by E_x and E_y. In principle, linearly polarised input light should remain polarised along the fibre. In practice, however, internal perturbations such as geometric imperfections, and material anisotropies and external effects (such as bends, stresses and temperature) break the mode degeneracy and create birefringence within the core. This causes both coupling and variations in phase between the components, factors which cause the polarisation state to vary.

The degree of birefringence, $\mathcal{B}$, established within the core by these effects is defined as (Kaminow, 1981)

$$\mathcal{B} = \frac{(\beta_x - \beta_y)\lambda}{2\pi} = n_x - n_y \qquad 2.17$$

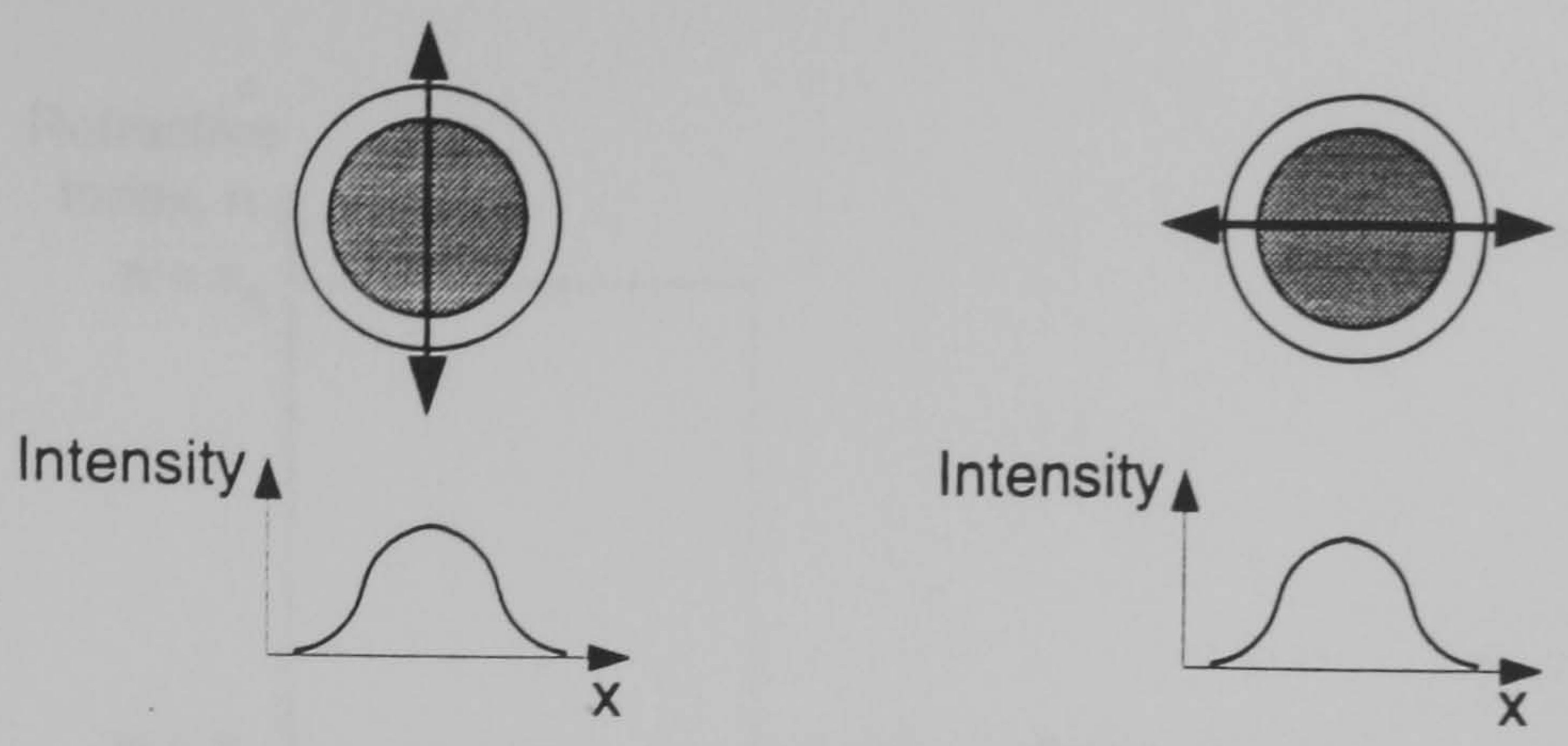

l = 0; LP_{01} Mode

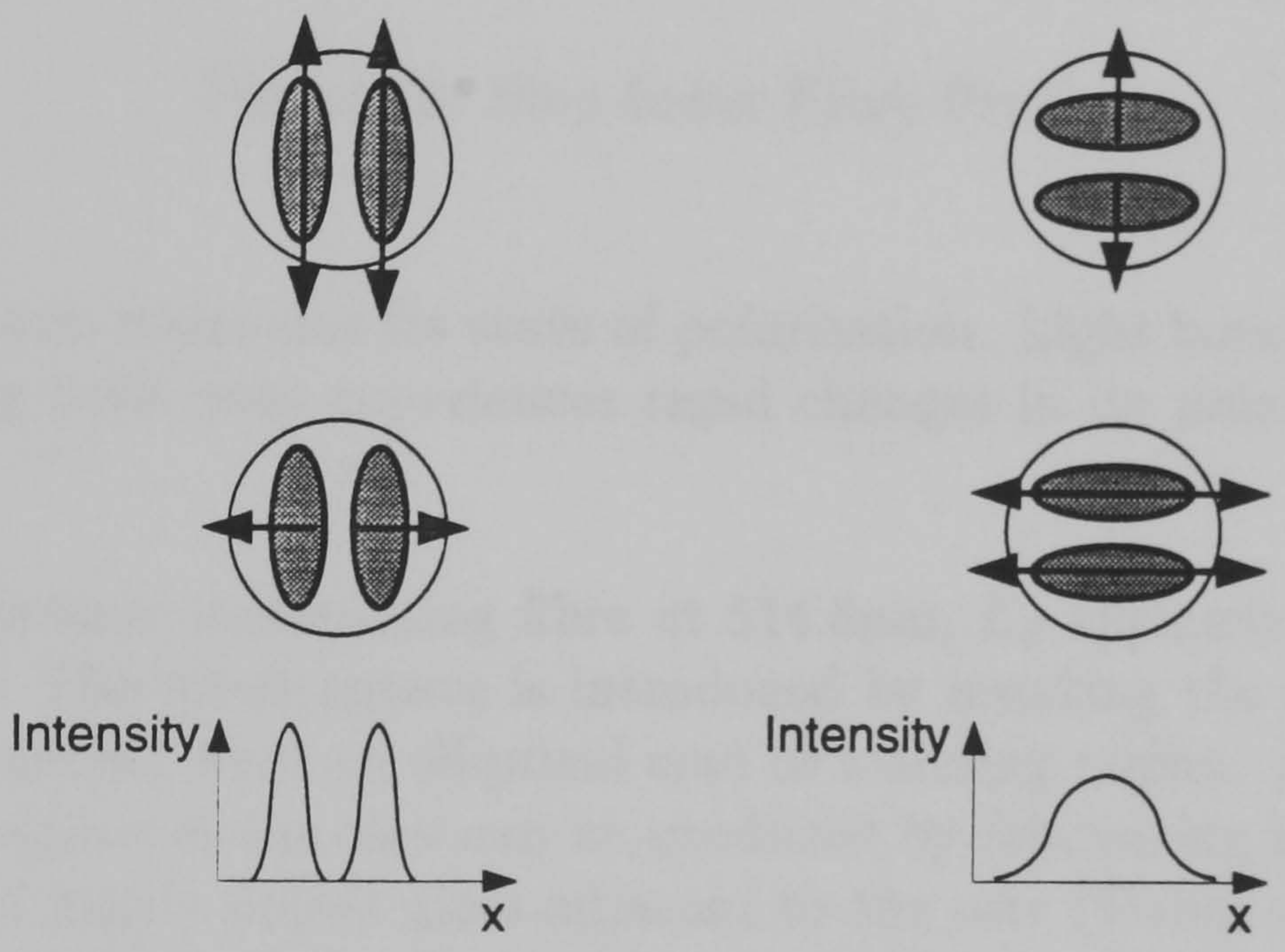

l = 1; LP_{11} Mode

Figure 12: Field Distribution and Polarisation Azimuth of Fibre Modes

where β and n respectively denote the propagation constants and refractive indices along the axes. The fibre beat length, L_B, is the length over which the phase difference between the two components cycles through 2π to reconstitute the original polarisation state and is given by

$$L_B = \frac{2\pi}{\beta_x - \beta_y} = \frac{\lambda}{n_x - n_y} \qquad 2.18$$

L_B typically varies between 10cm and 2m in circular core single mode fibres and can vary along the length. Polarisation modulation effects can be rendered insignificant by intentionally introducing into the core very high levels of birefringence. Two well-defined orthogonal axes are established possessing quite distinct propagation constants. Thus, linear polarised light launched

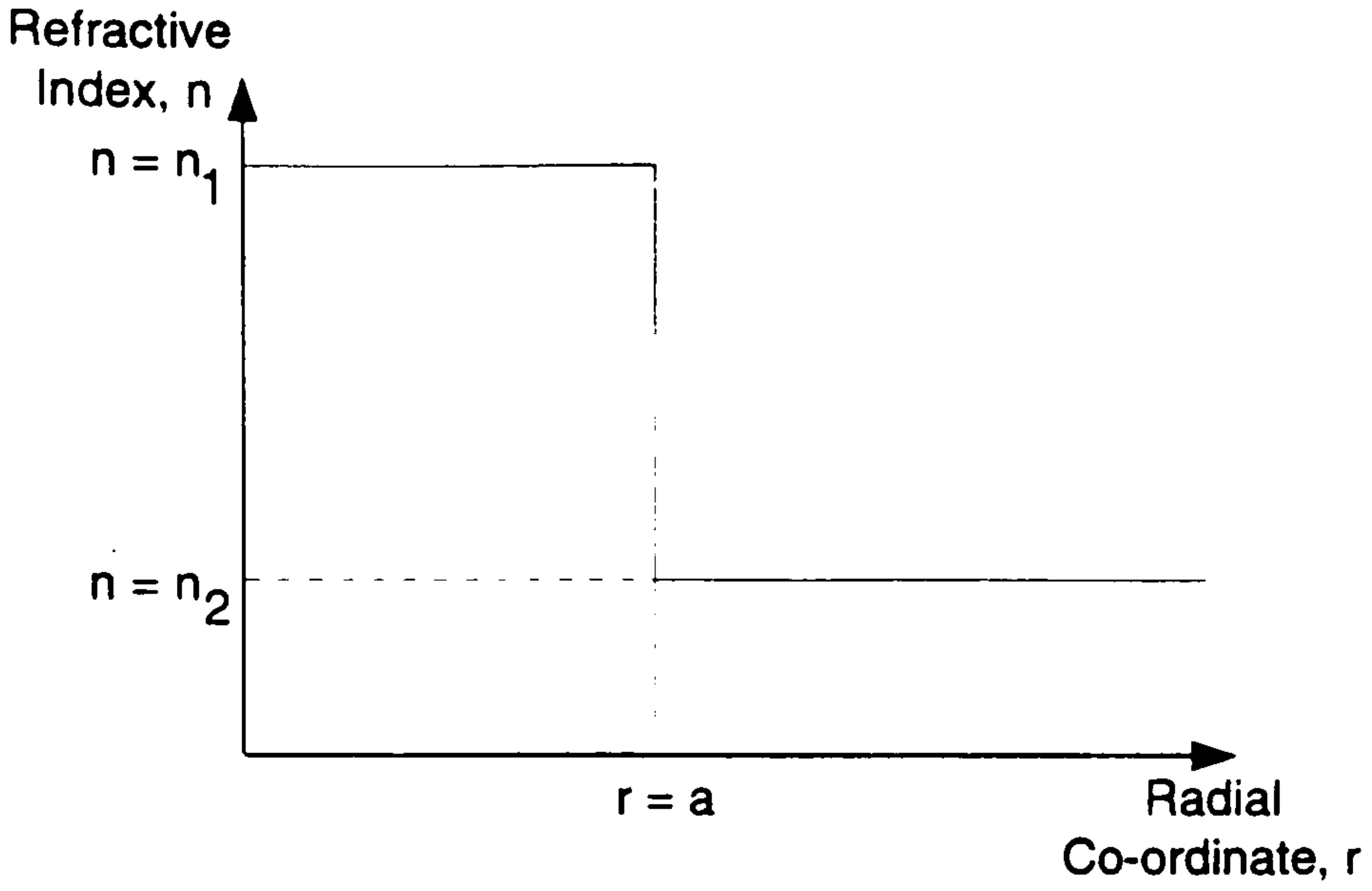

Figure 13: Step Index Fibre Profile

along either axis maintains its state of polarisation. Light launched simultaneously along both axes experiences rapid changes in its polarisation state with length.

For polarisation maintaining fibre at 514.5nm, L_B typically lies between 1 and 10mm. The birefringence is introduced by breaking the circular symmetry, for example, with an elliptical core or cladding region. Alternatively, large stress regions in the core can be produced by fabricating the fibre with two regions of highly doped glass adjacent to the core (Dakin and Culshaw, 1989). In an analogous manner, a fibre can exhibit circular birefringence by twisting the fibre about its central axis. Input circularly polarised light is then maintained in this state along the fibre. The fibres used in the study are detailed more fully in Chapter 3, since the polarisation properties of the fibre can dictate the efficiency of a given nonlinear process.

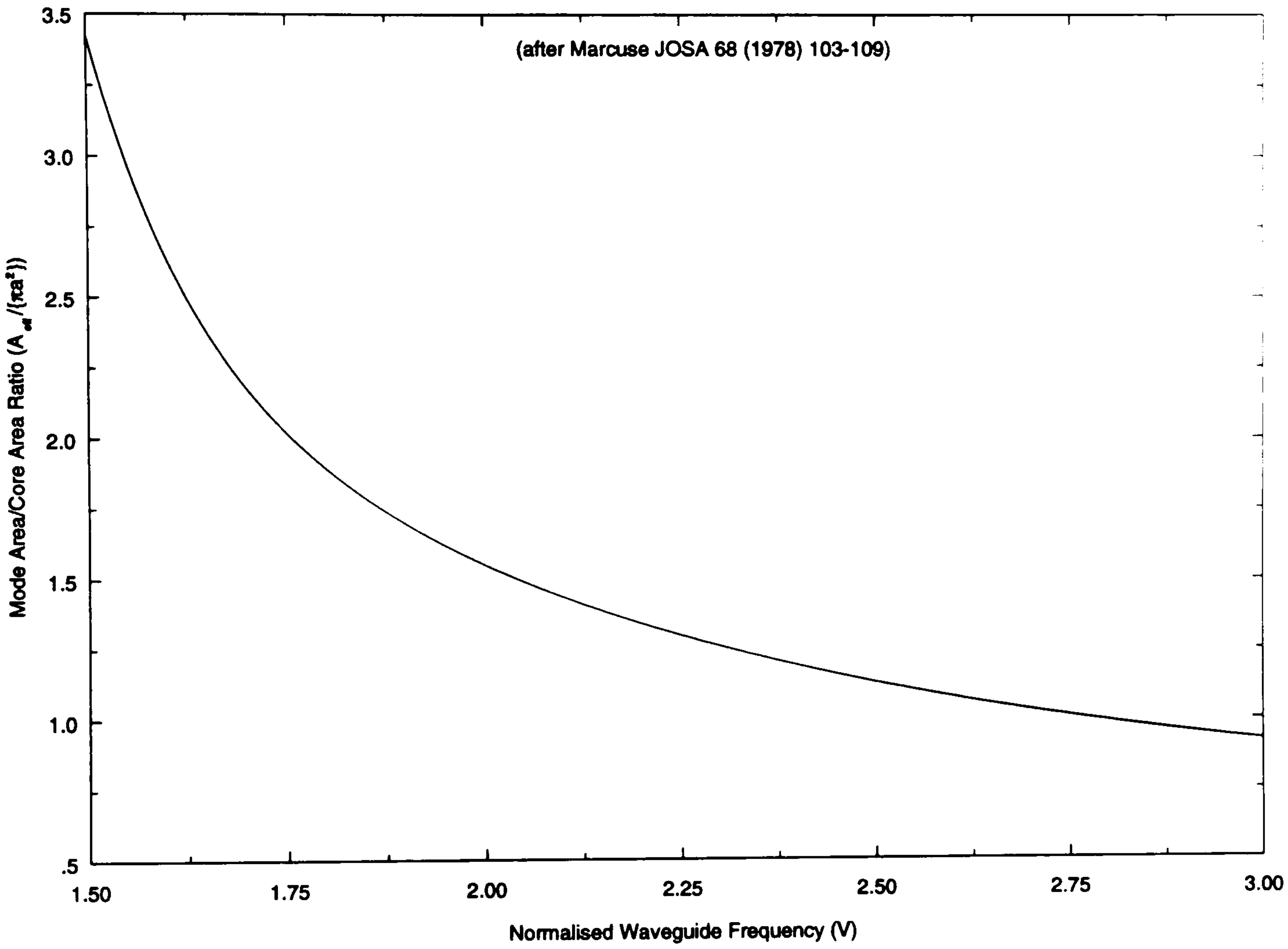

Figure 14: Ratio of Effective Mode Area to Fibre Core Area as a Function of Fibre V-Number

2.3 Characterisation and Comparison of Different Nonlinear Processes In Fibres

2.3.1 Introduction

The concepts of nonlinearity and waveguiding in optical fibres are now combined. This section lists the various mechanisms that can arise in terms of increasing susceptibility, $\chi^{(n)}$, and then describes the resultant experimental characteristics with regard to the properties of the optical fibres. Emphasis is placed on effects that directly perturb SBS systems. The starting point is the nonlinear relationship between medium polarisation, $\mathcal{P}$, and applied electric field (equations 2.7). For a multi-input system, there are numerous solutions to this equation. In this section, only $\chi^{(2)}$ and $\chi^{(3)}$ susceptibilities are considered since the magnitudes of higher order terms are negligible (Shen, 1984). Further, in this analysis, to retain simplicity, the number of input electric fields is limited to a maximum of two, possessing frequencies ω_1 and ω_2. The input electric field thus takes the form

$$\begin{aligned} E = \; & \mathcal{E}(\omega_1)\cos(k_1 z - \omega_1 t) + \mathcal{E}(\omega_2)\cos(k_2 z - \omega_2 t) \\ \equiv \; & \tfrac{1}{2}\Big(\mathcal{E}(\omega_1)\exp i(k_1 z - \omega_1 t) + \mathcal{E}(\omega_1)\exp -i(k_1 z - \omega_1 t) \\ & \mathcal{E}(\omega_2)\exp i(k_2 z - \omega_2 t) + \mathcal{E}(\omega_2)\exp -i(k_2 z - \omega_2 t)\Big) \end{aligned} \qquad 2.19$$

For a single input beam, obviously, $\mathcal{E}(\omega_2) = 0$. This term is substituted into equation 2.8 to produce a series of coupled wave equations. These are solved for fibres in terms of transverse waveguide modes (equation 2.10). In bulk media, E and $\mathcal{P}$ should be treated strictly as vector quantities and the susceptibilities, $\chi^{(n)}$, as tensors. In isotropic, one dimensional propagation media such as fibres, however, a complete description of the physics can be obtained by treating the electric field as a scalar quantity with amplitude components in the x and y directions. In our description, we assume that the incident electric field is linearly polarised, a state that is maintained throughout propagation.

Before describing the processes, it is worth commenting on why, in general, nonlinear processes can be initiated in fibres at modest input power levels despite silica, the principal constituent of optical fibres, possessing comparatively low ($\approx$1%) nonlinear susceptibilities compared with many other optical bulk materials. A general figure of merit for the efficiency of nonlinear processes is the product IL_{eff} (Ippen, 1975). I is the intensity of the optical flux and L_{eff} is the interaction length between the light and the medium. In bulk materials, the light is focussed to a spot, radius r_0, and L_{eff} is determined by the penetration depth of the focal plane. Thus, for light of wavelength λ and optical power P, the figure of merit is given by

$$IL_{eff} = \frac{P}{\pi r_0^2} \times \frac{\pi r_0^2}{\lambda} = \frac{P}{\lambda} \tag{2.20}$$

For optical fibres, I has the same form, though here, r_0 is the fibre core radius (or more specifically, the fundamental mode radius in single mode fibres). L_{eff} is determined from the optical loss mechanisms in the fibre (Ippen, 1975) by

$$L_{eff} = \int_0^L \exp(-\alpha z)dz = \frac{1}{\alpha}\Big(1 - \exp(-\alpha L)\Big) \tag{2.21}$$

where L and α are the fibre length and attenuation coefficients respectively. This length dependence of nonlinear processes becomes significant when determining the spatial resolution of sensors based on these effects. For fibres, therefore, the figure of merit becomes

$$IL_{eff} = \frac{P}{\pi r_0^2 \alpha}\Big(1 - \exp(-\alpha L)\Big) \tag{2.22}$$

The relative figure of merit, R, between fibre and bulk media is obtained by dividing equation 2.22 by equation 2.20, which gives

$$R = \frac{P}{\pi r_0^2 \alpha}\Big(1 - \exp(-\alpha L)\Big) \times \frac{\lambda}{P} = \frac{\lambda}{\alpha \pi r_0^2} \tag{2.23}$$

for large αL. In single mode fibre pumped at 0.5145μm, r_0 is typically 1μm and α is $6.9\times10^{-3}\text{m}^{-1}$($\equiv$30 dB/km loss). R is 2.4×10^{-7}, a factor which comfortably compensates for the low nonlinear coefficients of the host material.

2.3.2 $\chi^{(2)}$ Mechanisms

Inserting the expression for E (equation 2.19) into the second order term in equation 2.7, yields

$$\begin{aligned}\mathcal{P} = \epsilon_0\chi^{(2)}/4 \quad & \Big[2(\mathcal{E}^2(\omega_1) + \mathcal{E}^2(\omega_2)) + \mathcal{E}^2(\omega_1)/2.\cos 2\omega_1 t + \mathcal{E}^2(\omega_2)/2.\cos 2\omega_2 t \\ & + \mathcal{E}(\omega_1)\mathcal{E}(\omega_2)\Big(\cos(\omega_1 + \omega_2)t + \cos(\omega_1 - \omega_2)t\Big)\Big]\end{aligned} \tag{2.24}$$

excluding terms in kz for brevity. In principle, electric fields oscillating at both $2\omega_1$, $2\omega_2$ and $\omega_1 \pm \omega_2$ are generated as well as a d.c. contribution. However, since silica, the principal constituent of fibre, is a symmetric molecule, $\chi^{(2)}$ vanishes to zero – the polarity of the induced polarisation in such materials matches that of the driving electric field. Although second harmonic generation effects have recently been demonstrated in fibres (eg Bardal and

Wells, 1991), dopant-induced defect centres and $\chi^{(3)}$ mechanisms play a significant role in establishing a non-zero $\chi^{(2)}$ coefficient.

2.3.3 $\chi^{(3)}$ Mechanisms (Real)

$\chi^{(3)}$ are the most pronounced in optical fibres. The $\chi^{(3)}$ coefficient consists of both real and imaginary terms and is expressed as

$$\chi^{(3)} = \chi_R^{(3)} + i\chi_I^{(3)} \qquad 2.25$$

Mechanisms involving the imaginary component are initiated via material absorption and are discussed in the next section. $\chi_R^{(3)}$ terms are obtained by substituting the two component field of equation 2.19 into 2.7.

Thus, again neglecting terms in kz,

$$\begin{aligned}\mathcal{P} = \epsilon_0\chi_R^{(3)}/4 \quad &\Big[\Big(3\mathcal{E}^3(\omega_1) + 6\mathcal{E}(\omega_1)\mathcal{E}^2(\omega_2)\Big)\cos\omega_1 t\\ &+\Big(3\mathcal{E}^3(\omega_2) + 6\mathcal{E}(\omega_2)\mathcal{E}^2(\omega_1)\Big)\cos\omega_2 t\\ &+\mathcal{E}^3(\omega_1)\cos 3\omega_1 t + \mathcal{E}^3(\omega_2)\cos 3\omega_2 t\\ &+3\mathcal{E}^2(\omega_2)\mathcal{E}(\omega_1)\cos(2\omega_2 - \omega_1)t\\ &+3\mathcal{E}^2(\omega_1)\mathcal{E}(\omega_2)\cos(2\omega_1 - \omega_2)t\\ &+3\mathcal{E}^2(\omega_2)\mathcal{E}(\omega_1)\cos(2\omega_2 + \omega_1)t\\ &+3\mathcal{E}^2(\omega_1)\mathcal{E}(\omega_2)\cos(2\omega_1 + \omega_1)t\Big]\end{aligned} \qquad 2.26$$

Consider, firstly, terms in $\cos\omega_1 t$ and $\cos\omega_2 t$. The coefficients represent additional nonlinear contributions to the permittivity, denoted by ϵ_{NL}, as the polarisation oscillates at the fundamental optical pump frequency ω_1 (or ω_2). The resultant change in refractive index of the material for beam $\mathcal{E}_1(\omega_1)\cos\omega_1 t$ is given by (via equation 2.5)

$$\epsilon_{NL} = \frac{3\chi_R^{(3)}}{4}\Big(\mathcal{E}_1^2(\omega_1) + 2\mathcal{E}_2^2(\omega_2)\Big) = (n + \Delta n)^2 - n^2 \qquad 2.27$$

So, for small Δn,

$$\Delta n = \frac{3\chi_R^{(3)}}{8n}\Big(\mathcal{E}_1^2(\omega_1) + 2\mathcal{E}_2^2(\omega_2)\Big) \qquad 2.28$$

The first term, in $\mathcal{E}_1^2(\omega_1)$, represents the contribution to the index by the field E_1 itself - *self* phase modulation (SPM). The second term, the contribution to the index on E_1 from E_2, is the *cross* phase modulation (CPM). The magnitude of CPM is double that of SPM and occurs between waves of different frequency, polarisation ellipticity and propagation direction. The constant of proportionality between δn and applied *intensity*, denoted as n_2, takes the value of 3.2 × $10^{-20}\text{m}^2\text{W}^{-1}$ in fused silica (Cotter, 1987). However, the effects in fibres are enhanced when integrated over the interaction length. L_e. The total phase change, $\Delta\phi$, experienced is

$$\Delta\phi = \frac{2\pi}{\lambda}\frac{n_2 P}{\alpha A_{eff}}\Big(1 - \exp\left(-\alpha L\right)\Big) \qquad 2.29$$

where P is the power and A_{eff} is the effective area of the interaction. For single-mode fibre, this equates to the fundamental mode area (section 2.2.2). In multimode fibre, A_{eff} is the core area, πa^2. The effects of SPM and CPM on the SBS process are discussed in section 2.4.3.

Terms in $2\omega_2 - \omega_1, 2\omega_1 - \omega_2$, etc all describe third order *parametric* processes in which three input photons combine to produce a fourth at some intermediate frequency i.e. Four Wave Mixing (FWM). FWM also describes the process of two input pump photons of a given frequency being annihilated to produce a frequency downshifted (Stokes) and frequency upshifted (anti-Stokes) signals. For all these mechanisms, significant energy conversion occurs only when the phase-matching condition of equation 2.9 is obtained i.e.$\Delta k = 0$.

In optical fibres, the effective propagation constant encountered by a given frequency is determined by

- material dispersion, Δk_m
- modal dispersion, Δk_w
- nonlinear index terms, Δk_n

For efficient four wave mixing,

$$\Delta k = 0 = \Delta k_m + \Delta k_w + \Delta k_n$$

The material dispersion, Δk_m, for a generated signal at λ is given approximately by (Hill et al, 1978)

$$\Delta k_m = 2\pi\lambda^3 \frac{d^2 n}{d\lambda^2}\frac{\Delta f^2}{c^2} \qquad 2.30$$

where Δf is the frequency shift of the interaction. Modal dispersion, Δk_w arises in single mode fibres since the effective index of the guided mode is a weighted average of core and cladding indices determined by the signal wavelength (Gloge, 1971). In multimode fibre, Δk_w arises due to different phase velocities of the different modes. The sources of nonlinear index terms were discussed above.

In single mode fibre, the dominant material dispersion term generally precludes FWM involving large frequency differences. In conventional telecommunications fibre, for example, (dispersion ≈16ps/nm/km) only signals with separations less than 20GHz mix efficiently (Chraplyvy, 1990). An early example (Hill et al, 1978), used three input signals separated by approximately 10GHz obtained from Argon Ion lasers operating around 0.5145μm to pump a 150m, 2μm core radius fibre. Nine new frequencies were generated, representing the mixing combinations of the input signals. Similarly, two sources separated by 950MHz produced a Stokes/anti-Stokes pair shifted by 950MHz from the main components. Larger wavelength excursions can be obtained by exploiting the zero material dispersion point of fibres which lies in the 1.3 to 1.6μm spectral region. For example, two photons from a Q-switched Nd:YAG source at 1.319μm produced Stokes and anti-Stokes signals at 1.67μm and 1.09μm using 50m of 3.5μm core fibre. The use of different core areas allowed some frequency tunability through modification of Δk_w (Lin et al, 1981).

Overall, FWM is a versatile technique for producing signals over a broad spectral range with different source and fibre species. FWM was observed in the SBS systems of this study under appropriate experimental conditions as described in Chapter 3.

2.3.4 $\chi^{(3)}$ Mechanisms (Imaginary)

Processes involving the $i\chi_I^{(3)}$ term describe a coupling transition between an input photon at ω_1 to a second photon ω_2 via material absorption and subsequent re-radiation (ie scattering). Two quite distinct mechanisms are involved:

(i) the scattering via molecular vibrations or optical phonons which produces Stimulated Raman Scattering (SRS).

(ii) the scattering by propagating acoustic phonons which initiates Stimulated Brillouin Scattering (SBS).

As with FWM, output photons, frequency downshifted with respect to the pump and therefore transferring energy to the medium, are called *Stokes* signals; frequency up-shifted signals are *anti-Stokes*. In the latter, energy is extracted from the material which must therefore lie in an initial excited state. Stokes interactions therefore dominate many systems. Further, phase matching is automatically satisfied in both SRS and SBS.

The generation of a Stokes wave with intensity $I_s(z)$ and the depletion of the pump $I_p(z)$ in SRS is governed by two coupled wave equations derived from Maxwell's coupled wave analysis (Shen, 1984; Agrawal, 1989):

$$\begin{aligned} dI_p(z)/dz &= -\omega_1/\omega_2 . g_R I_p(z) I_s(z) - \alpha_p I_p(z) \\ dI_s(z)/dz &= g_R I_p(z) I_s(z) - \alpha_s I_s(z) \end{aligned} \qquad 2.31$$

where α_p and α_s denote the absorption coefficients at ω_1 and ω_2 respectively and g_R is the Raman gain. The gain is directly related to $\chi_I^{(3)}$ via the spontaneous Raman cross-section, $\sigma_0(\delta\omega)$. The cross-section is defined as the probability of an input photon at ω_1 being scattered by the material into a Stokes photon at ω_2. The gain is given by (Shen, 1984)

$$g_R = \frac{8\sigma_0(\delta\omega)\pi^3 c}{\omega_s^3 h \epsilon_r} = \frac{\sigma_0(\delta\omega)\lambda_s^3}{c^2 h \epsilon_r} \qquad 2.32$$

where h is Planck's constant. Since $\sigma_0(\delta\omega)$ varies as ω^4 (Stolen, 1979), g_R varies linearly with frequency. The dielectric constant, ϵ_r, is given by equation 2.5 and is related to the first order suseptibility only in this expression. Equations 2.31 are solved for optical fibres by assuming negligible pump depletion from the nonlinear process (Smith, 1972) to produce for $I_s(z)$

$$I_s(z) = I_s(0)\exp\Big(g_R I_p(0) L_{eff} - \alpha_s z\Big) \qquad 2.33$$

where L_{eff} was defined by equation 2.21. It is useful in fibre systems to define an input pump power in nonlinear systems at which a given nonlinear effect becomes significant, denoted as the *threshold power*. The Raman threshold, for example, is defined as the input pump power at which the Stokes power and undepleted pump power are equal at $z = L$ (Smith, 1972) and is given by

$$P_R^{thr} = \frac{16 A_{eff}}{g_R L_{eff}} \qquad 2.34$$

Since Raman scattering involves interaction with molecular vibration modes, g_R, or more strictly $g_R(\omega)$, is strongly material dependent.The gain spectra for fused silica (Stolen and Ippen, 1973) is shown in Figure 15.

The broadband nature arises from the amorphous non-crystalline material which creates a continuum of accessible, scattering vibration modes. For a single input pump, spontaneous Raman scattering generates photons with a spectral profile mapping the Raman gain spectrum. Each element then acts as a probe being amplified by $\exp\Big(g_R(\omega) I_p(z) L_{eff}\Big)$. Thus the component corresponding to the peak of the spectrum, $g_{R(max)}$, grows most rapidly and the process becomes *stimulated.*

For a 0.532μm pump source, $g_{R(max)}$ is approximately 1.9× 10^{-13}mW^{-1} for fused silica and occurs at a 13THz (12nm) downshift from the source. The gain scales inversely with wavelength and is reduced by a factor of two for

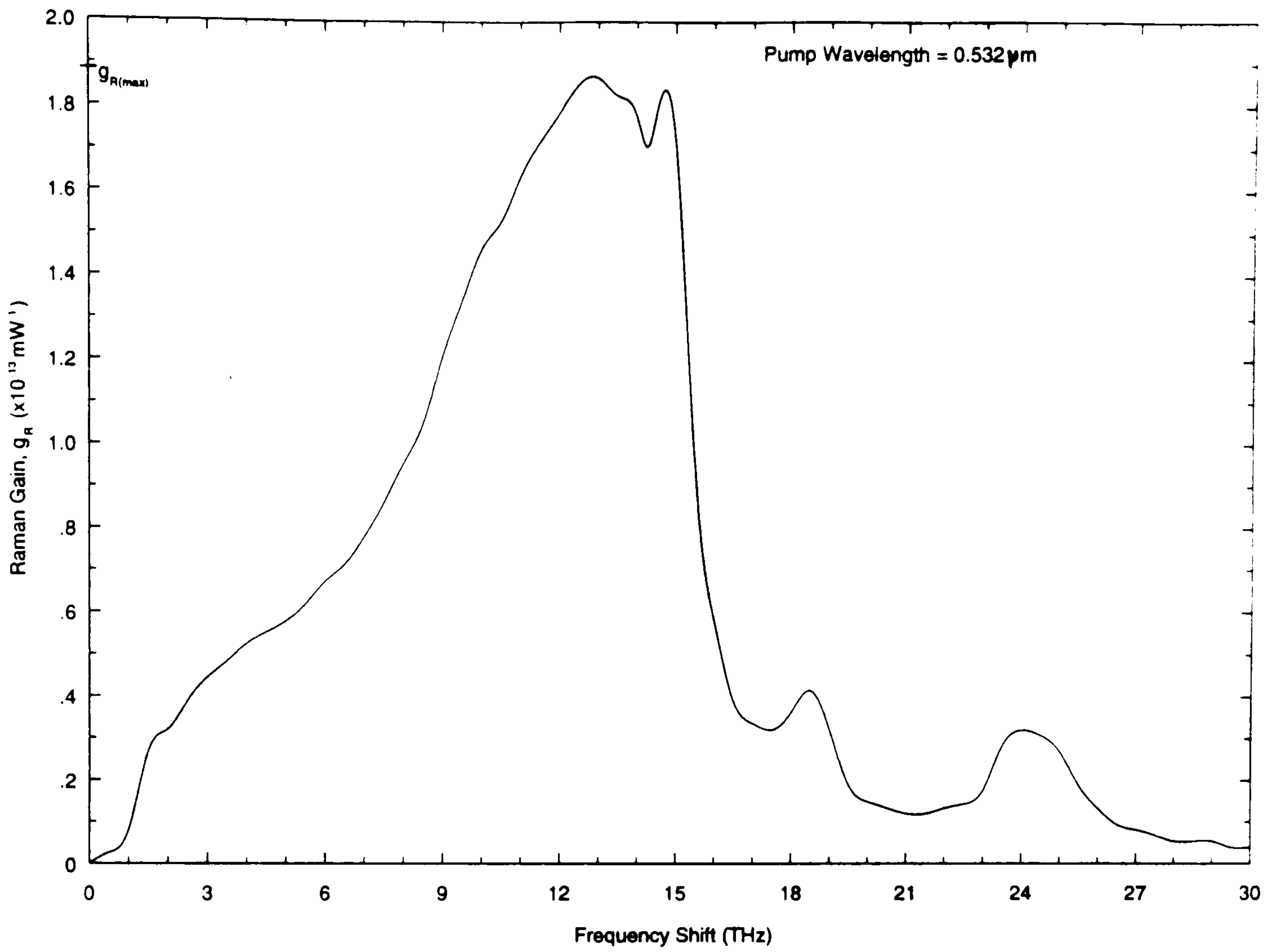

Figure 15: Raman Gain Spectrum for Fused Silica

non-polarisation maintaining systems. The SRS gain maximum is approximately half that of the equivalent term for parametric FWM. However, phase matching constraints tend to reduce the FWM gain in long fibre lengths so SRS dominates. In shorter fibre samples, however, the effective FWM gain can be greater. More often, the output spectrum arises from a complex interplay between both effects.

The Raman gain was first measured along 5.9m of fibre using a pulsed Xenon laser ($\lambda_p = 0.526\mu$m) and a probe derived from the same source (Stolen and Ippen, 1973).The gain, measured at 0.535μm, was 1.5$\times$10^{-13}mW^{-1}. The wide gain spectrum shown in Figure 15 suggests that silica fibre is a suitable medium for broadband amplification. For example (Pini et al, 1986), a two-fibre system used one fibre pumped by a 308nm pulsed excimer to produce a Stokes probe at 312nm. This was inputted into a second fibre and subsequently amplified with efficiencies in excess of 90%.

Dopants in silica significantly modify the Raman gain spectrum. Germania, for example, increases the net gain by directly increasing g_R and by simultaneously reducing the mode-field diameter of the fibre (Davey et al, 1989). However, the disadvantage of germania is that it introduces additional attenuation and reduce the effective interaction length (Lin et al 1977).

Once the Stokes signal attains the threshold power, a second Stokes wave is generated, downshifted by approximately 13THz from the first. For very high input pump powers, a cascade of higher order shifts is produced. This property has been exploited to generate a range of broadband sources for use in fibre characterisation (eg Lin et al, 1977). A pulsed Nd:YAG pump (20Hz rep-rate, 150ns pulse width) produced orders of SRS at 1.12, 1.18, 1.24 and 1.31μm respectively along 176m of 3μm core fibre. The bandwidth of higher orders increases due to competing process of SPM and FWM. Plates 1 and 2 show the undispersed and dispersed output spectra measured in preliminary experiments performed in the current study. A 90m, 3μm core, non-birefringent fibre was pumped with a frequency doubled Nd:YAG at 0.532μm. A cascade of 9 Stokes shifts was obtained producing peaks up to approximately 0.65μm.

More complicated spectra can result when FWM and SRS processes combine in either multimode fibres (Lin, 1986) or birefringent fibres (Chee and Liu, 1990). The Stokes signal from FWM can seed SRS if it falls within the Raman gain curve. Alternatively, anti-Stokes signals can be produced from the parametric coupling of the pump and SRS Stokes signals. A wide range of frequencies, both narrowband and broadband, can therefore be generated throughout the UV, visible and IR.

In contrast to SRS, SBS describes the interaction between two optical signals, the input pump and Stokes waves, and an *acoustic* phonon or sound wave propagating within the fibre core. The process is initiated via spontaneous Brillouin scattering from thermally induced acoustic phonons in the fibre. A brief resumé of SBS principles are listed here to enable direct comparison with the processes described in this section – a full description of both theoretical and experimental properties of SBS is given in section 2.4.

In single-mode fibres, the Stokes signal propagates in the reverse direction with respect to the pump and is frequency offset by ν_B where

$$\nu_B = \frac{2nV_A}{\lambda_p} \qquad 2.35$$

where V_A is the acoustic phonon velocity, n the effective core index and λ_p

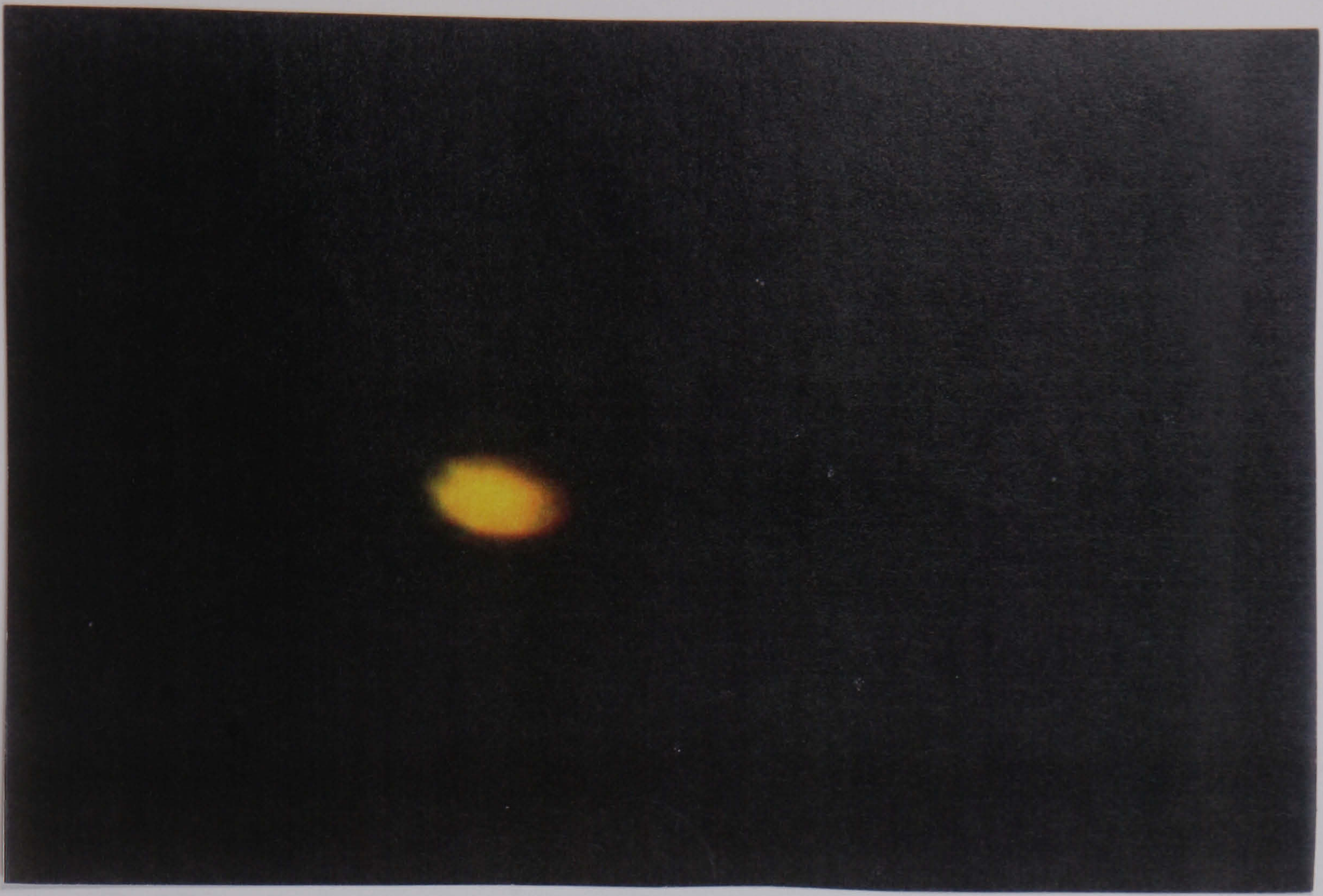

Plate 1 Non-Dispersed Raman Spectra From Monomode Fibre

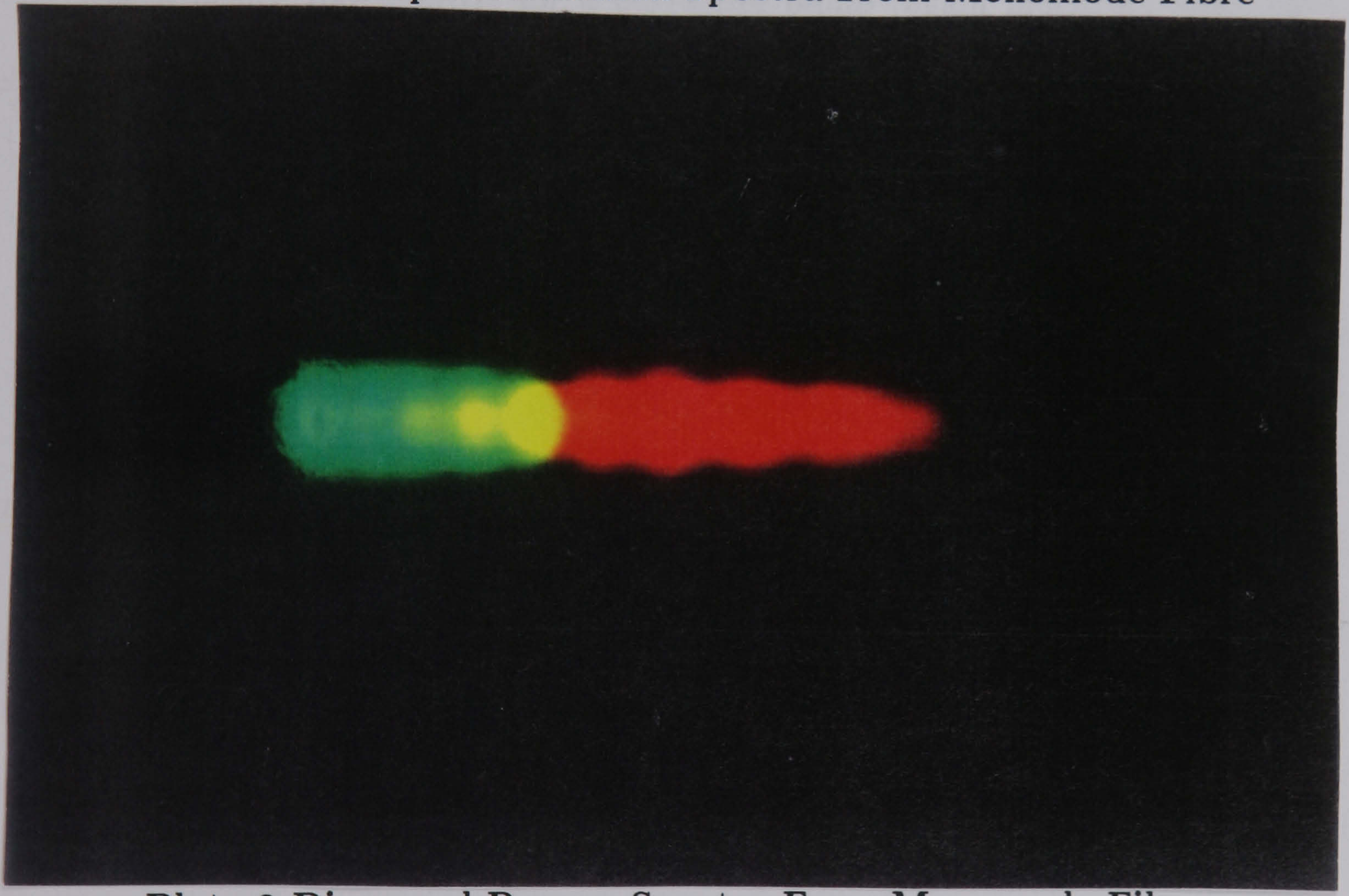

Plate 2 Dispersed Raman Spectra From Monomode Fibre
Showing Discrete Stokes Orders

the pump wavelength. The downshift is typically 34GHz (0.03nm) for a 0.514μm pump, significantly less than for SRS. As for SRS, however, SBS is described in terms of two coupled wave equations for $I_s(z)$ and $I_p(z)$ (Shen, 1984):

$$\begin{aligned} \frac{dI_p(z)}{dz} &= -g_B I_p(z) I_s(z) - \alpha_p I_p(z) \\ \frac{dI_s(z)}{dz} &= -\Big(g_B I_p(z) I_s(z) - \alpha_s I_s(z)\Big) \end{aligned} \qquad 2.36$$

Here, α is the material absorption coefficent ($\alpha_p = \alpha_s$ for SBS) and g_B is the Brillouin gain which, as for g_R, is directly related to $\chi_I^{(3)}$ via the Brillouin susceptibility (section 2.4). This is a measure of the probability of pump/acoustic phonon scatter.

An analytical expression for g_B at ν_B in terms of fibre and source characteristics has been derived (Tang, 1966; Cotter, 1983)

$$g_B = \frac{2\pi n^7 \rho_{12}^2 d}{c\lambda_p^2 \varrho_o V_A \Delta\nu_B} \qquad 2.37$$

where ρ_{12} is the elasto-optic coefficient, ϱ_o is the material density and $\Delta\nu_B$ the SBS gain bandwidth (FWHM). $\Delta\nu_B$ varies as λ_p^{-2} (Cotter, 1983) and is typically 100-150MHz for a 0.5145μm pump (again much less than the Raman bandwidth). Hence, g_B is approximately wavelength independent. The term d varies as $\cos^2\theta$ where θ is the angle between input polarisation azimuth and principal axis of the fibre. It is unity for fibres in which a linear input polarisation state is maintained and is 0.5 for unpolarised systems.

Equations 2.36 have been solved, assuming negligible pump depletion and $\alpha_s = \alpha_P$ (Smith, 1972) to yield, for $I_s(0)$, the output Stokes signal:

$$I_s(0) = I_s(L)\exp\Big(g_B I_p(0) L_{eff} - \alpha_s L\Big) \qquad 2.38$$

where $I_s(L)$ is the Stokes signal injected at $z = L$. The Stokes signal grows exponentially in the backwards direction. The threshold power for SBS, P_B^{thr}, is defined as the input pump power that produces a Brillouin output signal equal in power to the pump given by (Smith, 1972)

$$P_B^{thr} = \frac{21 A_{eff}}{g_B L_{eff}} \qquad 2.39$$

Again, A_{eff} is the fibre mode radius and L_{eff} is the core/pump interaction length which was originally defined by equation 2.21. Since fibre losses are more often expressed in terms of $\mathcal{N}$ dB per km, L_{eff} can be expressed as

$$L_{eff} = \frac{(10^{\mathcal{N}L/10} - 1)}{(10^{\mathcal{N}L/10} \ln 10^{\mathcal{N}/10})} \qquad 2.40$$

For fibres supporting several propagation modes, the inherent increased area will reduce the SBS threshold. Also, since each mode possesses a unique phase velocity, each mode should produce a characteristic Stokes signal from energy conservation considerations. The gain for signals lying towards the edge or even outside the gain bandwidth is thus significantly reduced. For silica fibre systems, g_B is typically $5\times10^{-11}\mathrm{mW}^{-1}$ (Ippen and Stolen, 1972), two orders of magnitude greater than both SRS and FWM gain values. Thus, SBS is the lowest threshold nonlinear process in many practical systems. The gain value decreases, however, for increasing pump bandwidth, $\Delta\nu_B$ by

$$\frac{\Delta\nu_B}{\Delta\nu_B+\Delta\nu_p} \qquad 2.41$$

Similarly, for pulsed sources, as the pulse halfwidth decreases relative to the acoustic phonon life-time, the gain is decreased.

A third absorption process linked to $\chi_I^{(3)}$ but in which *all* the absorbed energy is used to excite the material system is Two Photon Absorption (TPA). For a single input pump, frequency ω_1, and intensity $I_p(z)$, TPA is defined by(Shen, 1984)

$$\frac{dI_p(z)}{dz}=-\omega_1 g_t I_p^2(z) \qquad 2.42$$

where g_t, the TPA coefficient, is linearly related to $\chi_I^{(3)}$ and the total absorption, α, is given by

$$\alpha=\alpha_0+\alpha_1 I_p(z) \qquad 2.43$$

where α_0 is the linear absorption coefficient. TPA forms the basis of an extremely interesting range of photoabsorptive and photorefractive mechanisms in doped fibre systems which have important implications for SBS based systems and which are examined in Chapter 4.

In summary, the principal nonlinear mechanisms that occur in monomode optical fibres are

- SBS, which possesses the lowest threshold for cw, narrowband pump sources.
- SRS, which possesses the lowest threshold for pulsed, broadband sources.
- FWM, which can occur in conjunction with either SBS or SRS, and is constrained by the phase-matching conditions along the fibre.
- SPM and CPM, which possess no lower limit threshold. Their magnitude is generally small and insignificant in fibres.

A fuller, theoretical description of SBS is now presented.

2.4 Stimulated Brillouin Scattering In Optical Fibres

2.4.1 Steady State SBS Theory and Associated Brillouin Mechanisms

SBS is represented classically as a three wave interaction between an optical pump, $E_p(\omega_p)$, a scattered Stokes wave, $E_s(\omega_s)$ and an acoustic phonon or density wave, $\Delta\varrho$. Spontaneous acoustic phonons arising from thermal effects generate a moving refractive index grating in the fibre-core via the strain-optic effect. These scatter power from the pump to the Stokes signal through Bragg diffraction. The Stokes signal is frequency downshifted because it is Doppler shifted from the moving grating which propagates at the acoustic velocity V_A. The two optical signals then interfere and produce a moving interference pattern (because of the frequency differential) which, to initiate a stimulated process must phase match exactly to the sound wave. The acoustic wave experiences gain via electrostriction (dependence of pressure on the square of the local optical fields), increasing the modulation depth of the grating and enhancing the scattering process (Chaio at al, 1964). The process then continues.

SBS is governed by the conservation laws of momentum and energy:

$$k_p = k_s + k_A; \quad \omega_p = \omega_s + \omega_A \qquad 2.44$$

where the subscripts p, s and A refer to the pump, Stokes and acoustic waves respectively. Energy conservation, in particular, leads to the well-known expression for ν_B, the frequency downshift of the Stokes signal with respect to the pump,

$$\nu_B = \frac{nk_pV_A}{\pi}\sin\frac{\theta}{2} \qquad 2.45$$

where θ is the orientation between pump and Stokes waves propagation. In fibres, θ equals 0 or π and, in monomode fibres, the Stokes signal counter-propagates with respect to the pump.

As stated previously, the Brillouin gain bandwidth, $\Delta(\nu_B)$, is small when compared to, say, the Raman bandwidth. The spectral width (FWHM) is related to the acoustic phonon life-time, T_B, by

$$\Delta\nu_B = \frac{1}{\pi T_B} \qquad 2.46$$

and if the Brillouin waves decay as $\exp(-t/T_B)$, the Brillouin gain has a Lorentzian profile given by (Agrawal, 1989)

$$g_B(\nu) = \frac{(\Delta\nu_B/2)^2}{(\nu-\nu_B)^2+(\Delta\nu_B/2)^2}g_B(\nu_B) \qquad 2.47$$

where $g_B(\nu_B)$ is the peak of the gain given by equation 2.37. The form of the gain spectrum is dependent on the acoustic waveguiding characteristics of the fibre (discussed later in this section and in 2.4.2). For pump sources in which either the pulse width is less than T_B or whose phase varies rapidly over T_B (ie broadband pump), $g_B(\nu_B)$ can be significantly reduced. Transient SBS mechanisms arising from single-mode cw sources are discussed in section 2.4.3. For now, we consider only cw (steady-state) operation.

SBS results from a three wave mutual support system described by a trio of coupled wave equations in the form of equation 2.8 (Shen, 1984):

$$\begin{aligned} \left(\nabla \times \nabla \times \mathbf{E}_p(\omega_p) + \tfrac{\epsilon_r}{c^2}\tfrac{d^2\mathbf{E}_p(\omega_p)}{dt^2}\right) &= \omega_p^2\mu_0\mathbf{P}^{NL}(\omega_p) \\ \left(\nabla \times \nabla \times \mathbf{E}_s(\omega_s) + \tfrac{\epsilon_r}{c^2}\tfrac{d^2\mathbf{E}_s(\omega_s)}{dt^2}\right) &= \omega_s^2\mu_0\mathbf{P}^{NL}(\omega_s) \\ \left(\tfrac{d^2}{dt^2} + 2\Gamma_B\tfrac{d}{dt} - V_A^2\nabla^2\right)\Delta\varrho &= -\nabla.\mathbf{F} \end{aligned} \qquad 2.48$$

The acoustic wave is described by the density variation $\Delta\varrho$ and Γ_B is the acoustic damping coefficient which is inversely proportional to T_B. $\mathbf{F}$ is the driving force arising from the nonlinear coupling between $\mathbf{E}_p$ and $\mathbf{E}_s$.

The following substitutions are made into equation 2.48:

$$\begin{aligned} \mathbf{E}_p(\omega_p) = &\ \mathcal{E}(\omega_p)\exp i(k_pz - \omega_pt) \\ \mathbf{E}_s(\omega_s) = &\ \mathcal{E}(\omega_s)\exp i(k_sz - \omega_st) \\ \Delta\varrho = &\ \mathcal{A}\exp i(k_az - \omega_at) \end{aligned}$$

where $\mathcal{A}$ is the amplitude of the density wave. The slowly varying amplitude approximation is also invoked (Shen, 1984). This states that the energy transfer, dE/dz or j, between waves is significant only after the waves traverse many wavelengths. That is

$$|\frac{dj}{dz}| \ll |\frac{j}{\lambda}|$$

whence

$$|\frac{d^2\mathcal{E}(\omega_n)}{dz^2}| \ll |k\frac{d\mathcal{E}(\omega_n)}{dz}| \qquad 2.49$$

Equations 2.48 may be rewritten as

$$\begin{aligned} &-2ik_p\frac{d\mathcal{E}_p(\omega_p)}{dz}\exp i(k_pz - \omega_pt) = \omega_p^2\mu_0\mathbf{P}^{NL}(\omega_p) \\ &+2ik_s\frac{d\mathcal{E}_s(\omega_s)}{dz}\exp i(-k_sz - \omega_st) = \omega_s^2\mu_0\mathbf{P}^{NL}(\omega_s) \\ &+2iV_a^2k_a\Big(\frac{d}{dz} + \frac{\Gamma}{V_a}\Big)\mathcal{A}\exp i(k_az - \omega_at) = \nabla.\mathbf{F} \end{aligned} \qquad 2.50$$

The coupling terms, $\mathbf{P}^{NL}$, and driving force $\mathbf{F}$ are given by (Shen, 1984)

$$\mathbf{P}^{NL}(\omega_p) = \frac{1}{4\pi}\frac{d\epsilon}{d\varrho}\mathbf{E}_s\Delta\varrho$$

$$\mathbf{P}^{NL}(\omega_s) = \frac{1}{4\pi}\frac{d\epsilon}{d\varrho}\mathbf{E}_p\Delta\varrho \qquad 2.51$$

$$\mathbf{F} = \nabla p_r = \nabla\Big(\frac{1}{2\pi}\varrho_0\frac{d\epsilon}{d\varrho}\mathbf{E}_p\mathbf{E}_s\Big)$$

where p_r is the electrostrictive pressure and ϱ_0 the mass density. Qualitatively, two optical waves whose frequencies differ by ν_B drive a pressure wave due to the dependence of pressure on E and generate a beat frequency. Introducing these terms into equation 2.50, we form

$$\Big(\frac{d}{dz} + \frac{\alpha_p}{2}\Big)\mathcal{E}(\omega_p) = \frac{i\omega_p^2}{2k_p}\mu_0\frac{d\epsilon}{d\varrho}\mathcal{E}(\omega_s)\mathcal{A}\exp -i\Delta kz$$

$$\Big(\frac{d}{dz} - \frac{\alpha_s}{2}\Big)\mathcal{E}^*(\omega_s) = \frac{i\omega_s^2}{2k_s}\mu_0\frac{d\epsilon}{d\varrho}\mathcal{E}^*(\omega_p)\mathcal{A}\exp -i\Delta kz \qquad 2.52$$

$$\Big(\frac{d}{dz} + \frac{\Gamma}{V_a}\Big)\mathcal{A} = \frac{ik_a}{4\pi V_a^2}\varrho_0\frac{d\epsilon}{d\varrho}\mathcal{E}^*(\omega_s)\mathcal{E}(\omega_p)\exp i\Delta kz$$

where $\mathcal{E}^*$ denotes a complex conjugate and $\Delta k = k_p + k_s - k_a$ with $\Delta k \ll k_a$.

By assuming that the acoustic phonon is heavily damped, then

$$\frac{d\mathcal{A}}{dz} \approx i\Delta k\mathcal{A} \qquad 2.53$$

and $\mathcal{A}$ is eliminated from equations 2.52 to produce

$$\Big(\frac{d}{dz} + \frac{\alpha_p}{2}\Big)\mathcal{E}(\omega_p) = \frac{i\omega_p^2}{k_p}\mu_0\chi_B^{(3)}|\mathcal{E}(\omega_s)|^2\mathcal{E}(\omega_p)$$

$$\Big(\frac{d}{dz} - \frac{\alpha_s}{2}\Big)\mathcal{E}^*(\omega_s) = \frac{i\omega_s^2}{k_s}\mu_0\chi_B^{(3)}|\mathcal{E}(\omega_p)|^2\mathcal{E}^*(\omega_s) \qquad 2.54$$

where

$$\chi_B^{(3)} = \frac{k_A\varrho_0}{8\pi V_A^2}\Big(\frac{d\epsilon}{d\varrho}\Big)\frac{1}{\Delta k - i\Gamma_B/V_A} \qquad 2.55$$

and is called the Brillouin susceptibility. For Stokes amplification, the gain must exceed the loss. Equations 2.54 reduce to the simpler form described previously in equation 2.36 in terms of field *intensities*, $I_{p,s}(z)$, and which are repeated here

$$\begin{aligned} dI_p(z)/dz &= -g_BI_p(z)I_s(z) - \alpha_pI_p(z) \quad &\text{(a)} \\ dI_s(z)/dz &= -\big(g_BI_p(z)I_s(z) - \alpha_sI_s(z)\big) \quad &\text{(b)} \end{aligned} \qquad 2.36$$

The negative sign in equation 2.36(b) denotes backwards propagation. $\alpha_p = \alpha_s = \alpha$ and g_B is defined as in equation 2.37.

Analytical solutions to the coupled wave equations have been obtained for two special cases:

(i) In the absence of pump depletion, ie $g_B = 0$ in equation 2.36(a) (Smith, 1972).

The expression given by equation 2.38 is a measure of the Brillouin amplification of a Stokes signal incident at $z = L$ (L, fibre length). This is equivalent to injecting a single Stokes photon per mode into the fibre at the point where the SBS gain equals the fibre loss. The resultant expression for Brillouin threshold (equation 2.39) is an accurate indicator in estimating the effect of SBS on fibre systems, despite the assumptions involved.

In practice, the Stokes signal grows from noise or *spontaneous* Brillouin scattering within the fibre. An estimate of the spontaneous signal power 'injected' into the distal end of the fibre, $P_s(L)$, that produces a pump threshold P_B^{thr} can be directly obtained by combining equations 2.38 and 2.39.

$$P_S(L) = P_B^{thr} \exp(\alpha L - 21) = \frac{21 A_{eff}}{g_B L_{eff}} \exp(\alpha L - 21) \qquad 2.56$$

(ii) In the absence of fibre loss, ie $\alpha = 0$ (Tang, 1966).

Equations 2.36 can be readily solved to yield

$$I_p(z) = I_s(z) + I_p(0) - I_s(0)$$

$$I_s(z) = \frac{I_s(o)\Big(1 - I_s(0)/I_p(0)\Big)}{\exp\Big[\Big(1 - I_s(0)/I_p(0)\Big) g_B I_p(0) z\Big] - I_s(0)/I_p(0)} \qquad 2.57$$

The solution again provides an approximate assessment of the effect of SBS on fibre systems. In the experimental system studied in this project, both pump depletion and fibre absorption are significant. Thus, more accurate solutions to the coupled wave equations for SBS are necessary to obtain values of the Stokes and pump signal at the fibre outputs and along the fibre length.

Exact analytical solutions *can* be obtained for the *general* stimulated scattering (ie not necessarily Brillouin) coupled equations in which both pump and Stokes signals propagate in the positive z-direction. Thus, the solutions to the equations (Enns and Batra, 1969)

$$\frac{dI_{p,s}(z)}{dz} = \mp g_B I_p(z) I_s(z) - \alpha_p I_{p,s}(z) \qquad 2.58$$

were derived during the present study and are presented in Appendix A. In SBS, however, the signs on the right of equation 2.58 for $I_s(z)$ are reversed due to the counterpropagating Stokes signal (refer to equation 2.36(b)). Enns and Batra are often quoted as providing full solutions to the SBS mechanism (eg Kaiser and Maier, 1972). In fact, the SBS equations for pump depletion and lossy media have no *exact* analytical solutions (Bayvel and Radmore, 1990). However, it was found during the present study that, by making certain substitutions to the solutions for equation 2.58 (particularly equation A20 in Appendix A), an extremely accurate anaytical representation of the SBS system was obtained. The substitutions, referring to the notation of Appendix A, were

$$\beta \rightarrow -\beta$$

$$\gamma \rightarrow -\gamma$$

$$\exp(-\alpha z) \rightarrow \exp(+\alpha z) \quad \text{for the numerator only in A20(a)}$$

which produced the following expressions for $I_s(z)$ and $I_p(z)$

$$I_s(z) = \frac{(1-\beta) I_s(0) \exp(+\alpha z)}{G(z) - \beta} \qquad 2.59(a)$$

$$I_p(z) = \frac{(1-\beta) G(z) I_p(0) \exp(-\alpha z)}{G(z) - \beta} \qquad 2.59(b)$$

where $G(z) = \exp\big[+\gamma(1-\beta)\big(1-\exp(-\alpha z)\big)\big]$, $\beta = I_s(0)/I_p(0)$ and $\gamma = g_B I_p(0)/\alpha$. The equations were exact solutions for a zero gain system. Further, for finite g_B and α, equation 2.36b is satisfied. The validity of these expressions for SBS systems was demonstrated by firstly examining the trends that are obtained on modifying the key variables in the expressions and, secondly, by comparing the results with a well-established numerical approach to the solution of the SBS equations.

To ease algebraic manipulation in solving equations 2.59 for $I_p(z)$ and $I_s(z)$, a simple Fortran programme was written and is listed in Appendix B. The programme calculated output *powers* rather than intensities as in equation 2.59. The starting point of the calculation was the effective spontaneous Stokes power injected into the system at $z = L$, $P_s(L)$ from equation 2.56. This was constant for a given fibre system. If the source of the stimulated

Stokes signal had been from a second fibre. as in Brillouin amplifiers, then clearly the appropriate value for $P_s(L)$ obtained from that fibre is used. For a given pump power, $P_p(0)$, the output Stokes signal, $P_s(0)$, can be calculated iteratively by inserting the $P_s(L)$ value for the system into the left hand side of equation 2.59(a). The value of $P_p(L)$ is then obtained from 2.59(b). It is then straightforward to obtain numerical values for both Stokes and pump signals as functions of fibre length, $P_{s,p}(z)$.

An example of the data obtained from the programme is illustrated in Figure 16.

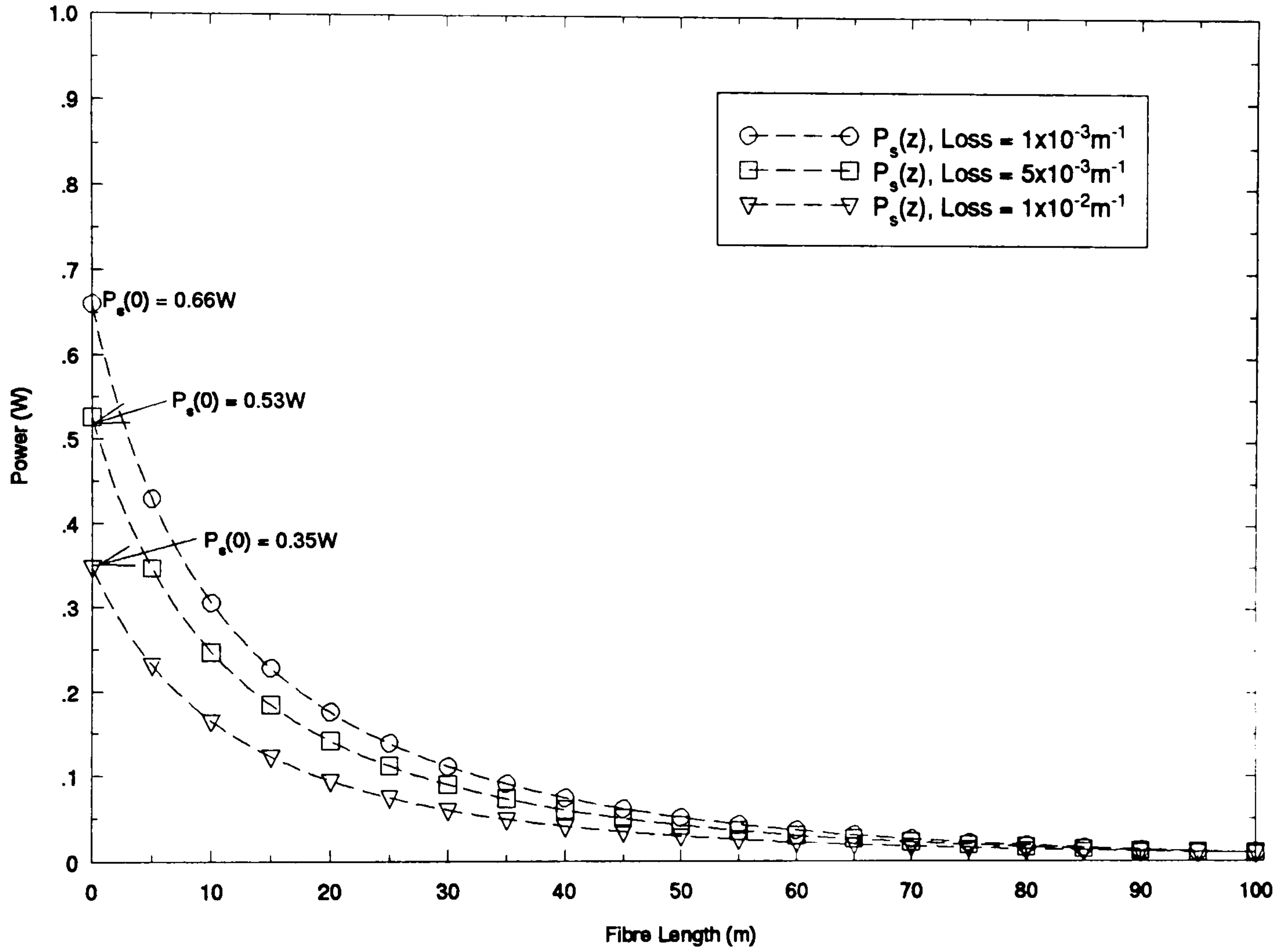

Figure 16: Variation of Stokes Signal, $P_s(z)$, Along Fibre Length for Increasing Fibre Attenuation

The graph shows how the Stokes signal, $P_s(z)$, varied along a fibre (which is acting as a Brillouin amplifier) as a function of increasing fibre loss. Pump and probe signals of 1W and 10mW were launched respectively from opposite ends of a 100m fibre. The fibre possessed a mode area of 10^{-10}m^2 and SBS gain coefficient of 10^{-11}mW^{-1}. The graph shows the effect of increasing the attenuation coefficient (the 'loss') from 10^{-3} to 10^{-2}m^{-1} on Stokes power. The decrease in power of the Stokes signals demonstrated the expected trend as the net gain of the system was lowered. Similar results were obtained on increasing the fibre area and reducing SBS gain and probe power.

Numerical solutions to the SBS coupled wave equations have been published which use fourth order Runge-Kutta algorithms to solve the first order differential equations describing the SBS process (Bayvel and Radmore, 1990). These results showed good agreement with experimental data over a range of SBS systems and amplifiers. A direct comparison between the approach developed in the present work (the 'analytical' solution) and those based on numerical solutions also yielded good agreement.

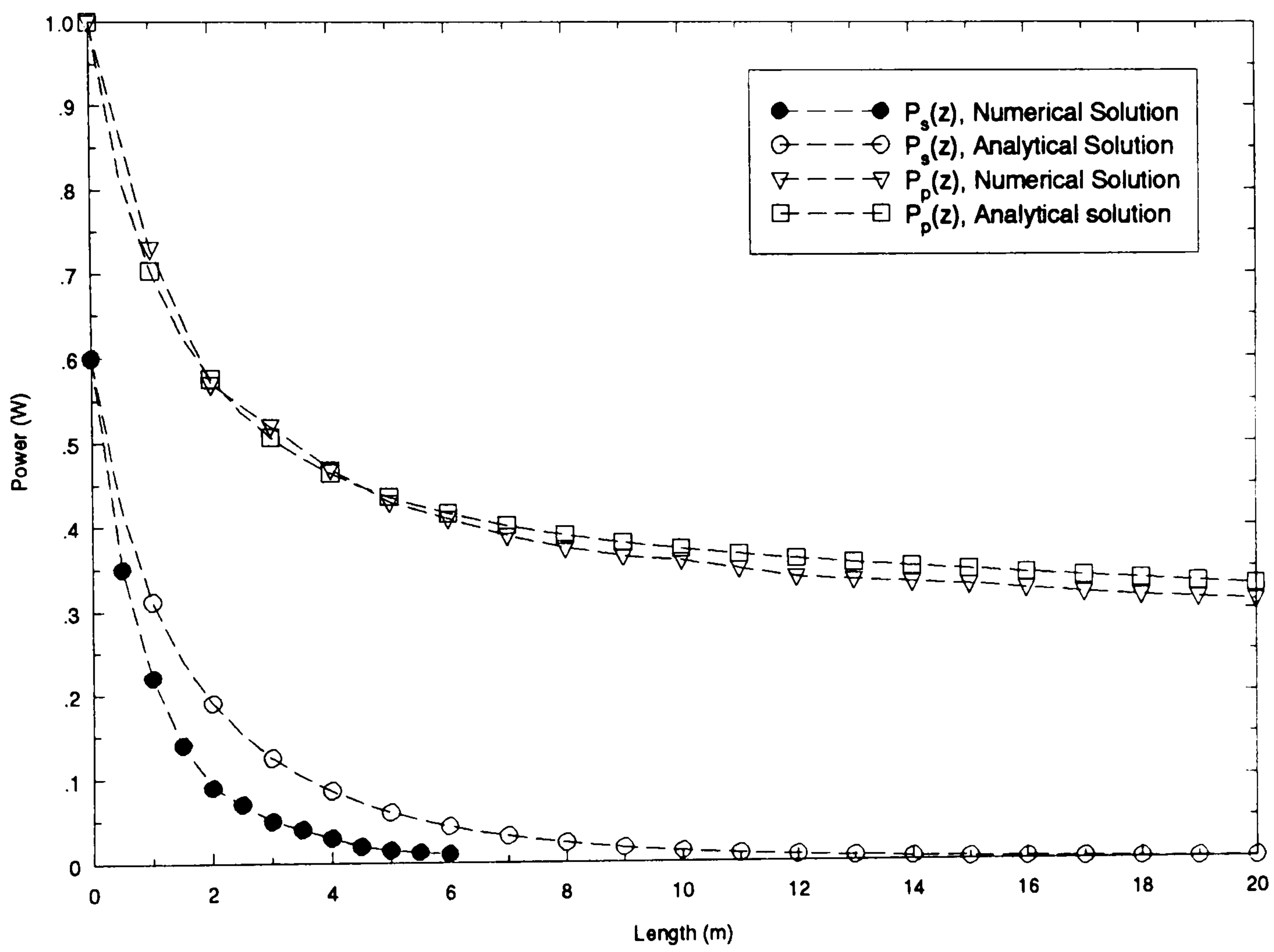

Figure 17: Comparison Between Numerical and Analytical Solutions of the SBS Coupled Wave Equations for $P_p(z)$ and $P_s(z)$

In Figure 17, for example, the variation in both $P_p(z)$ and $P_s(z)$ along the first 20m of a 100m fibre are presented. (The x-axis scale was chosen so that all signals could be displayed simultaneously). The fibre possessed a 10^{-11}m^2 mode area, a Brillouin gain of 0.8×10^{-11}mW^{-1} and attenuation, α, equal to 10^{-2}m^{-1}. An input power of 1W was used to pump the system, with $P_s(L)$ equal to 10^{-9}W. The relative values of the pump signals and output value of the Stokes signal at $z = 0$ correlated very well. There was a difference noted between the variation in Stokes signal along the fibre length. with the numerical solution decaying more rapidly. However, the differences are not significant in the context of the experimental systems described later in this thesis.

Both $P_p(z)$ and $P_s(z)$ depend on the value of $P_s(L)$, the effective spontaneous Brillouin signal (ie the thermally induced 'noise' term). An exact value of $P_s(L)$ is thus obtained by complicated quantum mechanical analyses though equation 2.56 provides a good approximation. We conclude, therefore, that equations 2.71 are a valid representation of the SBS process in fibres. They are exploited in Chapter 3 to model the fibre systems used in the experiments and to compare with the output theoretical signals ($P_p(L)$ and $P_s(0)$). In Chapter 5, the solutions are used to assess the suitability of SBS for multiplexed sensing techniques in single source systems.

Other SBS/fibre properties are now briefly examined. In a similar manner to their optical waveguiding properties, the fibres can support a discrete range of acoustic modes which significantly influences the SBS properties of the fibre. The acoustic modes are divided into two categories – transverse (shear) and longitudinal (Henry, 1992). For acoustic wave *guidance*, the condition

$$V_{A,core} < V_{A,clad}$$

must be satisfied. The acoustic velocity nomenclature is self explanatory and is analogous in the optical domain to the refractive index relationship between core and cladding. SBS arises from the optical interaction with longitudinal acoustic fields, since the scattering off shear modes is significantly lower in fibres (Henry, 1992). Interaction with longitudinal modes usually produces a single Stokes frequency peak downshifted by ν_B (equation 2.35). Multiple peaks, however, can occur in the gain spectrum due to simultaneous propagation of higher order acoustic modes (see section 2.4.2). Indeed, by choosing dopants of a fibre to support optical waveguiding and suppress acoustic modes (by increasing the modal velocity of the core) SBS may be reduced even in fibres possessing a nominally high g_B factor (Jen et al, 1991) from the thermally induced acoustic phonon model.

In addition to the backscattered Brillouin effect, *spontaneous* forward scatter of the pump may arise through an acoustic phonon-photon interaction. This is guided acoustic-wave Brillouin scattering (GAWBS) and involves the interaction of the light with thermally excited transverse (torsional and radial) phonons. These are acoustic eigenmodes of the cylindrical fibre structure and can produce a set of well-defined frequency peaks in the system output. This scattering can produce problems in communications systems since it leads to weak phase modulation and depolarisation. However, the scattering efficiency of GAWBS is very weak ($\approx 10^{-10}\mathrm{m}^{-1}$) and experiments using both pulsed (Poustie, 1992) and cw sources (Shelby et al, 1985) reveals that the GAWBS spectrum forms part of the system noise floor at -80 to -95dBm. GAWBS was not a contributary factor to the SBS systems studied here.

The *stimulated*, forward Brillouin scatter (FSBS) recently reported differs from GAWBS in that it is based on collinear phase matching between three guided waves and displays a stimulated threshold (Russell et al, 1991a). It is similar in principle to the backward mechanism. Intermodal beating between LP_{01} and LP_{11} modes of the fibre produces an interference pattern whose points of constructive interference alternate to and fro across the core with a period of L_B where

$$L_B = \frac{2\pi}{(k_{01} - k_{11})}$$

where k_{01} and k_{11} are the wave-vectors of the two spatial modes. Spontanoeus acoustic phonons generate travelling index gratings in the fibre core through the strain optic effect. When L_B matches the phonon wavelength, light is scattered between modes, producing the frequency conversion from pump to Brillouin signals. Intermodal frequency mixing produces a moving interference pattern which creates gain in the original spontaneous signal when it phase matches exactly to the acoustic wavefront. The direction of the acoustic wave depends on the pump launch mode. Pumping in the LP_{01} (LP_{11}) mode produces a forward (backward) propagating sound wave. In the current project, dual spatial mode fibre was used in several experiments. As shown in Chapter 3, however, no evidence of FSBS was encountered.

2.4.2 Experimental Characteristics of Steady State SBS

Brillouin scattering has been exploited as a spectroscopic tool in both solids and liquids for many years. In early work (Chaio et al, 1964), 50MW peak power pulsed ruby lasers (λ_p= 0.694μm) pumped anisotropic crystalline quartz and sapphire to determine the acoustic wave properties of the materials. Frequency downshifts of typically 18GHz and 41GHz respectively were generated. An identical source was also used to probe organic liquids such as methanol and acetone to obtain acoustic spectra (Garmire and Townes, 1964). More recently (Bucaro and Dardy, 1974), Brillouin scattering was used to assess the elastic and photoelastic mechanisms present in solids (fused quartz in this instance) that are influenced by structural effects. The Brillouin linewidth, $\Delta\nu_B$, frequency offset, ν_B, and intensity were measured to determine respectively the acoustic absorption coefficient, acoustic phonon velocity and material photoelastic coefficients. Measurement over a wide temperature range (eg Pelous and Vacher. 1976) has yielded important data on the thermal solid state physics of materials.

The first observation of SBS in optical fibres (Ippen and Stolen, 1972) used a 0.535μm line-narrowed pulsed Xenon source to pump a 5.8m silica core fibre. A high peak power pulsed source was required to counteract the short interaction length and high fibre losses ($\approx$ 1300dBkm^{-1}). A frequency downshift of 32.2GHz was measured, consistent with equation 2.35 when using the bulk silica value of acoustic velocity (5.89×10^3ms^{-1}). A measured threshold power of 2.3W implied (equation 2.39) a gain coefficient of 4.3×10^{-11}mW^{-1}. Insertion of the appropriate values for bulk optic silica into equation 2.37 gave a gain value of 5.9×10^{-11}mW^{-1}.

SBS was first observed with a cw source when a 9.5m long fibre sample configured as a hybrid resonator (Chapter 6 discusses these devices further) was pumped with a 0.5145μm Argon Ion laser source (Hill et al, 1976a). A threshold power of 250mW was observed. Subsequently, many groups have demonstrated SBS fibre systems with ever-decreasing threshold, as the losses in fibres have been reduced, and more narrowband pump sources developed. All have verified at least some of the important features derived in section 2.4.1, particularly

(a) For a given fibre, ν_B, the Stokes downshift, is inversely proportional to the pump wavelength.

(b) The gain of a given fibre is approximately independent of pump wavelength.

(c) The SBS threshold and pump-Stokes conversion efficiency scales directly with the fibre modal area and inversely with both gain and core-pump interaction length.

Examples of these developments are now considered. A 30.2mW threshold was reported (Uesugi et al, 1981) for a 0.71μm cw single frequency dye laser pumping a 3.8km long, 3.5μm core fibre. A 25mW threshold was predicted using a gain value of 5×10^{-11}mW^{-1}. The Stokes signal was downshifted by 25GHz with respect to the pump. Observation of SBS with a 1.32μm Nd:YAG source (Cotter, 1982a), highlighted for the first time the potentially debilitating effects of SBS on communications systems. A threshold power of only 5mW (at the time, a new minimum) was recorded along 13.6km length of GeO_2 doped silica fibre of loss 0.41dB/km. A 5.6mW threshold was predicted by theoretical analysis. The frequency downshift of the Stokes was measured as 12.7±0.2GHz (13.1GHz predicted from 2.35). Figure 18 illustrates the power emitted from the distal and front ends of the fibre as a

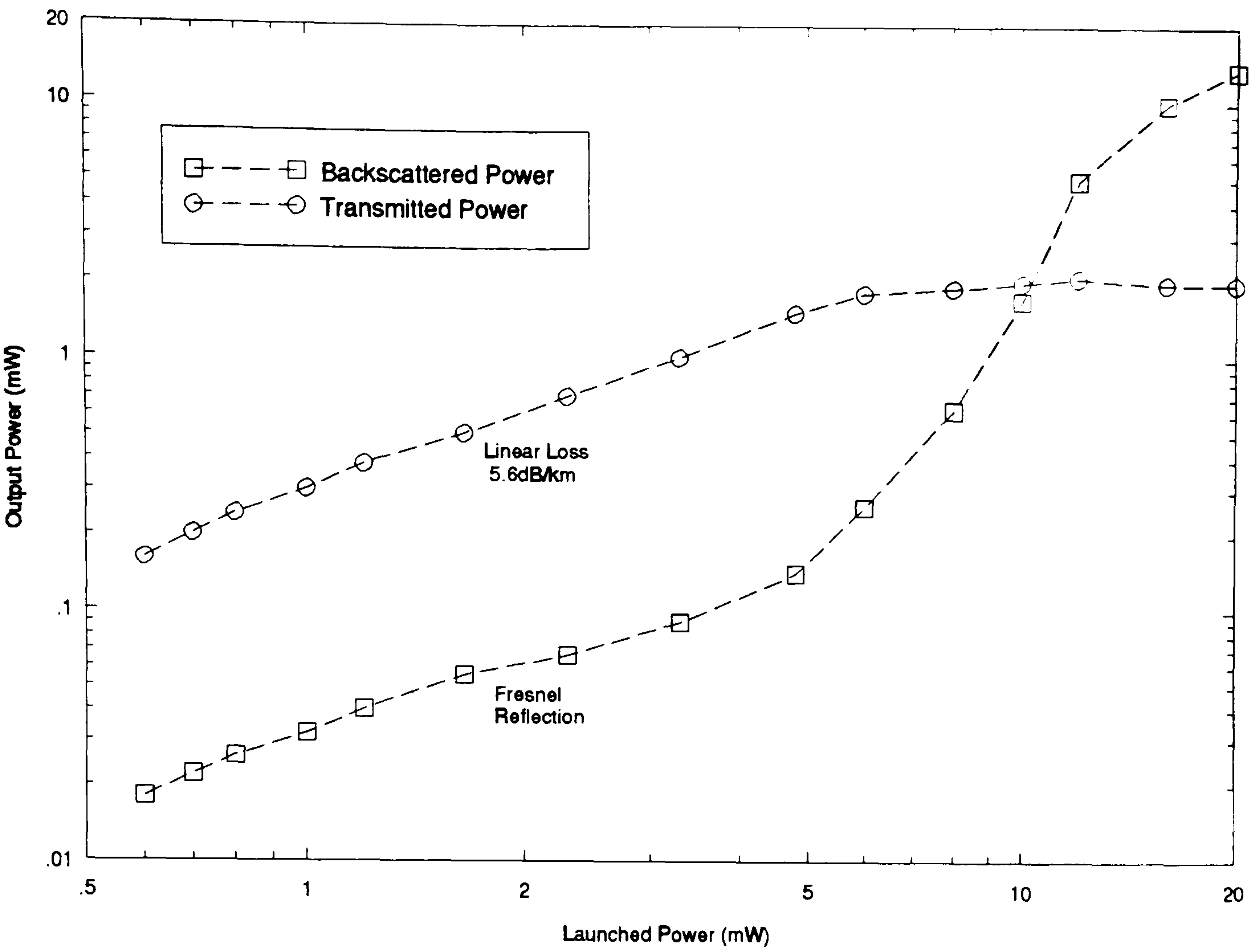

Figure 18: Power Emitted From 13.6km of Monomode Fibre at 1.32μm as a Function Of Launched Power

function of increasing launch powers in this work. At low input powers, the output power in the backward direction was the Fresnel reflection from the core/air interface. For powers greater than 5mW, the output backscattered power increased nonlinearly with input power. The pump power to Stokes power conversion efficency saturated at $\approx$ 65% for launch powers in excess of 12mW. In the forward direction, the power increases linearly and was a direct measure of the optical loss of the fibre until, at threshold, it began to saturate. In contrast, Aoki et al (1987) measured a 9mW threshold using a direct feed-back laser diode at 1.3μm to pump a 30km long fibre with a loss of 0.46dB/km. For 25mW input, only a 25% conversion efficiency was observed. The difference arose from the larger linewidth of the laser used, which partially suppressed SBS (15MHz in Aoki experiment compared to 1.6MHz in Cotter's).

As for SRS, the SBS gain, g_B, has a characteristic spectrum, defined by $\Delta\nu_B$, the FWHM gain bandwidth. The value quoted generally refers to the *spontaneous* linewidth as for SRS and is Lorentzian in form (equation 2.47).

Both the exact shape and magnitude of the gain spectrum are, however, very fibre dependent and influenced by dopant concentration, fibre index profile and the homogeneity of these parameters along the fibre length. As an example of the variation in $\Delta\nu_B$ that can occur in different fibres, for the two 1.3μm pump systems cited above, in one (Cotter, 1982a), the linewidth was 22MHz, whilst in the second (Aoki et al, 1987), the linewidth was measured as approximately 100MHz.

Early measurements of the spontaneous Brillouin gain spectrum in fibres were used to infer data on the molar composition of dopant species which helped to sustain optical waveguiding. Dual Brillouin peaks observed by probing multimode fused silica core/borosilicate clad fibre with 0.5145μm light (Rich and Pinnow, 1974) arose from different acoustic velocities present in the core and cladding. The frequency difference was proportional to the B_2O_3 concentration in the cladding. By measuring the linewidth of the gain spectrum, data on acoustic phonon life-times (inversely proportional to $\Delta\nu_B$) was attained for silica fibre (Rowell et al, 1979). The measured bandwidth of 140± 20MHz represents the interrelation between the number of acoustic modes that support scattering and the fibre diameter and index profile at the point where scattering occurs.

Germania dopant modifies the gain spectrum significantly (Tkach et al, 1986). A decrease in the frequency shift of the peak of the gain spectrum was observed (equal to 89MHz/%wtGeO_2 at 1.525μm) together with a broadening of $\Delta\nu_B$ due to a non-uniform core index profile and length dependent changes in Ge concentration. Indeed, in one sample investigated, two Brillouin peaks were observed and attributed to varying GeO_2 concentration *across* the core. The relationship between gain and fibre index profile has been investigated (Shibata et al, 1987). The spontaneous linewidth was broader by a factor of 2.5 in graded index fibre than step-index due to the slower change in Δn across the fibre cross-section and additional uncertainties along the fibre length. The effect of other dopants such as phosphates (P_2O_5) on the gain was also investigated. In Shibata's measurements, the gain spectrum was measured by optically mixing the pump with a counter-propagating probe whose frequency was modulated externally in time. The probe was amplified when the frequency differential between it and the pump passes through the gain spectrum. These measurement techniques are described in the context of sensors in Chapter 5.

All these results suggest that the Brillouin linewidth can be controlled by a suitable choice of core-cladding dopant and/or core index profile. Indeed, by considering in more detail the relationship between dopant and the *acoustic* guiding properties of the fibre, SBS can be enhanced or suppressed. The condition for acoustic waveguiding in the core discussed previously is that V_A in the cladding exceeds V_A in the core. Table 4 shows the qualitative effect of dopant on the values of both V_A and n (Jen et al, 1988).

Dopant:	GeO_2	P_2O_5	TiO_2	B_2O_3	F_2	Al_2O_3
1/n	↓	↓	↓	↑	↑	↓
V_A	↓	↓	↓	↓	↓	↑

Table 4 Effect of Dopant On Optical and Acoustic Properties of Fibres

By doping the core with germania, for example, the acoustic velocity of the core is lowered and both optical and acoustic waveguiding is enhanced. Since ν_B decreases with germania concentration, it can be inferred that the effect of germania on V_A is larger than on n (equation 2.35). Figure 19 shows the gain spectrum of two monomode fibres pumped at 1.286μm (Shibata et al, 1988). The first consists of a silica core and fluorine doped cladding (ie suppressed acoustic waveguiding), the second possesses a germania doped core and silica cladding (ie enhanced acoustic waveguiding). The core diameters and cut-off wavelengths of both are the same. In the latter (Figure 19), three peaks were present in the gain spectrum compared with only one in the former. The three peaks arise due to scattering off the three longitudinal modes supported by that fibre. Further, the magnitude of the largest peak in this fibre was greater than the peak in the pure silica core fibre due to the enhanced acoustic guidance.

SBS can, in fact, be suppressed even within a fibre that possesses a nominally high gain value (equation 2.37) via appropriate doping (Jen et al, 1991). In this work, the SBS thresholds of two fibres differed by a factor of 3.6 when only a 1.5 difference was predicted from theory (equation 2.39). Again, the fibres consisted of a germania doped core and fluorine doped cladding respectively.

Thus far, the spontaneous Brillouin gain spectra has been considered. As with the gain spectrum of SRS, the Brillouin bandwidth narrows as the scattering becomes stimulated, since the peak of the gain spectrum is amplified more quickly. Measurements of the Brillouin spectrum (Gaeta and Boyd, 1991) confirmed a narrowing of the Brillouin spectrum with increasing pump power. The spontaneous linewidth of 135MHz was reduced to 75MHz close to threshold before saturating at 29MHz for pump powers in excess of twice the threshold. Suppression of gain narrowing was due to the depletion of the pump, preventing the Stokes field from experiencing gain throughout the entire medium. In the present study, all work was undertaken at powers

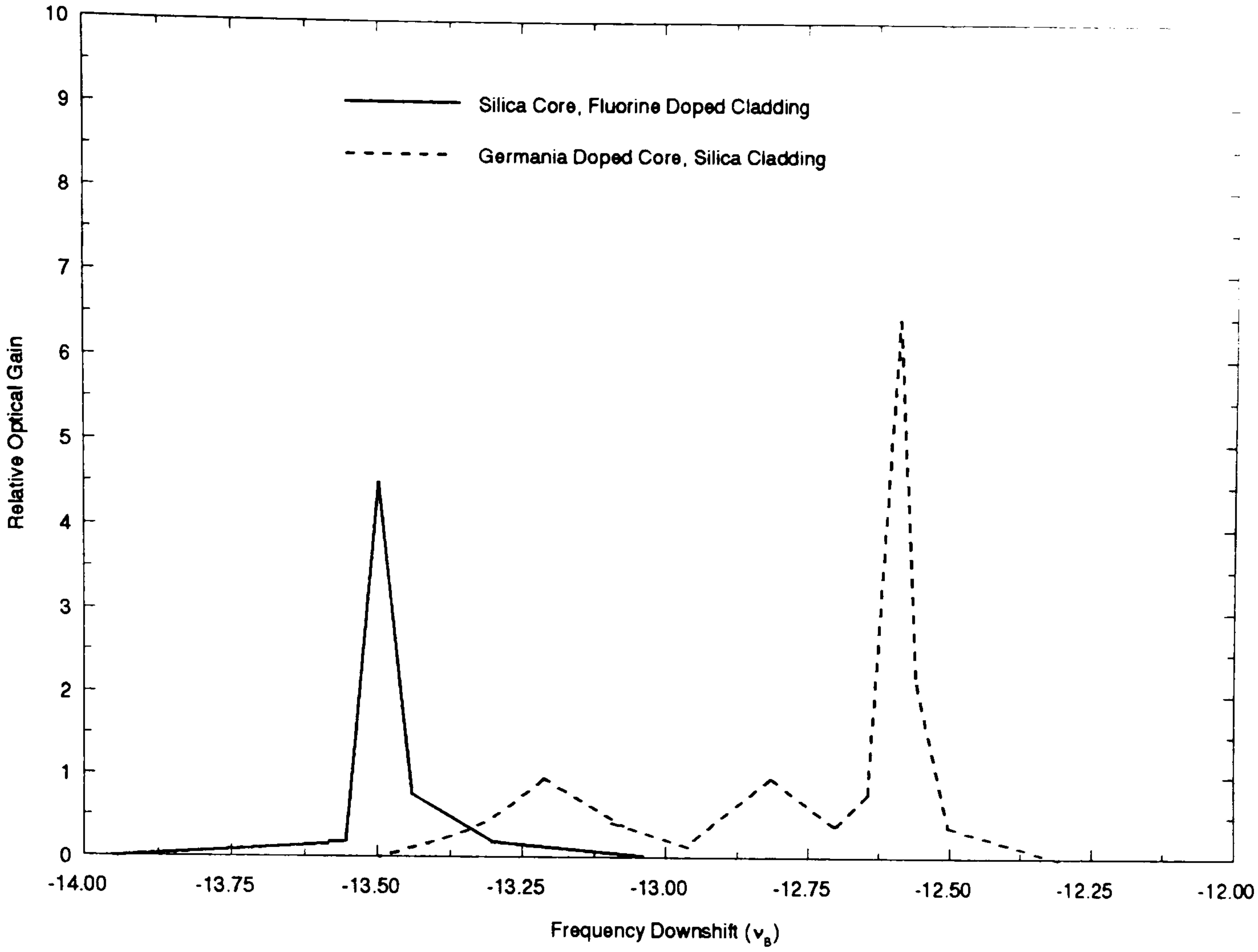

Figure 19: Brillouin Gain Spectra of Test Fibres Pumped at 1.286μm

above the stimulated threshold in the gain narrowed region.

Again, as noted for SRS, a cascade of higher Stokes orders can be induced in the fibre. Once the 1st order reaches a sufficient threshold, a second is generated which will copropagate with the original pump. Up to 10 Stokes orders have been observed in a fibre system (Hill et al, 1976b) by continually relaunching output signals. Significantly, a cascade of anti-Stokes signals was also present which arose via four-wave mixing between the original pump and relaunched 1st order Stokes. This interaction can generate both an anti-Stokes frequency, ω_a, and second Stokes frequency, ω_{2s}, thus (Labudde et al, 1980):

$$\omega_a = 2\omega_p - \omega_s \qquad 2.60$$

$$\omega_{2s} = 2\omega_s - \omega_p$$

The mixing does not require large reflectivities – for some systems, the Fresnel reflection at either end of the fibre is sufficient (as shown in Chapter 3). Phase matching constraints determine the exact system spectra.

The SBS process is strongly dependent on the temporal coherence characteristics of the pump. For broadband pumps, the gain is reduced by the ratio of spontaneous Brillouin to pump linewidths. Essentially, the SBS gain depends on the degree of correlation between the pump and Stokes waves. By modifying the correlation over the acoustic phonon life-time, by rapidly modulating the phase or frequency of the pump, for example, the gain can be suppressed. These methods have been applied to fibre communications systems in which the modulation technique used to impress information onto the optical carrier is chosen to maximise the data carrying capacity and also to minimise optical losses though SBS (eg Cotter, 1982b). In the present study, single-mode pump sources were utilised in all experiments so the gain was optimised.

The SBS properties of the fibres used in the study were measured and are reported in Chapter 3. Comparisons are then drawn with the systems described in this section.

2.4.3 Transient Properties of SBS

For sources whose amplitude (for pulsed pumps) and/or phase (for either pulsed or broadband pumps) varies over the acoustic phonon lifetime, T_B, transient effects arise in SBS systems as the gain acquires time dependence. The net result is to reduce the overall gain of the system. However, even for the single-mode (ie narrowband) cw pumps used exclusively during the study, some interesting time dependent effects were produced which cannot be described by the steady-state approach to SBS outlined in section 2.4.1. The origins of these mechanisms are now discussed, together with examples of their physical manifestation in SBS systems. Assessment of these mechansims on the experimental configurations investigated in this work are deferred until the appropriate chapters (principally 3 and 5).

The time dependence of $I_p(z,t)$ and $I_s(z,t)$ is governed by solving the modified coupled-wave equations (Johnson and Marburger, 1971):

$$\frac{dI_p(z,t)}{dz} - \frac{1}{v_g}\frac{dI_p(z,t)}{dt} = -g_B I_p(z,t) I_s(z,t) - \alpha_p I_p(z,t) \qquad 2.61(a)$$

$$\frac{dI_s(z,t)}{dz} - \frac{1}{v_g}\frac{dI_s(z,t)}{dt} = -\left(g_B I_p(z,t) I_s(z,t) - \alpha_s I_s(z,t)\right) \qquad 2.61(b)$$

where v_g is the group velocity of both pump and Stokes beams. The group velocity mismatch between the pump and counterpropagating Stokes gives rise to relaxation oscillations in the Stokes signal as it is initiated. These decay in amplitude within a few microseconds so the Stokes signal quickly approaches its steady state value. The period of the oscillations is 2τ, the round trip time of a photon in a fibre cavity of length L. Equations 2.61 have been solved numerically via a linear stability analysis (Johnson and Marburger. 1971) to demonstrate the effect on a system containing no optical feedback. aside from the Stokes signal itself. An intuitive understanding of the source of the oscillations may be gleaned as follows. The rapid growth of the Stokes signal near the fibre input (as shown in Figures 16 and 17, for example) depletes the pump. The effective gain experienced by ensuing Stokes photons is thereby reduced until the depleted pump propagates through the fibre. As the Stokes signal decreases, the incident pump propagates well beyond z=0 before becoming depleted. The gain then builds up again and the process is repeated periodically until the steady-state is achieved. Indeed, in the first experimental observation of SBS in optical fibres (Ippen and Stolen, 1972), oscillations of period 56nsec were observed in the scattered signal, consistent with the length of fibre used (5.8m).

The introduction of external optical feedback into the fibre, even by the relatively small amount provided by the Fresnel reflection at the air-core boundary can produce steady oscillations in the Stokes output which do not decay in time (Bar-Joseph et al, 1985). The steady oscillations are present over a limited range of input pump power and external reflectivity. Once again, equations 2.61 are solved numerically but the following boundary conditions are included:

$$\begin{aligned} I_p(0,\tau) &= I_p(0) + \mathcal{R}I_p(L,\tau-1) \\ I_s(L,\tau) &= \mathcal{R}I_s(0,\tau-1) \end{aligned}$$

where τ is the time of single photon transit along the fibre and $\mathcal{R}$ is the net reflectivity in the system. Two distinct operating regions were reported and verified experimentally (Bar-Joseph et al, 1985) as functions of the normalised SBS intensity $I_s(0)/I_p(0)$:

(a) For Stokes signals at and just above SBS threshold, steady oscillations accompany SBS whenever feedback is present. The oscillation consists of a fundamental signal of period 2τ and higher harmonics.

(b) Once the Stokes signals at $z=0$ reach a certain intensity (dependent on the product $g_B L I_p(0)$, but generally $I_s(0) \geq 0.67 I_p(0)$ for $g_b L I_p(0) \geq 10$), steady oscillations decay into relaxation oscillations and the Stokes signal attains a constant value in time, as for the zero feedback system.

Though this theory was developed for a loss-less medium, the effect of a finite absorption coefficient serves to increase the decay rate of the relaxation oscillations and reduce the overall amplitude of all oscillations. By increasing either the input pump power or the external reflectivity causes the transition between (a) and (b). The characteristics of the steady oscillations are investigated further in our fibres as a potential SBS based sensing mechanism (Chapter 5).

Recent reports of large scale *aperiodic* output instabilities in both pump and Stokes signals from optical fibre SBS systems (eg Harrison et al, 1990: Gaeta and Boyd, 1991) indicates that equation 2.61 still does not give a complete description of the time dependence of the SBS process. Indeed, irregular time evolution of the SBS system (as in any other) suggests chaotic behaviour (Baker and Gollub, 1990). The central feature is that the system does not repeat its past behaviour. Nevertheless, chaotic dynamical systems do follow deterministic equations.

In the cited experiments, a single-mode 0.5145μm laser generated SBS in 100m (Harrison et al, 1990) and 200m (Gaeta and Boyd, 1991) single mode fibre. The fibres were index matched to eliminate external feedback. In both experiments, sustained instabilities with modulation depths of 100% were generated over a wide spectral range using pump powers up to several times the threshold level. In the former, for example, the Stokes spectrum exhibited pure broadband features with a bandwidth of ≈30MHz. This was constant with increasing pump, though the overall magnitude of the spectra was enhanced by additional pump power.

Harrison's group, in particular, have extended the study to consider the effects on the nonlinear dynamics of optical feedback via both the core-air interface and an external mirror for increasing pump power (Lu et al, 1992). Dramatic changes in the behaviour of the dynamics compared with the zero feedback case were observed. Close to threshold, steady oscillations of period 2τ were observed (cf Bar-Joseph et al), augmented by a deeper, slower modulation. A second modulation of the same period, but phase shifted with respect to the first was observed. As the pump intensity was increased, the deeper modulation period decreased until, as it approached 2τ, the oscillatory dynamics of the system become complex and random. The Stokes signal then exhibited burst modes of operation superimposed on a d.c. level of Stokes emission. As the pump increased further, the duration of the bursts decreased and the separation increased indicating a trend to quasi-stable emission. Demonstration of complete stability was, however, thwarted by the onset of second order SBS. Similar results were obtained by modifying the cavity reflectivity via an external mirror. No evidence was found again for sustained stable emission.

Harrison's systems were modelled by including in the SBS coupled wave equations nonlinear refraction terms arising from both the self and cross phase modulation of the pump and Stokes signals. Hence, the terms

$$-i\frac{n_2\omega_p}{c}\Big(|\mathcal{E}(\omega_p)|^2 + 2|\mathcal{E}(\omega_s)|^2\Big)\mathcal{E}(\omega_p)$$

$$-i\frac{n_2\omega_s}{c}\Big(|\mathcal{E}(\omega_s)|^2 + 2|\mathcal{E}(\omega_p)|^2\Big)\mathcal{E}(\omega_s)$$

are introduced to the left-hand side of equation 2.54 where n_2 is the nonlinear index coefficient described in section 2.3.3. The equations can then be solved numerically by applying the appropriate boundary conditions. Omission of these terms produces the steady and relaxation oscillatory behaviour described above. Their inclusion, however, results in both temporal and spatial variations in the phase of the pump and Stokes signals and, as a result, dynamical instabilities. Excellent agreement between experiment and theory was obtained for systems with and without feedback. Similar results were obtained for increasing the pump or reflectivity in the finite feedback case since both induce stronger nonlinear refraction.

A qualitative explanation of the dynamical behaviour can be gleaned by considering the interplay between Brillouin gain and nonlinear refraction. The intensity modulation of the Stokes signal arises from time-dependent variations in g_B as the Stokes wave propagates. CPM and SPM in the fibre produce a time dependent ν_B in order to maintain the phase-matching conditions of the interacting beams. This, in turn, modifies the gain of the process as ν_B shifts away from the gain maximum. As a result, the intensity of the Stokes signal is modified, readjusting both CPM and SPM. The loop of cause and effect is therefore complete. Feedback increases the effective gain of the system since the twice-reflected Stokes signal is used to seed the process rather than the spontaneous Stokes signal. The effect of CPM and SPM is therefore enhanced and the Brillouin linewidth narrowed. These factors modulate the oscillatory dynamics of the system.

An alternative approach to modelling the unstable outputs based on stochastic perturbation analysis has been proposed (Gaeta and Boyd, 1991). A noise source, describing the thermal fluctuations in the fibre density that induce spontaneous Brillouin scattering, is included in the expression for F in equation 2.51. The model predicts large temporal fluctuations in the Stokes signal over a broad frequency range – not a surprising result since the SBS medium is merely amplifying the thermal noise that initiates the process. Though good agreement between theory and experiment was demonstrated, only a zero feedback system was modelled. The presence of feedback would not be expected to modify the dynamics significantly using this model. Thus, the experimentally observed differences between feedback and non-feedback systems suggest that the dispersive terms proposed by Harrison and co-workers are the principal source of instabilities. The effect of these mechanisms on the signal processing and sensing systems is discussed in subsequent chapters.

3 Optical Frequency Shifter Based On SBS

3.1 Overview of Chapter

The first application for SBS investigated in this work was a technique for the generation of carrier frequencies for use in fibre optic systems. A heterodyning element is a central component of many sensors such as fibre gyroscopes, vibrometers and Laser Doppler Velocimeters. Heterodyning is a well established technique in the context of signal processing for intrinsic fibre sensors as discussed in section 1.2.1. This investigation was undertaken because of both the relevance of the application to the aerospace industry and also because it allowed a full assessment of the SBS properties and other physical mechanisms of the available optical fibres. These results could then be applied to the important task of investigating novel sensor schemes based on SBS.

In section 3.2, then, a brief description of optical heterodyning is given. Techniques to produce a fibre-compatible heterodyning component reported in the literature are then assessed. All are based on the generation of acoustic waves within the fibre by an external element such as a piezoelectric transducer. In section 3.3, the SBS approach developed in the present work is described. The technique utilises the birefringent properties of fibres, with SBS, to induce carrier frequencies from a single fibre. The magnitude can vary, in principle, from 20kHz to 12MHz, depending on the nature of the birefringence. By using either Four Wave Mixing (FWM) in a single fibre, or two fibres of varying dopant concentration, the range of frequencies can be extended to higher values.

The experimental verification of these ideas is divided into two sections. In section 3.4.1, the basic steady-state properties of SBS for the six fibre species used in the study are described. The fibres were compared in terms of their SBS gain and pump-to-Stokes optical conversion efficiency. Other factors measured included the response of the fibre attenuation and polarisation properties to input pump power. Thus, the most appropriate fibres could be selected for the frequency shifter demonstration and for the later study of SBS sensors.

In the frequency shifter work (section 3.4.2), both single and dual fibre systems were investigated. Mean carrier frequencies were generated from 8MHz to 665MHz, using both ArI and Nd:YAG laser sources. In this work, the first demonstration of a single fibre frequency shifter based on SBS was recorded. The performance of all the fibre types was then compared with the principles espoused in section 3.3.

Transient phenomenon were also observed in the SBS systems. These yielded both a frequency modulation in the SBS-induced carrier and, a broadband intensity modulation in the system output. These effects are described and investigated further in section 3.5. Both were shown to be intrinsic to the SBS process, in agreement with the dynamical theory described in section 2.4.3. Experimental techniques to suppress the effects, in the context of the signal processing systems, are reported for the first time. These results are significant for the sensors based on SBS to be described in Chapter 5.

The principal results of the frequency shifter work are summarised in section 3.6.

3.2 Optical Heterodyning and Fibre Frequency Shifting Techniques

Heterodyne-based signal processing schemes are an attractive option for sensors, particularly interferometric systems, since they can provide benefits such as (Jackson 1985):

(a) constant, rather than cosinusiodal, phase sensitivity.
(b) potentially infinite, rather than single fringe, phase tracking range.
(c) a large dynamic range (of signal of interest).
(d) a large signal-to-noise ratio.
(e) information on fringe directionality.

Traditionally, a bulk optic Bragg cell is employed to provide a carrier signal up to 1GHz, though 40 to 80MHz central frequencies are most common. The device is incompatible with many fibre systems since light must be coupled out of the fibre and into the cell, before being relaunched back into the fibre. Thus, the cell can introduce coupling instabilities. Additional losses arise through ordinary scattering and Fresnel reflections from the extra optical interfaces introduced. An important criterion with regard to aerospace applications (section 1.1.1) is that the device is electrically driven which may preclude its insertion in explosive or high EMI environments. A fibre compatible device which addresses these problems has therefore been sought for many years. The basic principles and performance levels of several fibre systems proposed in the literature are now described and briefly compared.

In a Bragg cell, a travelling acoustic wave is generated by an electrical transducer such as a piezoelectric element. A moving refractive index grating is then set up across the device via electrostriction. Incident coherent light (the carrier wave) is diffracted and simultaneously frequency shifted by an amount equal to the acoustic frequency. The principles are similar in fibre devices. The incident and scattered beams are now two distinct guided modes of the fibre, the input carrier being launched along one mode only. Coupling between the modes is again initiated via a travelling acoustic wave, the frequency shift of the light in the second mode being equal to the acoustic frequency. In SBS, acoustic perturbations arise from the interaction between the light and the fibre core. These are longitudinal waves and do not induce coupling. The majority of techniques reported in the literature, however, rely on *externally* generated *transverse* acoustic waves to produce coupling. The fibres must guide two independent propagation modes and two types have been most commonly used – those that support two orthogonally polarised

LP_{01} (ie linearly birefringent fibre) and those that support the two lowest order spatial modes (LP_{01} and LP_{11} modes as depicted in Figure 12. Chapter 2).

The transfer of power between the modes over an interaction length, L_{eff} is described by coupled mode theory (Yariv, 1973). From the conservation of momentum, maximum coupling is obtained when the acoustic wavelength, λ_a, exactly equals the beat length of the fibre. This uniquely defines the magnitude of the frequency shift obtained in the second mode for the fibre. Light coupled from the fast (lower propagation constant) to the slow mode by a copropagating acoustic wave is frequency *upshifted* again through momentum conservation. Transfer of power from the slow to the fast modes produces a downshifted signal. If the acoustic wave counterpropagates with respect to the optical signal, the frequency shift direction is reversed.

In an early example (eg Risk et al, 1986a), a linearly birefringent fibre was clamped to a fused quartz block apon which surface acoustic waves were excited via a piezoelectric transducer. Phase matching was obtained by aligning the fibre at an angle θ to the propagation direction of the acoustic wave such that

$$L_B \cos\theta = \lambda_a$$

where L_B was the fibre beat length. This allowed tunability in the acoustic frequency through manipulation of θ. Since the coupling was initiated via the strain-optic effect which effectively rotated the fibre eigenaxes, a second condition for maximum coupling in birefringent fibres is that the bisector of the polarisation eigenaxes lies perpendicular to the substrate (This is *in addition* to the phase matching condition). In the cited system, a 95% conversion efficiency was obtained at 4.4MHz with a 3dB bandwidth of 4MHz. 25W of electrical power were used over a 32mm fibre interaction length. A useful figure of merit is the quotient of conversion efficiency and electrical power, which was equal to $3.8\%\mathrm{W}^{-1}$. Unwanted sidebands and carriers were suppressed using appropriate polarisation optics. Since the fibre beat length is wavelength dependent, a tunable optical filter may be formed (eg Risk et al, 1986b). As the acoustic frequency is modified, so the wavelength coupled most efficiently into the second eigenaxis is correspondingly shifted, a useful technique for WDM systems.

The system shown in Figure 20 produces guided acoustic energy *along* the fibre to enhance the intermodal conversion efficiency (Kim et al, 1986). Acoustic energy is focussed onto the dual spatial moded fibre through the silica horn. This caused the fibre to be periodically displaced laterally thereby causing a transverse wave to propagate down the fibre (analogous to waves on a string). Coupling was here initiated via both micro-bend and strain-optic effects. The 7.5cm long fibre section produced 100% conversion efficiency for only 0.25W input power at 8MHz, two orders of magnitude improvement (in $\%W^{-1}$ terms) on the system described above. Though no accurate axis alignment was needed, a mode stripper was required to suppress the unshifted carrier and other anomalous sidebands from spurious reflections in the system. Problems of modal incompatibility with single mode fibre can arise if the shifted signal emerges in the LP_{11} mode.

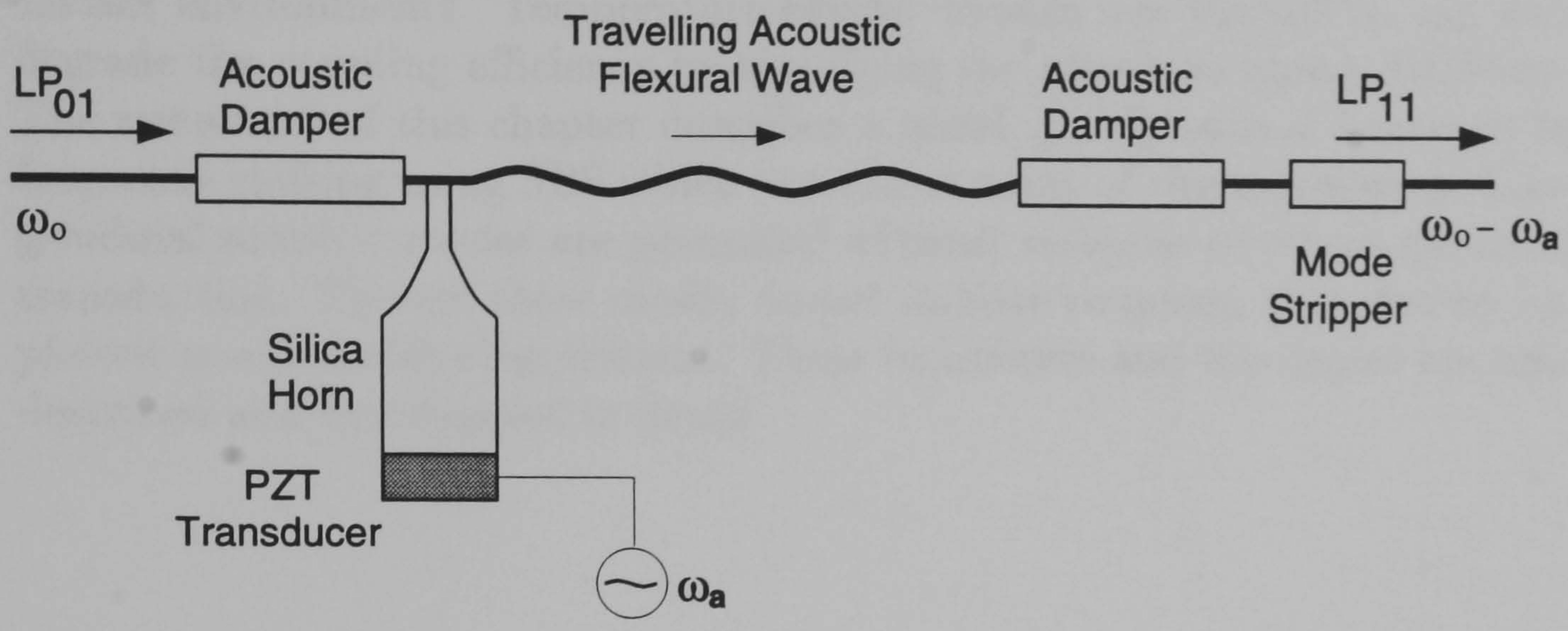

Figure 20: Schematic of Frequency Shifter Produced From Travelling Acoustic Flexural Wave in Dual Spatial Mode Fibre

The travelling flexural wave approach has been adapted for birefringent fibres (Pannell et al, 1988). Using a similar system to Figure 20, however, a conversion efficiency of only 2% for 150mW input power ($13\%W^{-1}$) at 791kHz was obtained for birefringent fibre. More recently, dual *core* fibres have been studied (Sabert et al, 1992) in which the cores possess an inherent phase velocity mismatch. Here, problems of modal compatibility and eigenaxis alignment do not exist. 100% inter-core coupling for 0.2W electrical power was obtained for a 560kHz signal at 1.064μm using flexural acoustic waves. The approach has a wide tuning range (0.5-20MHz, in principle) by adjustment of the input optical wavelength. This modifies the effective beat period between the cores and, hence, the shift frequency.

Several variations on all these themes have been proposed including a dual spatial mode fibre with two acousto-optic interaction regions in which acoustic waves co- and counterpropagate with respect to the input carrier (Askautrud and Engan, 1990). In the first region, coupling from the LP_{01} to LP_{11} modes produces the usual shifting. In the second, the shift is doubled and the light simultaneously coupled back into the LP_{01} mode. A 40dB sideband suppression and conversion efficiencies near 100% for 0.25W power were reported.

It is clear that fibre compatible frequency shifters are emerging with a wide frequency spectrum of operation, which overcome many of the disadvantages experienced with Bragg cells. However, all of the devices described in this section require an electrical input adjacent to the fibre to produce the acoustic energy. Additional optical components to isolate the original carrier and suppress unwanted sidebands are also necessary. Further, the interfacing technique between the acoustic emitter and fibre may be impractical in certain environments. Temperature effects, though not discussed, can also degrade the coupling efficiency by modifying the phase matching condition. The remainder of this chapter describes a novel, purely optical approach to frequency shifting using SBS which overcomes many of these problems. Longitudinal acoustic modes are generated without recourse to direct electrical transduction. Though these modes do not initiate coupling, they *can* be exploited as a heterodyning element. These techniques and topologies are now described and investigated in detail.

3.3 Principles and Theory of SBS Induced Frequency Shifter

The SBS approach to heterodyne carrier generation in fibres makes use of the linear relationship between the Stokes frequency downshift, ν_B, and the effective refractive index of the core along which the Stokes signal is generated (through equations 2.35 or 2.45). This relationship also forms the basis of the frequency modulated sensor systems discussed in chapter 5.

From equation 2.45, for a 0.5145μm source pumping a core of refractive index 1.46, a Stokes signal is produced, downshifted from the pump by 33.8GHz (0.044nm). This assumes that the acoustic velocity of silica takes its bulk value of 5.96×10^3ms^{-1}. The absolute frequency of the Stokes signal at approximately 400THz is only fractionally changed with respect to the pump and cannot alone be directly exploited in any heterodyning configuration. By mixing the Stokes signal with the pump, however, a signal consisting of both sum-frequency and difference-frequency components at 800THz and 33.8GHz respectively is produced. The former is again too large whilst the latter frequency also remains too high to be useful in the majority of electronic demodulation applications for sensors, though direct pump/Stokes mixing has been used to measure the Brillouin spectra of fibres up to 12GHz (Tkach et al, 1986). In this latter experiment, a high speed InGaAs PIN photodiode was used. More typically, in sensors, silicon based photodiodes are used which have rise times, limited by the capacitance of the device, to about 2nsec. This implies an upper limit of usable frequency of approximately 500MHz (3dB point) and partially explains why acousto-optic Bragg cells operating at 40 or 80MHz are useful components.

The magnitude of the downshift generated from the SBS systems must be reduced by at least two orders of magnitude for compatibility with these detectors. The principal technique used in the present work to achieve this is described as follows. The fundamental LP_{01} propagation mode consists of two degenerate orthogonal components (Chapter 2). In linear birefringent fibres, the two orthogonal axes are denoted as fast (index n_f) and slow (index n_s) respectively where n_s is greater than n_f. By launching pump light along the two axes simultaneously, with the power in each in excess of the SBS threshold (equation 2.39), two orthogonally polarised Stokes signals are produced, frequency downshifted from the pump by $\nu_{B,f}$ and $\nu_{B,s}$ where

$$\nu_{B,s} = \frac{2V_A n_s}{\lambda}; \quad \nu_{B,f} = \frac{2V_A n_f}{\lambda} \qquad 3.1$$

and assuming that V_A, the acoustic velocity, is the same for both modes. The two Stokes signals are optically mixed by orientating the transmission axis of a linear polariser at 45° to both. Sum and difference frequencies are produced where:

$$\nu_{B,s} + \nu_{B,f} = \frac{2V_A}{\lambda}(n_s + n_f) \qquad 3.2$$

and

$$\nu_{B,s} - \nu_{B,f} = \delta\nu_B = \frac{2V_A}{\lambda}(n_s - n_f) = \frac{2V_A}{L_B} \qquad 3.3$$

where L_B is the beat length of the fibre as defined in equation 2.18. The sum-frequency component (equation 3.2) at 67.6GHz is again too high for application in optical systems. The difference frequency component is, however, directly proportional to the degree of birefringence established within the core $(n_s - n_f)$. For a high birefringent fibre, single-moded at 0.5145μm, L_B is typically 1mm and an 11.9MHz signal is therefore predicted. This frequency is fully compatible with the bandwidth of optical detectors, being of the same order as the carrier produced from a Bragg cell. Thus, the frequency is extremely useful for sensor heterodyne demodulation. To reiterate, no direct external electrical power is used to generate the acoustic phonons – the process is *all-optical* and is fully intrinsic to the fibre. These factors enhance its compatibility with fibre sensor systems for harsh environments such as those encountered on-board aircraft.

The wide range of frequencies that can, in principle, be produced using the SBS technique is now illustrated with reference to the fibres investigated during the experimental study. The optical and geometric parameters of the six fibre types used are listed in Appendix C. All data was obtained from the manufacturer's specifications except for fibre attenuation which was measured in the laboratory (at 0.5145μm) for each sample using the cut-back technique (Senior, 1985). Four of the six types – the York high birefringent ArI fibre (hereafter referred to as HB450), the EOTec high birefringent He-Ne fibre (EOTec/HB), the Ensign Bickford birefringent fibre (EB450) and Fujikura fibre (PANDA) – are different examples of linear birefringent fibre. Their beat length values are substituted directly into equation 3.3 to determine the SBS-induced carrier for each fibre. These are, respectively, 11.4MHz, 9.2MHz, 1.3MHz and 11.9MHz.

During the present work, birefringence was introduced into fifth fibre type, the single-mode, circularly symmetric Argon Ion fibre (SM450), through an internal lateral stress obtained by bending the fibre uniformly around a mandrel of radius R. The degree of birefringence, $\mathcal{B}$, is given by (Ulrich et al, 1980)

$$\mathcal{B} = \frac{n^3}{4}(\rho_{11} - \rho_{12})(1 + \psi)\frac{a'^2}{R^2} \qquad 3.4$$

where ρ_{ij} denote elasto-optic coefficients, ψ is Poisson's ratio and a' is the fibre radius. Using the appropriate constants for fused silica at 0.5145μm

(ψ=0.17, $\rho_{11} - \rho_{12}$=−0.15 and $n = 1.46$),

$$\mathcal{B} = -0.136\frac{a'^2}{R^2}$$

For SM450 fibre, a' is 124.4μm so that, for a bend radius of 5cm, a birefringence of 8.43×10^{-7} is established. This is equivalent to a beat length of 0.61m at 0.5145μm which, from equation 3.3, produces a carrier frequency centred on 19.5kHz.

The twisted low birefringence Helium Neon fibre (EOTec/TW) is unique among the six in that it is *circularly* birefringent. Thus, circularly polarised signals are maintained in this state as they propagate along the fibre. The degree of circular birefringence, $\mathcal{B}_{circ}$, is given by (Ulrich and Simon, 1979)

$$\mathcal{B}_{circ} = \frac{-n^2\pi(\rho_{11} - \rho_{12})\tau_f}{k} \qquad 3.5$$

where τ_f is the twist rate of the fibre about its longitudinal z axis that induces the birefringence. In the EOTec/TW sample, τ_f is 40m^{-1} and $\mathcal{B}_{circ}$ thus equates to 3.29×10^{-6} at 0.5145μm, equivalent to a 0.156m beat length. Thus, for a linearly polarised pump, two left and right circularly polarised Stokes signals should emerge from the EOTec/TW fibre with a frequency difference of 76.4kHz. These combine to produce a linearly polarised state which rotates at the frequency offset rate (eg Tatam et al, 1986). Again, a linear polariser converts the polarisation data into an intensity modulation.

The range of frequencies attainable can be extended further if FWM effects occur. In section 2.3.3, it was shown that, under the appropriate conditions, two photons at frequency ν_2 can interact with one at ν_1 to produce an optical signal at $2\nu_2 - \nu_1$. If, in the frequency shifter set-ups described above, two photons of the Stokes signal (frequency $\nu_p - \nu_{B,s}$) interact with the pump (ν_p), then a new signal at $\nu_p - 2\nu_{B,s}$ would be formed. Similarly, along the fast axis, a signal at $\nu_p - 2\nu_{B,f}$ would propagate. Thus, on mixing the signal at the system output, a beat frequency of $2(\nu_{B,s} - \nu_{B,f})$ would be formed, double that obtained from SBS from equation 3.3. For FWM to occur, interacting beams need to copropagate so either the output pump or Stokes signal would need relaunching into the fibre through reflection.

Single fibre topologies can therefore be used to generate carriers over a wide frequency range up to approximately 12MHz using SBS (and further with FWM). Two fibre systems can be used to extend the frequency range further. In section 2.4.2, experimental work was cited in which the Brillouin frequency was shown to depend on dopant concentration. Germania, in particular, produced a change in Stokes frequency of 89MHz per %wt at 1.525μm

(Tkach et al, 1986). Thus, using two of the fibres listed in Appendix C, which possess different germania concentration, a wide range of carrier frequencies becomes accessible. The performance of these, and the single fibre shifters, is now described.

3.4 Experimental Results

This section is divided into two parts. Firstly, the steady-state SBS properties of the fibre samples described in Appendix C are detailed and, where, appropriate, compared to the theoretical and experimental observations made in section 2.4. Secondly, the results obtained on investigating the SBS-induced frequency shifter options described in the previous section are reported.

3.4.1 Steady State SBS Properties of Fibre Samples

The experimental set-up used to measure the SBS characteristics of the fibres is shown in Figure 21.

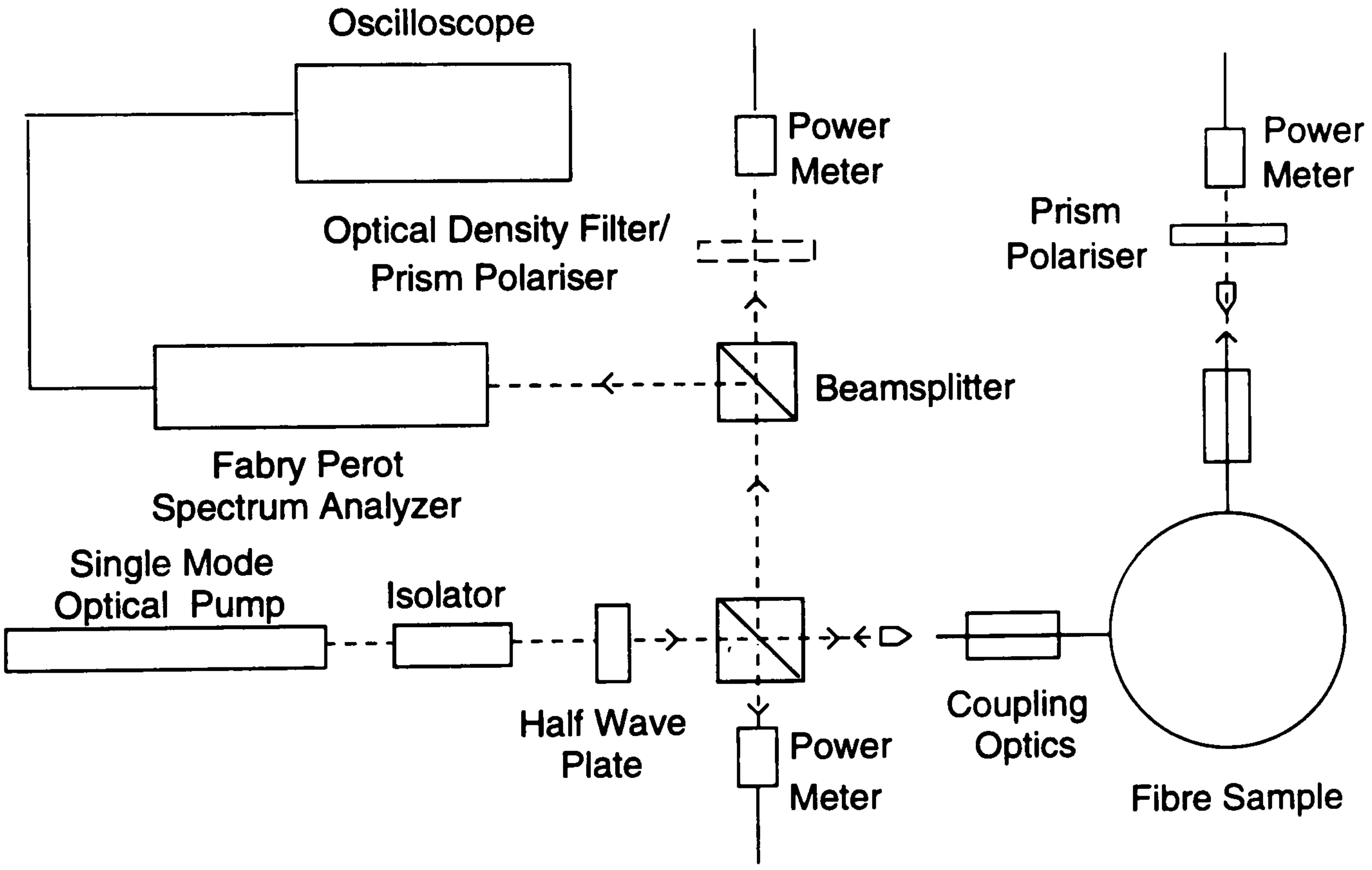

Figure 21: Experimental Arrangement for SBS Steady-State Property Measurements

The majority of experiments were performed using a water cooled *Lexel 3000* Argon Ion laser, emitting linearly polarised radiation at 0.5145μm. An etalon in the cavity ensured single frequency operation with a 3MHz bandwidth. Frequency stability of the output signal was specified as better than ±5MHz over a second and approximately ±60MHz for operation over an hour. Maximum output power for single (longitudinal) mode operation was measured at about 800mW, though 400-500mW was more typical over long operating periods. A second source used was an *Adlas* frequency-doubled diode pumped Nd:YAG c.w. source emitting at 0.532μm. A maximum power of only 150mW was available but with a linewidth of less than 20kHz. The frequency stability of the source was better than ±50MHz over several hours operation. The narrow linewidth of the two laser sources with respect to the spontaneous Brillouin linewidths of silica based fibres at these wavelengths (equation 2.41) implies that the temporal coherence of the sources does not affect SBS gain.

In Figure 21, system output powers were measured using surface-absorbing calorimeters manufactured by both *Photon Control* and *Lexel*. The measurement range extended from 10nW to 1W. Neutral density filters were used to control the power incident on any given detector and were combined with Glan-Thompson prism polarisers to investigate the polarisation properties of the SBS signals. An optical isolator (*OFR I05-VIR-HP*) prevented backscattered light from re-entering the laser cavity. The isolator was tunable from 0.5μm to 0.75μm and the model possessed a -44dB isolation at the operating wavelengths of interest and 90% forward transmittance.

The optical fibre was mounted on *Photon Control* piezo-electric micropositioners and a ×20 objective was used to focus the light into the fibre core. The power of the objective was selected to best match the input light beam with the fibre numerical aperture and core size. Coupling efficiencies of between 0.5 and 0.6 were obtained for all fibres during the study. In the system, the majority of optical surfaces were anti-reflection coated for visible wavelengths, reducing Fresnel losses at each interface to between 1 and 2% whilst minimising damage from high power c.w. radiation. The fibre ends were prepared using an *FK11 York* cleaver.

In Figure 21, a portion of the backscattered flux was directed onto a *TecOptics FPI-253* scanning Fabry-Perot spectrum analyzer. The instrument possessed a finesse of 80 at 0.5145μm. The free spectral range, adjustable by modifying the mirror separation, was maintained at 100GHz for the majority of the experiments. One mirror was attached to three piezo-electric ceramic blocks, enabling modulation of the mirror separation on application of ramped voltages. The output from the device's detectors (high performance silicon photodiodes) was downloaded to a *Lecroy 9400* 125MHz digital oscilloscope. The oscilloscope display thus provided a method of determining SBS threshold, independent of monitoring changes in the output powers of the system. A second method, involving observation of the broadband dynamical spectra produced in the SBS output is discussed in the next section.

Cubic beamsplitters, shown in Figure 21, provide amplitude division. These are polarisation sensitive due to the 45° internal dielectric interfaces. In experiments investigating the polarisation aspects of systems, microscope slides, tilted only by a few degrees were used to deflect the output power onto the detectors. Initially, the linear polarisation of the pump was aligned, via the half-wave plate, to be parallel with either of the fibre eigenaxes and the basic steady-state SBS properties of the fibres measured. This represents, for the linearly birefringent samples, the optimum gain configuration (ie $d = 1$ from equation 2.37).

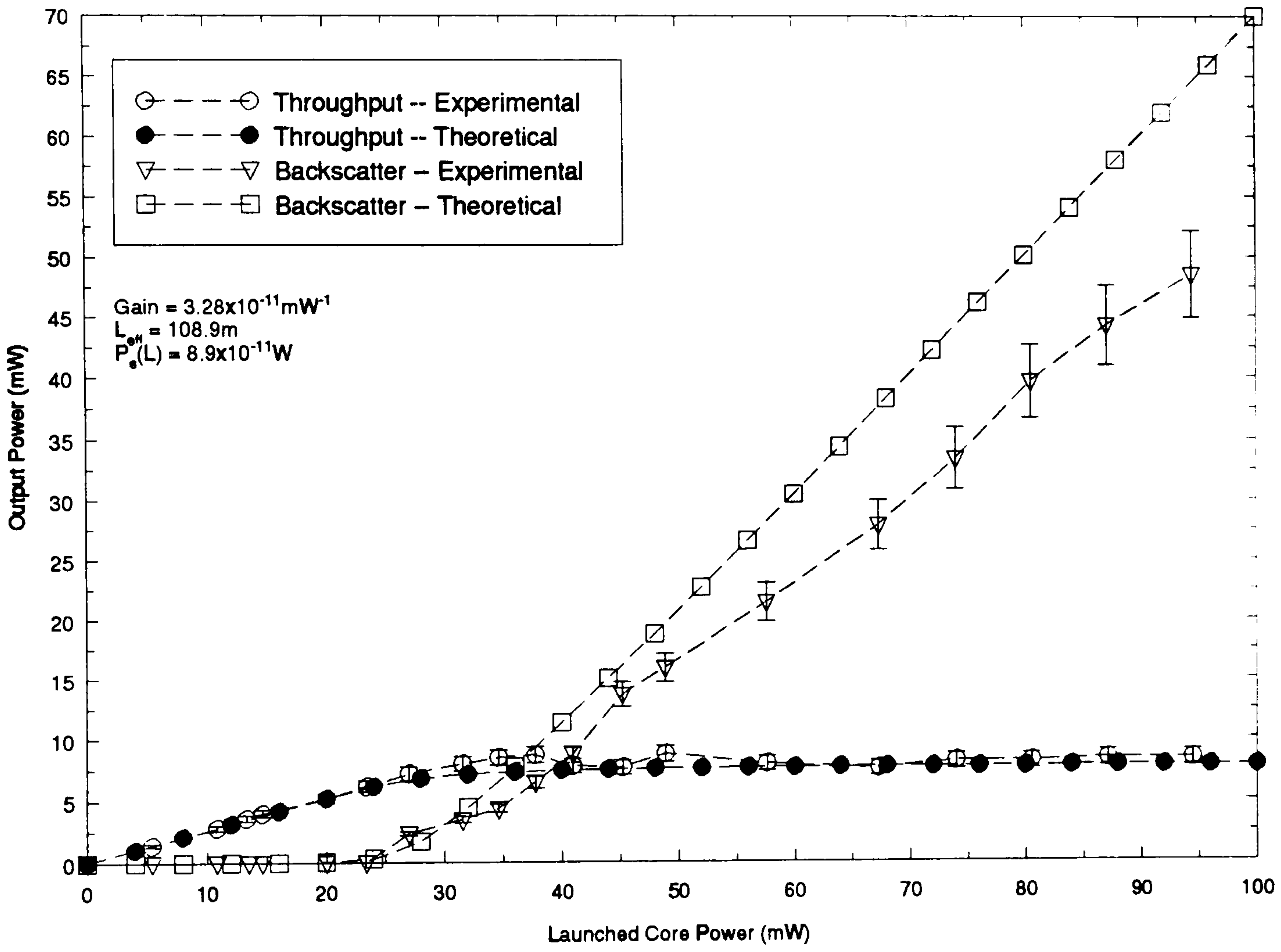

Figure 22: Theoretical and Experimental Output Powers From One Eigenaxis of EB450 Fibre Pumped at 0.5145μm

Figure 22 shows the forward and backward scattered output powers from 200m of EB450 fibre pumped at 0.5145μm. The throughput was linear for launch powers up to the SBS threshold (29.3mW), before saturating at approximately 8.5mW. For the backscatter, the contribution from Fresnel reflections has been removed, so the output was effectively zero up to SBS threshold. As the Stokes wave was generated, the backscatter increased as shown. At launch powers 2.5 times the Brillouin threshold. a level chosen to enable comparison with the results cited in section 2.4.2, a 52% conversion efficiency ($100P_s(0)/P_p(0)$) was attained. In all cases, experimental runs were repeated several times. The error bars shown in Figure 22 arose predominantly from fibre coupling variations, their values representing a standard deviation, typically ±5% of the mean value.

The theoretical values for forward and backscattered powers are also shown on the graph, based on the analytical representation of SBS developed in section 2.4.1. The value of the Brillouin gain coefficient, g_B, was deduced from equation 2.39, with the value for Brillouin threshold, P_B^{thr}, taken as the launched power at which the Stokes signal was detected by the Fabry Perot spectrum analyzer. As expected, this coincided with the change of gradients of both forward and backscattered powers in Figure 22 with launch power. The gain for the EB450 fibre was measured as $3.3 \pm 0.2 \times 10^{-11} \mathrm{mW}^{-1}$. Excellent agreement was obtained between the experimental and theoretical throughput values. Good agreement between the backscattered values was achieved for launch powers up to twice the threshold. Consistently lower experimental readings were measured as the launch was further increased, the difference widening in proportion to the launch power. This was due partly to the poor polarisation holding along the fibre which reduces the effective gain of the system (ie reducing d from unity in equation 2.37). This conclusion was confirmed by monitoring the transmitted polarisation state which did not remain constant even when the incident pump polarisation was aligned with either eigenaxis. The effect was further accentuated by power dependent photorefractive effects which are examined in more detail in Chapter 4.

Figure 23 shows the forward and backscattered signals emitted from 400m of EOTec/HB fibre pumped along one eigenaxis by the Nd:YAG source at 0.532μm. A gain of $3.5 \pm 0.2 \times 10^{-11} \mathrm{mW}^{-1}$ was measured, corresponding to a 25.6mW SBS threshold. A conversion efficiency of 54.2% was demonstrated at $2.5P_B^{thr}$. The limited power of the source prevented investigations at higher powers. Though the fibre supported two spatial modes at 0.532μm, the output spatial profiles of the SBS from each eigenaxis indicated that only the fundamental mode was undergoing SBS. No experimental evidence for Forward SBS (Russell et al, 1990) discussed in section 2.4.2 was obtained throughout this work. Indeed, in the present experiment, 'monomode-like' behaviour of the EOTec/HB fibre was confirmed by the very good agreement between theory and experiment for both forward and backscattered output powers shown in Figure 23. Errors were again characteristic of coupling variations.

A typical output trace from the Fabry Perot for the EOTec/HB fibre pumped at 0.5145μm as displayed on the Lecroy oscilloscope is shown in

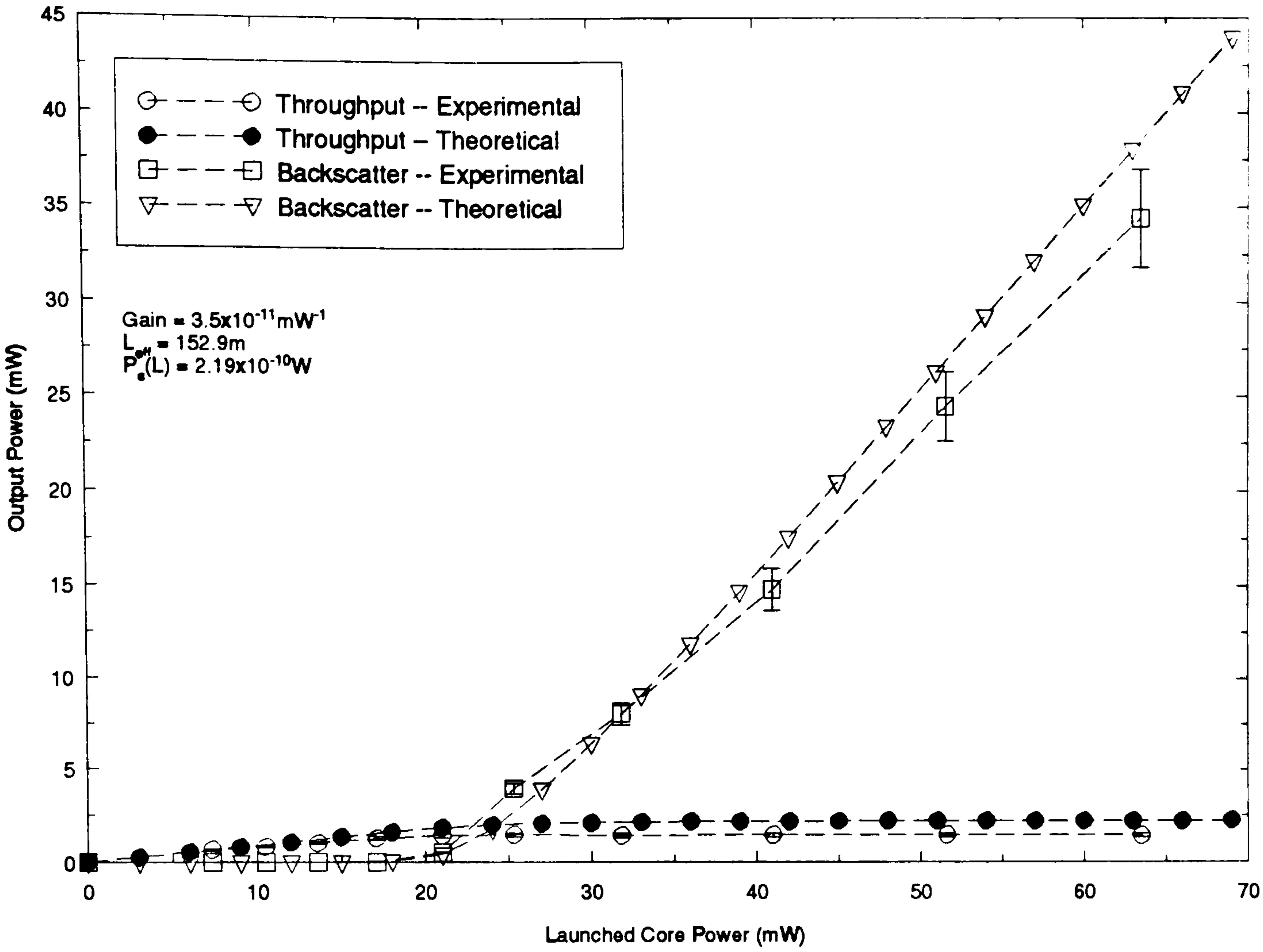

Figure 23: Theoretical and Experimental Output Powers From One Eigenaxis of EOTec/HB Fibre Pumped at 0.532μm

Figure 24. A 2.5V triangular waveform of 170Hz frequency was used to scan the Fabry Perot analyzer (upper trace). The (smaller) pump signals, arising from assorted Fresnel reflections in the system, were separated by the Free Spectral Range of the device (100GHz). The large Stokes peaks lay one third of the distance between the pump signals, consistent with the frequency downshift for the fibre system of 33.8GHz.

Figure 25 illustrates the variation in output powers from the two eigenaxes of the EB450 fibre as a function of input polarisation state for a 60mW launch power at 0.5145μm. When the polarisation was aligned with either of the fibre eigenaxes (θ equals 0 or 90°), the output Stokes power was a maximum as expected. The SBS power for a given eigenaxis was then reduced as the half wave plate was rotated. Similar trends were obtained at higher input powers and for the EOTec/HB sample, emphasising the monomode nature of this fibre. For comparison, the theoretical output powers for the two polarisation states derived from equation 2.59 are also shown. The input power was resolved into two orthogonal components proportional to $\cos^2\theta$ and $\sin^2\theta$

respectively where θ is the angle between the linear input state and one of the fibre eigenaxes. An important result for the frequency shifter studies was that it was only over a relatively narrow range of polarisation azimuths ($\approx \pm 5°$) that both eigenaxes emitted SBS simultaneously. The discrepancies between theory and experiment for the EB450 fibre, with consistently low experimental readings, were indicative of the poor polarisation holding capacity of the fibre (discussed further in Chapter 4). This instability was reflected in the error bar magnitude.

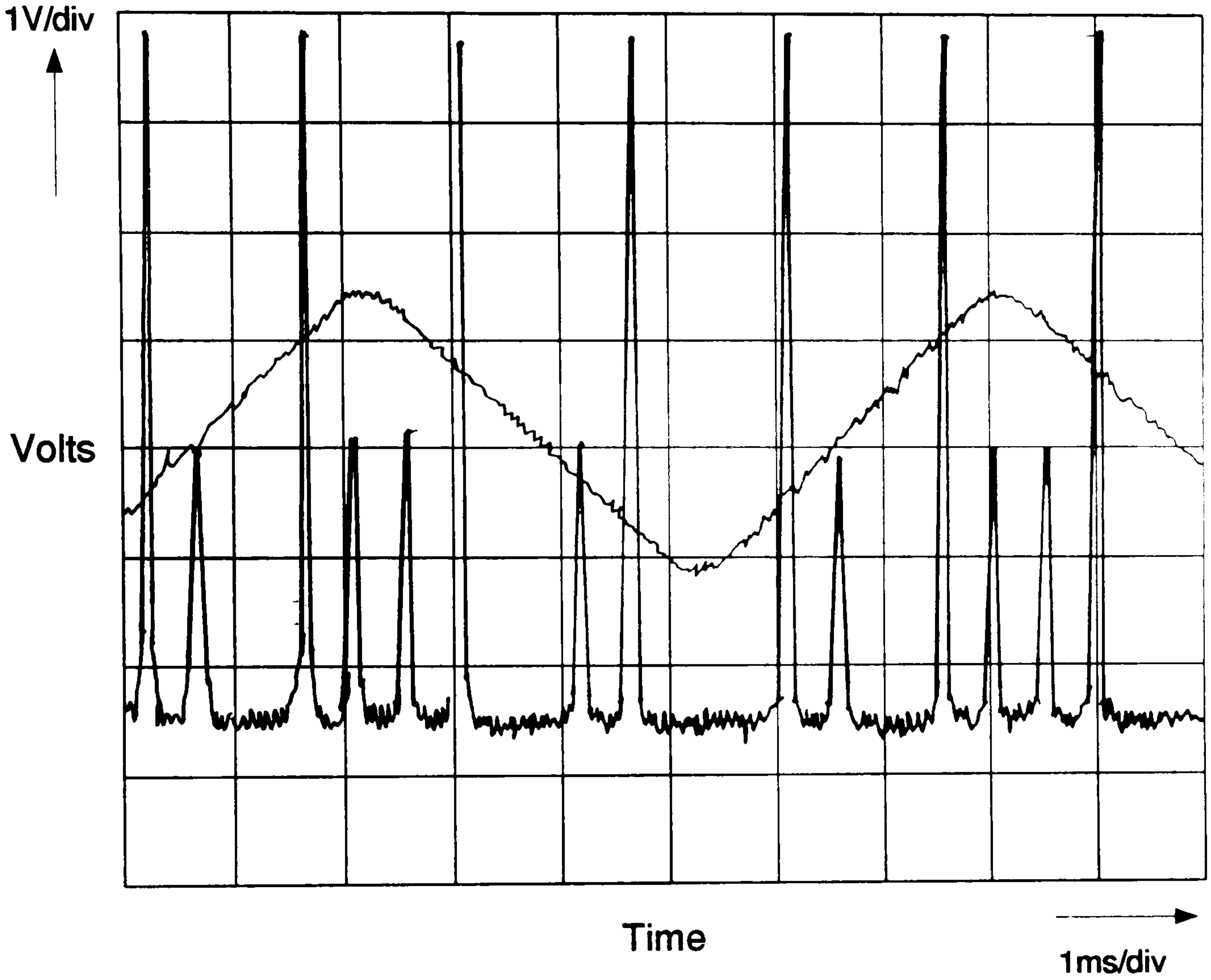

Figure 24: Fabry Perot Output Showing Both Pump and First Order Stokes For EOTec/HB Fibre Pumped at 0.5145μm

The steady-state SBS properties of all the fibre samples listed in Appendix C are summarised in Table 5 for pumping along a single eigenaxis. The available power from the ArI source varied considerably over the duration of the study, due to degradation in cleanliness and alignment of the

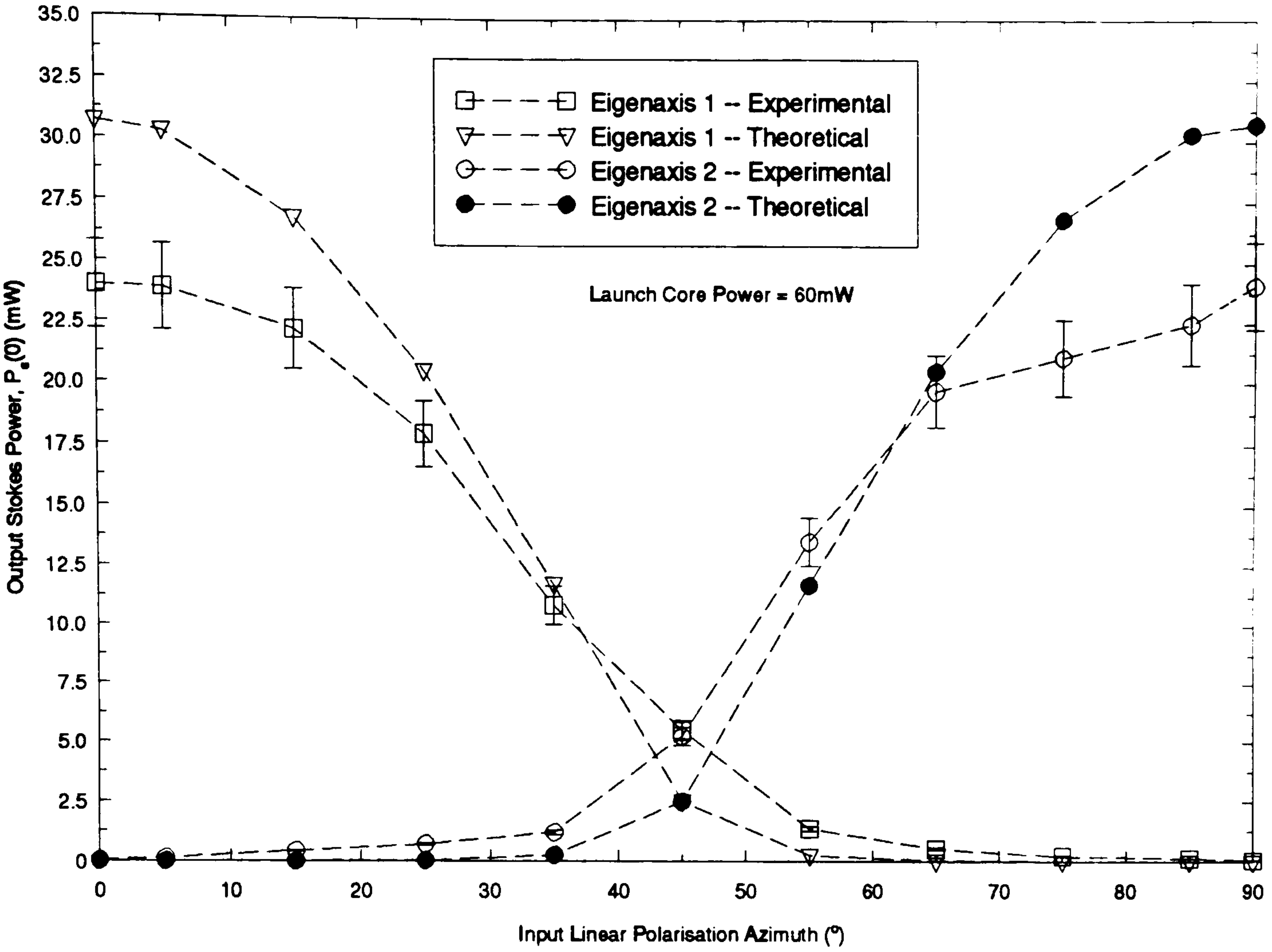

Figure 25: Output Stokes Power From EB450 Fibre Pumped at 0.5145μm as a Function of Input Pump Polarisation Azimuth

Fibre Type	Pump	P_B^{thr} (mW)	Measured Gain ($\times10^{-11}$mW^{-1})	Conversion Efficiency (% at $2.5P_B^{thr}$)
EB450	ArI	29.3±2.1	3.3±0.2	52.0±3.0
EB450	Nd:YAG	24.3±3.2	3.8±0.4	52.7±3.0
EOTec/HB	ArI	23.5±2.0	3.4±0.3	47.2±3.5
EOTec/HB	Nd:YAG	25.6±1.5	3.5±0.2	54.2±2.0
EOTec/TW	ArI	75.0±4.0	2.8±0.2	37.1±3.0
HB450*	ArI	64.0±5.0	2.4±0.2	20.1±1.5 at $2.25P_B^{thr}$
SM450*	ArI	90.0±5.0	2.6±0.3	N/A
PANDA	ArI	140±4.5	2.2±0.2	20.1±1.0 at $1.5P_B^{thr}$

*initial measurements only.

Table 5 Steady State SBS Properties of Fibre Samples

cavity components. Hence, the conversion efficiency of each fibre was again measured at a fixed point above threshold enabling direct comparison between the fibres. The gain value is derived from the measured threshold power via equation 2.39 which thus includes the contribution from the acoustic waveguiding nature of the fibre (section 2.4.2). At certain times (eg for SM450 fibre), only sufficient power was available for basic threshold measurements.

Some general comments can be made on the results presented in Table 5. The error for each threshold and conversion efficiency measurement was obtained by repeating the experiment at least five times and calculating the standard deviation of the output power variation for a set launch power. For a given linear birefringent sample, the results from each orthogonal eigenaxis were the same within experimental error. Thus, to demonstrate the frequency shifter concept in a single fibre, core launch powers must at least exceed twice the threshold of a single eigenaxis. This immediately invalidated the PANDA fibre as a candidate for the shifter in this study. Its low numerical aperture and large effective core area are specifically designed for high power delivery applications, a factor enhanced by the low Brillouin gain measured. Indeed, for all samples, gain and conversion efficiency were inextricably linked, as expected from equations 2.59.

The properties of the EB450 and EOTec/HB samples have already been described. Both the gains and conversion efficiencies were approximately constant for the two sources used. Further, the output intensities from both eigenaxes demonstrated the expected trends as the linear input polarisation state was rotated. The EOTec/TW fibre was pumped with a linearly polarised pump. This should, in principle, couple into two circular polarised eigenaxes which, at threshold, yield two circularly polarised Stokes signals of the appropriate handedness. However, as the input pump polarisation azimuth was rotated, the output SBS intensity showed a trend similar to that in Figure 25 for the EB450 fibre. This demonstrated that the circularly birefringence was negligible when compared with linear birefringence present in the fibre core. Further experiments using a Helium Neon source confirmed that the sample was linearly birefringent.

Interesting results were obtained with both the HB450 and SM450 fibres. The results presented in Table 5 were initial measurements, obtained on pumping the samples at 0.5145μm. Subsequent pumping after long intervals with the fibre stored at room temperature revealed a large increase in fibre attenuation and, hence, SBS threshold. These extra losses were partially bleached by repumping at 0.5145μm but the original transmittance was never recovered. These mechanisms are reported further in Chapter 4.

A second important characteristic of the HB450 fibre had direct relevance to the frequency shifter studies. The polarisation properties of the transmitted pump beam remained constant when the input was aligned parallel to either of the fibre eigenaxes as expected. However, when the input light was polarised at 45° to the two axes (necessary to obtain simultaneous SBS signals for the frequency shifter), the output transmitted polarisations measured along axes parallel to the principal axes (using a Glan Thompson prism polariser) were modulated in proportion to the applied power. The measured power cycled through regions of maxima and minima, the number of cycles proportional to the input pump power. This implied that the fibre eigenaxes were being rotated and meant that it was not possible to obtain two simultaneous SBS signals of orthogonal polarisations by pumping from one end. These attenuation and polarisation effects are again reported in more detail in chapter 4.

3.4.2 Frequency Shifter Demonstration

The basic experimental arrangement to demonstrate the frequency shifter in a linearly birefringent fibre is shown in Figure 26.

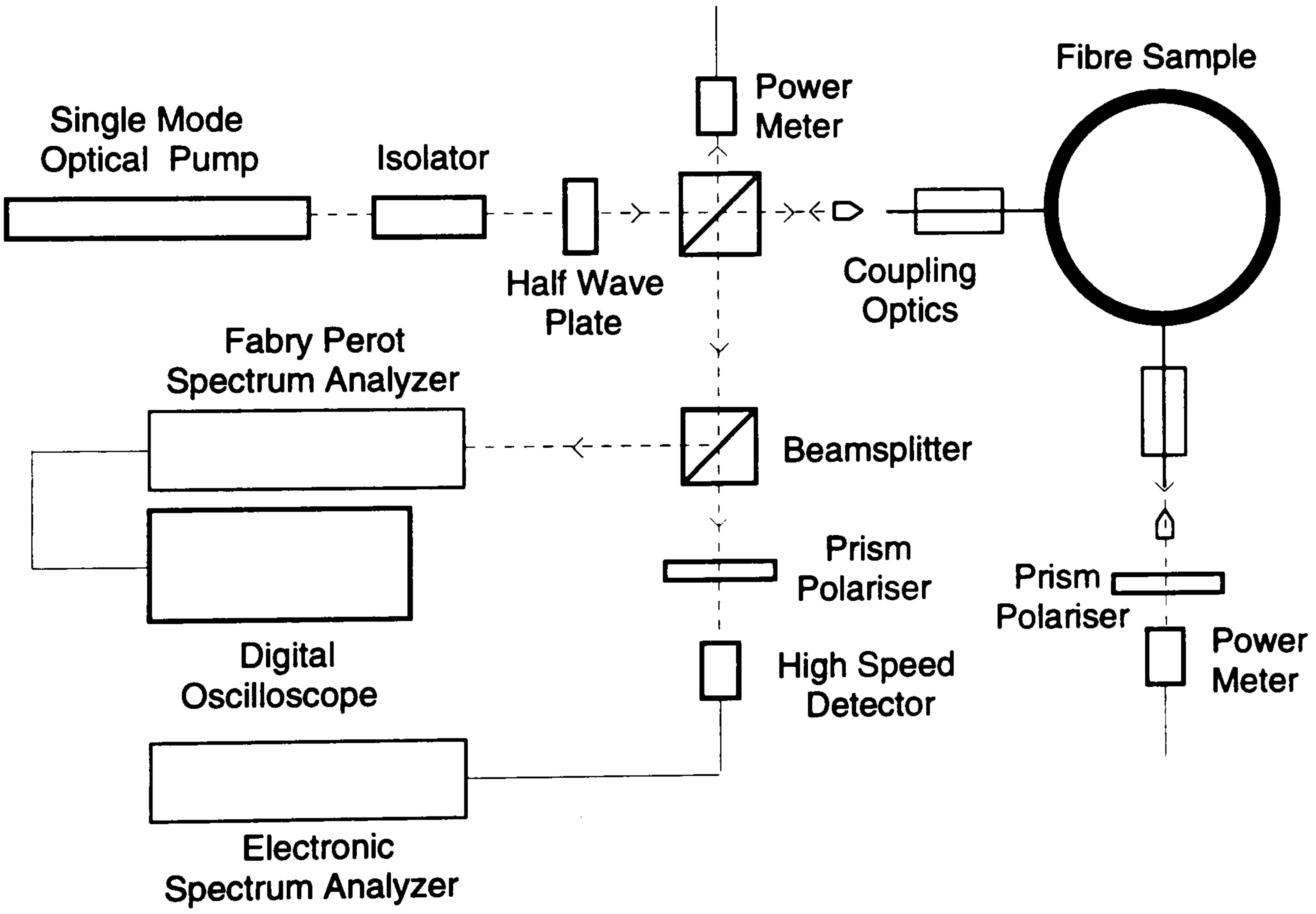

Figure 26: Optical Frequency Shifter: Single Fibre, Single Input System

The half wave plate was rotated to align the input polarisation plane at 45° to the fast and slow eigenaxes of the fibre. The backscattered signals were monitored via the Fabry Perot analyzer as before. The carrier was generated by mixing the two orthogonally polarised Stokes signals at the prism polariser and measured by the high speed detector. Two modules were used throughout the study. The first was a *Photodyne 1500XP* waveform analyzer which consisted of a high speed silicon avalanche photodiode. It possessed a -3dB response at 200MHz. The second consisted of a reversed biased silicon photodiode in circuit with a video amplifier chip. The 3dB response range of the device was measured from 0.1MHz to 30MHz (Khan et al, 1993), though signals from 5kHz to 700MHz were detected at various stages of the work. The detector's response was tested to ensure that it did not saturate for the incident power levels used in the experiment.

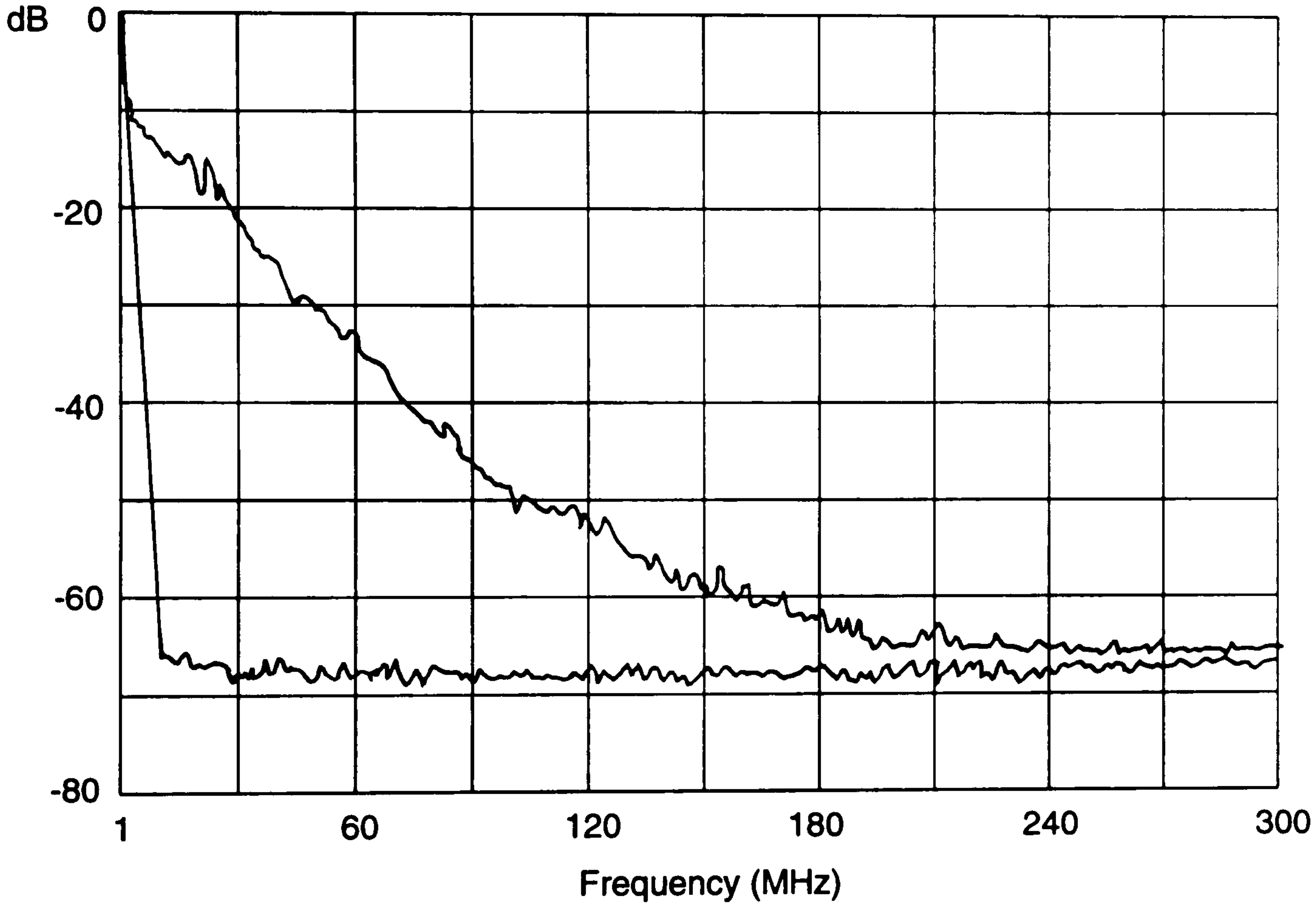

Figure 27: System (Figure 26) Output Spectrum for EOTec/HB Fibre Pumped at 0.5145μm: No SBS (Lower Trace) and SBS Along Single Eigenaxis (Upper Trace)

The detector outputs were connected to a *Hewlett Packard HP8591A* electronic spectrum analyzer. The total frequency range of this instrument extended from 9kHz to 1.8GHz. The resolution of the device varied between 0.1 and 1% of the frequency span (minimum 1kHz). The displayed spectrum was updated at 50Hz and possessed a frequency accuracy of ±3% of the span. The self-calibrated power range of between 0 and -80dB was used in all experiments.

The detection arrangement shown in Figure 26 additionally enabled the transient properties of the SBS (described in section 2.4.3) to be monitored. An example is shown in Figure 27, a spectrum analyzer plot of relative optical power (dB) against frequency. (This output format was maintained throughout the study.) The analyzer trace shows the spectrum produced when a single eigenaxis of the EOTec/HB fibre was pumped at 0.5145μm for input powers less than and greater than the SBS threshold (lower and upper curves respectively). The lower trace represents the effective noise spectrum of the detector and analyzer. The Stokes signal, however, comprised a broadband spectrum with a -3dB point of approximately 15MHz in this example. This spectrum is characteristic of the $\chi^{(3)}$ induced nonlinear instabilities which modulate the SBS process and were described in section 2.4.3 (eg Harrison et al, 1990). The broadband properties of the SBS are considered in more detail in section 3.5 for the different systems studied.

Figure 28 demonstrated that the steady oscillations discussed in 2.4.3 (Bar-Joseph et al, 1985) were observed, superimposed on the broadband spectrum. An array of steady oscillation harmonics is shown emitted from the HB450 fibre pumped above SBS threshold. The peak to peak separation of 1MHz was consistent with the fibre length of 100m and core index 1.456. The properties of the steady oscillations are examined further in Chapter 5 as potential sensing mechanisms.

The broadband spectra produced in each fibre at SBS threshold served as a third means of monitoring the threshold, in addition to the Stokes signal detection within the Fabry Perot analyzer and measurement of the output powers. The presence of the continuum also influenced the choice of system for initial demonstration of the frequency shifter. Systems were investigated which produced carriers in excess of approximately 60MHz where the broadband intensity modulations are reduced by several orders of magnitude. (In Figure 27, for example, it is approximately three orders.)

Two systems, in particular, were studied. The first, shown in Figure 29, consisted of two HB450 fibres of lengths 100m and 200m simultaneously pumped at 0.5145μm. The polarisation azimuth of the pump was aligned with an eigenaxis of each fibre, suppressing the polarisation modulation effects noted earlier and minimising SBS threshold. Experiments were performed whilst the losses remained at a manageable 60-70dBkm^{-1} before the photoinduced increases in attenuation took effect. The resultant carrier, as displayed on the spectrum analyzer, is illustrated in Figure 30. A carrier

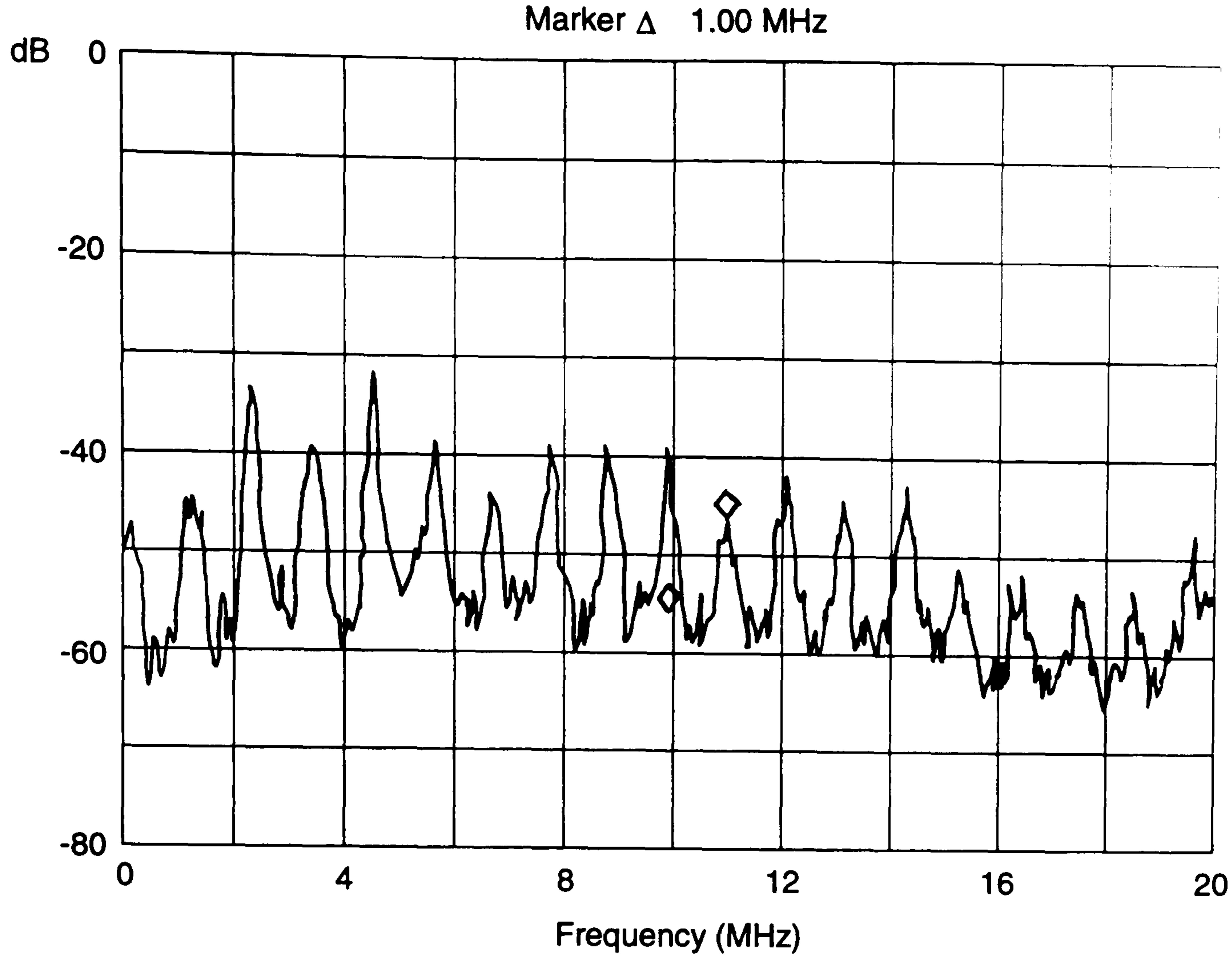

Figure 28: Steady Oscillations of 100m HB450 Fibre Pumped at 0.5145μm

centred on 665MHz was produced, equivalent to an effective core index differential of 0.029 between the fibres. Although both fibres were nominally HB450, the 100m sample was obtained from an early, developmental batch and contained different dopant concentrations. Assuming that germania is the principal dopant, a 665MHz carrier implied a 2.5% difference in germania concentration between the samples (after Tkach et al, 1986), though no manufacturer's data was available to confirm this result.

The frequency produced compared well with a similar experiment (Culverhouse et al, 1989b) in which two spools of conventional single-mode fibre were pumped at 0.5145μm to produce a 745MHz carrier. In the present experiment (Figure 30), up-shifted intensity modulations similar to those shown in Figure 27 were observed in the region of the carrier. The low detector response at this frequency, however, has largely suppressed this broadband spectrum. Thus, the corresponding high visibility carrier signal shown in Figure 30 demonstrated the efficiency of the heterodyne generation process using SBS, even at these high frequencies.

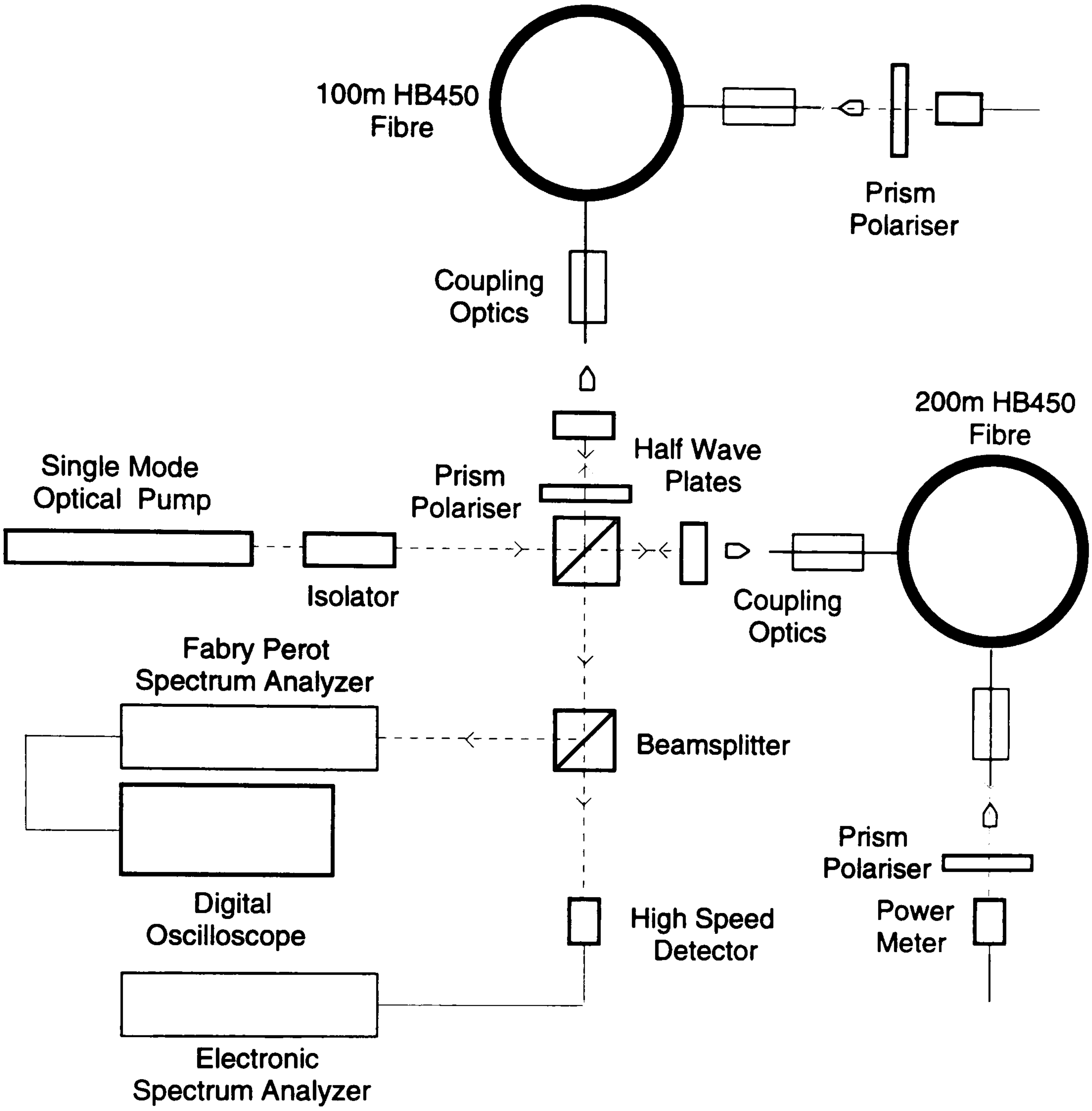

Figure 29: Optical Fibre Frequency Shifter: Dual Fibre, Dual Input System

An important characteristic of the SBS induced carrier which recurred throughout the study was the frequency modulation displayed by the signal. For example, a standard deviation of 13.6MHz around 665MHz was measured in this experiment based on 350 readings. A potential source of such instabilities in the carrier are frequency perturbations of the pump itself. However, the fact that the SBS signals are generated *simultaneously* (with a small $0.1\mu s$ delay due to different group velocities along the fibre eigenaxes) implies that any pump frequency jitter would be replicated in both signals and would have cancelled. In section 3.5, the relationship between carrier frequency modulation and the nonlinear dynamics of the system is examined. This frequency modulation can limit the resolution of sensor systems

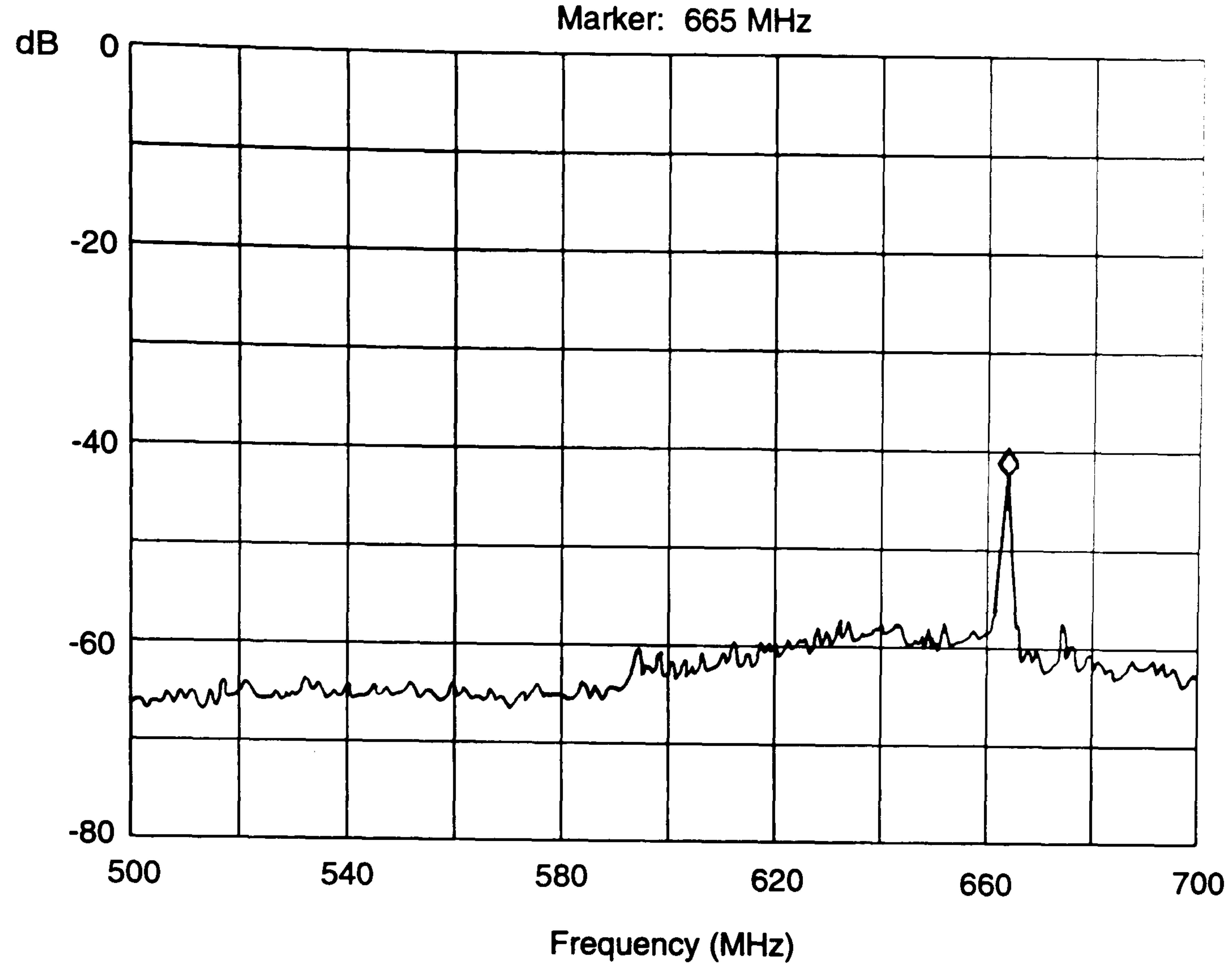

Figure 30: System (Figure 29) Result Showing Carrier Centred on 665MHz

requiring accurate frequency measurement.

The second system used to generate a carrier in excess of the broadband dynamical spectrum is shown in Plate 3. A single fibre was pumped from both ends simultaneously, along the fast axis from one end and the slow from the other. An *Isomet 1205C* acousto-optic modulator (partially obscured by the spatial filter assembly in the picture) was placed prior to one fibre input. The device imposed an 80 MHz carrier on one of the pump signals. The SBS induced carrier was then upshifted with respect to this, in excess of the broadband spectrum. The Bragg cell was designed for operation in the visible spectrum with an insertion loss of under 3% and a zero to first order deflection efficiency of 92% at $0.5145\mu m$. The Fabry-Perot spectrum analyzer (bottom left) and the corresponding oscilloscope output are also shown in Plate 3. The *1500XP* detector is to the right of the oscilloscope.

Preliminary experiments with this arrangement used the HB450 fibre. However, insufficient power was available to generate simultaneous SBS due to the photosensitive effects discussed earlier and the additional attenuation in the acousto-optic 'arm'. Thus, the low threshold EOTec/HB reel was introduced and a typical result shown in Figure 31 using the *1500XP* detector. The broadband spectrum from the nonlinear dynamics was present in the 0-60MHz region. Two carriers, centred on 80 and 160MHz were derived from the Bragg cell, the latter from light that passes through the Bragg cell twice. The mean upshift from these signals for the SBS-induced carrier was measured as 10.8MHz, a fair agreement with the theoretical value of 9.2MHz. Again, the carrier was modulated about this mean value with a standard deviation of 14MHz for 90 readings. The fact that the Bragg cell induced carrier remained at a constant frequency provided further evidence that the SBS carrier instabilities were intrinsic to the SBS rather than the pump.

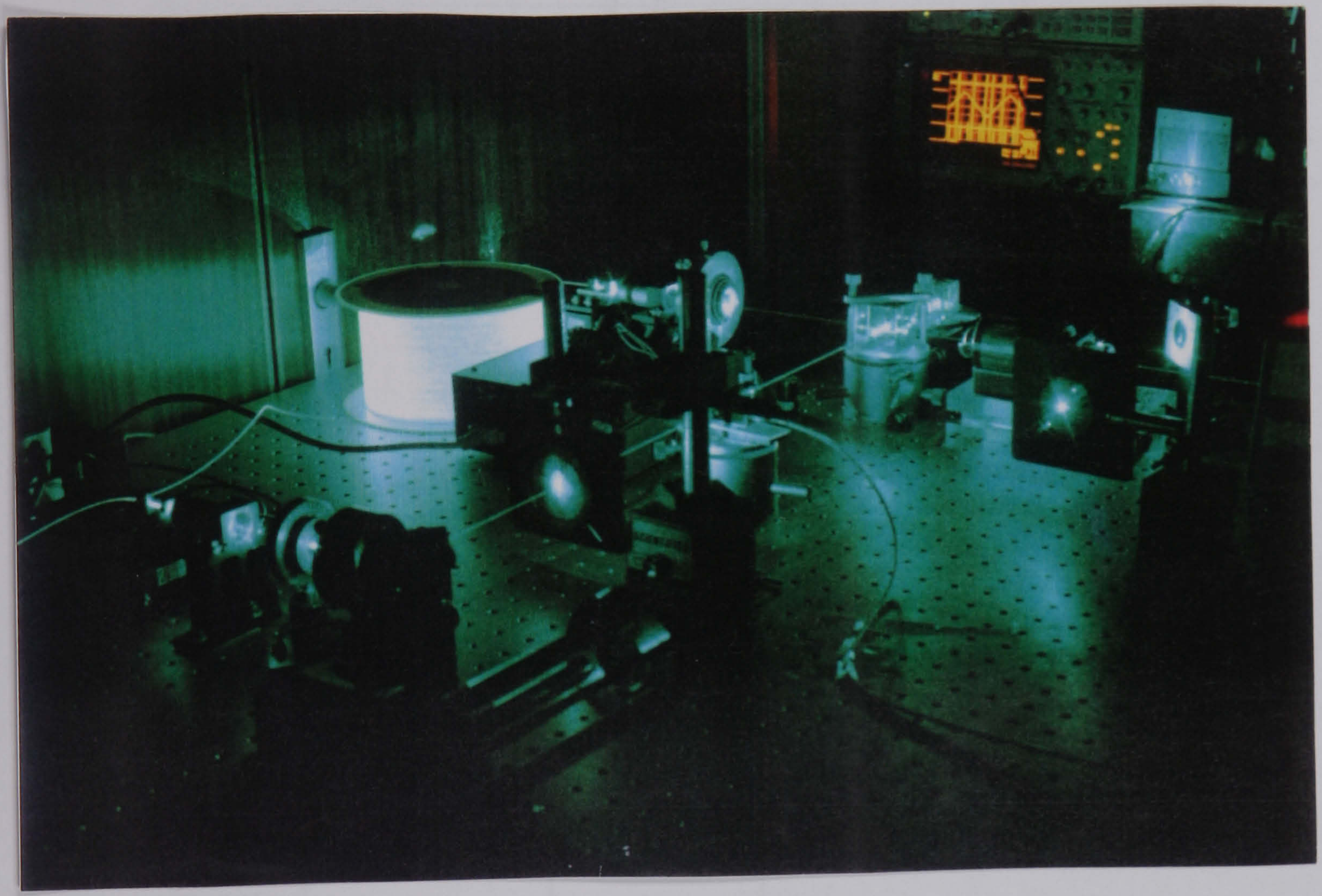

Plate 3 Frequency Shifter System: EOTec/HB Dual Input System, Incorporating Bragg Cell, Pumped at 0.5145μm

The two approaches discussed above were useful for demonstrating the principles of the frequency shifting concept. Neither, however, represented the most practical means of demonstration. In the former, two separate

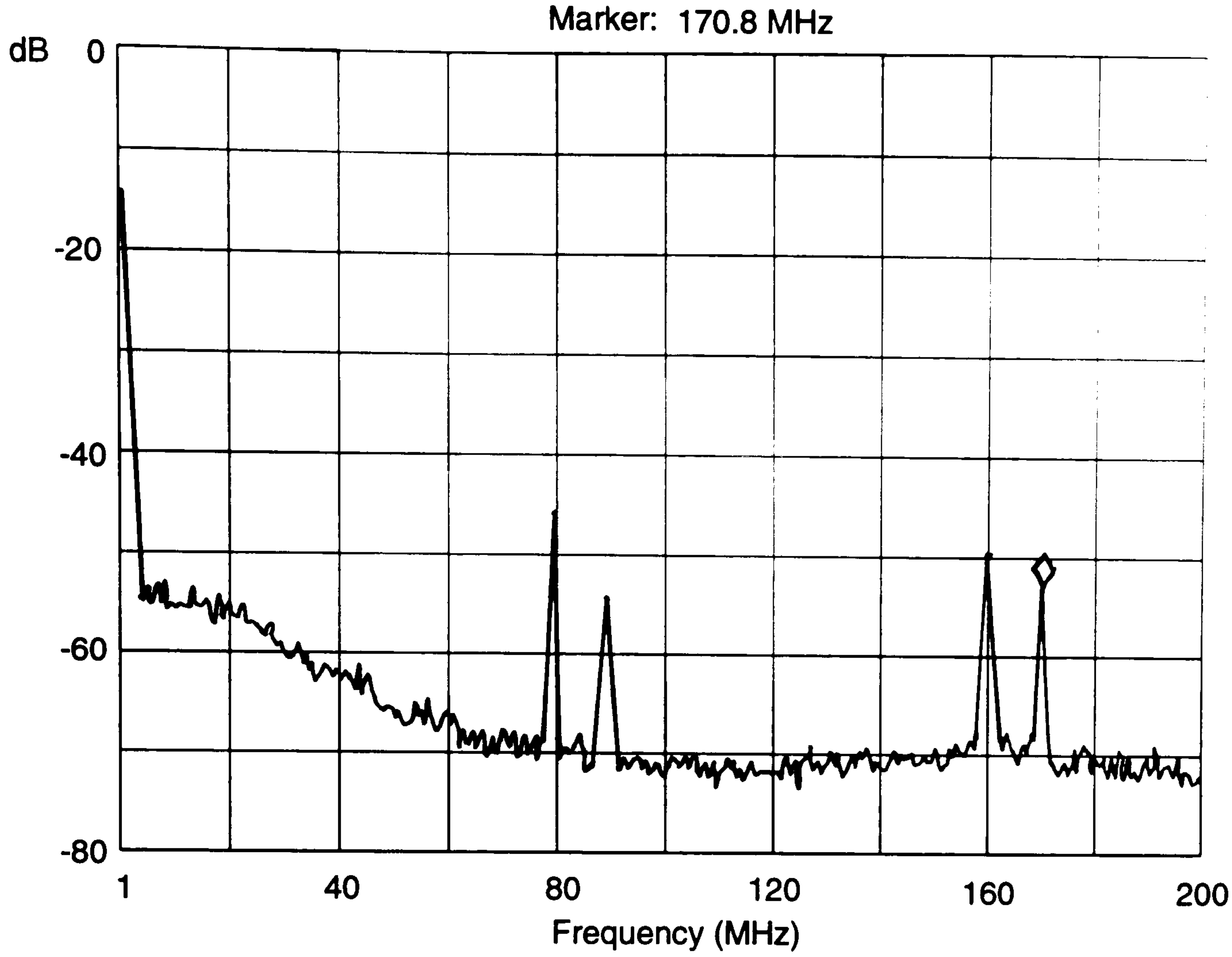

Figure 31: System (Plate 3) Result Showing Bragg Cell Carriers at 80 and 160MHz and the SBS Induced Carrier Upshifted by 10.8MHz

Fibre Type	Pump Source	$\delta\nu_B$, MHz (Predicted)	$\delta\nu_B$, MHz (Measured)	Standard Deviation	Number Of Readings
EOTec/HB	ArI	9.2	10.7	7.9	650
EOTec/HB	Nd:YAG	9.5	10.3	5.6	100
EB450	ArI	1.3	8.0	4.5	130
EB450	Nd:YAG	1.34	8.4	4.5	230
EOTec/HB + EB450	ArI	N/A	135.6	13.1	140
HB450 +HB450	ArI	N/A	665	13.6	250

Table 6 Summary of Results For SBS Induced Frequency Shifter

reels are necessary to generate the carrier. In the latter, the use of an electronically addressed Bragg cell, though demonstrating the pump stability. does rather invalidate the technique. It is this device that the all-optical SBS approach may replace. Instead, single fibre, single input systems were now investigated using the configuration shown in Figure 26, for the fibres listed in Appendix C.

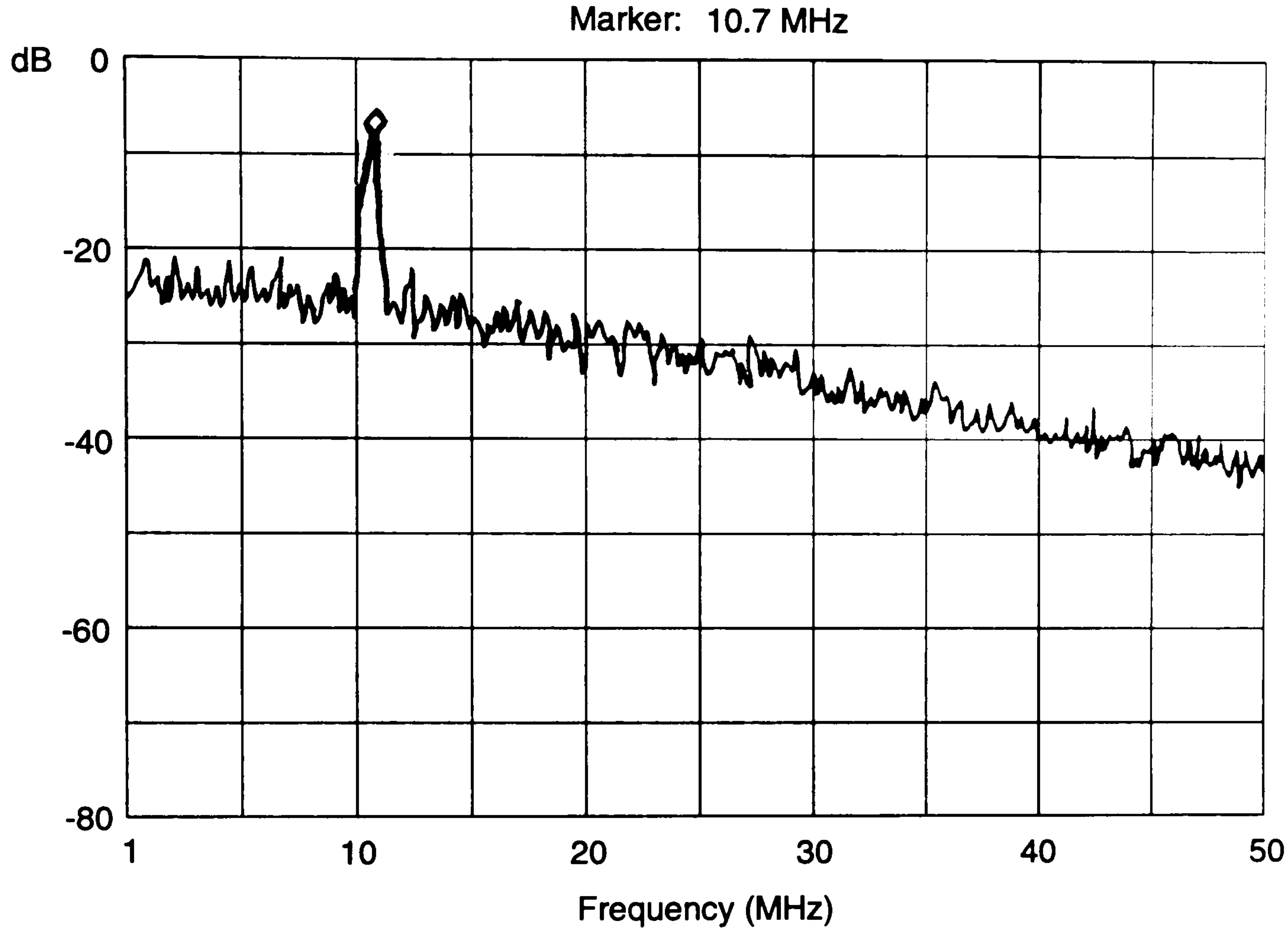

Figure 32: Single Fibre (EOTec/HB), Single Input Result Showing the Carrier Centred on 10.7MHz

Table 6 summarises the results from systems in which a carrier was generated. The EOTec/HB fibre produced a carrier in good agreement with the theoretical value for both ArI and Nd:YAG sources. Figure 32 shows the carrier centred on 10.7MHz, produced from the ArI pump, and 20dB above the broadband spectrum. From Table 6, the carrier produced with the EB450 fibre, though centred on a slightly lower frequency than for the EOTec/HB fibre, differed significantly from the predicted value at both pump wavelengths. Verification of the beat length quoted by the manufacturers was undertaken by observing the side-scattered Rayleigh signal from the fibre for input light polarised at 45° to the eigenaxes. Since the scattering is polarisation dependent, the irradiance pattern maps the periodicity of the beat length exactly.

The 9mm beat pattern (±1mm) was clearly defined. Non-maintenance of the polarisation state along the fibre cannot explain the large differential between theory and experiment. One possible explanation lies in the method used to measure the carrier from the spectrum analyzer. The displayed carrier is of course the result of mixing the SBS signal from the fast and slow axes. The analyzer measures the frequency *offset* between the two axes. In the present experimental arrangement, for carriers centred below approximately 10MHz, modulations in excess of 10MHz will appear as carriers centred on a few MHz. This increases the *average* value of the mean frequency. In contrast, the system shown in Plate 3 would produce a carrier centred just above the 80MHz carrier, but whose modulations extend above *and* below the 80MHz level. The *average* value is thereby reduced and approaches its 'true' value. As described in the previous section, the EB450 demonstrated some polarisation instability when pumped at 0.5145μm and a single end, leading to effective rotation of the eigenaxes and fading of the carrier.

Table 6 also shows the results of a second two fibre system similar to Figure 29 and pumped with the ArI. Both fibres (EOTec/HB and EB450) were pumped along a single eigenaxis and maintained at room temperature. A carrier centred on 135.6MHz was produced and the carrier modulation, 13.1MHz, was again at least double that produced from single fibre, single input systems. This indicated that in the single fibre systems, some common mode rejection reduced the overall modulation though the method of measurement cited above could also be a factor. The carrier frequency produced by the fibres was consistent with the manufacturer's data for germania concentration and the observations of Tkach et al (1986).

Neither HB450 sample was capable of individually producing two independent Stokes signals and no carrier was forthcoming, regardless of system topology. The low SBS gain measured in chapter 3.4.1 for the PANDA fibre also prevented this sample from being successfully implemented in the frequency shifter arrangement.

The SM450 fibre was tested by tightly coiling it onto a 5cm diameter former. From equation 3.4, a birefringence of 3.37×10^{-6} should be established producing a carrier of 78.1kHz in the SBS system. However, the SM450 fibre produced only one Stokes signal whose linear polarisation matched that of the pump, regardless of orientation. Further, the SBS intensity remained constant as the input polarisation was rotated, confirming that any birefringence set-up by virtue of fibre coiling was extremely small. If the fibre was not wound onto the mandrel uniformly (ie it was twisted), then the linear birefringence could have been averaged out along a given direction (Ulrich and Simon, 1979). In any case, as shown by Table 5, the high intrinsic losses of the fibre made dual SBS production difficult with the available power and, again, the introduction of photosensitive induced attenuation compounded the problem.

The steady-state properties of the EOTec/TW fibre produced an unexpected result by demonstrating characteristics more aligned with linear rather than circular birefringence. A carrier frequency centred on 2.5MHz was produced, implying a linear birefringent beat length of about 5mm. This is a remarkable result for a fibre which claimed to be circularly birefringent. One possible explanation is that the protective cladding designed to maintain the twist of the fibre has imposed its own stresses on the core and yielded this behaviour.

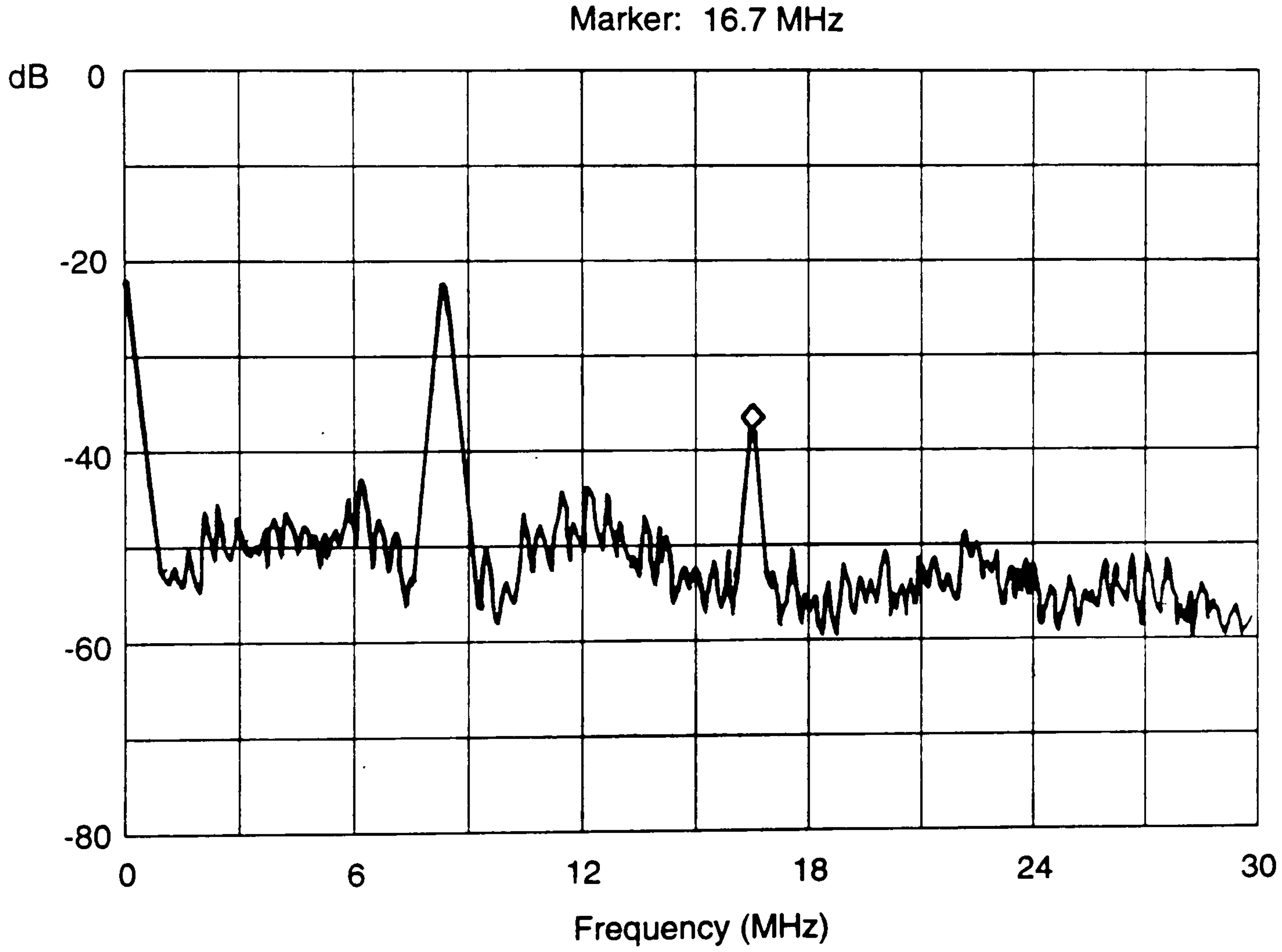

Figure 33: Result of EB450 Fibre Pumped at 0.532μm Showing Four Wave Mixing

Throughout this work, many examples of Four Wave Mixing (FWM) were produced by mixing the SBS induced carriers with the pump. Fresnel reflections at the fibre/air interfaces and from other components in the system often provided enough feed-back to initiate FWM, though this tended to be unstable. The result illustrated in Figure 33 arose from pumping the EB450 fibre system at $0.532\mu m$. Feedback into the fibre was enhanced by relaunching the undepleted pump at the distal end using a plane mirror. The effective reflectivity of the mirror, including the effect of coupling losses was approximately 30%. The basic carrier (equation 3.3) centered on 8.4MHz was visible above the broadband spectrum. A signal at twice the frequency (16.7MHz) is clearly visible. Thus, the use of FWM can significantly extend the basic range of frequencies attainable for the frequency shifter technique.

The bandwidth of the SBS carrier was monitored throughout these experiments. For all systems, measurement of the 3dB point of the carrier was limited by the resolution bandwidth of the spectrum analyzer ($\approx$1kHz). Thus, the carrier bandwidth was a *maximum* of 1kHz. It was not the bandwidth, therefore, but the modulation of the carrier central frequency which limited the usefulness of the signal for 'real' applications. A second disadvantage of the approach described in this section was the relatively high optical powers and long fibre lengths necessary to generate the SBS carrier. Both can be partially overcome by operating in the IR where fibre loss is lower and the interaction length is increased. In chapter 6, fibre ring resonator technology is discussed in the context of the SBS-induced frequency shifter in which the optical power and fibre length requirements can be reduced by several orders of magnitude. A miniature, self-contained unit, fully compatible with single-mode fibre systems can then be obtained. The results from such systems make interesting comparisons with the observations reported in this chapter.

3.5 NonLinear Dynamical Properties of SBS Systems

The purpose of this section is to analyse in more detail the SBS instabilities reported in the context of the frequency shifter in the previous section. Instabilities in *intensity* were manifested as the broadband spectrum shown in Figure 27 and reduced the effective visibility of the SBS-induced carrier. Instabilities in the *frequency* of the carrier itself meant that it could not be effectively deployed in heterodyning and also lowered the measurement resolution if exploited directly in sensors (as in section 5.2). In this section, the properties of both the broadband spectrum and carrier modulation are described for different experimental systems to identify trends in behaviour. A technique for reducing both is then considered. Throughout, the results are compared with the transient SBS characteristics reported in section 2.4.3 and other SBS systems cited in the literature. The aim is to gain a qualitative understanding of the source of the phenomena. Components can then be selected which minimise transient SBS.

The first task was simply to ascertain that the broadband signature of Figure 27 was present only when the fibre systems were producing SBS. This was quickly confirmed. The output of the laser itself was then monitored whilst the fibre was emitting a Stokes signal. This was to ensure that the

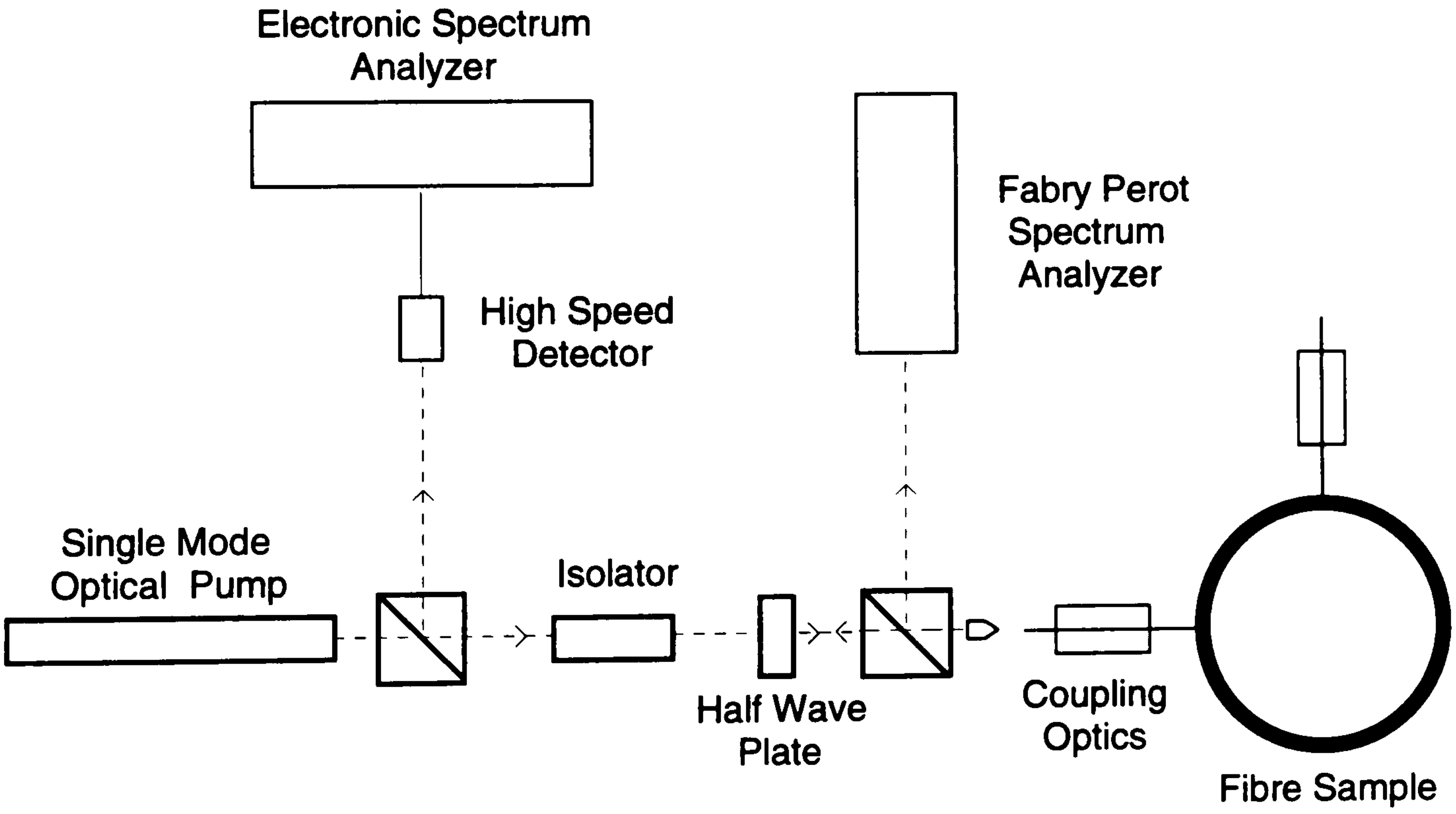

Figure 34: System Used to Monitor the Output Spectrum of the Laser for Fibre Pumped Above SBS Threshold

inherent high levels of backscatter (despite the presence of the isolator) were not reentering the cavity and causing output intensity instabilities. The output of the laser was monitored using the system shown in Figure 34, again using the Fabry Perot analyzer to independently monitor for SBS. The resultant spectrum displayed only the noise features of the detector and electronic spectrum analyzer, matching the lower trace of Figure 27. Thus, the broadband spectrum was characteristic of the Stokes signal alone and arose from the interaction with the fibre.

By connecting the high speed detector to the Lecroy oscilloscope, the SBS emission was monitored in the time domain. A typical example is shown in Figure 35 which illustrates the output from one eigenaxis of the EOTec/HB fibre pumped at approximately three times the threshold power.

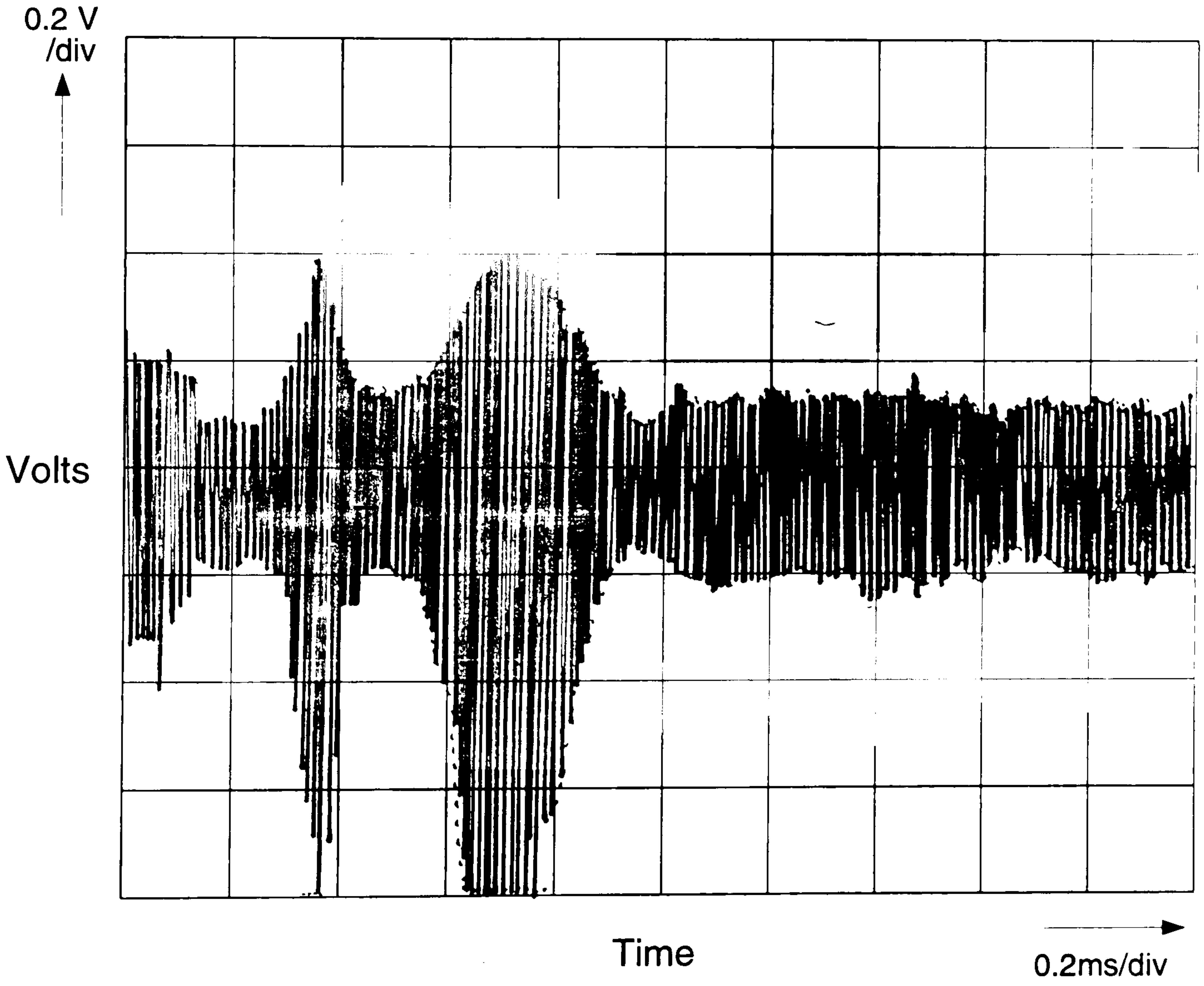

Figure 35: Typical Output of the SBS System in the Time Domain

The scope was ac coupled. The general form of the output agreed well with the results cited in section 2.4.3 (see, for example, Johnstone et al. 1991) for pump powers in excess of SBS threshold.

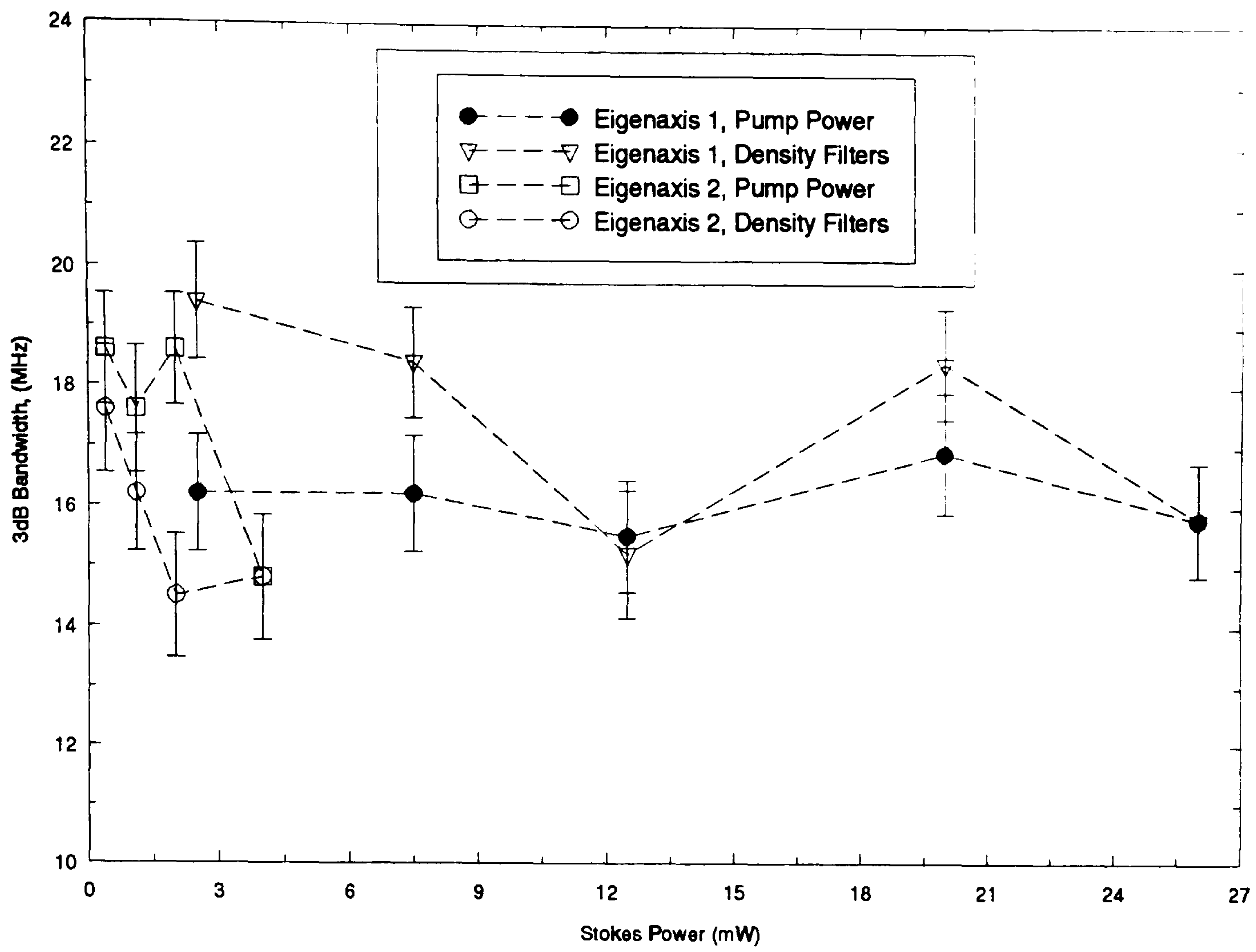

Figure 36: Plot of 3dB Bandwidth of Stokes Spectra Against Stokes Power Incident on Detector

Trends in the profile of the broadband spectrum were examined for different systems. Figure 36 illustrates the results for the 780m EOTec/HB fibre pumped, in turn, along each eigenaxis at 0.5145μm. The graph shows the measured 3dB bandwidth plotted against the Stokes power incident on the high speed detector. This power was varied by modulating either the pump power (in the manner of Figure 22), input polarisation azimuth (as in Figure 25) or by inserting optical density filters prior to the detector. The filters were used to distinguish between changes in profile arising from detector response or changes inherent to the SBS spectra. As it transpired, the bandwidth was constant with input power, typically 16±2MHz, for the three situations (though only two are shown). Prior to these experiments, the noise spectra of the analyzer and detector had been measured, enabling accurate readings of the bandwidth. The detector had also been calibrated to ensure unsaturated response.

The results obtained for the EOTec/HB fibre were representative of all the fibres studied over a wide range of pump powers, and were highly reproducible. The broadband features are largely independent of pump power with only the signal amplitude changing. Figure 37, for example, shows the broadband features of the Stokes signal of 200m EB450 fibre sample pumped by a Nd:YAG laser along one eigenaxis. A 3dB bandwidth of 15MHz was measured at 2.5 times the threshold, though the overall magnitude of the spectrum was low compared with the EOTec system (Figure 27).

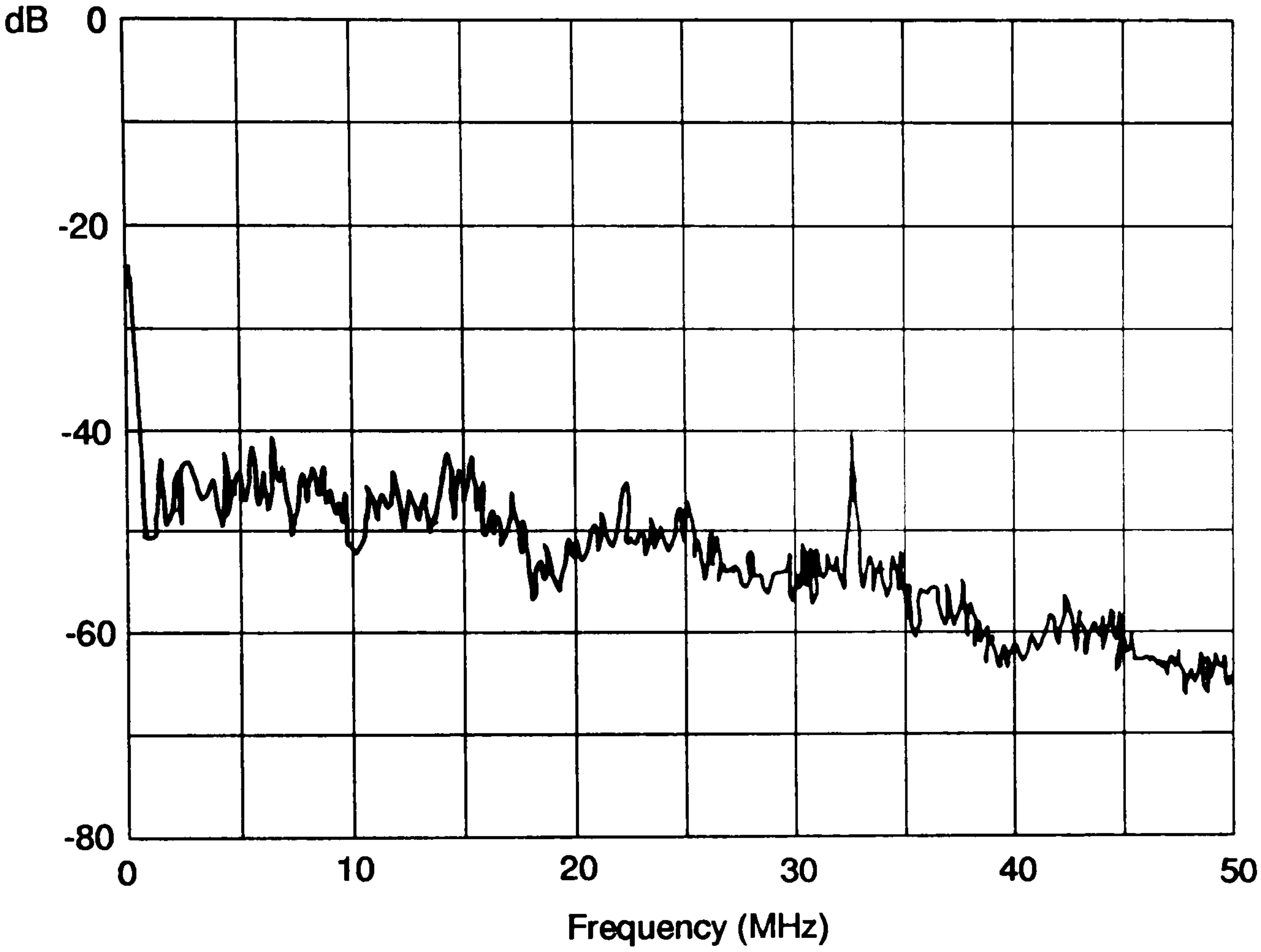

Figure 37: Broadband Spectrum of EB450 Fibre Pumped at 0.532μm

The results again concurred with the detailed studies into the dynamics of the SBS process discussed in section 2.4.3 for systems possessing no external feedback. In these, the same features of broadband behaviour were displayed. This indicated that the output intensity again possessed the same sustained aperiodic oscillations with modulation depths of almost 100% for all powers above threshold and for all fibres (similar to the results of Johnstone, 1992). The inclusion of *optical feedback* can modify the spectra and we discuss this shortly.

Note in Figure 37, the presence of an anomalous peak at about 33MHz, despite only one eigenaxis being pumped in the EB450 fibre. These oscillation spikes occurred at regular intervals during the experiments though were only present for a short sampling time (single frame). Further investigations to establish any significant trends in their appearance were performed. Using a VCR to record the screen of the spectrum analyzer, a frame-by-frame analysis of the system output was undertaken for a variety of experimental topologies. Whilst the average number of spikes per frame increased with Stokes intensity for a given fibre and eigenaxis, the spikes were spread evenly across the spectrum (0-500MHz). In order to ensure distinction between systems with and without the heterodyne carrier, graphs such as that shown in Figure 38 were constructed.

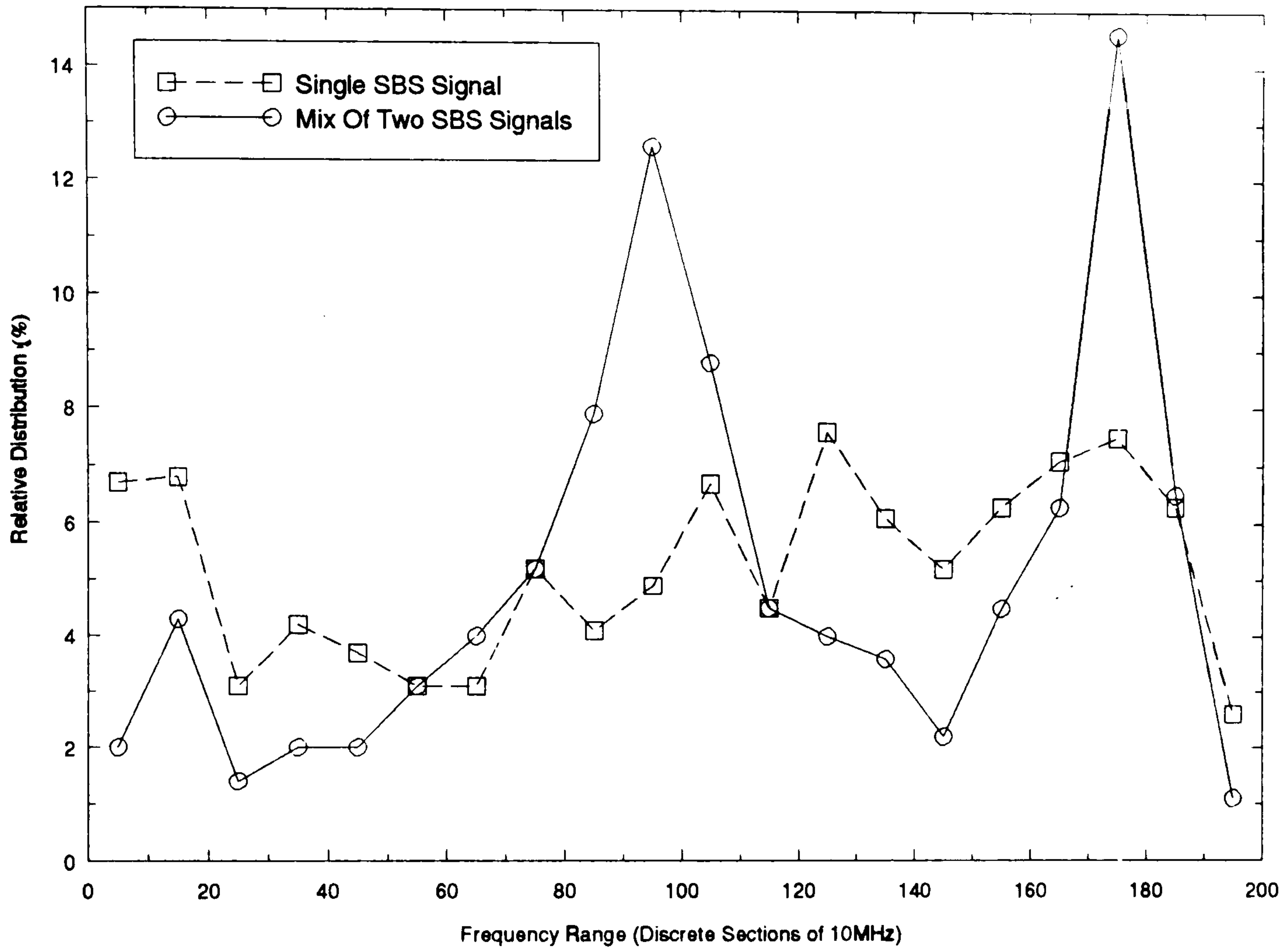

Figure 38: Distribution of Frequency Peaks From the EOTec/HB Fibre for the Examples Shown

Figure 38 shows the relative distribution of a frequency peak within a 10MHz segment of the spectrum analyzer range (0-200MHz) for the dual input/Bragg cell SBS system of Plate 3. In the first experiment, only the eigenaxis of the EOTec/HB fibre was producing SBS (4.5mW Stokes signal). In the second, both eigenaxes simultaneously produced SBS. For the latter, the constant Bragg cell peaks at 80MHz and 160MHz are obviously excluded. Again, for the single Stokes signal, the peaks are fairly uniformly spread across the spectrum (average number of peaks was 1.6 per frame). For the mixed signal, clear peaks in the distribution in the 80-100 and 160-180MHz regions are visible (average of 3.6 peaks per frame). The graph emphasised the frequency instability associated with the SBS induced carrier as the carrier peaks were prevalent across several 10MHz regions. Outside of these, the rate of occurrence of the bursts is approximately constant.

From these observations, the frequency spikes appeared to occur randomly and evenly across the frequency spectrum. It was not possible to determine whether they were induced electronically or were real manifestations of the optical system. The spikes were observed in the time domain via the oscilloscope so were not a function of the spectrum analyzer and were present for all fibres emitting SBS. The peaks were consistently lower in power than the SBS-induced carrier.

In section 2.4.3, the transient properties of SBS were described and, in particular, the aperiodic instabilities which account for the broadband spectra (Harrison et al, 1990). In Harrison's work, external feedback was shown both experimentally and theoretically to alter the dynamics of the process. The Stokes outputs showed a trend to quasi-stable emission via burst modes of operation (these contain set frequencies governed by the photon round trip time in the fibre and NOT related to the random peaks described above). The effects of feedback on both output spectra and SBS induced carrier were investigated in the present study and the results now described.

In Harrison's work, the feedback arose from both Fresnel reflections at the core-air interface and via an external mirror. Short lengths of fibre (typically 25, 40 and 100m) were used, necessitating higher input powers to generate SBS and hence maximising Fresnel feedback. In the present study, fibre lengths of between 130m and 800m were pumped such that feedback Fresnel reflections was significantly reduced. The effect of this type of feedback was assessed by index matching the distal end of the fibre, reducing the reflectivity at this interface to zero. For all the fibres studied (200m HB450, 195m EB450 and 800m EOTec/HB), no difference in overall broadband spectral power or profile was noted with or without index matching. Further, no change in Stokes power for a given pump power between the two cases was noted. (An increase is predicted in short fibres as the Stokes signal is built up more quickly through amplification of the reflected Stokes signal rather than from the spontaneous signal at $z = L$) We conclude therefore that the effect on Fresnel reflections of the systems investigated in this study is negligible.

The system used to study the effect of *external* feedback on the SBS process is shown in Figure 39. A plane mirror was positioned to reflect the undepleted pump and backreflected Stokes signals back into the fibre 'cavity'. Both the output spectrum and output power were recorded as before. A representative sample of results is now given.

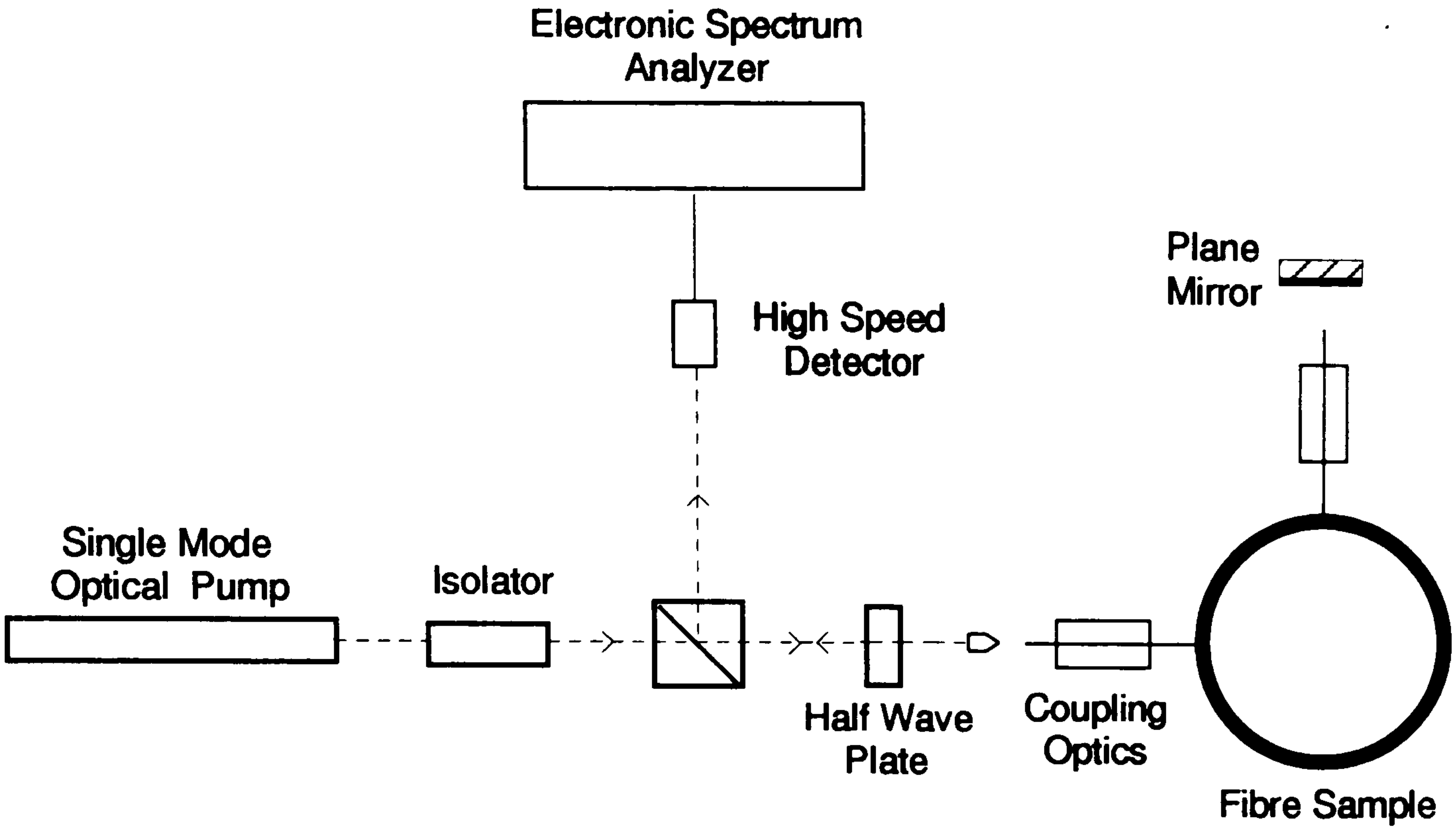

Figure 39: Experimental System Used to Study the Effects of Feedback

Figure 40 shows two output spectra from the 195m EB450 fibre pumped at 0.532μm in the (single input) frequency shifter configuration both with and without feedback. The latter trace has been shown previously in Figure 33. In this experiment, approximately 30% of the output power (1.5mW) at the distal end of the fibre was relaunched by the mirror. The coarse adjustment screws of the mirror and tight alignment constraints prevented fine-tuning of the reflectivity, however.

Several interesting trends emerged. Firstly, the output Stokes signal was increased since the relaunching of the Stokes signal increases the effective gain of the cavity. Secondly, FWM was initiated, the second peak at 16.7MHz in Figure 40 being indicative of this mechanism. Thirdly, though the overall profile of the broadband spectrum remained constant, its power was reduced by 10dB across the whole spectrum for the EB450 fibre shown in Figure 40. This confirmed the observations reported in the literature (Lu et al, 1992) of more quasi-stable behaviour with feedback though no evidence of the reported pulsed mode structure was observed in the frequency domain. This may have been due to the 20ms sampling time of the spectrum analyzer. Broadband reduction implies that the visibility of the carrier was enhanced.

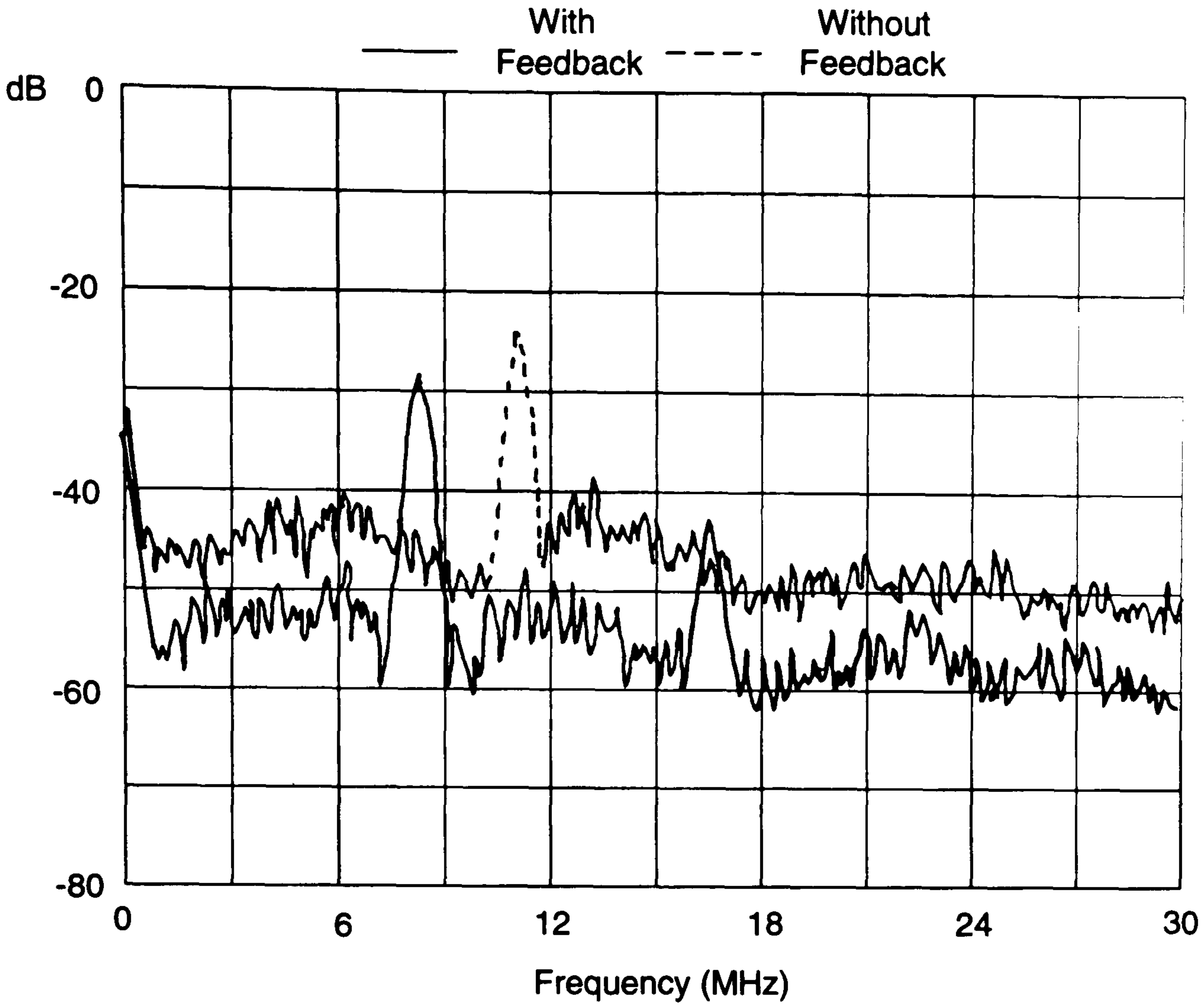

Figure 40: Output Spectrum From EB450 Fibre Pumped at 0.532μm With and Without Feedback

Fibre Type (Length)	Pump	$\delta\nu_B^*$ (MHz) (No Feedback)	Readings	$\delta\nu_B$ (Feedback)	Readings
EB450 (195m)	Nd:YAG	8.4±4.4	230	7.2±3.7	150
EOTec/HB (400m)	ArI	10.7±7.9	650	10.4±6.8	400
EB450 (195m)	ArI	8.0±4.5	130	5.9±2.7	85
EOTec/HB (164m)	ArI	10.7±7.9	650	10.9±6.7	150

* Results repeated from Table 6.

Table 7 Effect of Feedback On SBS Carrier Modulation For Systems Shown

Fourthly, and importantly, in the systems containing feedback, the modulation of the SBS-induced carrier frequency was consistently reduced. Table 7 summarises these results. Again, a frame-by-frame analysis of the spectrum analyzer monitor using a VCR facilitated calculation of the carrier frequency. The standard deviation of the modulation is listed in the table. For the EB450 fibre pumped with the Nd:YAG, the modulation was reduced by 18%. In the EOTec/HB sample pumped by the ArI, the reduction was 14%, despite obtaining a 70% reflectivity of the output power (equivalent to 1.25mW). The longer sample length suppressed the effect of the additional feedback. The broadband spectrum was however reduced again by between 5 and 10dB over the sampling range (0-30MHz). The consistent lowering of the mean frequency in the presence of feedback was directly linked to the overall reduction in modulation.

Fewer readings of carrier frequency were obtained with the EB450 fibre pumped at 0.5145μm due to light induced polarisation instabilities. Again, the spectra was reduced by about 8dB over the (30MHz) sampling range. Significantly, large improvements in frequency stability were also measured. Arrays of carrier signals induced via FWM were prevalent in the system output. An example is shown in Figure 41 for a 150mW input power and 70% reflectivity at the rear of the fibre. The arrays consisted of a fundamental frequency at 2.4MHz and up to 10 harmonics. These were stable over a period of a few seconds before the system reverted to its more 'conventional' state with an unstable carrier and only one or two FWM orders. Note that the fundamental frequency much better matches the predicted carrier of the system shown in Table 6.

The principal limitation of investigating the EB450 fibre at 0.5145μm was the aforementioned polarisation instabilities. The large power budget at this wavelength could not therefore be fully exploited. Hence, a shorter sample of EOTec/HB fibre (164m) immune to the photosensitive effects, was inserted and tested both with and without feedback for pump powers up to 500mW. The results were unfortunately rather inconclusive. Only a small reduction in carrier frequency modulation and broadband spectrum was obtained in the feedback systems. The mean frequency actually increased slightly, in contrast to the other systems listed. However, a FWM array was again induced with up to 10 orders and a fundamental centered on 10MHz.

In summary, then, the transient properties of the SBS systems have been examined. The broadband spectrum was intrinsic to the SBS process and represented an intensity modulation distribution with a 3dB bandwidth of 15MHz which was constant with fibre type, pump and pump power. Externally generated feedback increased the effective gain of the system and was shown to

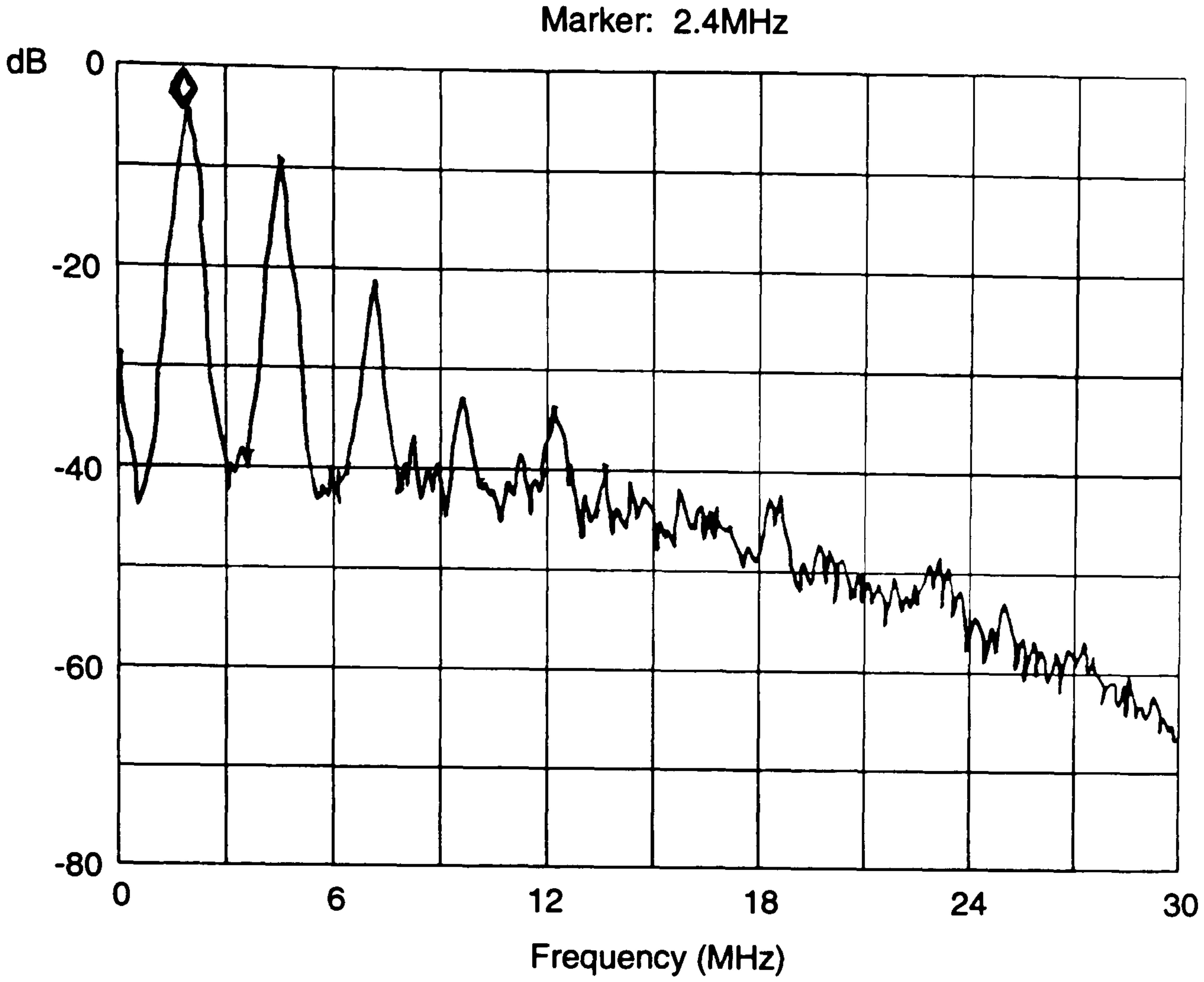

Figure 41: Output Spectrum From EB450 Fibre Pumped at 0.514μm Showing Array of Frequency Peaks

(a) reduce the power of the broadband spectrum

(b) reduce the modulation of the mean frequency of the SBS induced carrier

(c) produce FWM.

Many of the observations reported in this section are in good agreement with the results cited in section 2.4.3. The trends in broadband emission reported here map those for Harrison's zero feedback systems. In the case of feedback, no dominant $1/2\tau$ components were observed (2τ is the round-trip time of photon in fibre cavity) though the sustained oscillations were present throughout. The spectrum remained predominantly broadband, though some pulsed mode behaviour was observed in the time domain (Figure 35). The trend to quasi-stable output was manifested as the general lowering of the broadband power spectrum, though no reductions above 10dB were measured.

Of special interest to the frequency shifter and sensor work was the modulation of the SBS induced carrier. Observations (a) and (b) above suggest a link between the broadband spectrum and this modulation. The qualitative description of the dynamical behaviour given in 2.4.3 reinforces this interpretation. In the present experiments, the pump itself was eliminated as a source of the instability, despite deviations in its output frequency over the duration of the experiments. It is, however, difficult to envisage cross and self phase modulation of the pump and Stokes beams alone producing the frequency modulation. For example, for the EOTec/HB fibre pumped by the ArI, the instability in the carrier was ±7.9MHz (Table 6). From equation 2.35, a 7.9MHz change in carrier frequency is equivalent to an index perturbation along one of the eigenaxes of 3.4×10^{-4} over the interaction length. This would be sufficient to almost erase completely the intrinsic birefringence of the fibre ($\delta n \approx 5\times10^{-4}$) and no evidence for this was found in the steady-state properties of the fibre (section 3.4.1).

Neither the broadband effects nor the frequency modulation of the carrier have been directly reported in the literature in the context of SBS for sensors or signal processing. There are probably valid reasons for this. In sensors (discussed Chapter 5), most measurements are made in the GHz domain such that spectra in the d.c. to 100MHz region would not be recorded. The use of a two source counterpropagating, pump/pulse amplification arrangement is common rather than the single source system used in this study. Measurements of output frequency are sampled over a short time domain. In the one previous example of a frequency shifter using similar techniques to those described here (Culverhouse et al, 1989b), heterodyne carriers were generated in the 700-800MHz region, again well in excess of the broadband region. Interestingly, however, four different values of SBS induced carrier (ranging from 748 to 761MHz) were reported for the same experiment. Three were obtained from an identical sensing arrangement to the one used in the present study (PIN photodiode and spectrum analyzer), the fourth from a Fabry Perot analyzer device. No comment was made on this instability. In SBS systems utilising fibre ring resonators to reduce the threshold (eg Kalli et al, 1991), neither effect – broadband spectrum or frequency modulation – has been noted. The ring resonator approach to SBS generation is compared, in Chapter 6, with the results obtained in this chapter.

3.6 Summary of Principal Results

The steady-state SBS properties of the six fibre types used in the study were measured and shown to differ significantly (Table 5). The EB450 and EOTec/HB fibres (respectively, elliptical core and elliptical cladding birefringent fibres) demonstrated most commonality. The values of gain, within experimental error, were approximately $3.5\times10^{-11}\mathrm{mW}^{-1}$ for both ArI and Nd:YAG laser sources. Excellent correlation between the measured and predicted output signals for the EOTec/HB fibre, using the theory developed in Chapter 2, was obtained. Further, its polarisation properties remained constant for all available pump powers (up to 250mW). The polarisation properties of the EB450 fibre were modified marginally at high pump powers, producing some discrepancy between experimental and theoretical outputs. However, the work demonstrated that these two fibres were the most suitable for the subsequent frequency shifter and sensing experiments.

Of the remaining four fibres, the EOTec/TW sample, nominally a circular birefringent fibre, demonstrated all the attributes of a low SBS gain, linear birefringent fibre. The PANDA fibre possessed an SBS gain of only $2.2\times10^{-11}\mathrm{mW}^{-1}$ and SBS thresholds of 140mW, invalidating it for the present studies. The most intriguing results concerned the HB450 ('bow-tie' birefringent fibre) and SM450 (single-mode) fibres. After initial pumping at high ArI pump powers and subsequent storage at room temperature, both showed large increases in attenuation and, hence, SBS thresholds. Further, the polarisation properties of the HB450 fibre were modified under certain pump conditions. These effects, linked to the creation of dopant-related defects, are described in more detail in Chapter 4.

In order to validate the SBS frequency shifter concept, the EOTec/HB and EB450 fibres were used in a single fibre configuration. Carrier signals of approximately 10 and 8MHz respectively were produced for both pump sources. This represented the first practical demonstration of a single fibre, SBS-based frequency shifter. Two-fibre systems were also investigated. Two samples of HB450 fibre (from different batches) produced a carrier centred on 665MHz. Alternatively, by using the EOTec/HB and EB450 fibres in the same arrangement at room temperature, a carrier at 135.6MHz was generated. The magnitude of the frequency, in both cases, was attributed to different levels of dopant concentration (principally germania) in the fibre cores. Neither the EOTec/TW nor SM450 fibres produced the expected signals at 80kHz and 20kHz. The former displayed properties akin to linear birefringence (a 2.5MHz carrier at 0.5145μm). In the latter, the photosensitive mechanisms precluded any carrier generation.

For all frequency shifter systems, the carrier was modulated about its mean value by between 4 and 13MHz (Table 6). This is unacceptable for sensor applications in which frequency stability of the carrier critically determines the sensor resolution. In addition, the visibility of the carrier in all systems was reduced due to the presence of broadband intensity modulations in the output. Both these transient processes were shown by experiment to be intrinsic to the SBS process and in accord with the dynamical theory described in section 2.4.3. By introducing external feedback into the systems (in the form of undepleted pump radiation), both effects were partially suppressed. Reductions in both the broadband spectrum (by up to 10dB across the spectrum) and carrier frequency modulation (up to 20%) were measured in the EB450 and EOTec/HB frequency shifter systems. Further, the increase in FWM with feedback produced intermittent quasi-stable output arrays of the fundamental carrier frequency. The results from the feedback experiments were used to improve the resolution of the sensors addressed in Chapter 5.

4 Photosensitivity In Optical Fibres

4.1 Introduction and Overview

In Chapter 3, several frequency shifter systems were unsuccessful in generating a carrier because of changes in either fibre attenuation, fibre polarisation properties or both. These changes were induced through the interaction of the pump light itself with the fibre core. For example, as described in Chapter 3, both HB450 and SM450 samples demonstrated large increases in fibre loss after high power pumping at 0.5145μm, resulting in higher SBS thresholds. The HB450 and EB450 samples demonstrated additional polarisation instabilities. In the HB450 fibre, this compounded the problems of increased loss to make carrier generation impossible. In the EB450 fibre, an unstable carrier output (in time) was produced. In this chapter, these properties are examined in more detail, with the focus being on their implications for SBS systems (both frequency shifters and sensors). However, the results are equally applicable to any high power fibre delivery system employing UV or visible radiation such as in Laser Doppler Velocimetry.

This chapter is divided into four further sections. In the first, the photoinduced attenuation properties of the fibre samples are described. In the second, the polarisation properties of the fibres that were modified by the pump are reported, together with measurements of direct core index changes with respect to pump power. Section 4.4 compares the results of the present study with equivalent data from the literature and places the results into the context of theories proposed in the literature to explain photoinduced effects in fibres. The principal results are then summarised in section 4.5.

4.2 Photoinduced Attenuation Measurements

During the measurements of the steady-state properties detailed in section 3.4.1, it was noted that in certain fibre samples, the losses through the fibre increased significantly in the visible spectrum between measurements taken days and weeks apart. For example, an attenuation of 60dB/km was measured in fresh HB450 fibre. This steadily increased between subsequent experiments (ie no pumping) to 98dB/km and higher (assuming a constant coupling efficiency). The corresponding SBS thresholds for single eigenaxis pumping thus rose from 64mW to 96mW and beyond respectively. All the initial pumping of the HB450 fibre predominantly used the cw ArI source at launch powers up to 250mW, though SRS experiments had been undertaken with one sample using a pulsed, frequency doubled Nd:YAG source (λ_p =0.532μm). Remarkably, this dramatic increase in attenuation could be partially reversed by pumping again with cw radiation at 0.5145μm.

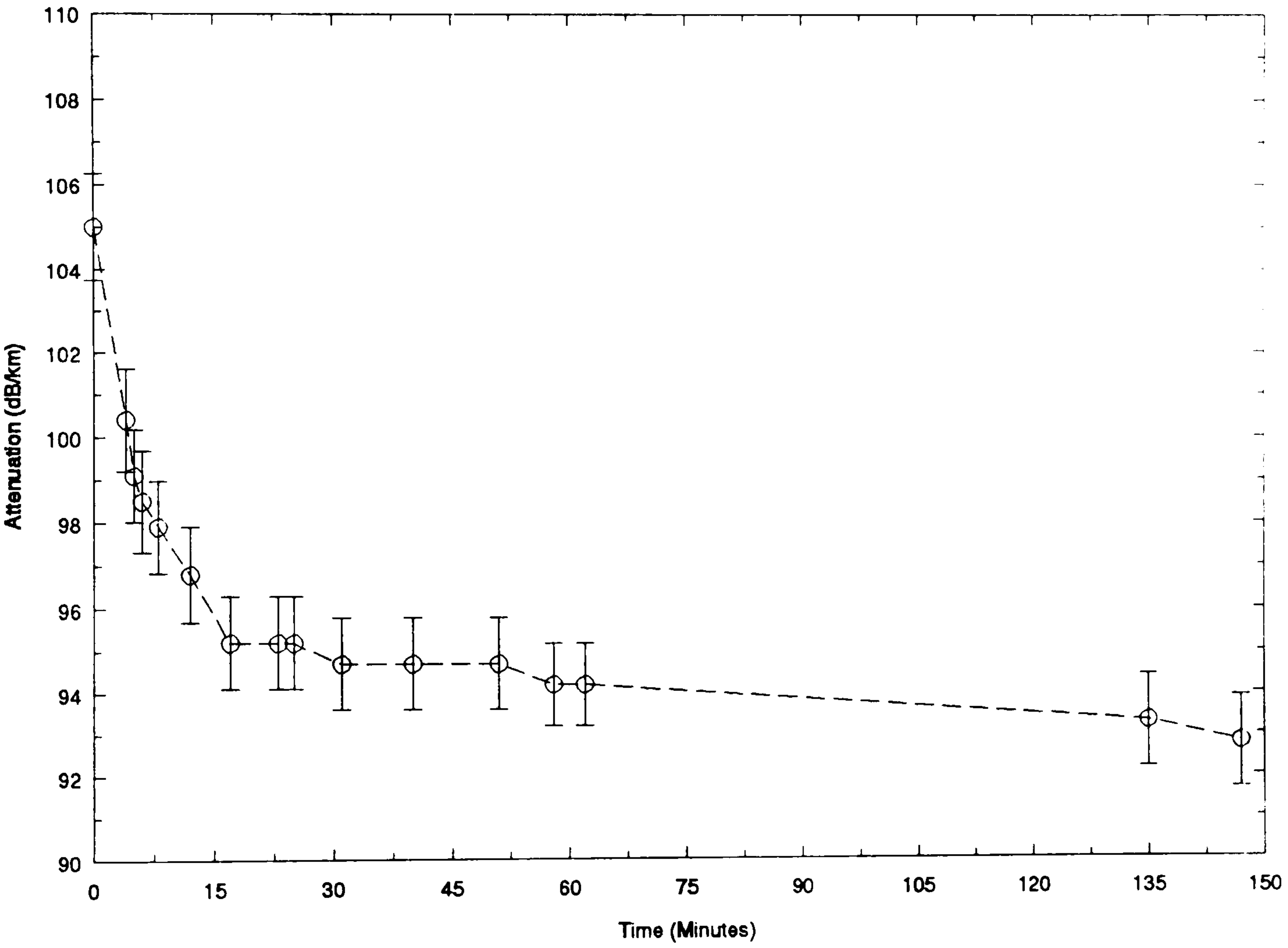

Figure 42: Time Evolution of Attenuation at 0.5145μm of HB450 Fibre Pumped at 0.5145μm for 33mW Launched Core Power

Figure 42 illustrates this effect for the HB450 fibre pumped along a single eigenaxis. The transmittance of the 0.5145μm radiation was measured as a function of time for 33mW input power launched into the core. The attenuation steadily decreased from an initial value of 105dB/km, before becoming constant at 93dB/km. The virgin fibre value of 60dB/km was never regained. On blocking the pump, the attenuation slowly increased back to its pre-pump value of 105dB/km.

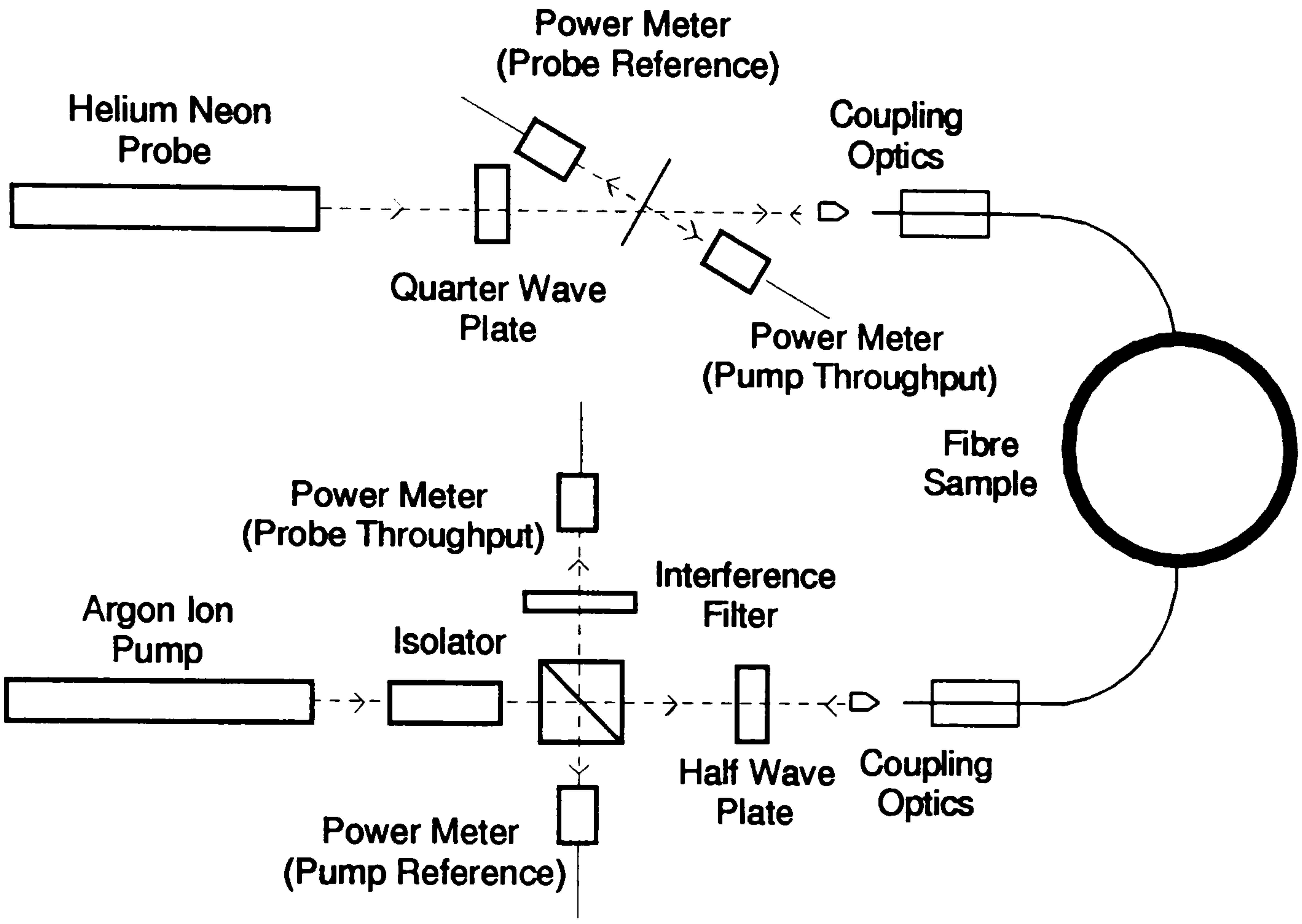

Figure 43: Experimental Arrangement to Monitor Photoinduced Attenuation Changes Along the Fibre

In order to measure more accurately and in more detail the attenuation changes and the variation between fibre samples, the system of Figure 43 was employed. A circularly polarised, counter-propagating probe from a Helium Neon laser at 0.6328μm monitored changes in loss of the fibre arising from its interaction with the pump source, though the throughput of the pump was also measured simultaneously. Figure 43 was similar to that reported in recent fibre photosensitivity studies (Kanellopoulos et al, 1991). In the present system, drifts in power from the sources were nullified using reference photodiodes. The half wave plate again allowed each eigenaxis of the fibre to be pumped (when appropriate) in turn. The circularly polarised probe permitted polarisation independent attenuation measurement.

Figure 44 shows the change in attenuation of the 200m HB450 sample

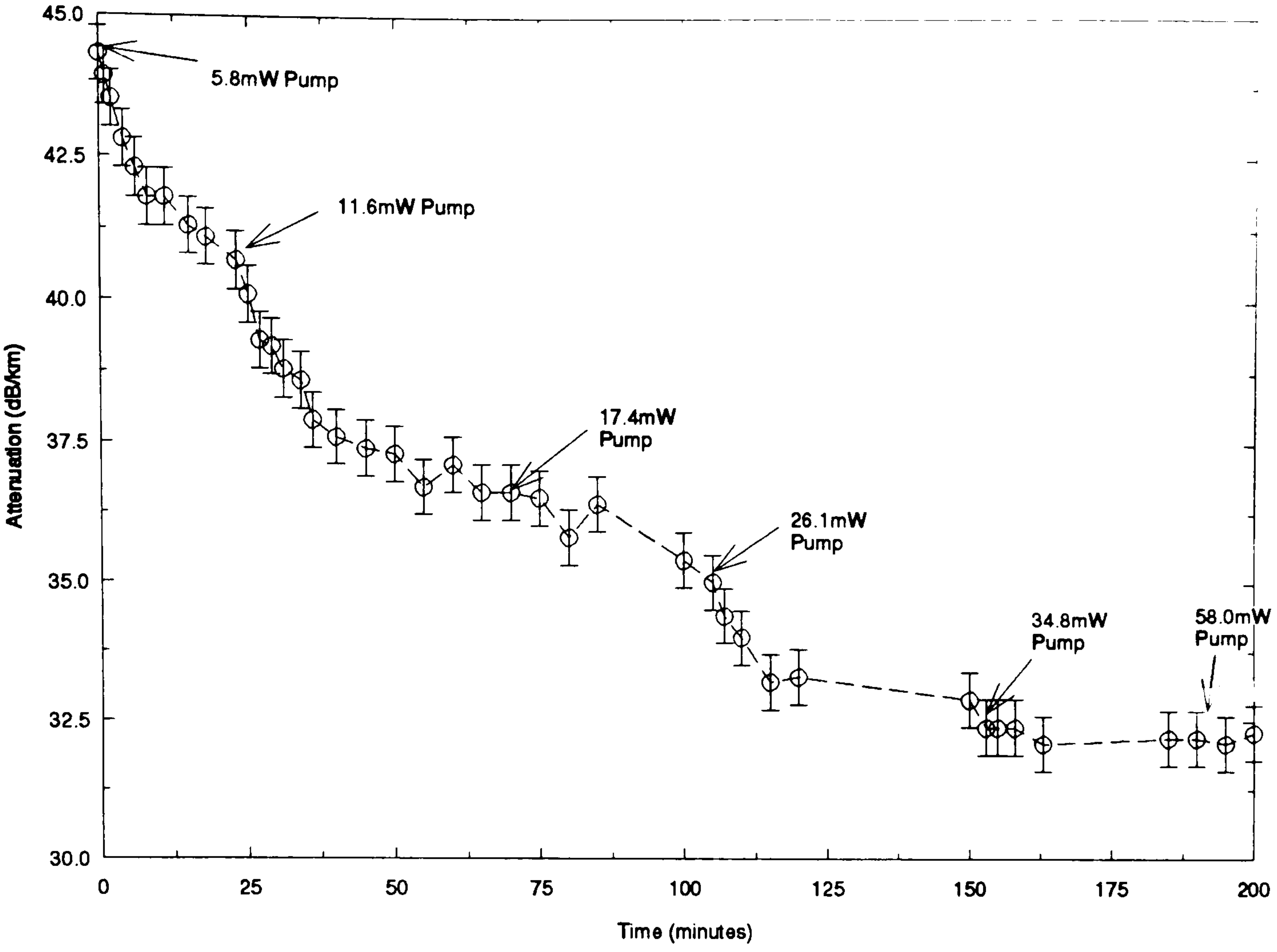

Figure 44: Time Evolution of Attenuation at 0.6328μm of HB450 Fibre Pumped at 0.5145μm for Increasing Launched Core Power

at 0.6328μm, pumped along a single eigenaxis at 0.5145μm. The power launched into the core was steadily increased in time as shown. The results demonstrated a clear reduction in fibre attenuation from the initial value of 44dB/km both with time and with pump power, in accordance with the trend of Figure 42. For a given pump power, the rate of reduction in attenuation slowed with time. The rate was increased by pumping the fibre at greater powers. The process eventually saturated at a loss of 32dB/km even for higher pump powers. The error bars represented the resolution of the respective power meters. However, it is the *trends* demonstrated in the graph that are more important than the absolute values of attenuation. Though the fibre loss has been significantly reduced, a value of 12dB/km is typical for a 'fresh' sample of HB450 at 0.6328μm. Clearly, the initial pumping of the fibre at high ArI cw and Nd:YAG pulsed powers had introduced additional losses into the fibre core which were only partially removed by the renewed pumping at 0.5145μm. These processes are placed into the context of dopant related defect formation in the fibre cores and SBS systems in section 4.4.

The attenuation at 0.5145μm itself followed a similar pattern to that of Figure 44, though over a wider range of values. An initial loss of 130dB/km was measured, the upward trend in losses noted during the initial experiments with the fibre eventually saturating at this value. Renewed pumping reduced this to a constant value of 92dB/km, for pump powers in excess of 50mW, over the 200 minutes of the experiment. On either blocking the pump or reducing it below 50mW, a slow reversal of the process commenced and the attenuation eventually returned to its maximum level (ie 130dB/km and 44dB/km for 0.5145μm and 0.6328μm respectively). This reversal process took up to two days to complete. On pumping the orthogonal eigenaxis, identical results were obtained.

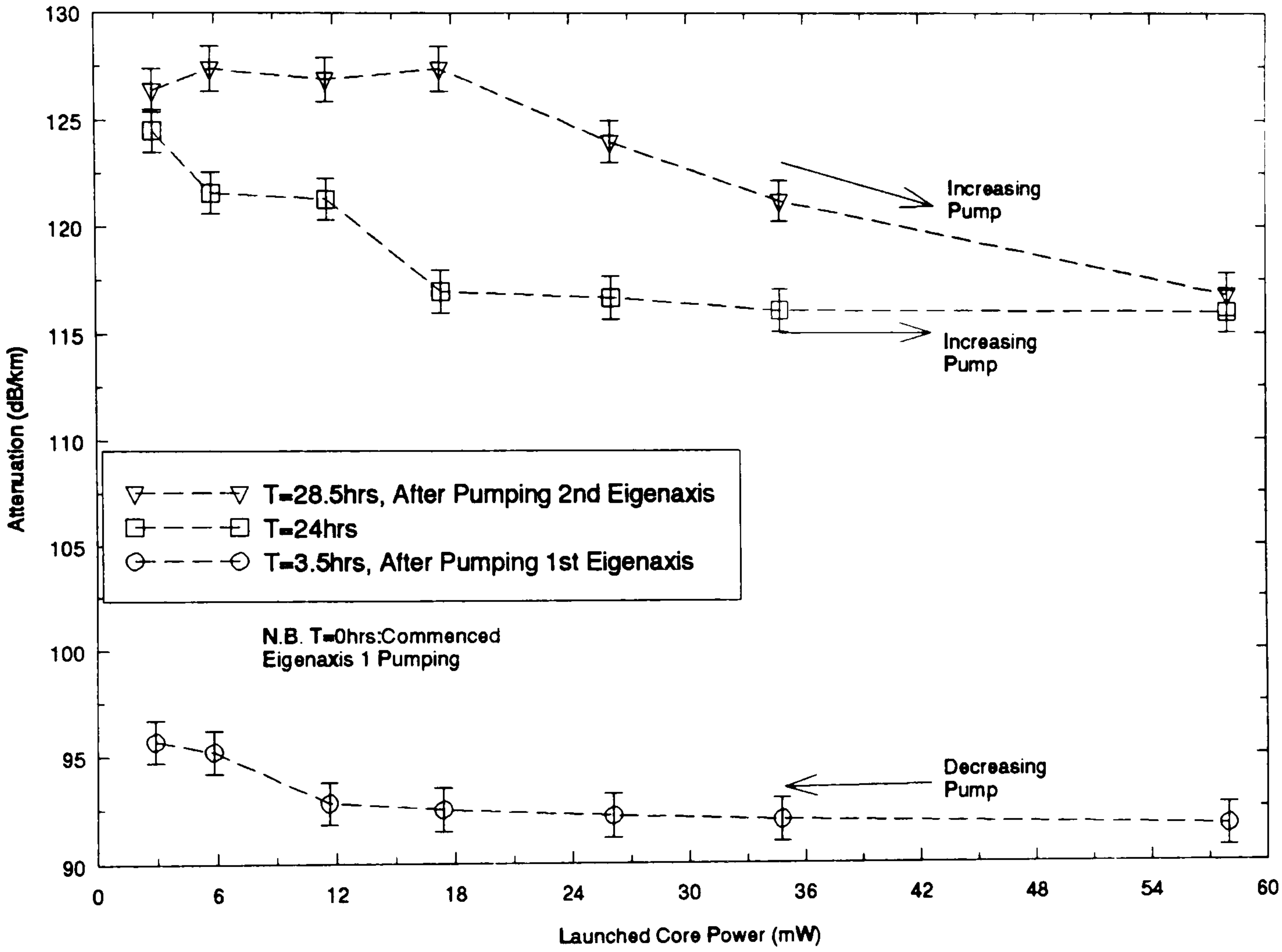

Figure 45: Photobleaching 'History' of Eigenaxis of HB450 Fibre Measured at 0.5145μm for Situations Shown in the Graph

Figure 45 further illustrates the characteristics of the photosensitive processes. Three curves are shown, the losses all measured at 0.5145μm. The bottom trace shows the attenuation along the first eigenaxis immediately after the pumping shown in Figure 44. The measurements were made for decreasing launch power, the reversal of the bleaching process commenced as soon as the pump had been reduced. The middle curve shows the loss measured one day later. The fibre had been decoupled from the system and stored at room temperature in the intervening period. The curve shows that the drift to a higher attenuation value had continued over this time. These measurements were made for *increasing* pump powers. To analyze the polarisation characteristics of these processes, the loss for light polarised along the first eigenaxis *after* the orthogonal eigenaxis had been pumped was measured (Top curve). The drift to higher losses had continued along this eigenaxis despite the presence of orthogonally polarised pump power within the core. Thus, whilst the loss along the second eigenaxis had been reduced to 92dB/km, the losses along the first eigenaxis had continued to increase towards 130dB/km. The bleaching mechanism that partially decreased the loss was thus sensitive to polarisation.

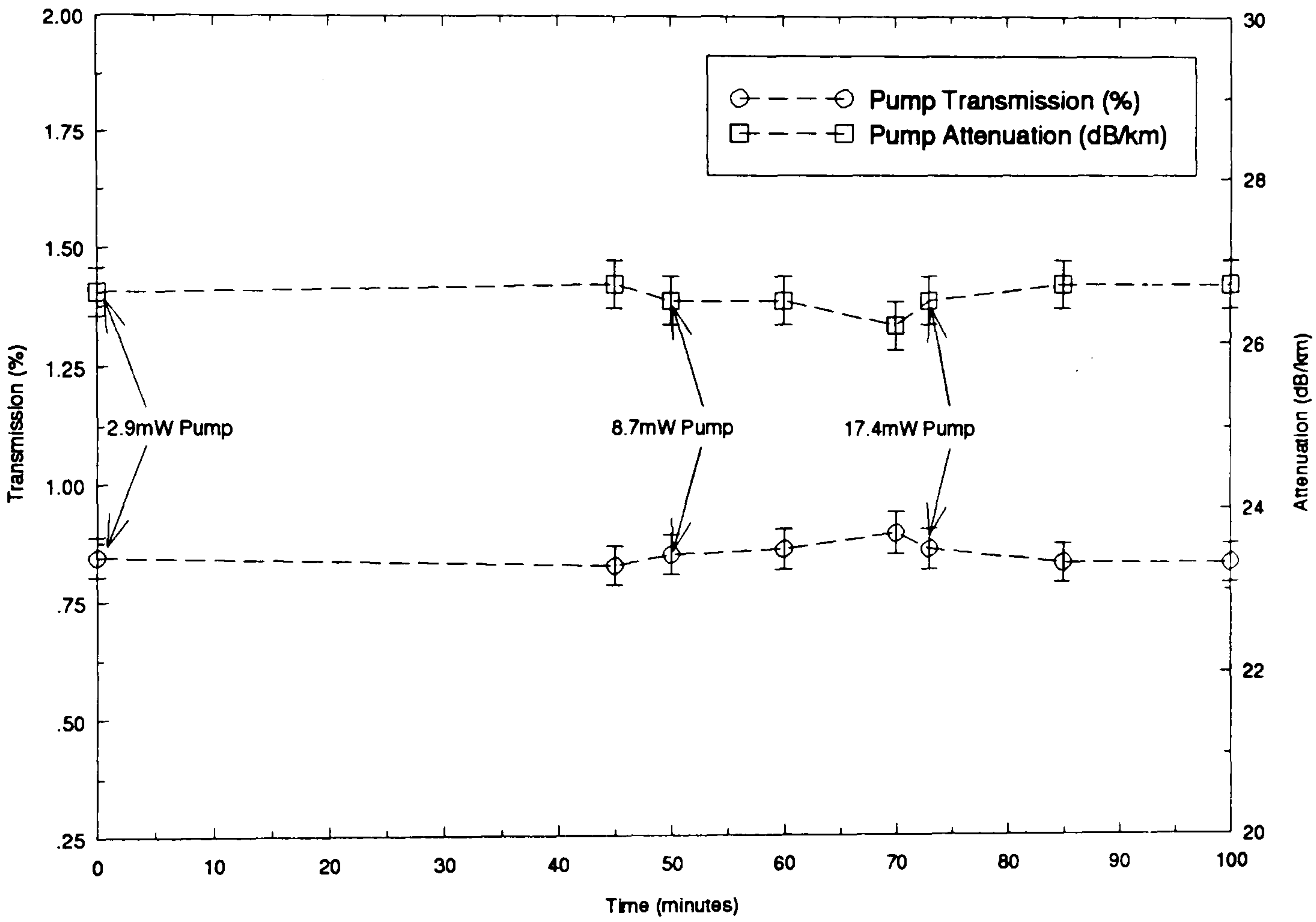

Figure 46: Time Evolution of Attenuation at 0.5145μm of EOTec/HB Fibre Pumped Along One Eigenaxis at the Same Wavelength

The attenuation characteristics of the other fibre samples (Appendix C) were studied. Figure 46 shows the losses measured in the 780m EOTec/HB sample at 0.5145μm, pumped along one eigenaxis at the same wavelength. Both transmittance (expressed as a percentage) and attenuation are depicted for increasing launch powers. Despite being subjected to the same high levels of cw pump at as the HB450 fibre, no changes in transmission were measured in the fibre in this experiment or, indeed, during the whole study. Thus. the SBS threshold remained constant throughout. Higher pump powers are not shown in Figure 46 since SBS was initiated for powers in excess of 23mW (Table 5, section 3.4.1). Similar stable transmission properties were found for both the PANDA and EOTec/TW samples.

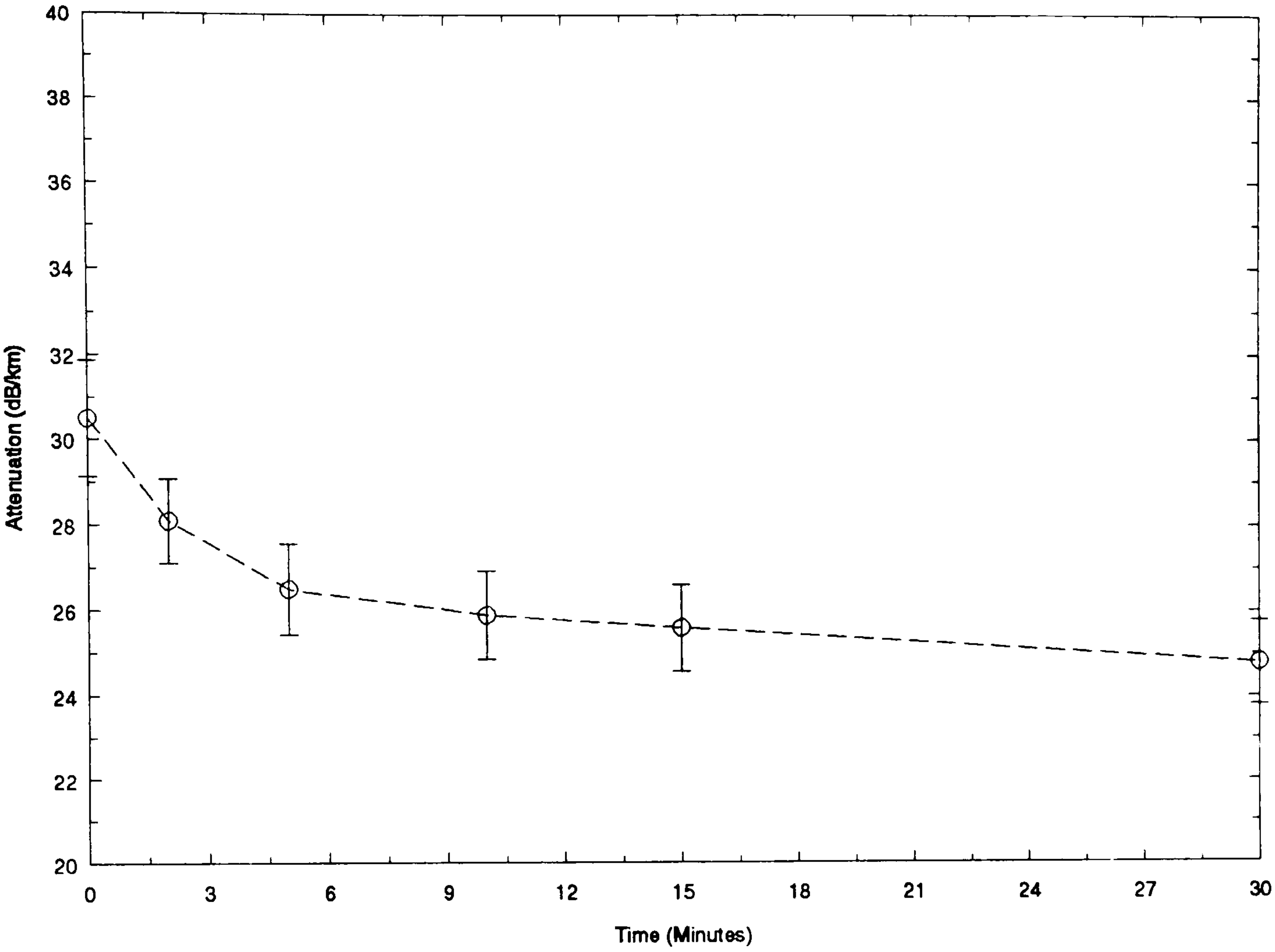

Figure 47: Time Evolution of Attenuation at 0.532μm of SM450 Fibre Pumped at 0.532μm

The EB450 fibre exhibited photosensitive transmission, though to a lesser degree than the HB450 fibre. The loss increased from to 29.5 to 39.8dB/km over the 18 month duration of the experiments, which produced a corresponding increase in SBS threshold of 16% per eigenaxis (29 to 34mW). No significant bleaching of these additional losses occurred. More serious problems in the context of SBS generation arose with the polarisation maintaining capacity of the fibre (discussed in section 4.3).

Like its high birefringence counterpart, the *York* manufactured SM450 fibre demonstrated significant changes to its transmittance. In the initial steady-state SBS assessment, a loss of 32dB/km was measured at 0.5145μm. The fibre was subsequently pumped only with this radiation and similar characteristics to the HB450 fibre were exhibited. The overall loss of the fibre slowly increased over the weeks of experiments to 51dB/km. This was partially bleached back to 40dB/km for launch powers of 30mW or greater over 30 minutes. Again, on blocking the pump, the loss slowly returned to 51dB/km. Figure 47 shows the bleaching effect at 0.532μm from the cw Nd:YAG source. An initial loss of 31dB/km was improved to 25dB/km along the 169m sample by pumping at 25mW for 30 minutes. This was the minimum loss attained and the drift upwards on removal of the pump was again recorded.

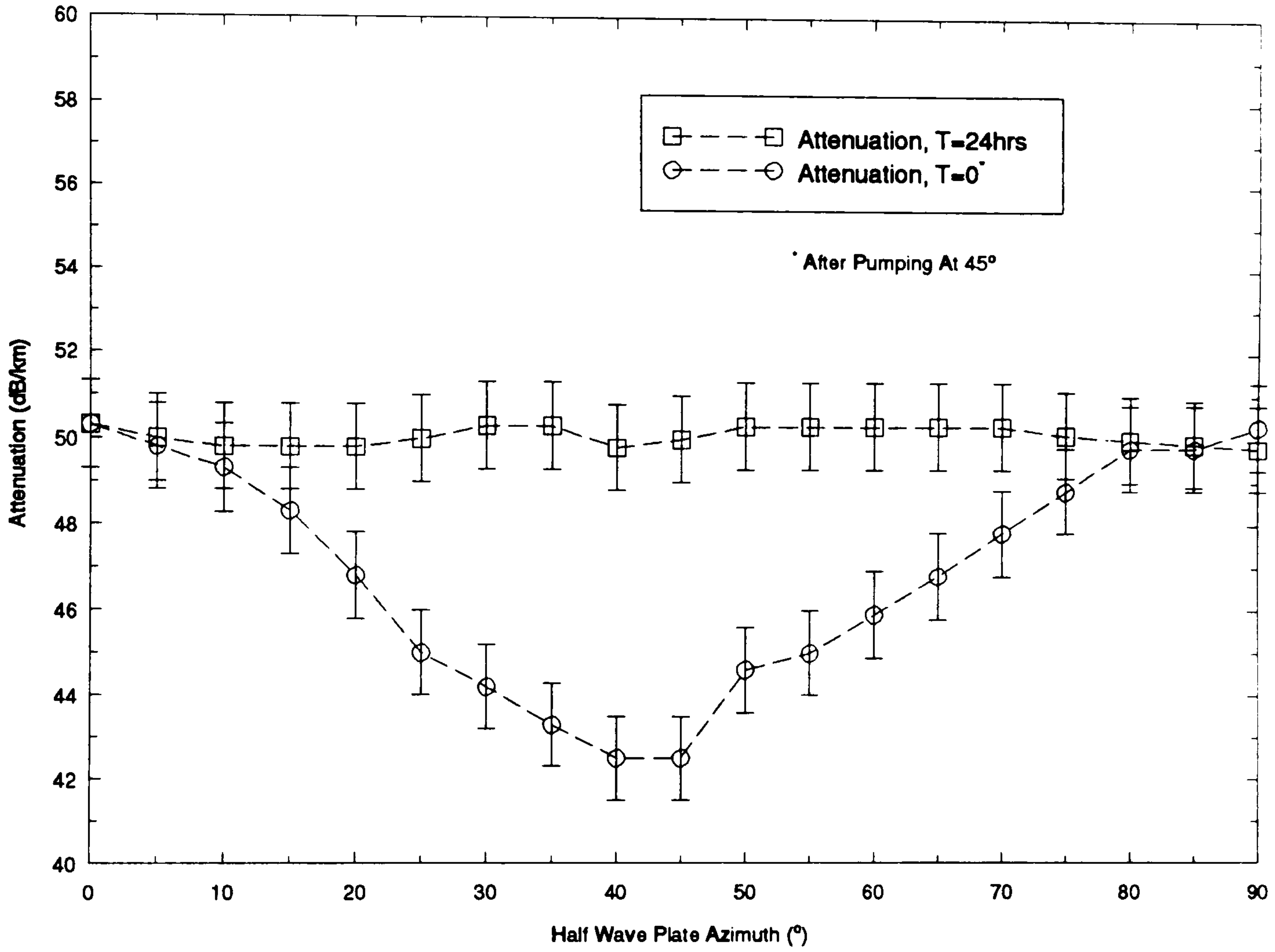

Figure 48: Attenuation of SM450 Fibre at 0.5145μm as a Function of Half Wave Plate Azimuth for the Cases Shown in the Graph

As for the HB450 fibre, the bleaching mechanisms in the SM450 fibre were sensitive to the polarisation of the pump. To demonstrate this (Figure 48), the input polarisation of the pump light (0.5145μm) was orientated at an azimuth of 45°, relative to the vertical axis of the core. (Since the fibre was circularly symmetric, the choice of azimuth was purely arbitrary).

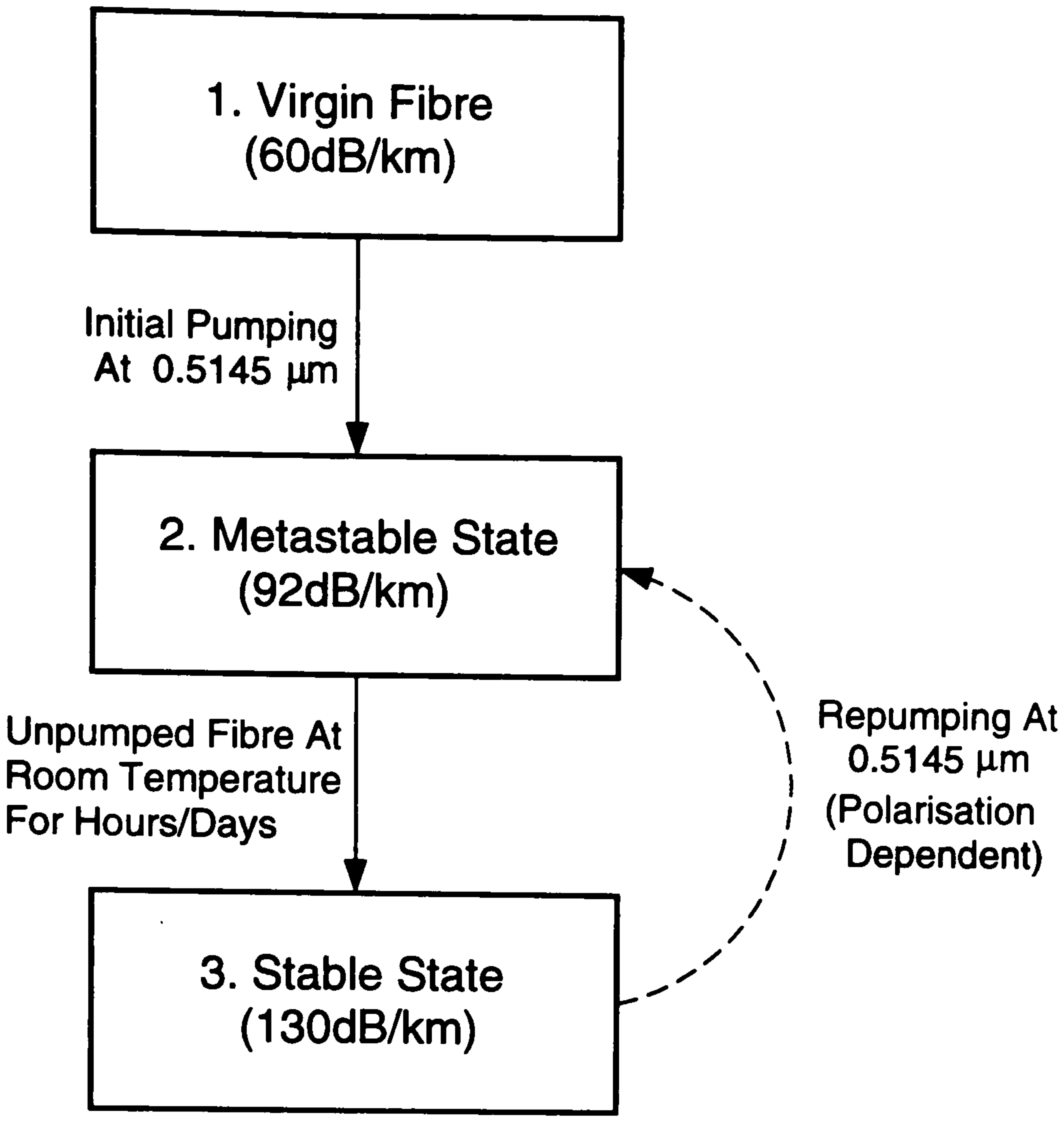

Figure 49: Three Stages of the Photoinduced Attenuation Process

The core was then pumped at 34mW for 20 minutes. As before, the loss was reduced from 50 to 42 dB/km at the pump wavelength. The pump was attenuated to 5mW and the loss measured at the other input polarisation azimuths by rotating the half wave plate in increments of 5°. It was important to make the measurements reasonably quickly as the system started (within minutes) to relax to its higher loss state as the pump was reduced. The lower curve in Figure 48 shows the result. The bleaching of the initial loss mechanism (that caused the fibre to attain 51dB/km loss) was clearly polarisation dependent. The attenuation increased as the azimuth between probe and bleaching pump was widened. Indeed, for probe polarisations orthogonal to the bleaching pump, the fibre attenuation was unchanged. The asymmetry of the curve around the 45° axis was due to the small time delay in making the measurements.

In the upper trace of Figure 48, the small signal attenuation of the fibre was measured as a function of probe polarisation 24 hours after the initial pumping at 45°. The results showed a constant loss of 50dB/km independent of polarisation. The partial bleaching initiated by the pump at 45° had been completely reversed.

More detailed discussion of these results is reserved until section 4.4. The results, however, do indicate a three stage photosensitivity process. This is summarised in Figure 49, using the data representing the one eigenaxis pumping of the HB450 fibre at 0.5145μm as an example. Pumping of the virgin fibre (60dB/km), at both 0.5145μm and 0.532μm, had created a metastable state at 92dB/km. This evolved into a more stable state at 130dB/km by decoupling of the fibre from the pumping process. Subsequent pumping at 0.5145μm resurrected the metastable state (which mapped the pump polarisation) until the pump was blocked. The drift back to stability then commenced. The initial loss value of 60dB/km was never again attained. Details of the mechanisms that may produce these effects are discussed in section 4.4

4.3 Photoinduced Polarisation and Refractive Index Measurements

The first experiment undertaken investigated the ability of the linearly birefringent fibre samples to maintain a linear state of polarisation along the fibre eigenaxes, under high cw $0.5145\mu m$ pump powers. The experimental set-up was quite simple and was incorporated into the frequency shifter topologies shown in Figures 26 and 29 of Chapter 3. The input polarisation of the pump was again adjusted with the half wave plate. The polarisation of the transmitted pump was monitored with a Glan Thompson prism polariser and power meter. The transmission axis of the polariser was aligned parallel with one of the fibre eigenaxes. Thus, if the polarisation properties of the fibre (ie eigenaxis orientation) remained intact, the power transmitted through the prism polarizer would have remained constant, independent of input pump polarisation azimuth.

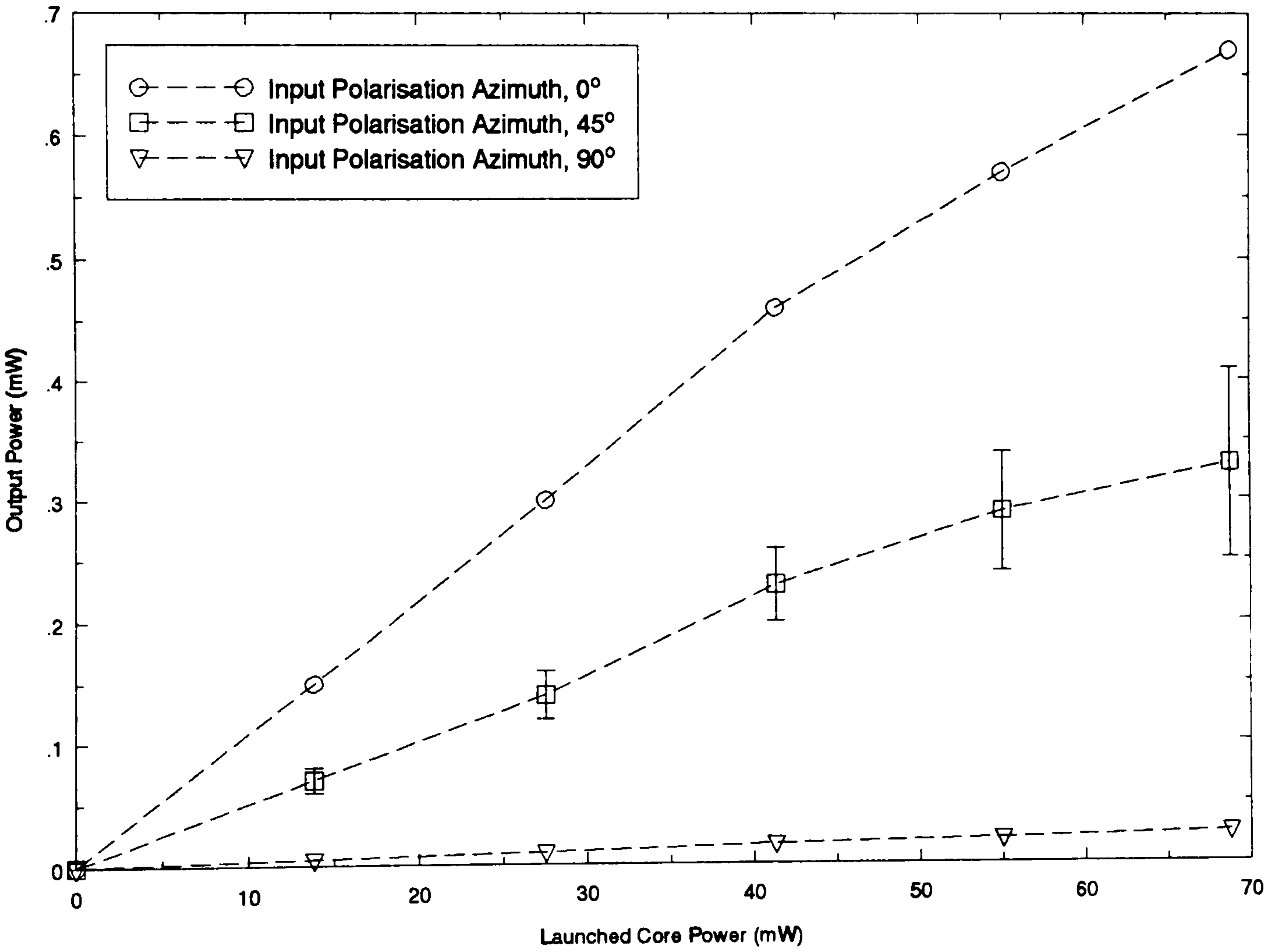

Figure 50: Polarisation Modulation of HB450 Fibre for Increasing Pump Power and Different Input Polarisation Orientations

Figure 50 shows the polarisation modulation results for the HB450 fibre pumped at $0.5145\mu m$ for three input pump polarisations. The Glan-

Thompson prism was aligned with the eigenaxis corresponding to input polarisation azimuth 0°. In the upper trace, the input pump polarisation was aligned parallel with this axis and the output power increased linearly with launched core power as expected. The transmission corresponded to a loss of 100dB/km, the experiment being performed before the maximum loss for that eigenaxis (130dB/km) was attained. The measurements were taken in quick succession before the photobleaching properties reported in section 4.2 took effect. The bottom trace corresponded to light launched initially into the orthogonal eigenaxis and, as expected, showed almost complete extinction. In all polarisation preserving fibres, there will always be a small amount of leakage between modes due to Rayleigh scattering and the effects of fibre curvature (Dakin and Culshaw, 1989; Chapter 8). Again, the small fraction of light that *was* transmitted increased linearly with launch power. The third trace represented the significant result for input light polarised at 45° to both eigenaxes. This was, of course, the experimental arrangement for the single fibre, single input frequency shifter. The *mean* power increased linearly with launch as expected. However, the power was modulated with a period of about one second by the amount signified by the bars of trace. (These are NOT error bars). The modulation increased with launch power as shown. For reasons discussed in section 4.4, pumping at this orientation can induce a small oscillating rotation in the fibre eigenaxis orientation. In this experiment, measurements were taken to deduce trends only. Detailed analysis of the Stokes parameters of the light is necessary to yield exact data on eigenaxis rotation. The results represented by Figure 50 do, however, illustrate why simultaneous SBS was not attained by pumping the single end of the HB450 fibre.

The polarisation properties of the EOTec/HB fibre were similarly measured and shown to remain constant throughout the study. The PANDA fibre was not investigated due to its inherent low SBS gain. The eigenaxes of the EB450 fibre demonstrated some response to the pump polarisation azimuth. The eigenaxes were rotated by up to 10° for launch powers above 100mW. This was clarified by measuring at which orientation SBS threshold was a minimum. Polarisation modulations were small compared with the HB450 fibre but enough, when coupled with the intrinsically poor polarisation maintaining capacity of the fibre (through non-photosensitive effects), to produce output carrier intensity instability.

Changes in polarisation map the *differential* phase changes between the orthogonal eigenaxes in the fibre. To measure direct phase changes within the fibre, from photorefractive mechanisms, the Mach-Zehnder interferometer shown in Figure 51 was employed. As in the photobleaching experiments, the input half wave plate aligned the pump polarisation with one or other of the fibre eigenaxes. A circularly polarised probe from a Helium Neon source was amplitude divided at the input beamsplitter. Thus, in the signal arm containing the fibre sample ($\approx$ 0.9m in length), probe light was launched along both eigenaxes simultaneously. In the reference arm, one mirror was driven over a path length equivalent to a single fringe in the output, by a piezoelectric transducer and function generator. This allowed pseudo-heterodyne processing techniques to be employed at the post-detector stage to ease the signal processing.

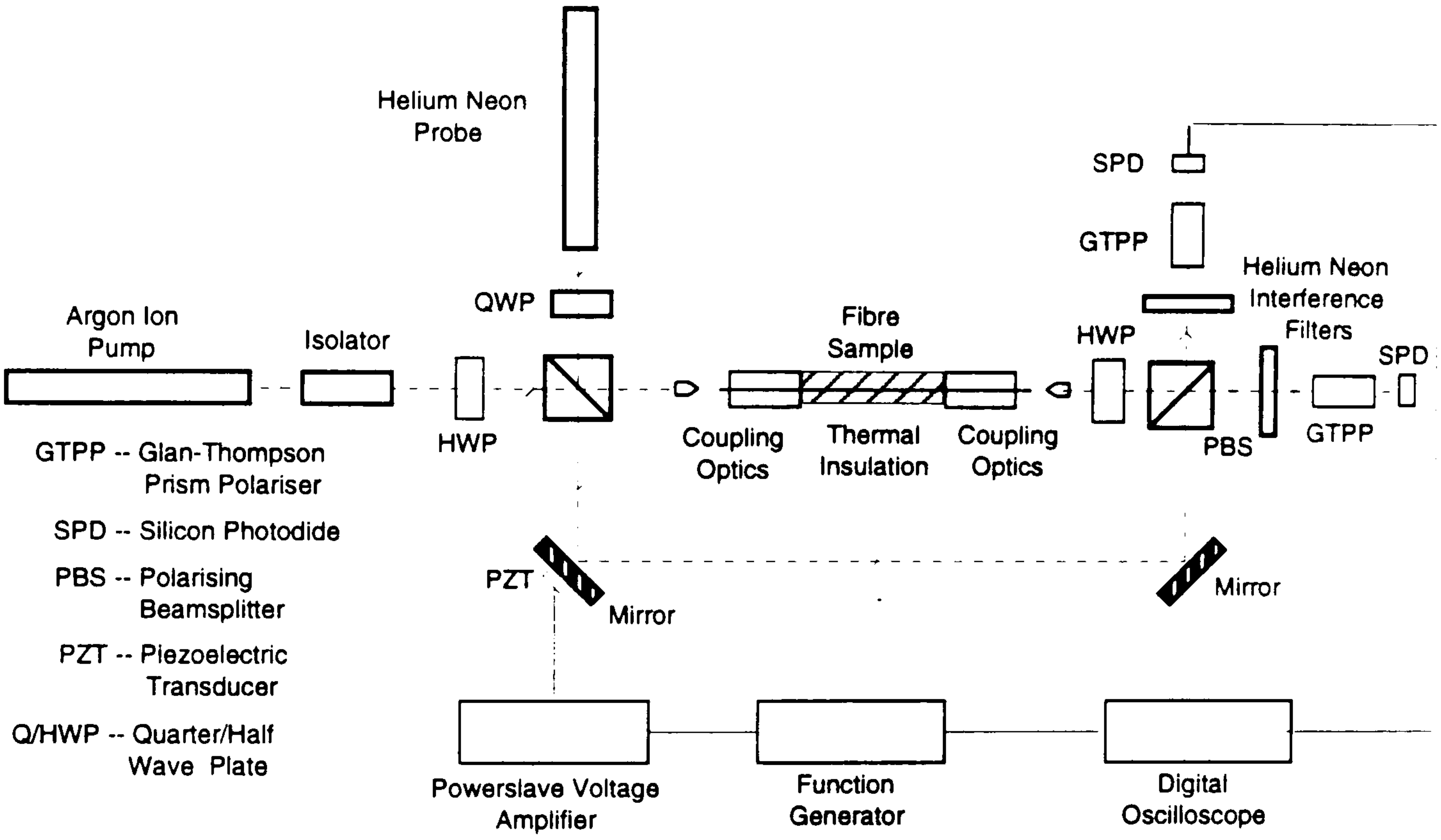

Figure 51: Experimental Apparatus to Measure Direct Photorefractive Changes Within the Fibre

The two probe beams were recombined at the polarising beamsplitter (PBS). A second half wave plate, designed for operation at 0.6328μm, aligned the polarisation azimuths of the fibre eigenaxes with the transmission and reflection axes of the PBS respectively. The pump light was completely extinguished by the two He-Ne interference filters (80% transmittance at 0.6328μm). Since the recombining beams from the interferometer had orthogonal polarisations by the nature of the PBS, fringes were formed by transmission through the prism polarisers. The polariser was rotated to produce optimum fringe visibility at the detectors. The path difference between the two arms was balanced to within 1cm, well within the coherence length of the Helium Neon probe ($\approx$30cm). Circular fringes were obtained at each output with effective visibilities of approximately 70%, reduced from the optimum value by the finite size of the detectors and backreflections in the system. The output of the photodiodes was connected to the digital oscilloscope, triggered from the same function generator that drove the PZT. Significantly, the configuration meant that each detector output mapped the phase change along only one of the fibre eigenaxes. Simple fringe counting from the oscilloscope inferred the phase change directly.

The number of fringe shifts l is related to the measured refractive index change Δn by

$$l = \frac{\Delta n d}{\lambda} \qquad 4.1$$

where d is the fibre length over which the change occurs and λ is the probe wavelength. Since only a finite fraction of the probe beam was guided by the core, the ***absolute*** index change within the core, Δn_c, is related to the measured change by

$$\Delta n_c = \frac{\Delta n}{\left(1 - \exp -(2a^2/r_0^2)\right)} \qquad 4.2$$

where a is the fibre core radius and r_0 the fibre mode radius, corresponding to the exp(-2) point of the Gaussian power distribution. The derivation of this formula is listed in Appendix D. Owing to uncertainties in the uniformity of the modal profile, this expression is at best accurate to ±10% (Hand and Russell, 1990).

The fibre was thermally isolated from the laboratory by enclosing it within a polystyrene insulator. Thermal effects restricted the accuracy of all measurements to within ±0.5 fringe. Using the data presented in Table 1, Chapter 1 for the phase sensitivity of silica fibres to temperature (Akhavan Leilabady et al, 1985), this fringe modulation implied a temperature fluctuation of $\pm 2.6\times 10^{-2}$°C in 0.9m of fibre at 0.6328μm. The system thus demonstrated excellent thermal stability.

Figure 52 shows the photorefractive behaviour of the HB450 fibre pumped with increasing launch powers at 0.514μm. This sample was an offcut of the fibre used in the photobleaching experiment of section 4.2. The index change at 0.6328μm increased linearly with launch power. The change was instantaneous and no further increase accrued even when the fibre was pumped for many minutes. From the graph, a launch power of 100mW induced an index change of 3.42×10^{-6}. Since the fringes displayed on the oscilloscope travel in the same direction as if the fibre had been heated, the photoinduced index change is *positive*. Strictly, in Figure 11, error bars representing the thermally induced index change ($\equiv \pm 5\times 10^{-7}$) should have been displayed. However, these occurred over a slow time scale (several minutes) compared with the index change shown in the graph. On removal of the pump, the core index returned immediately to its original value.

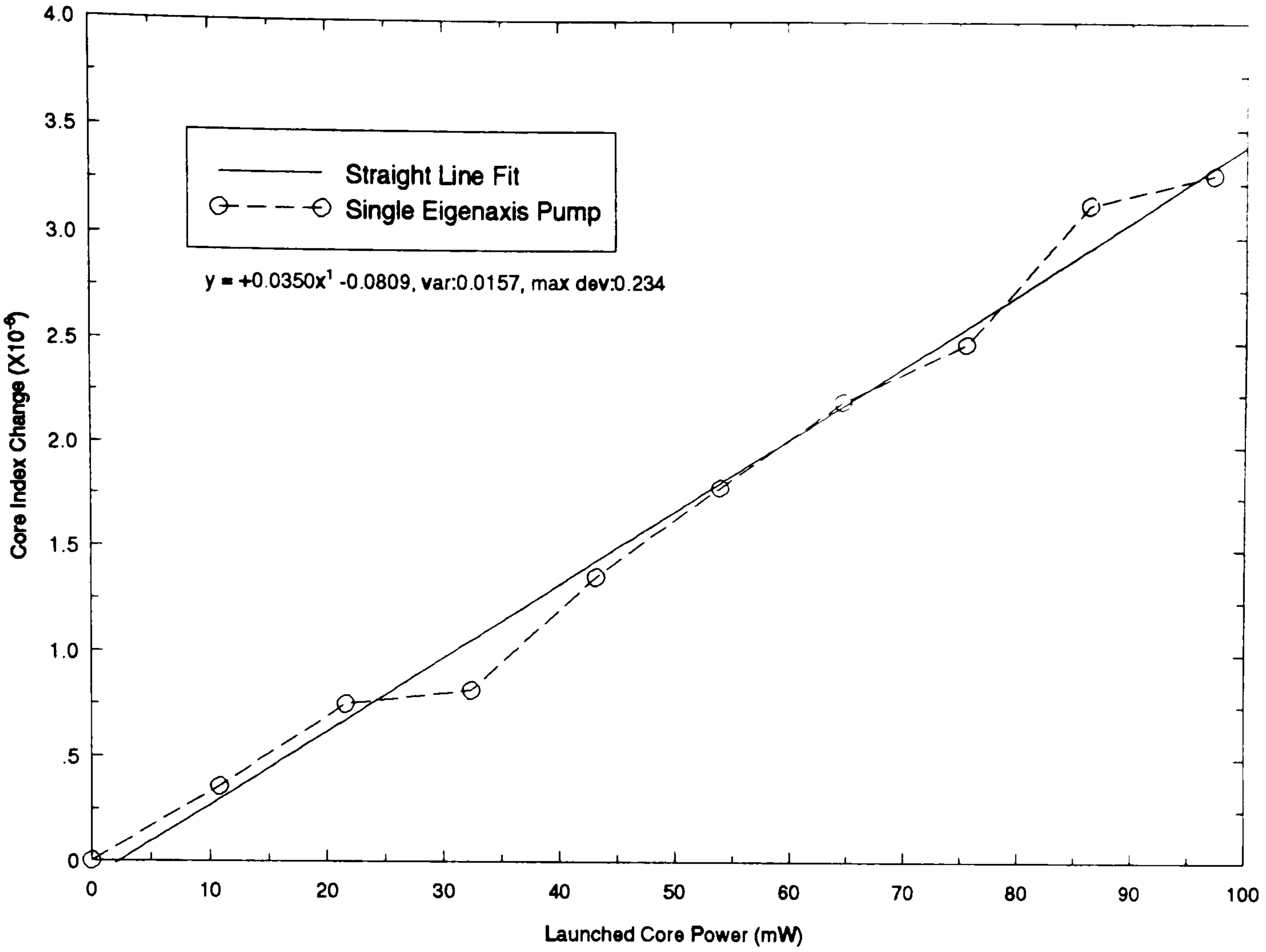

Figure 52: Photoinduced Index Change of HB450 Fibre for Increasing Pump Power

The gradient of the straight line fit (derived from linear regression analysis as part of the available graph plotting routine) allowed direct comparison between different fibre samples. Identical results were obtained on pumping the orthogonal axes of the HB450 fibre at 0.5145μm. The pumping of a virgin sample of HB450 fibre, direct from the manufacturers, again produced a linear index change, with a slightly reduced gradient of 3.1×10^{-8}mW^{-1}. Again no changes to the index were measured with time for even the highest launch powers (100mW). EOTec/HB and PANDA fibres also yielded linear responses with gradients 2.4 and 4.5×10^{-8}mW^{-1} respectively.

No significant differences between the measured core index changes with power were obtained with the different samples measured, in contrast to the attenuation properties. These results are now compared with a selection of photosensitive phenomena reported in the literature.

4.4 Discussion

The partial bleaching of the attenuation-inducing effects described in section 4.2 has been reported for a *pulsed* pump at 0.532μm in bow-tie birefringent fibre (Kanellopoulos et al, 1991). Though the absolute values of attenuation were not quoted, the transmission of a He-Ne probe was enhanced by 150% through the 100m sample. The transmission increase eventually saturated in time for a constant pump power. Increasing the pump correspondingly increased the saturation level. The saturated increase in transmission scaled quadratically with the pump peak power. As for the HB450 fibre in section 4.2, the fibre in this work had previously been subjected to long term irradiation at 0.532μm, hence the higher than expected initial attenuation. Again, as for the HB450 sample, once the light was removed, the bleaching process was reversed and the fibre attenuation relaxed back to its initial state. The time scale for this was noted as weeks rather than days, however. Interestingly, the authors reported that the return to the 'darker' state was accelerated by heating the fibre to 240°C for several hours.

Additionally in the experiments by Kanellopoulos and co-workers, negative core index changes were measured simultaneously with the decrease in the fibre loss. Though the exact results are discussed separately in the second half of this section, the index perturbations do have consequences for the loss measurements. For example, a decrease in the core index lowers the numerical aperture of the fibre which, in turn, depresses the normalised frequency or V-number (equation 2.13) of the fibre. Figure 14 (Chapter 2) demonstrated that lowering V enlarges the effective area of the LP_{01} mode in the fibre core. Thus, the coupling efficiency – determined by the overlap between the Gaussian focussed image of the input light and fibre mode cross-section area – is decreased. This clearly can be misinterpreted as an increase in fibre attenuation. Indeed, in section 4.2, it was assumed that all changes in fibre loss arose directly from attenuation modulation. The error, however, was small. In Kanellopoulos' paper, for example, changes in mode-spot size of up to 2.3% were measured, enough to induce a reduction in coupling efficiency of approximately the same order (we assume). Consider then the experimental results shown in Figure 44 for the HB450 fibre. Over the 200 minutes of the experiment, assume that the coupling efficiency of the He-Ne probe has decreased by 5% (a worst case figure) from its initial measured value of 54% to 49%. Thus, the true saturated attenuation value at 200 minutes would be 30.2dB/km, rather than the 32.5dB/km shown. The photoabsorption mechanism is actually slightly enhanced. Similarly for the measurements at 0.5145μm, where the relative losses are greater, saturation would have occurred at 90 rather than the measured 92dB/km. Thus, strictly, changes in transmission map both attenuation and coupling efficiency perturbations, though the former remains the dominant factor.

Much research effort has been expended in recent years on analysing and understanding the photosensitive mechanisms that induce both the higher losses and bleaching effects in optical fibres. Compelling evidence for a model based specifically on the interplay of the input pump light with germanium (Ge) related defects in fibres has emerged, though the nature of some of the arguments remains hypothetical. Germanium doping of the core is perhaps the most common method of raising the core index to give wave-guiding. Experiments in 'virgin' bow-tie high birefringent fibre (Poyntz-Wright et al, 1988) have shown that the initial high loss induced in germanosilicate fibres by pulsed radiation at 0.47μm scaled quadratically with peak power. Further, the losses continued to rise on blocking the pump and the final attenuation level attained scaled linearly with germanium concentration. The wavelength sensitivity of the absorption creation process was measured in this work and revealed that maximum loss was obtained (for a given fibre type) after initial pumping at 0.48μm, though high losses were also induced for initial pump signals between 0.42 and 0.54μm.

These facts suggested that the precursors to the process were the Ge-Ge or Ge-Si bonds that proliferate in germanosilicate glasses. These bonds are known to possess a characteristic absorption band, peaking at approximately 0.24μm (Friebele and Griscom, 1986) but which extends from 0.22 to 0.27μm. Poyntz-Wright and co-workers proposed, therefore, that these bonds can be broken by Two Photon Absorption (TPA) most efficiently at 0.48μm though as Poyntz-Wright's work demonstrated, any pump in the 0.42-0.54μm range yielded an effect. The bond breakage releases free electrons into the glass matrix and the original constituents of the bond become oxygen-deficient Ge defects in their own right, denoted by GeE$'$, which act as electron hole-traps. The free electrons thus migrate until they are either retrapped at a GeE$'$ site, or are trapped at Ge(1) or Ge(2) dopant sites to form colour centres (Russell et al, 1991b). These sites are also electron traps and are characterised as having 1 and 2 germanium nearest neighbour atoms respectively. (N.B. GeE$'$ defects are often called Ge(3) under the assumption of 3 nearest Ge neighbours). In any case, each colour centre possesses a characteristic absorption spectrum. These are reproduced in Figure 53, together with the Ge-Ge/Si bond spectrum (reproduced from Friebele and Griscom, 1986).

The Ge(1) spectrum is centred on 0.281μm but extends well into the visible. The Ge(2) spectrum is narrower, peaking at 0.213μm. The GeE$'$ defect, though detectable using electron spin resonance which shows an increase in population after exposure to UV or the appropriate visible radiation, displayed no specific absorption band, though one may be situated in the deep UV. It is thought therefore that the migration of free electrons between the

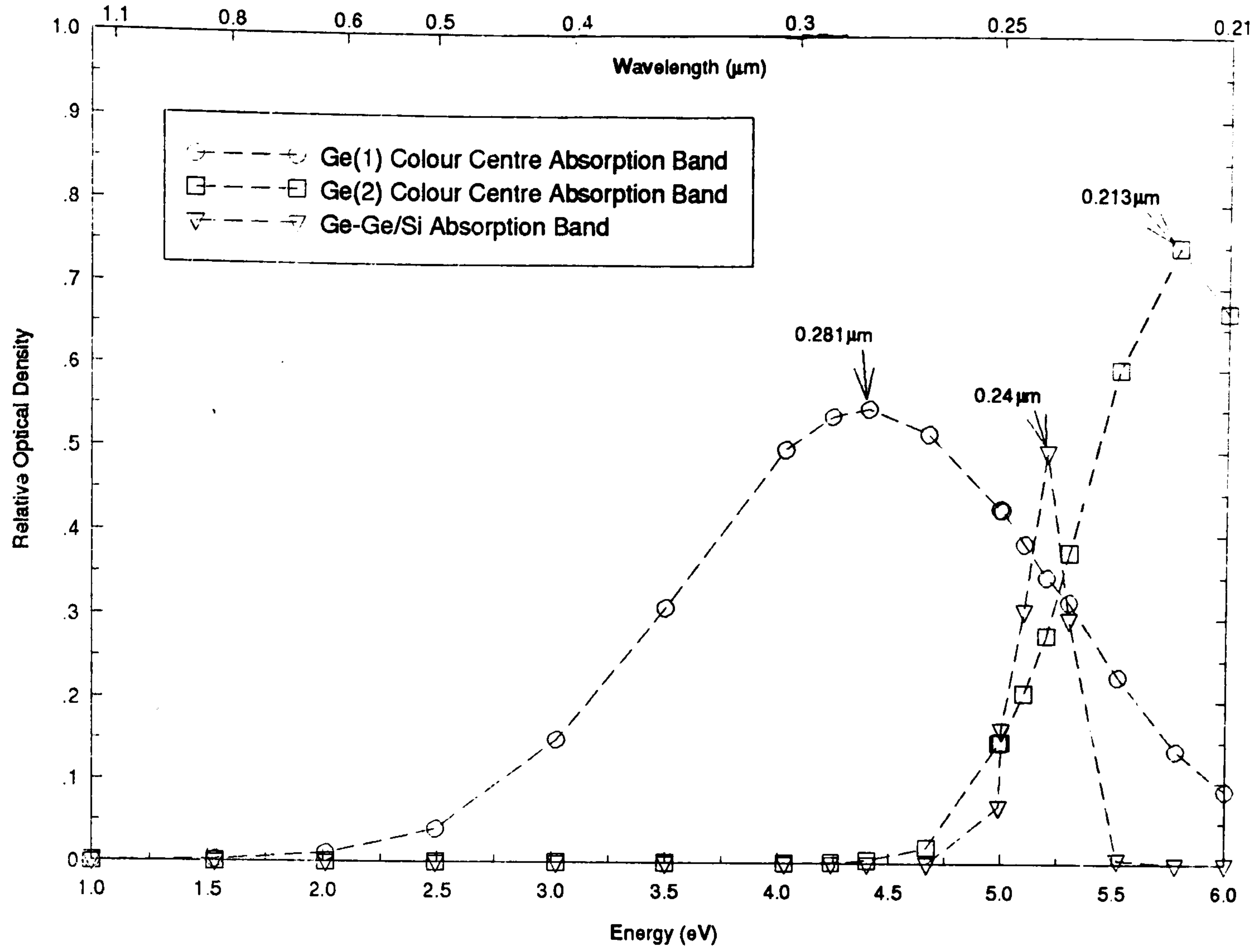

Figure 53: Absorption Spectrum of Germanium Defects in Germanosilicate Glasses

principal defect sites - Ge(1), Ge(2) and GeE′ - either spontaneously or under the influence of pump irradiation (or heat), determines the attenuation properties of the fibre.

The mechanism can be summarised as follows. After the initial TPA-induced bond breakage, electrons are trapped at all three dopant sites. causing the inital surge in loss. After blocking the pump, a spontaneous release of electrons from GeE′ to Ge(1) and Ge(2) sites occurs and the overall loss continues to rise. Once the GeE′ site is depleted of electrons, a transfer from Ge(2) to Ge(1) sites occurs (Poyntz-Wright and Russell, 1989). This latter process was manifested in the present study as the slow increase in loss of the HB450 fibre, eventually saturating at 130dB/km. The optical bleaching seen in the present work and by Kanellopoulos and co-workers, partially reversed the process, as electrons transferred back to the Ge(2) and GeE′ sites, producing the metastable state of 92dB/km in the HB450 fibre. Removal of the pump caused a re-release of electrons back to the Ge(1) sites. The initial Ge-Ge/Si bond breakage was irreversible so the initial low loss state was never again attained.

Though the trends exhibited by the fibres in the present study are consistent with Ge-related phenomenon reported in the literature, some important questions remained unanswered. For example, the EOTec/HB fibre did not exhibit any photosensitive characteristics despite possessing 50% greater Ge concentration than the HB450 fibre according to manufacturer's data. Assuming that this information was accurate, and in the absence of significant levels of other dopants, this suggested that the birefringence formation process within the fibre core was important in defect creation. There is evidence, for example, that GeE′ defect centres are concentrated in regions of high stress gradients (Bardal et al, 1992) such as are present in bow-tie birefringent fibres. Clearly, a more detailed study of the dynamics of the process is necessary to determine the exact cause of the disparity.

A second question concerned the polarisation sensitivity of the photobleaching process that transferred the fibre from a stable to a metastable state. In both SM450 and HB450 fibres, bleaching along a given polarisation direction (in the latter, the fast or slow axis) produced no effect in the corresponding orthogonal axis. Thus, only colour centres whose dipole moments aligned with the polarisation of the incident light released electrons into the glass matrix. Whether the initial TPA defect initiation process was similarly polarisation dependent was not investigated. No evidence for this specific behaviour has been reported in the literature.

In parallel with photoabsorption changes in the fibre, several authors have reported substantive changes to the core index as the defects are created and then partially bleached (eg Hand and Russell, 1990; Kanellopoulos et al, 1991). In the former experiment, direct interferometric techniques were used to monitor the index change in fresh fibre, cw pumped at 0.488μm. The index change mapped the absorption behaviour in that its initial rate of increase scaled as the square of the applied intensity, the initial bond breakage being a TPA effect. Further, as the defect creation process saturated in time, so did the index change, attaining 1.8×10^{-4} at 0.488μm. The change was positive, indicating the creation of defects. In the latter citation, *negative* changes in index up to 4×10^{-4} were recorded since, here, Ge(1) defects were bleached optically (and the attenuation was similarly reduced).

To relate these index changes directly to the attenuation changes has proved difficult. It is well-known that perturbations to the imaginary part of the refractive index (n_I in equation 2.6) produce a corresponding change to the real part through the Kramers-Kronig relation (eg Ashcroft and Mermin, 1981). By considering the bleaching of the 0.24μm absorption band (by breaking the Ge-Ge/Si bonds) and augmentation of the other defect-related absorption peaks, calculations predict an index change saturating at approximately 10^{-6} (Russell et al, 1991b), two orders below the measured value. Two further processes have been proposed by Russell and co-workers in contributing to the index change. The first arises directly from the Ge-Ge/Si bond breaking process which triggers a compaction or density change within the glass, yielding the index change. The second is again Kramers-Kronig related, but through a band edge shift in the deep UV ($\approx 0.18\mu m$) which produces a much greater impact on the refractive index than the relative change in colour centre population.

The direct index change measured in the fibre samples in section 4.3 was also two orders below that recorded in the literature, for equivalent input powers. Potential origins of these results are discussed presently. Before this, returning to the literature, the index changes reported therein have been shown to be birefringent, the slow axis aligning with the input linear polarisation of the exposing radiation. Birefringences up to 10^{-5} have been measured (Russell et al, 1991b) which can result in an unstable output polarisation state in low birefringence fibre. This birefringence characteristic has been proposed for use as a wavelength filter (Russell and Hand, 1990) and, significantly, may explain the polarisation modulation behaviour of the HB450 fibre shown in Figure 50. By exposing high birefringence fibre to linearly polarised light orientated at 45° to the eigenaxes at the photosensitive wavelength, the induced birefringence follows the major axes of the pump polarisation state as it propagates along the fibre. The *net* birefringence (intrinsic plus induced) thus rocks to and fro over the beat period of the fibre. Thus, phase-matched power coupling between the original orthogonal polarisation states at the writing wavelength occurs (Russell and Hand, 1990). In Figure 50, for light launched along either eigenaxis, additional birefringence did not perturb the output polarisation state of the fibre (and only would in the rare instance of the induced birefringence completely cancelling the intrinsic birefringence). Thus, in the upper and lower traces of Figure 50, no modulation to the output polarisation was seen. For light launched at 45°, however, a small rotation of the axes can occur through the above effect. This modified the output polarisation state as the effect grew, yielding periodic modulation of the centre trace of Figure 50.

The measured linearity between the core index change and launched core power (eg Figure 52, section 4.3) was less easily explained. For the fibres studied, positive index changes of between 2.4 and 4.5×10^{-6} were measured for 100mW launched core power. Three potential sources were considered.

(a) From equation 2.29 (chapter 2.3.2), a process based on the Kerr effect would yield an index change, Δn,

$$\Delta n = \frac{n_2 P}{A_{eff}} \qquad 4.3$$

where n_2 equals $3.2\times10^{-20}\mathrm{m}^2\mathrm{W}^{-1}$ in fused silica. For a power of 100mW and effective area, A_{eff}, of $4.9\times10^{-12}\mathrm{m}^2$ for HB450 fibre, the Kerr induced index change is approximately 7×10^{-10}, much less than that measured.

(b) The TPA-induced Ge-Si/Ge bond breakage mechanism was considered. Figure 52, however, showed no quadratic power dependence expected for a TPA effect. Further, the index changes were instantaneous (within the response time of the system) and did not grow, or show any tendency to saturate, in time. The results were also independent of whether the HB450 sample was fresh or had been pumped previously. Thus, the photobleaching related mechanism was eliminated.

(c) The effect on refractive index on the localised core heating due to the light itself was considered. The temperature rise, $\Delta\mathcal{T}$, in the core from an optical power P is given by (Hand and Russell, 1990):

$$\Delta\mathcal{T} = \frac{\alpha P}{2\pi k'} \ln\left(\frac{r_f}{r_o}\right) \qquad 4.4$$

where r_f is the fibre cladding radius, r_o the fibre mode radius, α the attenuation coefficient (units of m^{-1}) and k', the thermal conductivity, equates to $9.2\mathrm{Wm}^{-1}\mathrm{K}^{-1}$. For HB450 fibre, r_f was 62.5μm, r_o 1.24μm and α varied from $1.4\times10^{-2}\mathrm{m}^{-1}$($\equiv$ 60dB/km) in fresh fibre to $3\times10^{-2}\mathrm{m}^{-1}$($\equiv$130dB/km) in previously pumped samples. Even taking the higher loss value, this predicts a thermal rise of 3×10^{-4}K for 100mW incident power. For silica glass, the temperature coefficient of refractive index is 9.9×10^{-6}/°C at 0.6328μm and room temperature (Malitson, 1965). Thus, a temperature rise of 3×10^{-4}K produces an index change of 3×10^{-9}, again three orders below the measured value. The source of our measured index change was thus unknown.

A full understanding of the specific role of Ge related and other defects with respect to both attenuation and refractive index perturbations has not yet emerged. Defects, other than the Ge(n) species described above, may play some role. These mechanisms are interlinked with two further processes exciting much interest in the optical fibre community, namely the production of in-fibre Bragg gratings (for sensing and signal processing applications) and second harmonic generation in the core of photosensitive fibre. A detailed resumé of these mechanisms is beyond the scope of this discussion (for further details consult, for example, Ouellette et al, 1991 and the references therein). However, what *can* be concluded from the studies reported in this chapter is that by pumping fibres which contain significant levels of Ge concentration (ie $> 1\%$ with the exception of the EOTec/HB sample) in the 0.42-0.54μm region, irreversible changes to fibre transmission were induced. In the context of SBS, these significantly raise the SBS threshold and simultaneously degrade the pump/Stokes conversion efficiency. Alternative SBS systems which take up these themes to reduce the power requirements of SBS systems are discussed in Chapter 6.

4.5 Summary of Principal Results

Pump induced attenuation and polarisation perturbations to the fibres used in the study have been reported. In particular, the attenuation of the HB450 and SM450 fibres increased significantly after pumping with high power levels (in excess of 100mW) of ArI 0.5145μm radiation. For the HB450 fibre, the loss rose from 60 to 130dBkm^{-1}. For the SM450 fibre, the attenuation increase saturated at 51dBkm^{-1} from an initial 32dBkm^{-1}. This 'dark' state was partially bleached by further pumping at the same wavelength, a process that was sensitive to pump polarisation. The high attenuation levels returned, however, once this additional pumping was curtailed. The EB450 demonstrated a less pronounced attenuation change whilst three fibres - the EOTec/HB, the EOTec/TW and PANDA samples - were immune to such effects.

In contrast, measurement of absolute refractive index changes with input pump power showed little variation between the six samples. The birefringent properties of the HB450 fibre were modified, however, by orientating the pump polarisation at 45° to the fibre eigenaxes. This prevented the fibre from being successfully used in the single fibre, frequency shifter systems of Chapter 3.

The trends exhibited by the photosensitive fibres, with regard to attenuation, were generally consistent with germania related phenonomena reported in the literature. A TPA-based mechanism creates germania defects in the fibre core which, in turn, modify its absorption characteristics. The exception was the EOTec/HB fibre which showed no sensitivity, despite possessing similar germania concentration to the HB450 fibre. Overall, therefore, in order to minimise photosensitive effects on SBS systems, the germania concentration within the fibre core should be minimised and pump wavelengths in excess of 0.54μm utilised.

5 Stimulated Brillouin Scattering Sensor Systems

5.1 Introduction and Overview

In this chapter, the SBS sensing systems investigated during the study are described. The sensor types fall into two categories, both of which evolved from work previously reported in this thesis:

(a) Sensors based on direct modulation of the SBS carrier signal by the measurand

(b) Sensors based on sustained oscillations previously described in section 3.4.1.

The majority of the work concentrated on the first and utilised the heterodyning concept successfully demonstrated in Chapter 3 for the optical frequency shifter. The principles are described in section 5.2. Two systems were investigated for this concept, specifically for temperature measurement:

(i) a 'quasi-point' system, in which the sensor 'head' comprised the *whole* fibre sample, is reported in section 5.2.2 and

(ii) a multiplexed sensor system in which a single fibre was used to interrogate several sensing regions simultaneously. The results are presented in section 5.2.3.

Such 'frequency-out' sensors offer the advantages of absolute measurement and potentially high signal-to-noise characteristics compared with many other types of sensor.

The theoretical background to both (i) and (ii) is described in section 5.2.1. The experimental results are then placed in the context of other point, multiplexed, and distributed systems based on Brillouin scattering that have been cited in section 5.2.4. Development of these techniques to sense other measurands such as strain are described. In this work, only single source sensing systems have been considered in order to minimise the complexity of the system for aerospace applications. The significance of this in terms of the compromise to system performance is also discussed in section 5.2.4.

The second sensor approach investigated arose directly from the observations of sustained oscillations previously described in the SBS systems. The oscillation spectrum in the frequency domain provided a direct measure of the fibre length, information which is pertinent to distributed sensors. Experiments investigating the basic properties of the oscillations and two simple sensor schemes are presented in section 5.3.2, together with a brief discussion on the viability of the approach.

The principal results of the sensor study are then summarised in section 5.4.

5.2 SBS Sensor Schemes Based On Optical Heterodyning

5.2.1 Theory

The sensing scheme based on direct frequency modulation of the Stokes signal used many of the basic ideas developed in Chapter 3 for the frequency shifter. In Chapter 3, two SBS signals were generated independently along a single fibre (in the majority of examples) and optically mixed externally to produce a carrier of up to 11MHz. In the sensors investigated in this chapter, *two* fibre systems were generally used, each producing a Stokes signal (For a given high birefringent fibre, only one of the eigenaxes was pumped to minimise power requirements). One fibre was maintained at a constant temperature – the reference fibre – whilst the second was heated or cooled, as appropriate. The two Stokes signals were again mixed remotely to produce a carrier within the frequency response range of the conventional optical detectors. Using the nomenclature of Chapter 3, the basic carrier frequency (with no temperature modulation) is given by

$$\delta\nu_B = \left|\nu_{B,ref} - \nu_{B,sen}\right| = \frac{2V_A n_{ref}}{\lambda} - \frac{2V_A n_{sen}}{\lambda} \qquad 5.1$$

Subscripts ref and sen refer to reference and sensor fibres respectively rather than the fast and slow axes as in Chapter 3. The change in output frequency with respect to temperature, $\mathcal{T}$, is the change in Stokes signal from the sensor fibre only and is therefore given by

$$\frac{d}{d\mathcal{T}}(\delta\nu_{B,sen}) = \frac{2}{\lambda}\Big(n_{sen}\frac{dV_A}{d\mathcal{T}} + V_A\frac{dn_{sen}}{d\mathcal{T}}\Big) \qquad 5.2$$

This forms the basis of both the point and multiplexed sensors in the present study. Clearly, $\mathcal{T}$ could represent any applied measurand. In section 5.2.2. a differential sensor is reported in which both SBS signals were generated along the two orthogonal axes of the birefringent fibre. The output here took the form

$$\frac{d}{d\mathcal{T}}(\delta\nu_B) = \frac{2}{\lambda}\frac{d}{d\mathcal{T}}\Big(n_s V_A - n_f V_A\Big) \qquad 5.3$$

where s and f again refer to the slow and fast axes respectively.

The multiplexed systems of section 5.2.3 reverted to the two fibre reference/sensor pairing. In principle, each sensing region along the fibre should emit a unique Stokes signal whose frequency is proportional to the temperature (for example) of that region. Thus, for l sensing regions, l basic output carriers are produced:

$$\delta\nu_{B,l} = \frac{2V_A n_{ref}}{\lambda} - \frac{d}{dT}(\frac{2V_{A1}n_1}{\lambda}) \; ; \; \frac{2V_A n_{ref}}{\lambda} - \frac{d}{dT}(\frac{2V_{A2}n_2}{\lambda}) \; .... \qquad 5.4$$

$$.... \; \frac{2V_A n_{ref}}{\lambda} - \frac{d}{dT}(\frac{2V_{Al}n_l}{\lambda})$$

Terms produced via Four Wave Mixing (section 2.3.3) have been ignored. More significantly, terms arising from the intermixing of the carriers from the different sensing regions have been neglected. Strictly, these latter terms should be included so that, for l sensing regions, a total of $l(l+1)/2$ carriers are produced.

In assessing theoretically the individual capability of a fibre sample to sustain several sensing regions, it was assumed that a single pumping source was available and the theoretical approach described in section 2.4.1 was applied. Equations 2.59(a) and (b) were used to obtain $P_s(z)$ and $P_p(z)$, the Stokes and pump powers respectively as functions of fibre length. In particular, the variation in $P_p(z)$ with input pump power, $P_p(0)$, was calculated. The principal question to be addressed was at what value of z did $P_p(z)$ fall below P_B^{thr}, the SBS threshold power of the fibre. This factor determined the multiplexing capability of the sample since a length of fibre will only support SBS provided the pump power entering that length exceeds P_B^{thr}. The results of these calculations, together with the resultant multiplexing experiments, are described in section 5.2.3.

5.2.2 Quasi-Point Sensor Systems

The basic system used to investigate sensors is shown in Figure 54 and was identical in most respects to the dual fibre, dual input topology depicted in Figure 29, Chapter 3. The whole of the sensing fibre was heated or cooled in an oven or refrigerator as appropriate and the temperature of the sample independently monitored via a thermocouple. The Stokes signal was then mixed with that generated from the reference fibre which was maintained at constant temperature using insulating materials. The resultant beat signal generated at the high speed detector was a function of the temperature along the *total length* of the sensor fibre. Though single measurement sensors are usually denoted as 'point' sensors, the sensor spatial resolution in this system was determined by the exact distribution of the whole length of the sensing fibre and, hence, the system was denoted as a 'quasi-point' sensor.

Since six fibre samples were available in the study, there were up to 30 reference/sensor fibre combinations possible for the system of Figure 54. How-

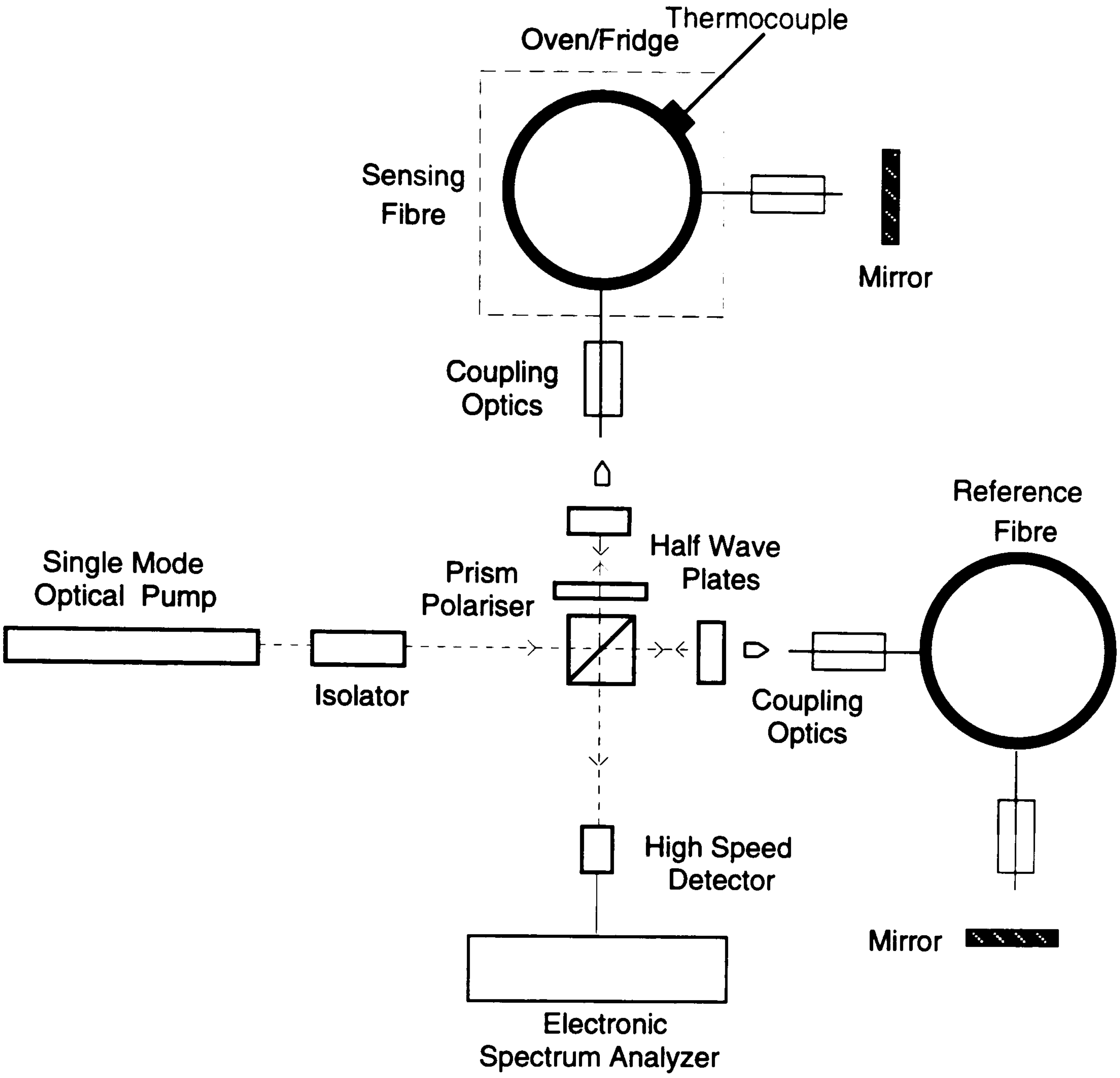

Figure 54: Experimental Demonstration of the 'Quasi-Point' SBS Sensor

ever, as was demonstrated in Chapters 3 and 4, certain samples were unsuitable for both this and the multiplexing work that followed. Both HB450 and SM450 samples were excluded due to photosensitivity whilst the high SBS threshold of the PANDA fibre also rendered this inappropriate. Further, the disparity in properties of the EOTec/TW fibre from the manufacturer's specifications meant that only two fibres – the EB450 and EOTec/HB samples – were used in the sensor work. The mean carrier obtained on mixing the Stokes signals from these fibres when both were pumped by the Argon Ion laser at 0.5145μm in the laboratory ($\mathcal{T}$=25.5°C) was centered on 135.6MHz (Table 6, Chapter 3). The response of both fibres to temperature was now examined.

Figure 55 shows the output beat frequency of the system plotted against temperature with the EOTec/HB fibre maintained at constant temperature and the EB450 fibre as the sensor. Over the temperature range shown (5°C to 50°C), a linear relationship between beat frequency and temperature was demonstrated. The gradient was 4.3±0.5MHz°C^{-1}. The square on the graph at a given temperature represented the mean frequency measured off the spectrum analyzer. The carrier was still modulated due to the nonlinear dynamics of the process discussed in section 3.5. The magnitude of the vertical error bars represented twice the standard deviation of this modulation (typically ±13MHz). Thus, in theory, the instability limited the sensing resolution to ±3°C. However, for all measurements, the *mean* frequency was centred within ±8MHz of the straight line fit which indicated that the averaging process undertaken at the post-detector stage improved the resolution to ±2°C. The horizontal error bars are the measurement error associated with the thermocouple. Thermocouple readings were made at three separate points along the fibre.

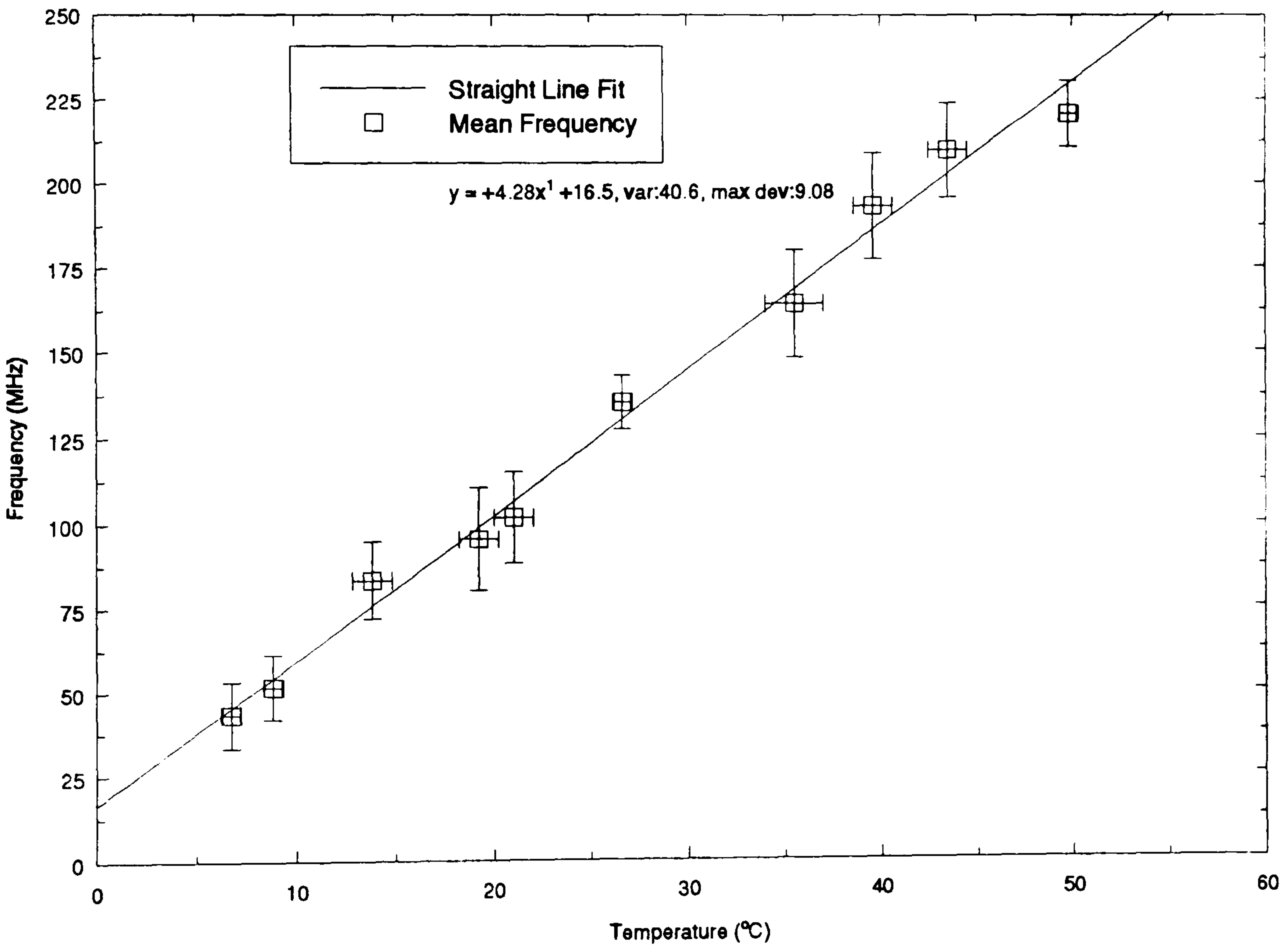

Figure 55: Output Beat Frequency against the EB450 Fibre Temperature Using EOTec/HB Fibre as the Reference

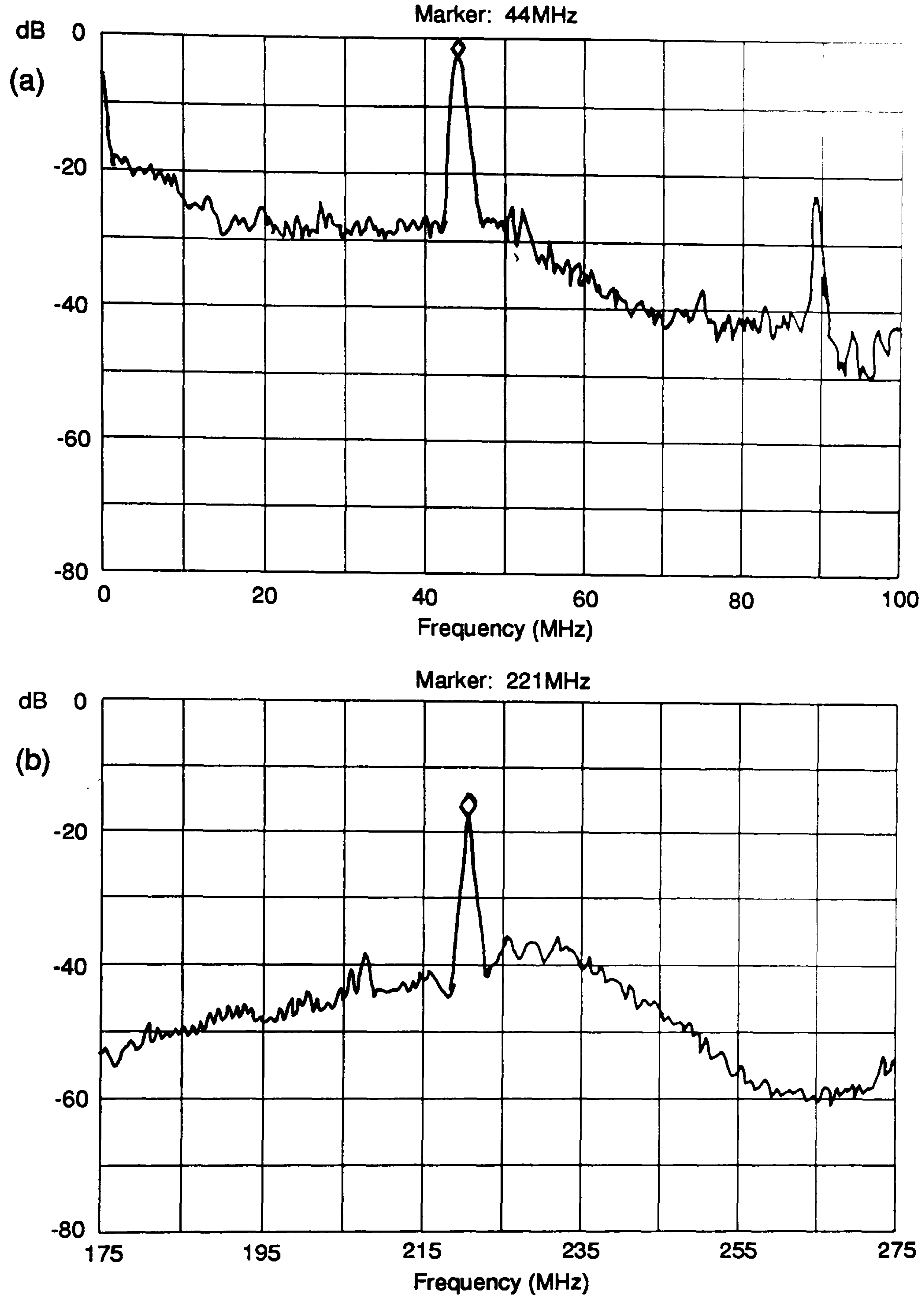

Figure 56: Output Spectra From the 'Quasi-Point' Sensor for the EB450 Fibre at (a) 6.5°C and (b) 50°C with EOTec/HB as the Reference

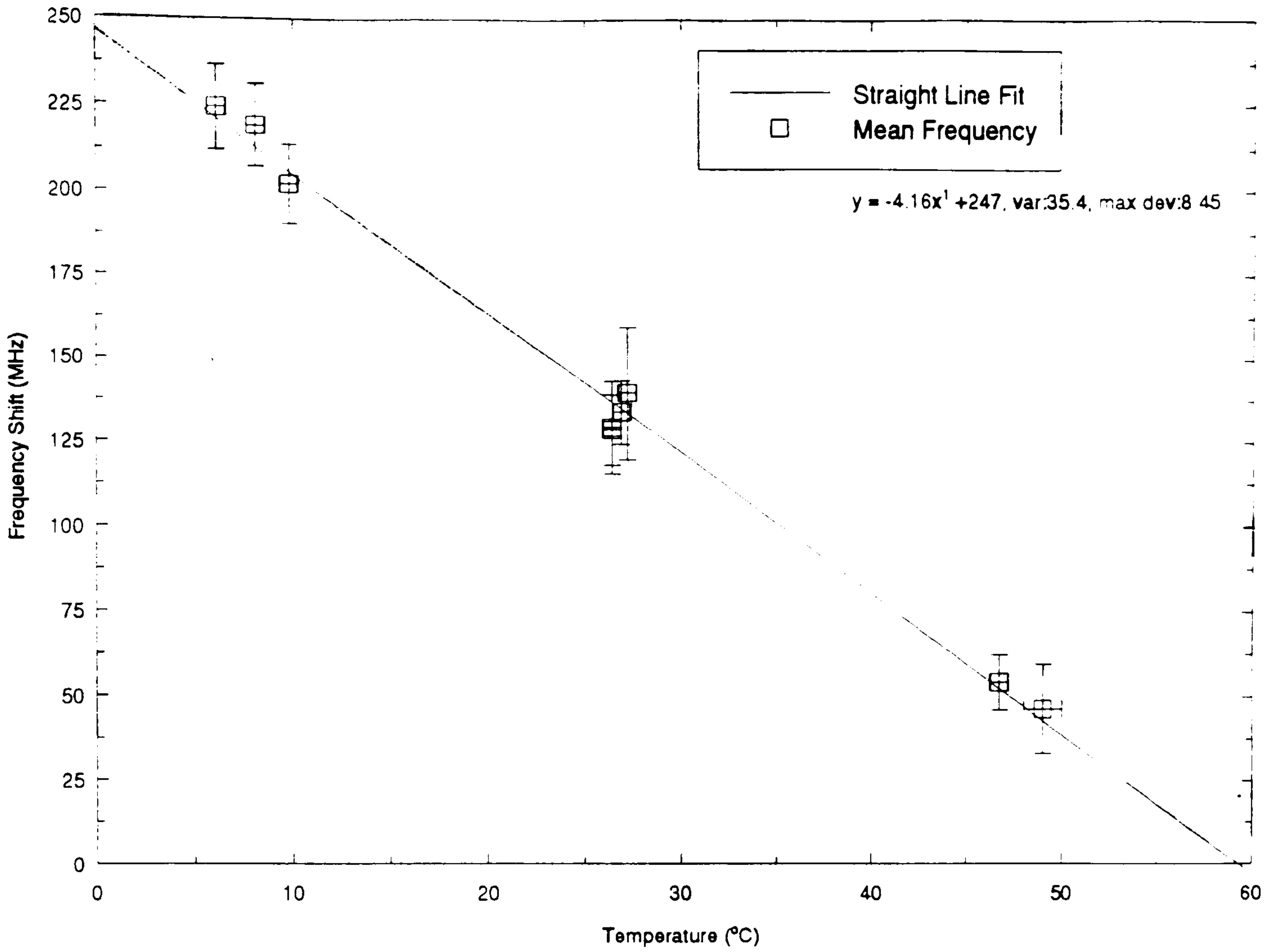

Figure 57: Output Beat Frequency against the EOTec/HB Fibre Temperature Using the EB450 Fibre as the Reference

Figure 56 shows the output signals as displayed on the electronic spectrum analyzer. These are

(a) a carrier centred on 44MHz, corresponding to a temperature, of the EB450 fibre, of 6.5°C. Note the presence of a harmonic at ≈89MHz associated with Four Wave Mixing.

(b) a carrier at 220.8MHz, corresponding to a temperature of 50°C.

In both (a) and (b), the broadband spectrum previously discussed in Chapter 3 recurred.

The fibre samples were then interchanged and a similar set of experiments performed. Figure 57 summarises the results. Again, a linear relationship between beat frequency was obtained over the 5 to 50°C temperature range. The gradient was measured as -4.2±0.5MHz°C^{-1}. The two fibres therefore possessed very similar thermo-optic coefficients. As expected, the slope of the curve was the opposite to that in Figure 55 and was consistent with the manufacturer's data on germanium composition. In Appendix C, the relative core concentrations of Ge are listed as 7.5±1% and 6.5±0.5% respectively for the EOTec/HB and EB450 fibres. From Table 4, section 2.4.2. and Tkach et al (1986), the basic Stokes frequency, ν_B, of the EOTec/HB fibre was less than the EB450 fibre, all other parameters being equal. As the latter was heated (Figure 55), its Stokes signal increased (through a positive $dn/d\mathcal{T}$ and $dV_A/d\mathcal{T}$) and the resultant beat frequency increased further with temperature. In Figure 57, the opposite was true as the EOTec/HB Stokes signal converged to the EB450 value. Thus, the values of Ge concentration supplied from the manufacturers appeared consistent.

In section 3.5, it was shown that the introduction of external optical feedback (in the form of undepleted pump power) reduced the carrier frequency instability (eg Table 7). In the context of sensors, this clearly offered the opportunity to enhance the measurand resolution further. Thus, using the mirrors shown in Figure 54 (effective reflectivity ≈30%), undepleted pump was relaunched first into one and then both fibre samples. (The EB450 fibre was used as reference, the EOTec/HB as sensor.) Again, a consistent 15% reduction in carrier frequency modulation was observed, though this appeared independent of input power and also independent of whether either one or two fibres were supporting feedback. The former was in accord with the results for the frequency shifter as was the noted reduction in the broadband spectrum. The decrease in carrier modulation was consistent across the temperature range and was equivalent to an improvement in temperature resolution of ±0.5°C to ±1.5°C.

The system shown in Figure 54 was analogous in many respects to a two beam interferometer in which the optical phase difference between a signal and reference arm is converted to an intensity modulation. In a differential fibre interferometer, both signal and reference arms share one fibre, typically the two orthogonal eigenaxes of birefringent fibre. The SBS analogue of such a sensor is, of course, the single input, single fibre, frequency shifter arrangement (Figure 26, Chapter 3). An experiment was therefore undertaken to measure the temperature response of the generated carrier for the EOTec/HB fibre in this arrangement. Table 1 in Chapter 1 lists the measured sensitivity of fibres in direct and differential interferometric arrangements to strain and temperature. Specifically, these are measures of dn/di where i is the measurand. For both, the differential system was approximately two orders of magnitude less sensitive than the direct systems. Thus, for the 'differential' SBS system, a similar result would be anticipated, assuming that $dn/d\mathcal{T}$ was the major source of the Stokes frequency change. The temperature sensitivity would then become ≈43kHz°C^{-1}. Attempts to measure this proved futile, however, due to the comparitively large modulations of the carrier even in the presence of feedback (±6.8MHz). This experiment illustrated the limitation imposed on the SBS process by the nonlinear dynamical feedback effects. The source of the thermal response of the beat frequency and a general comparison with the literature on the subject of SBS for sensors is discussed in section 5.2.4.

5.2.3 Multiplexed Sensor Systems

In the multiplexed study, as in the previous section, only the EB450 and EOTec/HB samples were suitable for use in the experiments. The fibre lengths were, respectively, 190m and 400m. The EOTec/HB therefore had the potential to support more, individual, sensing elements and so was selected for the sensing channel, whilst the EB450 fibre again provided the reference signal. Equations 2.59 from Chapter 2 were evoked to obtain the variation in pump power along the EOTec/HB fibre length. This was to theoretically determine the number of sensing elements the fibre could support. The results are shown in Figure 58 for increasing pump power values (50, 100 and 150mW) at 0.5145μm up to 40m into the fibre.

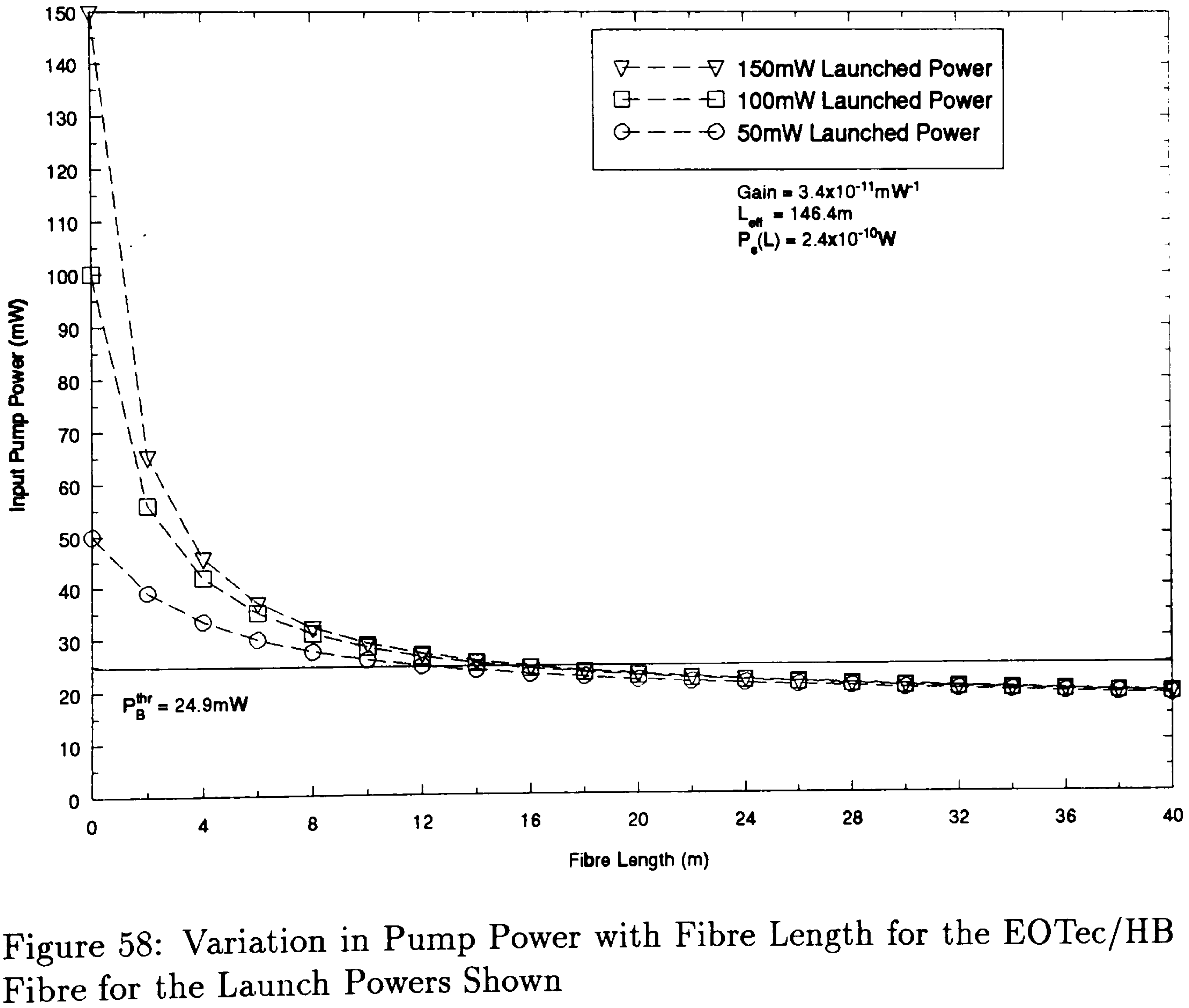

Figure 58: Variation in Pump Power with Fibre Length for the EOTec/HB Fibre for the Launch Powers Shown

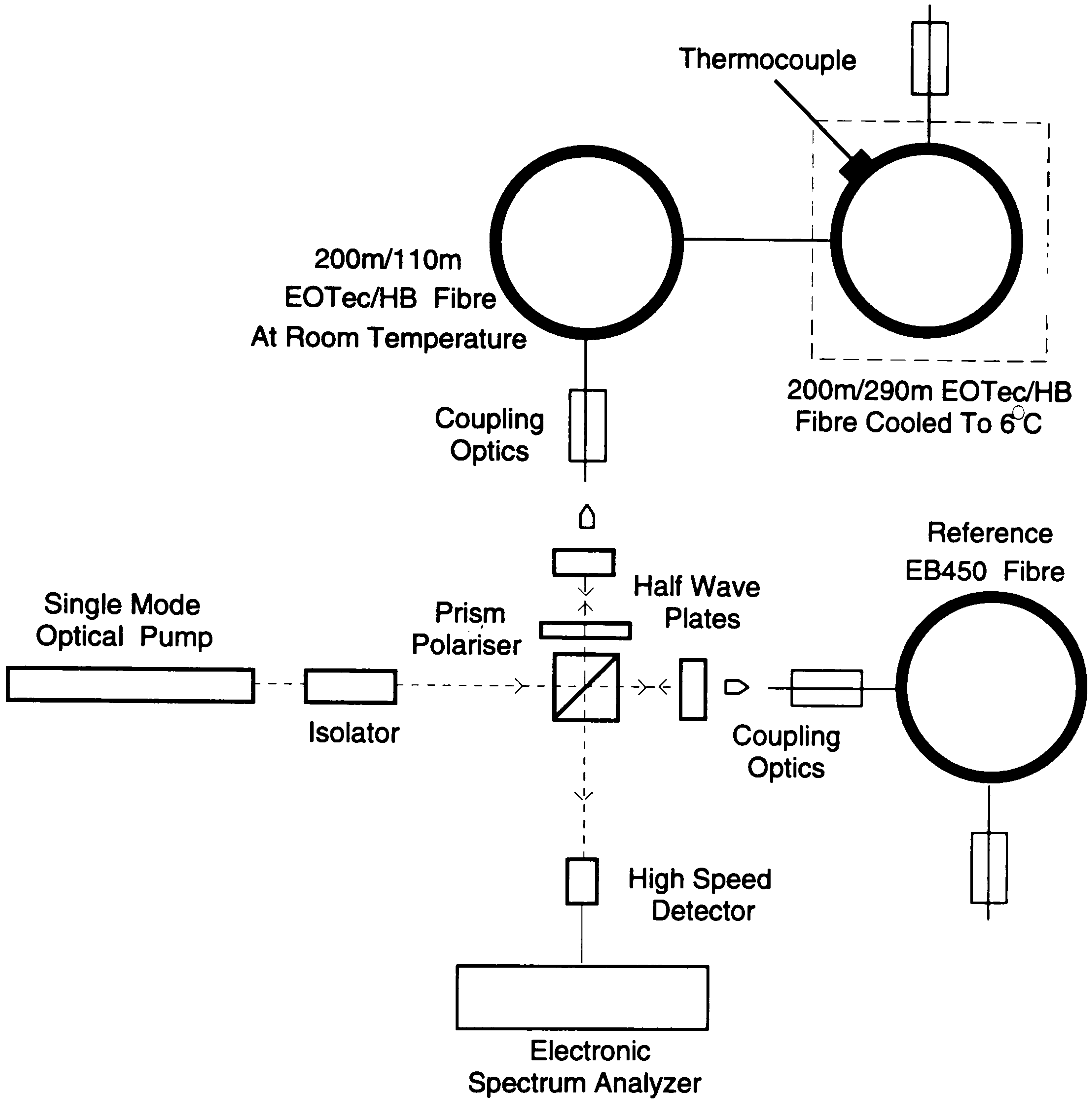

Figure 59: System Demonstrating the Multiplexing Capabilities of a Single Input Sensing Arm

The SBS threshold for the EOTec/HB fibre was 24.9mW, from equation 2.39, using the gain value measured in section 3.4.1. The pump/fibre interaction length, L_{eff}, from the earlier loss measurements, was 146.4m. The output Stokes signal, $P_s(0)$, and pump, $P_p(400)$, were also consistent with the experimental findings of section 3.4.1. For all three curves, the pump rapidly decayed as it propagated along the fibre. Indeed, the distance into the fibre at which the pump decreased to the threshold value, P_B^{thr}, increased from only 12m for 50mW input to 15m for 100mW and 16m for 150mW input. The output pump value at 400m was approximately the same for all three input pumps (1.9mW) so decay of the pump was much slower outside the initial 40m region. The appropriate parameters for the EB450 fibre were inserted into equations 2.59 and the programme re-run to investigate whether this rapid decay was a feature of the EOTec/HB fibre only. The same trends were evident including the rapid depletion of the pump within the fibre. This suggested that for a single input fibre system, only one Stokes signal would be produced. Hence, a multiplexed system would yield one sensing element per input. Experiments were undertaken to investigate this further.

The apparatus is shown in Figure 59, a relatively simple extension of the quasi-point sensor of Figure 54. With the EB450 fibre as reference, the input half (200m) of the EOTec/HB fibre was initially maintained at room temperature whilst the second half was cooled to 6°C. For all input pump powers available from the Argon Ion source (up to 400mW), only one carrier was obtained in the output, centered on 136MHz and characteristic only of the portion of the EOTec/HB fibre at room temperature. This is in accord with the observation from the theoretical analysis.

In a second experiment, only 110m of the EOTec/HB fibre was exposed to room temperature (ie a fraction of its interaction length), whilst 290m was refrigerated to 6°C. Again, only a single carrier was generated. The frequency was, however, centered on 160MHz (again with a ±10MHz modulation) which was equivalent, using Figure 57, to a temperature of 21°C. This is clearly an *intermediate* temperature between the cooled portion and room temperature. Now, L_{eff}, the interaction length of the fibre, was 146.4m. 110m of the fibre (≈75% of the interaction length) was heated to 25.5°C. Assuming that

(i) dn/dT was again the dominant mechanism for the frequency change,

(ii) the refractive index of the core at room temperature was n_0 and

(iii) dn/dT was linear over the temperature range

then the index of the core at 6°C, n_1, would have been

$$n_1 = n_0 - 19.5\Delta n \qquad 5.5$$

where Δn is the change in refractive index per unit temperature. Thus, the *average* refractive index across the interaction length, n_{av}, in this experiment is

$$n_{av} = \frac{3n_o + n_1}{4} = \frac{3n_0 + n_0 - 19.5\Delta n}{4} = n_0 - 4.9\Delta n \qquad 5.6$$

This was equivalent to a temperature of 20.6° over the interaction length. The carrier, therefore, appeared to map the *average* temperature across L_{eff}.

The fibres were interchanged again and the experiment repeated with the first 80m of the EB450 fibre (L_{eff} =108m) at room temperature with 120m cooled. The result was again repeated in terms of the carrier mapping

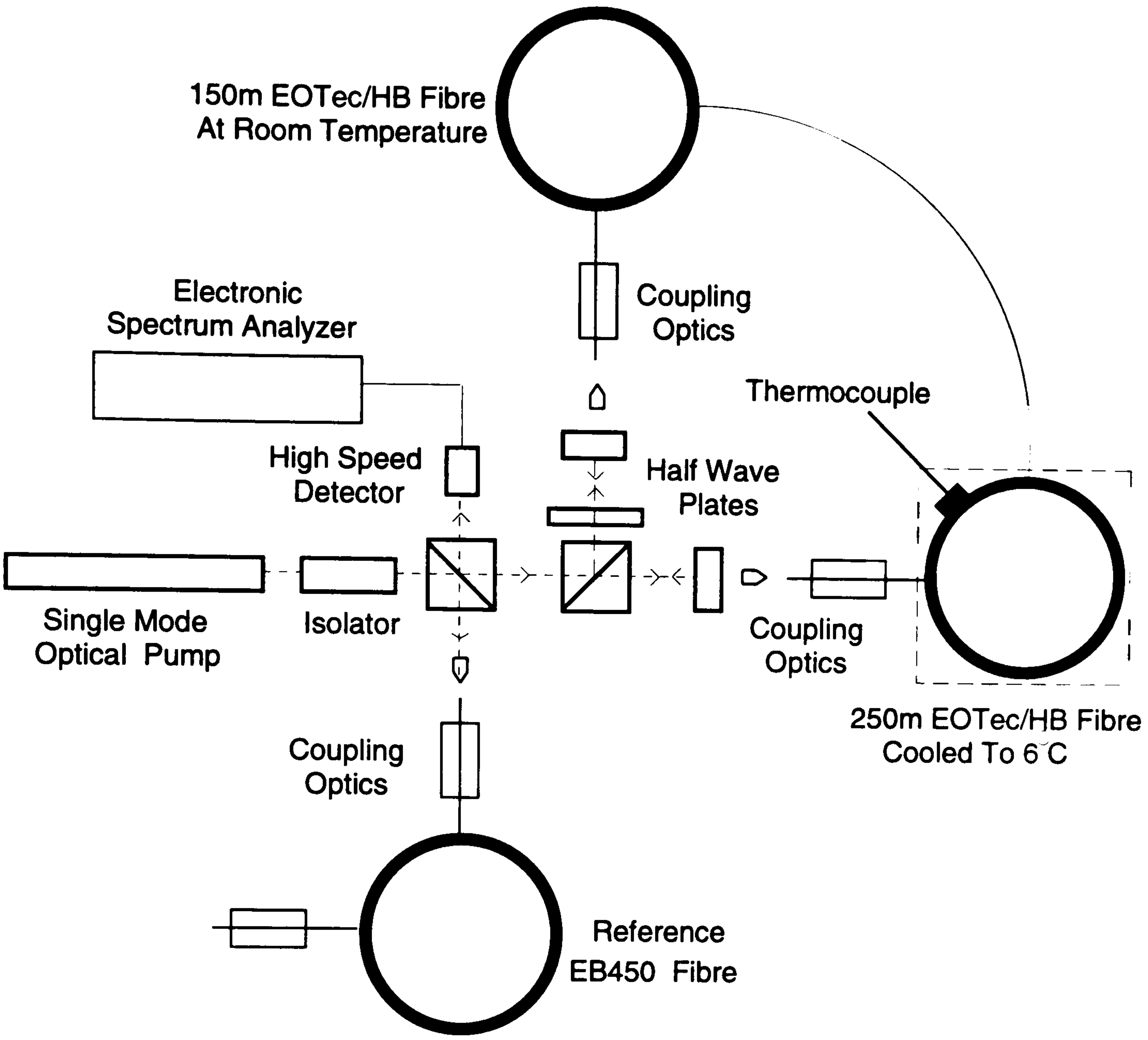

Figure 60: Experimental Configuration of a Two Element Multiplexed Array

the average temperature over the fibre interaction length. From these initial results, it was deduced that

(a) for a single pump, single input SBS system, only one Stokes signal was generated,

(b) the mean frequency of the carrier generated appeared to map the average measurand value across the interaction length and

(c) the spatial resolution of sensors based on these systems is limited to the interaction length.

In order to demonstrate a 'true' multiplexed system for the fibres and source available, the configuration depicted in Figure 60 was constructed. The EOTec/HB fibre was spun onto two reels, of lengths 150m and 250m respectively. The former was cooled to 6°C whilst the latter was maintained at room temperature (25.5°C). The EB450 fibre again acted as the reference. The difference here, of course, was that there were two inputs to the sensor fibre such that two Stokes signals were simultaneously produced from the EOTec/HB fibre.

The result is shown in Figure 61. In addition to the broadband dynamical spectrum, three peaks were obtained in the output (i.e. $l=2$ from equation 5.4). The first, peak 1, centred on 215MHz, represented the beat between the Stokes signals from the reference fibre and the EOTec/HB fibre cooled to 6°C (ie $\Delta\mathcal{T}=19.5°C$). The second was the mix between the reference and EOTec/HB fibres at room temperature. Peak 3 was the result of the two carriers from the EOTec/HB fibre, mixing and was centred on 75MHz, a measure of the temperature difference between the two regions. Modulations of approximately ±10MHz were again produced for each principal carrier. These results are now discussed further and compared with other SBS-based multiplexed and distributed topologies reported in the literature.

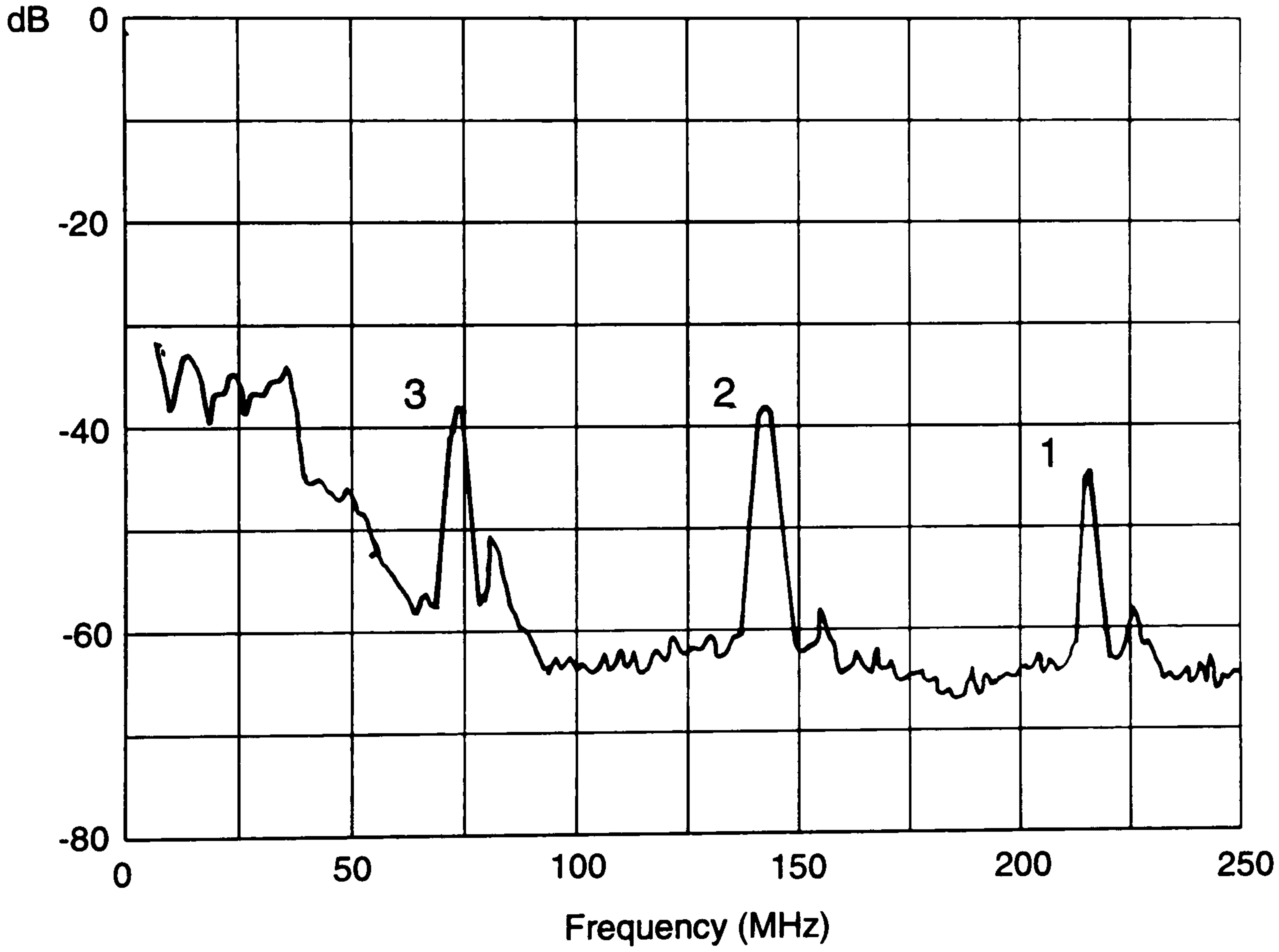

Figure 61: Output Spectrum of the Two Element Multiplexed Sensor Showing Peaks at 75, 140 and 215MHz

5.2.4 Discussion

The difference between the beat frequency of the EOTec/HB and EB450 fibres at room temperature (135.6MHz) has been related to differences in germanium dopant concentration between the two samples (section 3.4.2). The dependence of the beat frequency with temperature of both samples is now discussed. Early work in Brillouin spectroscopy of fused quartz measured a linear response at 0.5145μm between 0 and 500°C equivalent to 2.6MHz°C^{-1}(Bucaro and Dardy, 1974). Measurements were made with a Fabry Perot interferometer with a 40MHz resolution. Later work (Pelous and Vacher, 1976) measured a response of 3.1MHz°C^{-1} from 0-350°C and 2.6MHz°C^{-1} up to 850°C. Differences in the two experiments were attributed to impurities and the thermal histories of the respective samples.

These temperature sensitivities for bulk quartz were consistently lower than the values obtained for the fibre samples in section 5.2.2. However, the effects of dopants again, and the mechanism and materials involved in jacketing the fibre, can all affect the thermal sensitivity of the Stokes signal, facts highlighted by comparing the results obtained from the literature *for fibres.* For example, two (unspecified) fibre samples were shown to exhibit respective sensitivities of 2.7MHz°C^{-1} from 24 to 35°C and 6.4MHz°C^{-1} over 0 to 24°C when pumped at 0.5145μm (Culverhouse et al, 1989a). The difference was attributed to varying dopant levels, though no details were given. Interestingly, measurement of the beat frequency was made using a confocal Fabry Perot of unspecified resolution with the fibres alternately acting as sources of a reference Stokes signal.

Thermal effects on the Brillouin gain spectra have also been measured using the pump-probe configuration first suggested by Shibata and co-workers (1986) and briefly discussed in section 2.4.2. The technique used two frequency tunable diode pumped Nd:YAG lasers at 1.32μm to launch counter-propagating signals into the fibre. The frequency of the pump was periodically swept over a known range by varying the Nd:YAG crystal temperature. When the frequency difference between pump and probe matched the Stokes frequency, the probe was amplified. The frequency was a function of local temperature. (This technique also formed the basis of distributed sensors discussed later in this section.) Two fibres were studied, one being a Ge-doped core with pure silica cladding sample and the second a pure-silica core and fluorine doped cladding sample. The temperature coefficients of Brillouin shift were measured as 1.17 and 1.33MHz°C^{-1} respectively at 1.32μm, equivalent to shifts of 3 and 3.4MHz°C^{-1} at 0.5145μm since the Brillouin shift, to a first order, is inversely proportional to wavelength (equation 2.35).

In work by the same authors (Kurashima et al, 1990a), the effect of the jacket on otherwise identical fibres was considered. Nylon coated fibres (diameter ≈900μm) demonstrated an additional Brillouin shift of 2.5MHz°C^{-1} at 1.32μm compared with only 0.05MHz°C^{-1} for UV cured resin coated fibres (diameter 250μm). The difference arose principally from thermally induced strain along the fibre. Thus, a suitable choice of jacketing can be used to optimise the thermal sensitivity of a given fibre.

The additional dependence of the Stokes signal on strain suggested that SBS may be suitable for this sensing application. In a separate experiment to these temperature based systems but using the same pump/probe principle (Horiguchi et al, 1989), a Stokes frequency/strain dependence of 5.2×10^{4}MHz per unit strain was measured. This involved straining 400m of the fibre sample simultaneously by wrapping it onto two mandrels and displacing one with respect to the other. The point sensor technique described in section 5.2.2 would not therefore be suitable for small, localised strain regions. Measurements would be averaged over the interaction length as was demonstrated for temperature. Techniques which can improve the spatial resolution for strain are described later in this section.

Returning to the fibre used in the point sensors of the present study, the Brillouin shift sensitivity agrees well with values reported in the literature. The source of the shift still requires clarification, however. There are two principal origins:

(a) the direct variation in Brillouin frequency with the core index, n, and the acoustic phonon velocity, V_A, given by equation 5.2 and

(b) an additional frequency shift associated with thermally induced strain.

The jacket coatings of the EB450 and EOTec/HB fibres were composed of UV-cured acrylate which was identified by Kurashima and co-workers in the experiments described above as *minimising* thermal strain effects. The good linearity between beat frequency and temperature shown in Figures 55 and 57 confirmed the lack of thermal strain so source (b) was discounted. This leaves the temperature variation of both n and V_A.

In their experiments on fused silica, Bucaro and Dardy (1974) measured a 7% increase in acoustic phonon velocity over the 20-1620°C temperature range. Measurement was inferred directly from the Stokes frequency shift, having eliminated simultaneous thermally induced changes in refractive index in their analysis. The increase was equivalent to a change in V_A of 0.26ms^{-1}/°C. From equation 5.2, this translates to a frequency shift, at 0.5145μm, of 1.5MHz°C^{-1}. This is significant contribution to the overall variation and appears at odds with a report in the literature (Culverhouse et al, 1989a) which quoted the same Bucaro and Dardy paper in its justification for neglecting the dV_A/dT term. If present in the EOTec/HB and EB450 fibres (and there was no independent means of verification), it has important consequences for both the point and multiplexed systems discussed. In Figure 55, section 5.2.2, the resultant beat frequency increased at the rate of 4.3MHz°C^{-1} on heating the EB450 fibre. Assuming for now that the change in V_A matched that of bulk fused silica, this result implied that the dn/dT term contributed 2.8MHz°C^{-1}. Similarly, in Figure 57, an increase in V_A with temperature decreases the resultant beat frequency by 1.5MHz°C^{-1}. The thermo-optic coefficient again induced 2.7MHz°C^{-1}. The assumption of identical thermo-optic coefficients between the fibres is confirmed.

In the discussion on single input, two element multiplexed sensors in section 5.2.3, it was assumed that the resultant beat signal mapped the average refractive index of the core. It appears that dV_A/dT made a significant contribution to the thermal sensitivity. The beat frequency thus represented the average changes of both n and V_A with respect to temperature over the interaction length.

The measurements of Bucaro and Dardy were, as have been stated, for bulk fused silica. No equivalent measurements for dV_A/dT in fibres, to the best of the author's knowledge, have been made independent of dn/dT. The value of the latter is, of course, well known in optical fibres from interferometric measurements and is typically 1.3×10^{-5}°C^{-1} (deduced from Table 1, Chapter 1). This can be used in conjunction with the measured value of $d\nu_B/dT$ and equation 5.2 to gauge more accurately the fibre value of dV_A/dT. Thus, from equation 5.2

$$|\delta\nu_B| = 4.3 \times 10^6 = \frac{2}{\lambda}\Big(n\frac{dV_A}{dT} + V_A\frac{dn}{dT}\Big) \qquad 5.7$$

The core index, n, is approximately 1.46 and V_A is 5.96×10^{3}ms^{-1} for single-mode fibre at 0.5145μm, Hence dV_A/dT for the fibres was 0.7ms^{-1}/°C, equivalent to a frequency shift of 4.0MHz°C^{-1}. Thus, though both n and V_A increased with temperature, it was the change in V_A which dominated the interaction. The dn/dT term contributed only 0.3MHz°C^{-1}.

The linear response of the frequency change to temperature will ultimately be determined by the relationship of dV_A/dT and dn/dT to temperature, provided that thermally induced strain is minimised since this usually exhibits nonlinear behaviour (Horiguchi et al, 1989). The dn/dT term is approximately a parabolic function of temperature in fused silica (Dynasil Corporation, 1986) but is approximately linear over the region 0 to 200°C. More importantly, after the previous discussion, is the linearity of dV_A/dT. This was shown to be linear from 0-700°C (Bucaro and Dardy, 1974). The range of the device was therefore probably limited by the response of the detector as the beat frequency is increased and the thermal characteristics of the fibre jacket at elevated temperatures.

The temperature resolution measured in section 5.2.2 was limited by the nonlinear dynamical induced effects. These were partly offset by the introduction of feedback and the use of post-detector averaging but the maximum resolution remained at approximately ±2°C. These FM effects have not been reported in the literature in any SBS sensor systems described above. It is believed that this was because many of these measurements were made directly in the 100MHz-10GHz region using Fabry Perot interferometers which would not generally possess the required resolution. Another reason was the pump/probe method of measurement which we discuss presently for distributed sensors.

The spatial resolution of the systems described in 5.2.2 was the fibre-pump interaction length, typically between 100-150m. This is clearly unacceptable in many applications requiring localised (and cost effective) measurand sampling. In section 6, SBS systems based on ring resonators will be discussed in which comparitively small amounts of fibre are used to generate SBS and which can boast both high spatial resolution and high frequency stability.

For the reasons outlined in Chapter 1, new fibre sensor technologies must demonstrate some multiplexing capability to compete with conventional technologies. Ultimately, the aim is to develop fully distributed systems. The single source, single input system in section 5.2.3 measured the average temperature along the interaction length. The rapid depletion of the pump along the fibre meant only one sensor per input was possible. In a similar experiment (Culverhouse et al, 1989a), two sections of the same (unspecified) fibre were maintained at 0 and 30°C respectively. (The sample lengths were 150 and 350m). The Stokes signals were mixed with the pump and measured directly on a confocal Fabry Perot interferometer. For a single input, it was stated that two simultaneous Stokes signals were generated representing the two different temperature regions. It was also stated that both regions lay within the fibre-pump interaction length. Fibres typically possess losses of 25dB/km at 0.5145μm (see Appendix C for fibres used in current study). In a 500m fibre, this loss produces a 164m interaction length. Thus, the two regions are 150m and 14m in length (assuming this loss level) in the cited experiments. What can be categorically stated was that, for both the EOTec/HB and EB450 fibres used in the present work, two simultaneous independent Stokes signals were *never* produced (except when propagating along orthogonal eigenaxes of the same fibre, of course) and this observation was confirmed by the theory. Thus, in the present systems, although the spatial resolution may be improved by reducing the interaction length, this is at the expense of a higher SBS threshold from increasing the fibre loss or shortening of the fibre. This is clearly impractical.

In recent years, an elegant technique has been developed which has enabled the Brillouin process to be extended to distributed systems. It differs from the approach adopted in the present work in that it exploits

(a) two optical sources (one pulsed and one cw) and

(b) an instantaneous, Brillouin amplification process.

The technique has been termed Brillouin Optical Time-Domain Analysis (BOTDA) and the principles (Horiguchi and Tateda, 1989) have already been outlined in this discussion. A pulsed pump signal counterpropagates with respect to a cw probe. The centre frequency of both are closely spaced but can be continuously tuned over a small range. If, when the pump and probe overlap, their frequency difference matches the Brillouin Stokes frequency, then the probe is amplified. The frequency depends on local temperature (and/or strain) as demonstrated earlier. The time difference between the amplified probe being detected and the launch of the pulsed pump, relates the position of the measurement. By modulating the frequency of either source, a complete map of temperature along the fibre can be established.

The first Distributed Temperature Sensor (DTS) based on this scheme (Kurashima et al, 1990c) used a tunable diode-pumped Nd:YAG laser as a pump and a cw external cavity, semiconductor laser as a probe, both emitting at 1.32μm. The tuning range of the pump was not specified but a linear variation of 1.25MHz°C^{-1} from -28°C to +60°C was measured (equivalent to 3.2MHz°C^{-1} at 0.5145μm). The peak to peak variation in Brillouin frequency (4.2MHz at 1.32μm) limited the sensing accuracy to 3°C, similar to the present work. An acousto-optic cell was used to gate the pump, limiting its pulse width to 1μs, and equivalent to a 100m spatial resolution over the 1.3km range used. The key point was that the pump was only depleted in the brief time that the frequency differential of the sources matched the Stokes frequency.

The fundamental limitation on the spatial resolution of this approach occurs when the pump width approaches the acoustic phonon life-time. Here, the Brillouin gain and, hence, amplification are substantially reduced. At 1.32μm, the Brillouin gain bandwidth is typically 50MHz, setting the acoustic phonon lifetime, τ_B, as 6.4ns (equation 2.66). Setting a lower limit of the pulse width to $2\tau_B$, to ensure minimal depletion of the gain, this is equivalent to a spatial resolution of 1.3m. In a recent experiment identical to the principles of Kurashima (except that the frequency of the *probe* was modulated), a 10m spatial resolution was demonstrated over 22km range with a temperature sensitivity of 1°C (Bao et al, 1993a). Only 7mW probe and 5mW peak power pump signals were used and a shift of 1.3MHz°C^{-1} measured over 20-80°C range. The same authors have recently improved the spatial resolution and range to 5m and 32km respectively by monitoring the Brillouin *loss* induced in the probe (Bao et al, 1993b). Here, the pump frequency is less than the frequency modulated probe. The *pump* thus experiences gain under the appropriate conditions and this extends the total length of operation.

Similar approaches to measure strain distribution have been developed, a resolution of 50m and 100μstrain being reported (eg Tateda et al, 1990). A combined strain and distributed sensor has been recently reported (Bao et al, 1994) based again on Brillouin loss with a 20μstrain and 2°C sensor resolutions respectively over 22km. The spatial resolution is 5m. This pump/probe approach therefore shows potential improvement over the commercially available DTS system based on Raman gain described in Chapter 1. Issues such as the simultaneous measurement of the same temperature along different sections of the fibre must still be resolved. However, compared with the systems reported here, operation at near IR wavelengths avoids photosensitive effects. Further, the mode of operation of the sensor means that the output is inherently immune to the FM fluctuations in Stokes signal. The change in probe *power* is being measured and this is correlated with the frequency difference between pump and probe in a separate reference (non-Brillouin) fibre system.

In summary, then, the results of the point and elementary multiplexed have been discussed in the context of other work in the field of Brillouin based fibre sensors. The limitations of the single source approach to multiplexing in particular have been highlighted due to the rapid depletion of the pump, low spatial resolution and modulation of the output carrier. Techniques which overcome these limitations have been described.

5.3 Investigation of Steady Oscillation Based Sensors

5.3.1 Introduction

In section 2.4.3, it was described how, under certain pump conditions, steady oscillations (Bar-Joseph et al, 1985) were prevalent in the output Stokes signals. Figure 28 in Chapter 3 showed how these were manifest as an array of harmonics on the spectrum analyzer during the present study. The peak to peak separation (in frequency space) was inversely proportional to fibre length. A brief series of experiments were therefore undertaken to investigate further the properties of the oscillations and assess their potential for simple sensing schemes.

Firstly, the variation in the steady oscillation spectrum with pump power and fibre end-face reflectivity were measured. The latter measurement, in particular, gives an estimate of the effects of index change at the fibre/air interface on the oscillations and was directly relevant to sensors. Two simple sensing schemes were then set-up. In the first, the effect on the output frequency array of heating the fibre was examined. In the second, the effect on coupling light between two eigenaxes of birefringent fibre via microbending was studied. From these simple approaches, conclusions were drawn as to the usefulness of the oscillations in sensors.

5.3.2 Experimental Results and Discussion

The properties of the oscillations were studied in the EB450 fibre, pumped at 0.5145μm along one eigenaxis. Firstly, the variation in oscillation 'visibility' was measured with increasing pump power, $P_p(0)$. Here, 'visibility' was defined as the difference between the maximum and minimum of the modulation measured in the frequency domain by the electronic spectrum analyzer. The experiment showed that, for the pump powers available (up to 270mW), no significant changes to visibility were measured. This was the expected result from the earlier description of their properties in section 2.4.3. The steady oscillations should remain present as long as the Stokes output, $P_s(0)$, is less than $0.67 \times P_p(0)$ (Bar-Joseph et al, 1985) for all input pump powers above SBS threshold. Figure 22 in Chapter 3 showed the experimental and theoretical values $P_s(0)$ for increasing $P_p(0)$ in EB450 fibre at 0.5145μm. By extrapolating the experimental curve to larger values of $P_p(0)$ than are shown on the graph, this condition is reached only when $P_p(0)$ attains 340mW, well in excess of the available power. (At this point, the steady oscillations should decay into relaxation oscillations and disappear.)

In a second experiment, the distal end of the EB450 fibre was successively immersed into a series of index matched oils of increasing refractive index. The variation in oscillation 'visibility' was again observed. The fibre was known to possess a core index value of approximately 1.46 so oils of index between 1.4 and 1.7 were selected. Figure 62 plots the variation in 'visibility' against oil index. The points were discrete and are linked for clarity. The minimum in visibility for an oil index of around 1.46 was consistent as, at this point, the reflectivity of the fibre was also a minimum. The error bars represented, again, the standard deviation of the visibility modulations and showed that the system was sensitive to an output δn of ± 0.02.

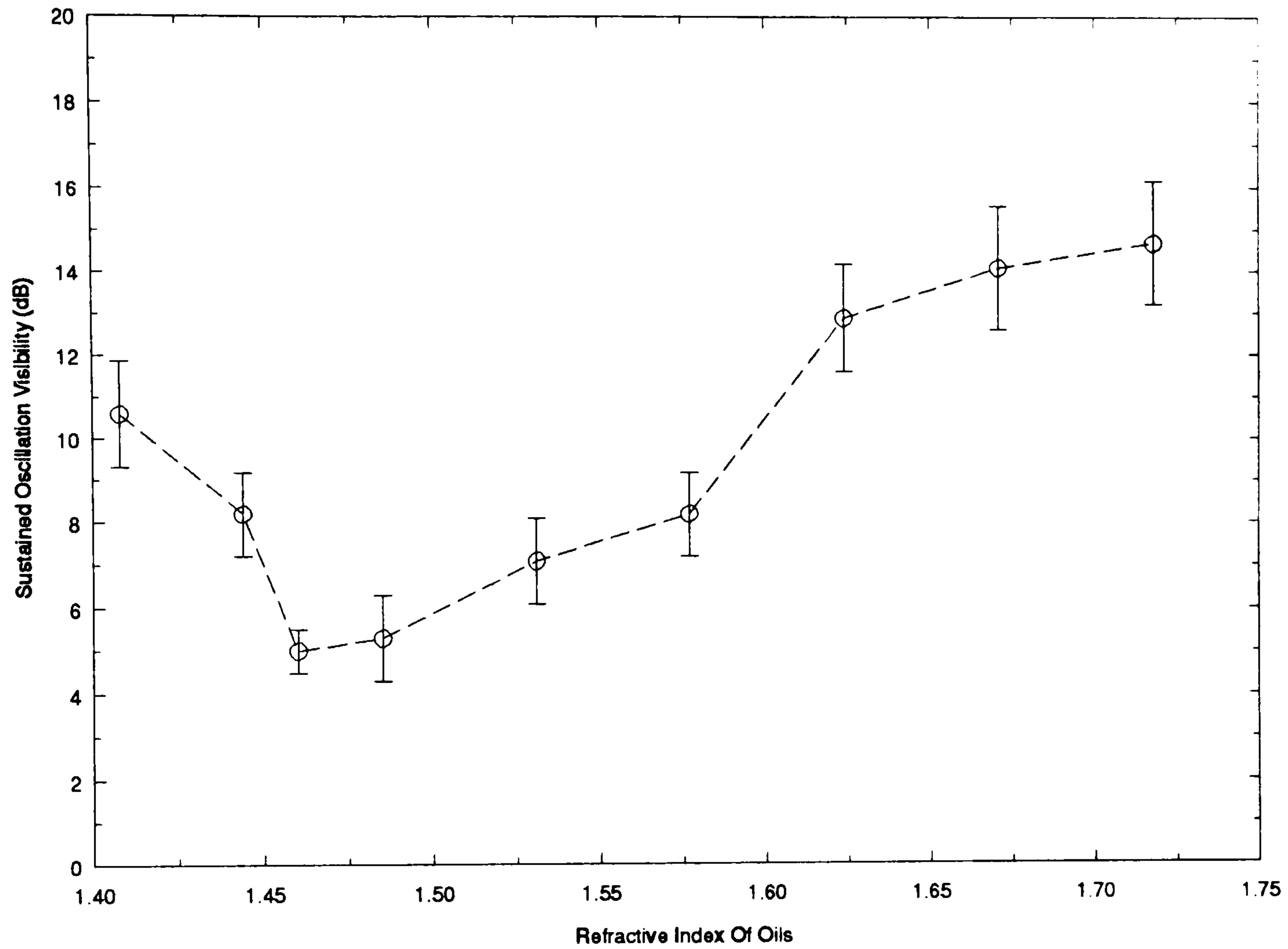

Figure 62: Measured Steady Oscillation Visibility Plotted Against Refractive Index of Oil at Fibre Distal End

Figure 63 illustrates the output as seen on the spectrum analyzer for n equal to 1.46 and 1.624 (grids (a) and (b) respectively), highlighting the difference in the two cases. Thus, though the oscillations were insensitive to input pump power, they responded to changes in fibre reflectivity, though it was the *amplitude* of the oscillations which decayed. It is debatable whether this can be applied effectively in sensor applications. For example, a 0.02 change in refractive index would be produced by heating silica to 1500°C.

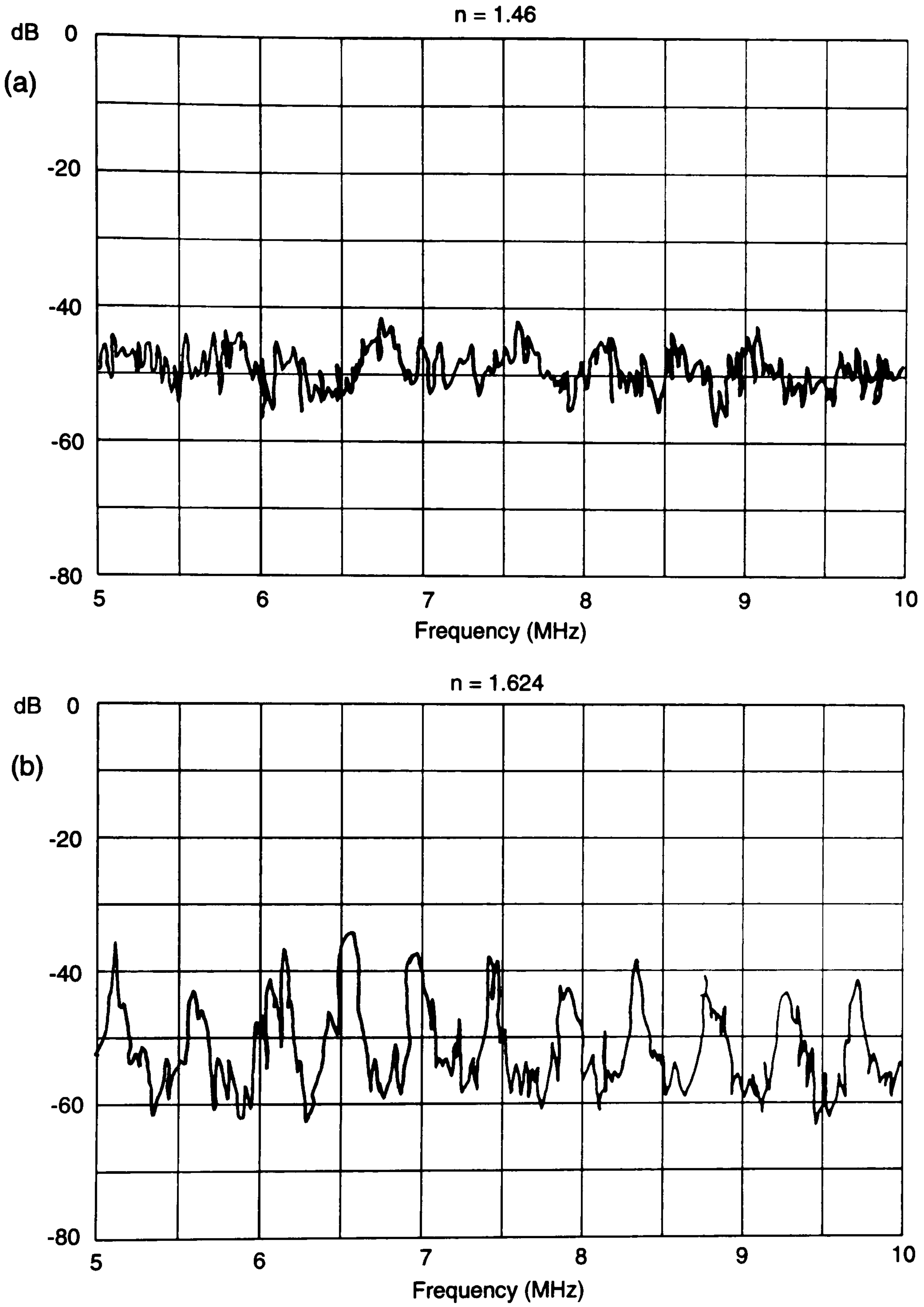

Figure 63: SBS Output Spectra for EB450 Fibre for Distal Fibre End/Liquid Interface Reflectivity of (a) Zero and (b) 3×10^{-3}

For sensors, the frequency information of the oscillations held most interest and this was now investigated.

The frequency spacing of the oscillations, f_i, is given by

$$f_i = \frac{c}{2Ln} \qquad 5.8$$

where L is the fibre length, n is the core index and c the speed of light in vacuum. The change in index over 45°C, for example, would amount to 5.9×10^{-4} (Table 1, Chapter 1). From equation 5.8, this would produce a change in frequency array spacing of under 0.2kHz. Since the electronic spectrum analyzer resolution was 1kHz, the minimum detectable temperature change using this approach would be approximately 225°C. More sensitive phase sensitive detection techniques would be required in the present system to detect the frequency modulation in the output signals. This limitation was confirmed when the whole EB450 fibre was heated from room temperature to 50°C and then cooled to 6°C. At selected temperatures over this range, the average sustained oscillation spacing (in frequency) was measured on the spectrum analyzer. However, over this range, no change in spacing was detected.

Finally, a second sensor example was investigated using the principle of externally induced coupling between the polarisation modes of high birefringent fibre. In section 3.1, a series of fibre frequency shifters were described which relied on externally generated transverse acoustic waves to produce coupling between modes in fibres and, hence, a frequency shift. Maximum coupling was obtained when the acoustic wavelength matched the fibre beat length. In a similar way, coupling can be induced by introducing periodic microbending using ridged mounts (such as that shown in Figure 4, Chapter 1 and called static mode coupling) along the fibre length. In fact, for this method, maximum coupling occurred for microbend periods of twice the beat length (Pannell et al, 1988). In the context of SBS and steady oscillations, undepleted pump would be coupled into the orthogonal axis. This would be translated into an effective change in n from equation 5.8 and hence a perturbation to f_i. The birefringence of the EOTec/HB fibre, for example, 5×10^{-4}, was again too small, when converted to an effective change in f_i, to be measured by the spectrum analyzer. To confirm this, pairs of blocks were therefore constructed which interlinked as shown in Plate 4 and whose ridged spacing was manufactured to be double the fibre beat length. By aligning the birefringent fibre between the blocks such that the ridges of the blocks pressed down at 45° to the eigenaxes, maximum coupling should occur. For the EOTec/HB fibre, no changes were measured, irrespective of the position of the block along the fibre length.

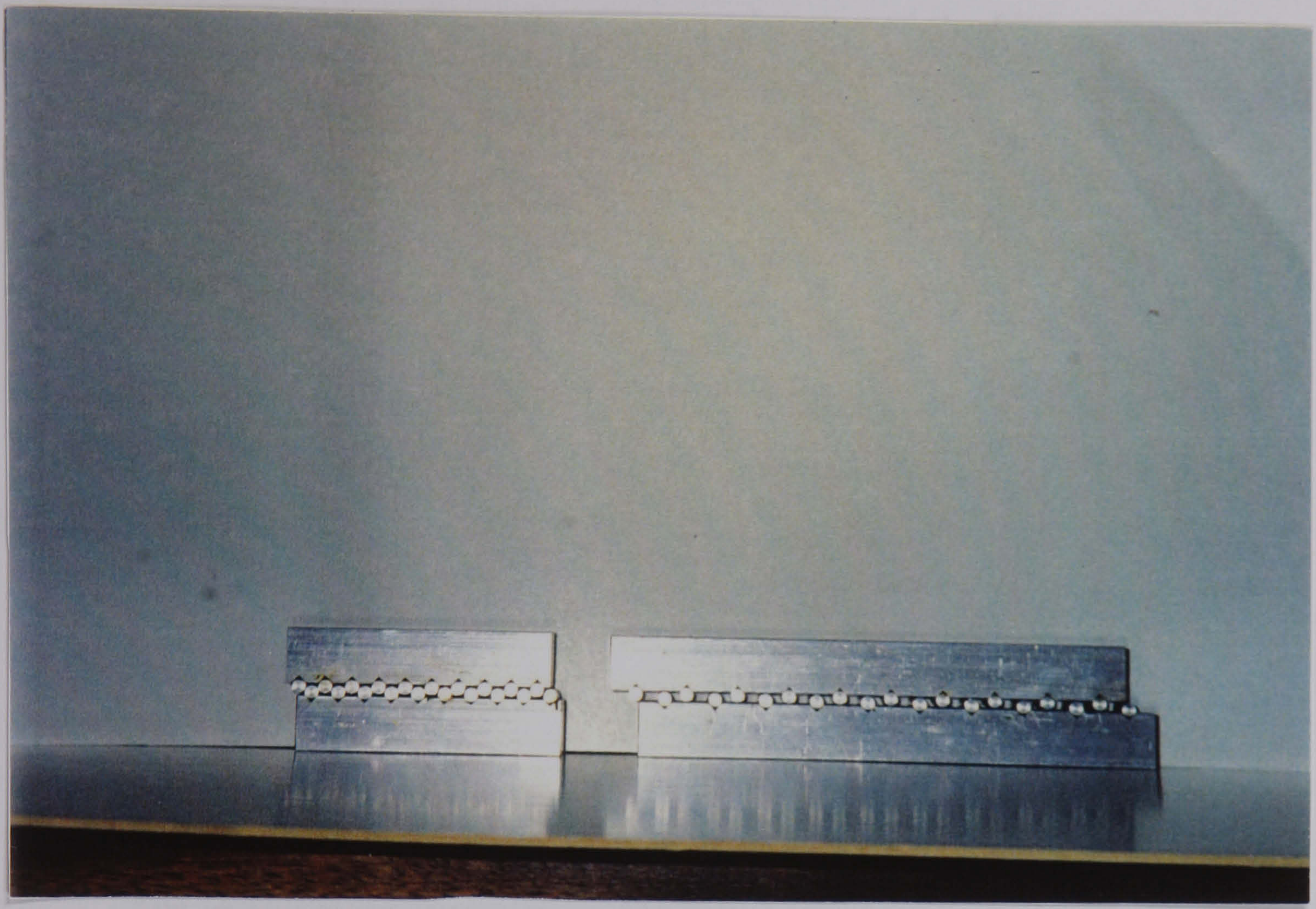

Plate 4 Static Mode Couplers Used To Impart Periodic Microbending On Birefringent Optical Fibre

In summary, the sustained oscillations that were present for all SBS systems above threshold were investigated for sensor applications. Despite the frequency information contained within the oscillations, they did not appear to offer any straightforward sensor opportunities.

5.4 Summary of Principal Results

Sensors based on direct frequency modulation of the SBS carrier signal by temperature were investigated in both point and multiplexed systems. The EOTec/HB and EB450 fibres were used throughout, pumped by the 0.5145μm ArI source. In the point systems, the fibres demonstrated an SBS beat frequency response of 4.2 and 4.3MHz°C^{-1} respectively which was linear over the 5-50° range investigated. The sensing resolution, limited by dynamical instabilities, was nominally ±3°C, but was reduced to ±2°C through post-detector averaging. The use of optical feedback to suppress these transient processes improved the resolution by a further ±0.5°C. The frequency instability remained too high, however, for the single birefringent fibre systems to be implemented as a 'differential' SBS sensor.

For the multiplexed system, it was shown both theoretically and experimentally that only one Stokes signal was produced (per eigenaxis) per fibre input. Further, the frequency of the Stokes signal appeared to map the average temperature along the fibre/pump interaction length. Thus, the spatial resolution was set in these systems as this interaction length. A two-element spatial division multiplexed arrangement was demonstrated. Input power limitations prevented a higher number of sensors from being interrogated.

The temperature sensitivity of the SBS frequency for the fibres was consistent with the values reported in the literature. Thermally induced strain effects were not a factor for the fibres used. It was demonstrated that the temperature dependence of the acoustic velocity, rather than the refractive index, is the dominant factor in modulating the Stokes frequency. The sensor systems presented here were then compared with the pump/probe SBS configurations from the literature, which have the potential for fully distributed operation.

The properties of the sustained oscillations in the SBS outputs (section 3.4.1) were assessed as functions of pump power and fibre reflectivity. Though the oscillation spectrum provides a direct measure of fibre length, the spectrum showed no measurable change on modifying the fibre's refractive index through either heating or static mode coupling. Thus, the sustained oscillations provided minimal sensing opportunity.

6 SBS System Developments and Overall Discussion

6.1 Introduction

Individual aspects of the experimental work reported in this study have been discussed within each chapter and compared, where appropriate, with equivalent research in the literature. The three major experimental chapters, 3 through 5, have therefore formed fairly self-contained units. Within these, many potential improvements to the systems investigated and solutions to the problems exposed by the present research have already been suggested. It is the purpose of this chapter, therefore, not to repeat these points, but to take a more global view of the SBS approach and its applicability to aerospace applications. Firstly, systems based on fibre ring resonator technology are described which can potentially improve the performance of all the experimental systems described in this study. Secondly, since the thesis commenced with an assessment of both non-linear effects in fibres and the requirements of the aerospace industry for fibre sensors in general, these themes are now unified. Alternative non-linear based approaches to fibre sensing and signal processing are briefly described (restricting the discussion to intrinsic systems) before the overall technical impact of this area is summarised. Suggestions for further work are then listed for the SBS systems.

6.2 Fibre Ring Resonator Technology For SBS Systems

A common theme linking all the SBS systems discussed in this work has been the long fibre lengths and comparatively high cw pump powers necessary to generate SBS. These are undesirable features in fibre systems and, in the present work, contributed directly to the instability of the Stokes signal via the photosensitivity of fibres and non-linear dynamical processes. Both can be overcome, however, by the introduction of fibre optic ring resonators.

The key features of the device are shown in Figure 64 (the full frequency shifter arrangement shown in the figure is discussed presently). Light from the pump source enters a 2×2 directional coupler, selected to maximise coupling from port 1 to 3. Ordinarily, the circulating light will be coupled out of the ring via port 2 to port 4. However, the device becomes resonant when the light in the loop entering port 3 interferes constructively with the light at port 2. Correspondingly, a sharp minima is observed at port 4 through destructive interference. The loop length control electronics maintain the device at resonance when, for example, thermal effects modify the optical path length of the ring. At resonance, the power circulating within the ring grows in principle until the losses in the loop equal the input power from port 1 (Stokes at el, 1982a). The operation is entirely analagous to that of a Fabry Perot interferometer and, as a result, the device possesses a finesse, $\mathcal{F}$, given by

$$\mathcal{F} = \frac{\pi\sqrt{\kappa}}{1-\kappa} \tag{6.1}$$

where κ is a measure of the total transmittance across the directional coupler from port 1 to 3 and around the fibre loop. It is equivalent to the reflectivity term in Fabry Perot devices. By selecting a low-loss coupler and fibre, κ can approach unity, in which case, very high finesse systems are achievable. Since the pump power is coherently adding within the ring, conditions are appropriate for SBS. Indeed, in the first demonstration of SBS in fibres with a cw source (Hill et al, 1976a), a ring was set-up using a combination of fibre and bulk optic components to recirculate the pump. Once high quality couplers and fibres were developed, demonstration of SBS in an all-fibre system soon followed. The SBS threshold power, $P_{B,r}^{thr}$ has been derived (Stokes et al, 1982b):

$$P_{B,r}^{thr} = \frac{2A_{eff}\pi^2}{g_B L \mathcal{F}^2} \tag{6.2}$$

where L is the loop length of the resonator and all other terms have been previously defined. The ratio of Brillouin threshold between rings and conventional systems (ie systems of Chapters 3 and 5) using equation 2.39 is approximately $L_{eff}/L\mathcal{F}^2$. Finesses of 80 (κ=0.96) were observed in early ring systems (eg Stokes et al, 1982a). Thus, for example, the Brillouin threshold for a 10m loop of the EOTec/HB fibre used in the present study and pumped at 0.5145μm would be reduced by a factor approaching 500 (to below 100μW). Greatly enhanced conversion efficiencies per unit of input power are also possible. The need for high input pump powers and long fibre samples to enhance L_{eff} is therefore negated.

In an early demonstration of these principles (Stokes et al, 1982b), a He-Ne laser pumped a 10m ring and SBS was obtained at less than 0.5mW of pump power. Output instabilities arose because the resonator length was not stabilised and resonance was dependent on thermal drift in the ring. The Free Spectral Range of the device (c/nL) was 20.6MHz, ensuring that one of the resonant peaks of the device lay near the peak of the Brillouin gain curve ($\Delta\nu_B \approx$100MHz).

Several groups have developed these basic ideas to produce higher finesse, lower threshold SBS systems with ever more compact sources. Applications extend from ring gyroscopes (eg Zarinetchi et al, 1991) to high resolution optical spectrum analyzers (Kalli and Jackson, 1992). For example, in the former, a $60\mu W$ Brillouin threshold was demonstrated for a $1.15\mu m$ He-Ne source pumping a 2.5m ring. The finesse was 270. In the latter, a resolution of 20kHz was obtained for a 40m ring of finesse 250 illuminated with sources at $1.3\mu m$. Importantly, the ring approach can be applied to the type of systems investigated in the present study for frequency shifters and sensors.

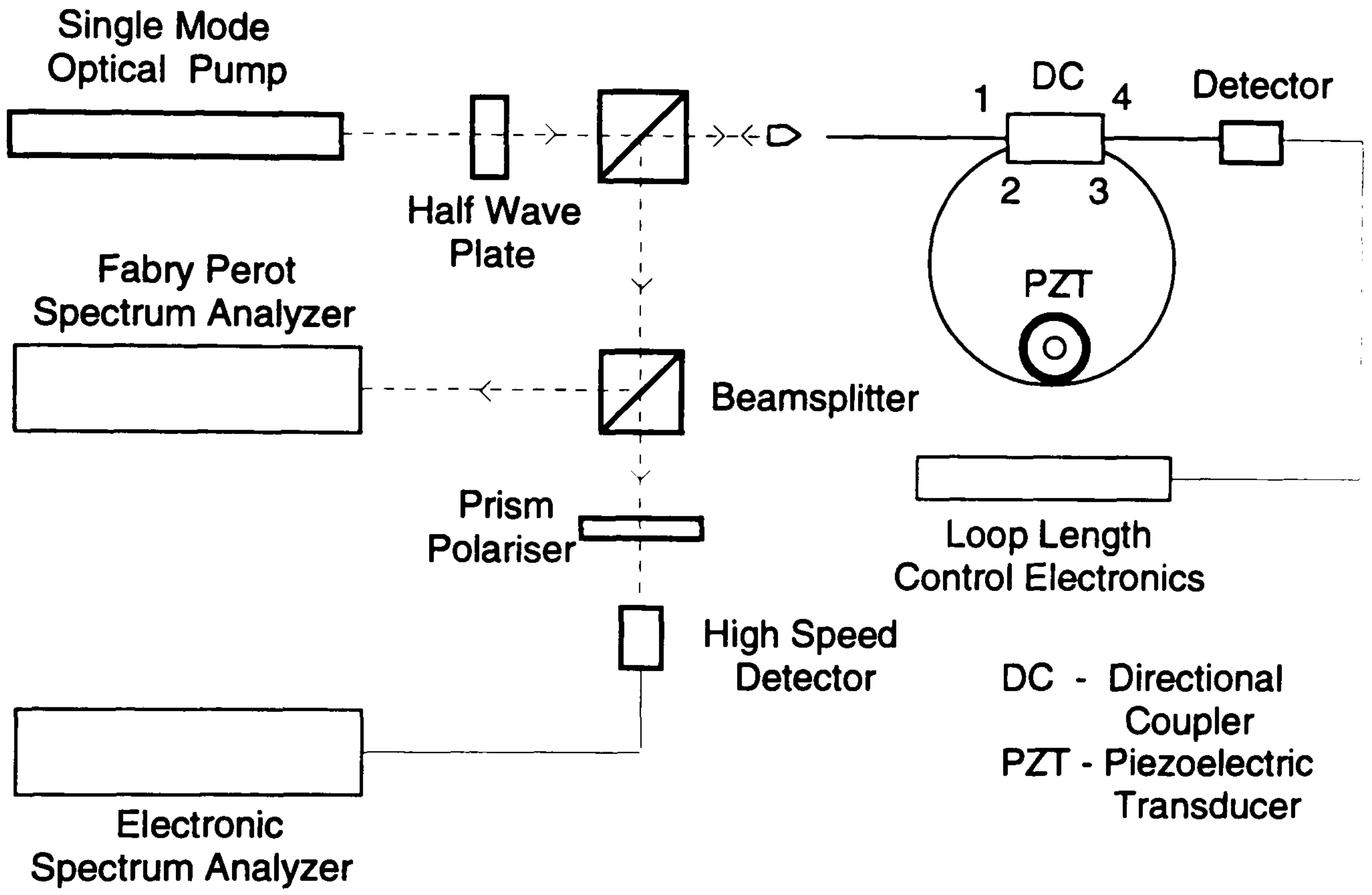

Figure 64: Optical Fibre Frequency Shifter Based on SBS in a Birefringent Optical Fibre Ring Resonator

Figure 64 illustrates a frequency shifter based on SBS in high birefringent fibre using identical principles to those in Chapter 3 but incorporating a ring resonator (Khan and Tatam, 1993). A 15m loop pumped at $0.6328\mu m$ from a single frequency He-Ne source produced a finesse of 125. An active length stabilisation technique using a piezoelectric modulator and servo-control to feedback data from the detector compensated for random phase variations and maintain both eigenaxes at resonance. This process does not in itself change the Stokes frequency as it predominantly modifies resonator length. SBS threshold powers of $2\text{-}3\mu W$ were measured and the device boasted a 20% conversion efficiency for 1mW input. The resultant carrier on mixing the two Stokes signals at resonance was centred on 11.68MHz and demonstrated remarkable stability. A thermal drift of $6.7kHz^{\circ}C^{-1}$ was measured in the carrier, limited predominantly by the thermally induced differential refractive index change between the fibre eigenaxes (equivalent to a phase change of 4rad°$C^{-1}m^{-1}$). The change in acoustic velocity with temperature between the eigenaxes contributed only 0.4kHz°C^{-1} to this figure.

Interesting comparisons were made with the systems described in Chapters 3 and 5. Firstly, in the sensors studied in the present work, it was shown that the dV_A/dT term dominated the interaction. Further, since the above system used a He-Ne pump, no photosensitive mechanisms would be induced in the fibre, so the polarisation and attenuation properties of the fibre would remain constant. Importantly, neither modulation in the output carrier frequency (apart from the small thermally induced drift) nor broadband intensity spectrum were observed in the system output (using the identical detector and spectrum analyzer as for the frequency shifter study described in Chapter 3). This provided further evidence that these properties may be inherently linked. The low pump values for SBS may account for this stability (ie minimising non-linear dynamical effects). Alternatively, since the high finesse ring is essentially a high feedback system, this may be a factor, recalling how both carrier modulation and broadband spectrum were reduced in Chapter 3 with feedback. The resonating nature of the device (Free Spectral Range of 13.7MHz) may also preclude broadband intensity spectra from appearing in the system output. This demonstration of a stable carrier is crucial to the development of the SBS approach for sensor and shifter applications.

Ring resonators can be applied to the type of sensors studied in Chapter 5. This was demonstrated indirectly in the literature by the simultaneous pumping of 2 rings at 0.6328μm to generate a basic 20MHz carrier (Kalli et al, 1991). The rings possessed a finesse of 400 and 25μW SBS threshold. Both devices were extremely temperature sensitive and needed to be stabilised to within ±0.03°C for a ±0.1MHz carrier stability. High temperature sensitivity, whilst it presented problems for this frequency shifter application, is potentially of significance in sensor systems. In a point sensor arrangement, for example, one ring would be used to generate a reference Stokes signal as in the system of Chapter 5 whilst the second would sense temperature. Both would contain a loop-length control assembly to maintain the devices at resonance. The presence of an electrical component at the heart of the system may render the approach redundant for certain harsh environments as explained in Chapter 1. A better approach may be to ramp the frequency of the pump which, since it effects reference and sensor fibre equally, will not corrupt the temperature information contained within the output carrier. Ensuring thermal stability of the reference channel is clearly problematic but high resolution FM sensors are feasible with this approach.

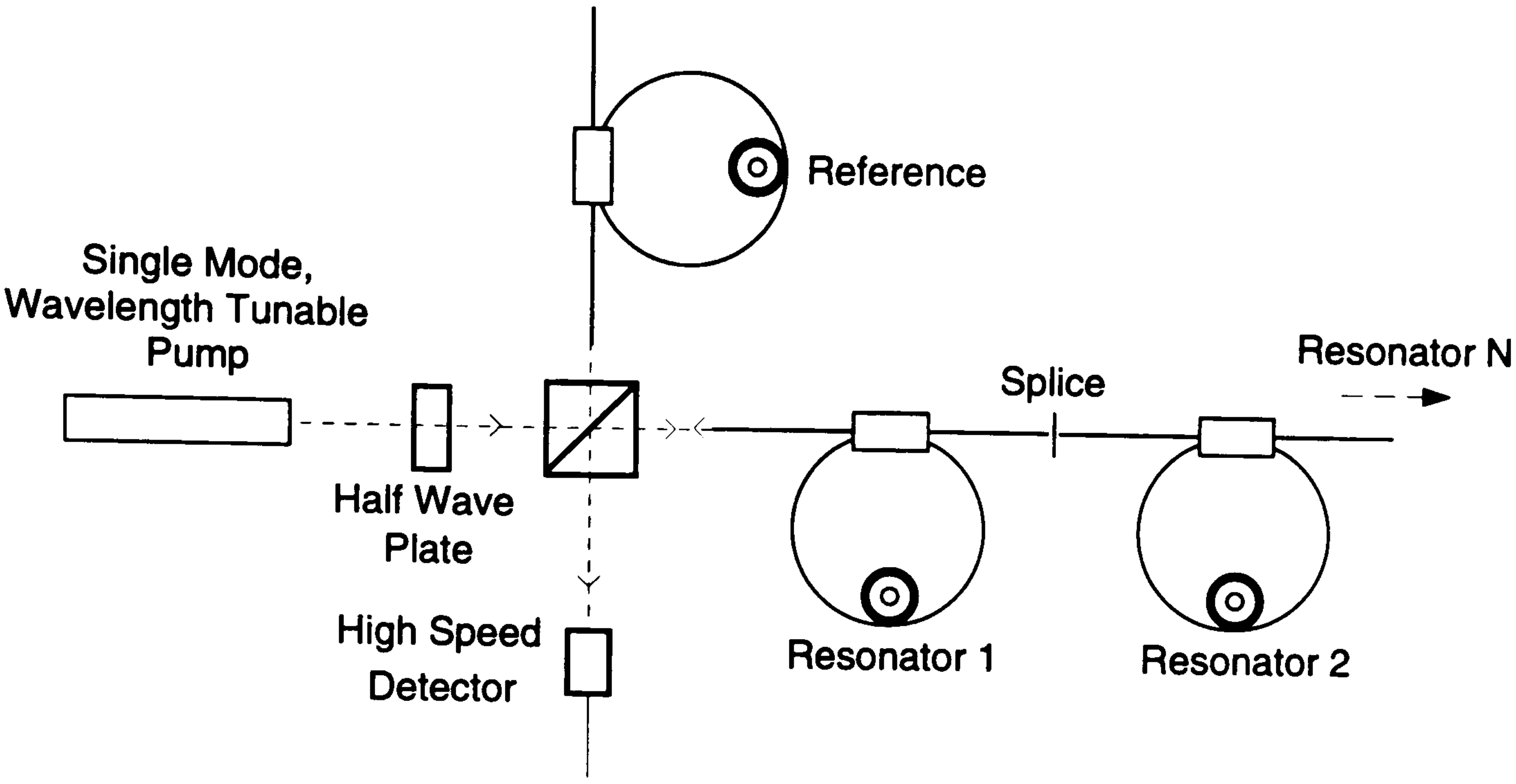

(a) Serial Array

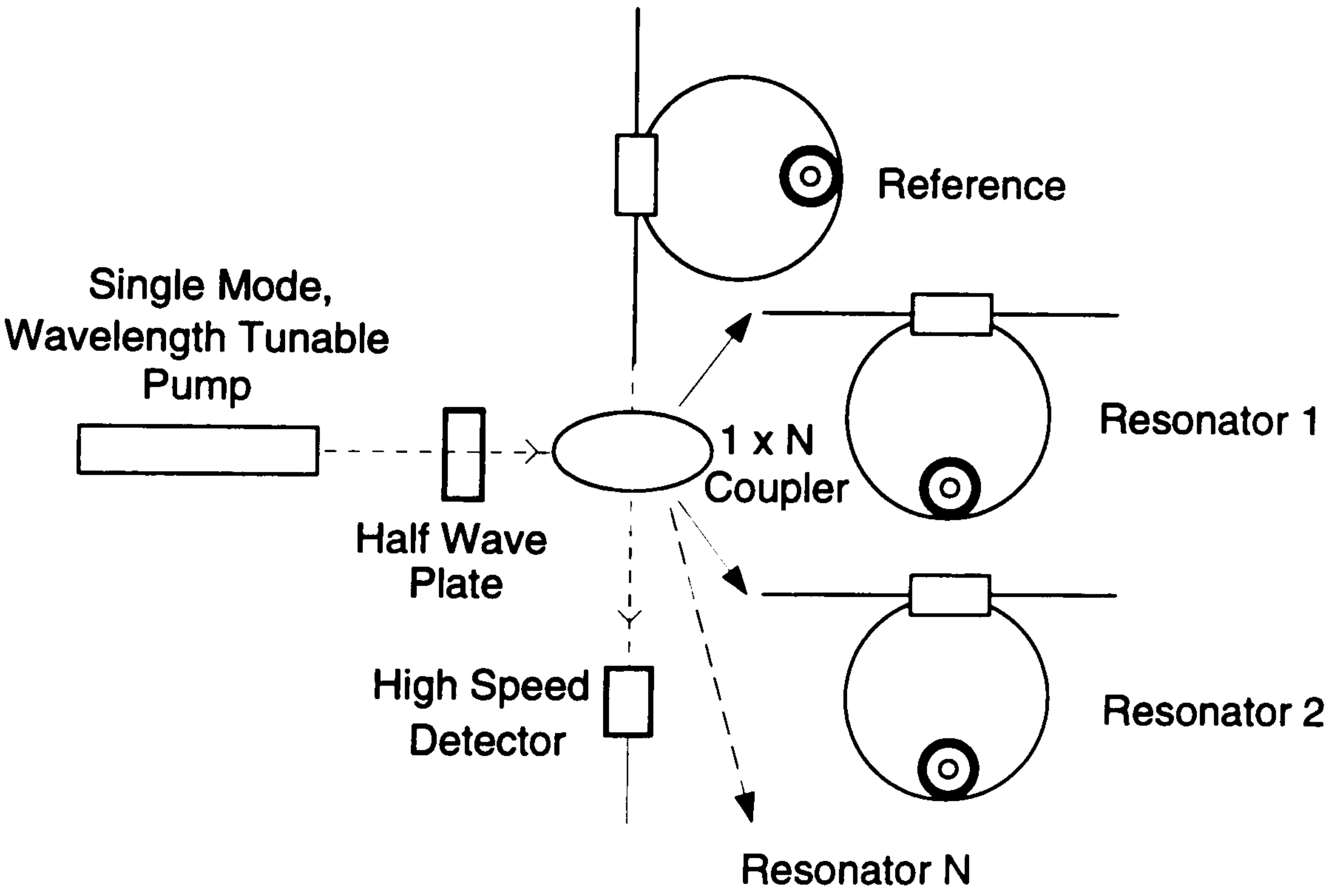

(b) Parallel Array

Figure 65: Possible Multiplexed Sensor Arrays Based on SBS and Ring Resonator Systems

The approach could also be extended to multiplexed systems by splicing together an array of rings arranged in series or in parallel (eg Figure 65). In the former, two simultaneous measurements in different rings are not possible since, when one ring is forced to resonate, no light propagates further along the network. For parallel systems, this is not a problem in principle though a high quality 1×N coupler would be necessary. Sensor identification could be achieved by using a wavelength tunable pump source. The length of each ring would be selected so that the ring resonates only over a narrow range of the pump wavelength. The length of the reference ring would require modulation via a piezoelectric element to provide a continuous reference carrier as the pump is tuned.

For strain measurement, the problem, as stated in Chapter 5, is that all the ring must be subjected to uniform strain. This is impratical in rings a few metres in length. Thus, the ring approach holds no advantages for high spatial resolution, strain measurement applications. However, as the above discussion illustrated, it can be applied to temperature sensors in both point and multiplexed topologies. This approach for fully distributed sensors has been superceded by the pump-probe BOTDR techniques discussed in Chapter 5.

In summary, ring resonators can produce a stable FM carrier in SBS systems requiring minimal optical energy for both heterodyning purposes and sensors. Further, the systems are fully compatible with fibres and contain a large potential for miniaturisation.

6.3 Alternative Sensor Strategies Based On Non-Linear Fibre Optics

Several systems have been reported in the literature based on alternative non-linear effects in fibres, rather than SBS, particularly for distributed temperature sensor applications. In Chapter 1, the *York* DTS sensor based on spontaneous Raman scattering in fibres was described. Several groups report variations on this basic theme. For example (Paton and Scott, 1990), by using a UV pump in fibre less than 100m in length and exploiting the higher Rayleigh scattering component, spatial resolutions of 50cm were measured over a measurement range of 20-250°C.

Other systems have been proposed and assessed using similar pump-probe techniques as used in BOTDR (eg Rogers, 1988). Indeed, one, based on Stimulated Raman Scattering, predated the *York* system (Farries and Rogers, 1984). A pulsed pump was used to amplify a counterpropagating probe lying at a convenient Raman Stokes wavelength. The amplification was a function of the relative polarisation states between pump and probe, being a maximum when they coincide. This, in turn, was dependent on the local temperature, strain or pressure. Therefore, the temporal variation in the power of the emerging probe mapped this polarisation data and the external measurands. A similar theme was recently reported based on the optical Kerr effect in high birefringent fibre (Parvaneh et al, 1992). A pulsed pump was launched at 45° to the fibre eigenaxis so its polarisation state was continually modified as it propagated. A counterpropagating cw probe was launched along only one eigenaxis. On encountering the pump, the probe was coupled into the second mode since the Kerr effect from the pump plus any additional measurand modifies the local birefringence. Again, the time dependent variation in cw power maps the birefringence and the measurand. Further development in both the systems is required before performance similar to the BOTDR approach is attained.

Perhaps the most significant development in fibre technology in recent years has been the emergence of the fibre Bragg grating for use as a sensor or component in sensor and communications systems (eg Morey et al, 1992). The gratings are in-core devices manufactured by interfering beams of UV light on the side of the fibre. Photosensitive mechanisms, linked to germanium dopant concentration, produce the effect, in a similar way to the processes of Chapter 4. The grating acts as a reflection filter for light of a certain wavelength (the Bragg wavelength) but allows other wavelengths to transmit. When temperature and/or strain is applied to the grating, the Bragg wavelength changes as the grating spacing is modified. Hence, the reflected signal provides an absolute measurement of the measurand. Since the grating is intrinsic to the core and is usually only a few millimetres in length, many sensors can be written into a single fibre to form a quasi-distributed topology. The strain sensitivity of the grating does depend on grating characteristics and fibre type but a reflection wavelength sensitivity of 0.7pm/μstrain is typical (Melle et al, 1993). Similarly, for temperature, a sensitivity of 16pm°C^{-1} has been measured (Morey et al,1992). The separation of the strain and temperature response may therefore be necessary in certain applications. The sensitivity of the devices and number of elements in a fibre is dependent on the optical interrogation method for the array though the gratings can be manufactured to respond to specific sources or a portion of a broadband source. For a given system, there is a general trade-off in terms of maximum element number, sensitivity and dynamic range achievable. Because of the advantages outlined above, however, the technology is providing much interest, particularly for structural health monitoring applications described in Chapter 1.

6.4 General Comments and Future Work

At the start of this thesis, the advantages of fibre optic sensors for aerospace applications were detailed and the study placed into this context. An important feature of the fibre optic approach was its inherent ability to form multiplexed sensor networks. A second important facet was that the sensors on the network, though employing different measurement principles, may modulate the same property of light (eg wavelength) to determine the measurand. One common signal processing unit may therefore be shared. Frequency modulation, in particular, has been identified as a powerful sensing tool. The work on SBS systems was therefore initiated as it potentially satisfied these requirements.

Overall, the properties of SBS have been fully assessed for frequency shifter and sensor applications. The limitations of SBS for these systems have been identified and analysed. As a result, a range of sources, fibre types and system topologies were identified which at least partly overcame the limitations and, in many cases, eliminated them completely. For sensors, the sensitivity of the SBS to temperature confirmed it as a promising candidate to measure this quantity. Its relative insensitivity to small, localised strain suggests it may be best suited in a parallel reference channel (to monitor thermal drift) for separate strain measurement systems (eg based on fibre gratings). The single source, long fibre length point and multiplexed sensors investigated were impractical in their own right in terms of low spatial resolution and high unit cost. Ring resonator technology in conjunction with SBS partially overcomes both problems for sensors and frequency shifters and addresses the general miniaturisation requirement of aerospace systems. However, it is only by employing two source pump/probe systems that the full benefits of the approach for SBS sensors can be realised in a distributed network as discussed in Chapter 5.

The research described in this thesis has opened up several areas of investigation which could not be addressed during the present study. These could be used as the basis of future research in this area. The principal topics include:

- The use of alternative sources and fibre types to extend the frequency shifting range to below 1MHz and to demonstrate in a sensor system.
- The role of feedback on the transient properties of SBS systems.
    - An analysis of ring resonators in this context
    - The use of in-fibre techniques such as Bragg gratings to maximise feedback

- An experimental verification of the theory describing Stokes and pump signal variation along the fibre length using specially designed fibre couplers
- The development of ring resonators for multiplexed sensor arrays without recourse to a piezoelectric component within the loop.
- To investigate further the polarisation dependence of certain photosensitive bleaching mechanisms within germanosilicate fibres.
- To investigate the use of alternative dopant materials to suppress photosensitive effects but enhance the optical and acoustic waveguiding properties of the fibre.

7 Management Training

7.1 Introduction

In the introduction to the thesis, both the technical and strategic motivations for undertaking the research were described. This partially fulfills one requirement of Cranfield University's SERC-supported *Total Technology* PhD programme. A second feature is to undertake a project management exercise which, though generally non-technical in nature, is directly related to the research described in Chapters 1 through 6.

Two central issues that will determine whether fibre optic sensors will be successfully implemented in aircraft are cost and performance. Chapter 1 described in some detail how the performance of many fibre optic sensors at least equals and, in many cases, exceeds that of conventional transducers. In this chapter, we address the economic issues. Cost Benefit Analysis (CBA) is a technique widely used in industry to discriminate between different courses of action such as, in this case, whether fibre sensors should or should not be installed aboard aircraft. In general (Walshe and Daffern, 1990), a CBA commences by listing the costs and benefits as they arise over time. The second step is then to attribute values to both, in present value terms. It was not possible to conduct an accurate CBA on fibre optic sensors for aerospace, however, for two reasons. Firstly, there is a shortage of relevant data in the open literature. The information that is available makes only general statements on the economic advantages and disadvantages of fibre optic sensors. Secondly, aerospace companies are extremely reluctant, for similar commercial reasons, to provide quantitative information on different costings of components, manufacturing processes and operational matters. Instead, then, this chapter describes the practical issues on which an analysis can be based, using examples from both the commercial and military aircraft sectors.

7.2 Fibre Optic Sensors For Aircraft – CBA Issues

Several independent studies in recent years (eg Eversole, 1994) on the performance levels of new products in the marketplace have shown that factors such as technological superiority, a favourable competitive environment and efficient production processes all contribute to the success of that product. The most important factor, however, is that the product matches a market-driven requirement. Conversely, new products fail for three principal reasons – an inadequate market analysis by the manufacturer, an inherently bad product and higher than anticipated costs. These surveys demonstrate the importance of undertaking studies such as a CBA prior to the development of a new product line.

In the aircraft industry, aircraft design objectives differ significantly, depending on aircraft configuration. Subsonic transport aircraft, for example, are designed for economy, military aircraft for agility and super- and hypersonic transport aircraft for speed. Safety is equally importance for each. Another objective common to all of these aircraft configurations, however, is minimisation of cost (Schmidt and Boller, 1993). The need for new technology to undergo a rigorous CBA is therefore very relevant for the aerospace sector.

The precise methodology employed in CBA is very much dependent on the subject matter. In every CBA, however, the first step is to set out costs and benefits, both current and future, ensuring that all benefits obtained and all resources expended are accounted for, as a result of taking a given option. Once these benefits and costs (including, importantly, benefits foregone) are correctly listed, the second step is to assign a quantity to each, using current values. Whilst it may be difficult to attach numbers to items or events which may be intrinsically unmeasurable, the alternative comparitive methods will be, at best, subjective and, at worst, random. Neither would commend themselves to commercial institutions. Traditionally, then, in CBA, four methods of valuation are considered (Walshe and Daffern, 1990).

(i) Market Price and Quantity Information

This is the basic and most frequently used method which directly compares capital costs (materials, manpower, etc) between the different options.

(ii) Cost Savings

An option can produce a saving in either capital or recurrent cost. As will be discussed, this is the area where many of the cost benefits for fibre sensors will accrue.

(iii) Transaction Cost Method

This refers not to direct market price data, but the increased willingness to incur costs in consuming unpriced outputs, indirectly related to taking one option.

(iv) Related Market Pricing Methods

These are referred to as 'hedonic' pricing methods, an assessment, crudely, of the 'feel-good' factor a customer is willing to pay. For example, a change in work safety regulations may affect the risks of certain occupations and, all things being equal, the wage rates in these occupations.

Examples of all four valuation types will be given in the following discussion. As stated above, due to the dearth of reliable, quantitative data on the cost of fibre sensors for aircraft, we examine instead the main issues that need to be quantified when performing a CBA on the subject. We discuss, firstly, the direct savings arising by implementing the principal applications identified in Chapter 1. Examples are then given on the effects of introducing the technology on typical life-cycle costs for both military and commercial platforms.

In Chapter 1, many examples of point fibre sensors for flight and propulsion control systems were described, in which the fibre sensor would directly replace the conventional electrical transducer. The starting point of a CBA would, therefore, be to compare the relative unit costs of the sensors. Overall, due to the boom in communications, the cost of many fibre components used in sensors (eg cables and connections) is being driven downward. However, the cost of individual fibre sensors remains generally much higher (eg Paton, 1988). One key aspect of the technology – and motivation for this whole study – is the ability to multiplex an array of sensors on a single network, sharing a common input and output processor. The unit cost of the sensors would be reduced, though the costs associated with signal processing would necessarily rise as the sensor array itself increased in size. The ability of the sensors to interface with other aircraft sub-systems, particularly the optical communications network, must also be taken into account. Some conventional electronic interface hardware may be rendered redundant, for example. These methods of valuation fall into categories (i) and (ii) listed above.

The indirect benefits of introducing fibre technology, such as improved electrical and chemical safety, would be valued using method (iv) above. These are clearly more difficult to quantify but a CBA could commence by assessing the failure rate, say, of electrical malfunctions in conventional systems and the consequences of such failures arising. These could then be compared with equivalent fibre data. A number of fibre sensors have undergone flight tests over recent years, in harness with conventional systems, so a corresponding database of safety information on fibre systems will soon emerge. A related factor is the degree of redundancy used in conventional sensors. Many current systems use dual or triple redundancy to mitigate against a single-point failure. Each will require separate input and output (electrical) connections, increasing their cost significantly. In a fibre sensor network, however, the inherent increased multiplexing capability should reduce the dependence on separate, discrete sensors and needs accounting for in the CBA.

The third application area identified in Chapter 1 for fibre sensors was in using embedded and surface mounted sensors for the health monitoring of the airframe, particularly the new structures based on composite materials. The embedding function is unique to fibre sensors due to the flexible coverage afforded by, and non-intrusive nature of, the fibres within the composite. Thus, whilst a CBA may be undertaken using cost some of the factors discussed in the previous two paragraphs, no *direct* comparison with conventional sensors can be drawn since no conventional analogue exists. However, other additional factors can be considered. For example, due to stringent safety considerations, most of the maintenance effort on aircraft is related to structural monitoring, with only a small fraction related to repair. Such monitoring is highly labour intensive and performed on the ground with the aircraft out of commission. Non-destructive testing procedures are used after fixed service time intervals according to prescribed instructions (Boller and Dilger, 1993). Regardless of the technology involved, man-power is the major cost in maintenance, leading for a demand to develop more reliable procedures for automated, on-board (and, ultimately in-flight) aircraft health monitoring. Fibre sensors are one of the leading candidates to assist in these systems.

In order to illustrate these points on the significance of maintenance costs further, consider the Life Cycle Cost (LCC), expressed as percentages of the total, for a typical military aircraft as shown in Table 8 (Schmidt and Boller, 1993). The table assumes 25 years total service. The LCC is used by aircraft manufacturers to express the effectiveness of military aircraft and is divided into two main sections – acquisition cost and operational cost as shown.

Stage	Item	Percentage Cost (of Total)
Acquisition	Initial Support	4.3
	Development	14.5
	Production	34.8
Operation	Spares	5.8
	Maintenance Labour	7.2
	Fuel	5.8
	Operator Base Costs	17.4
	Aircrew	10.1

Table 8 Life Cycle Cost Breakdown For A Typical Military Aircraft (25 Years Lifetime)

In the military sphere, survivability is an important objective which is achieved by enhancing the aircraft's capabilities and availability. Developmental work on capabilities is focussed on improving system performance and enhancing the aircraft range, maneouverability and sensor capability. Availability is improved by better reliability and maintainability, and a more rapid repair rate. Health monitoring, in all its forms, impinges on all these aspects. The early detection and localisation of damage and structural defects further extends the aircraft's life. Automatic health monitoring therefore reduces directly the maintenance labour, spares and operational base costs shown in Table 8, a large proportion of the LCC. All these factors need costing through the CBA.

The LCC can also be reduced through the weight and size reductions afforded by fibre systems. In the military sphere, replacement of the propulsion and flight control systems with fibre components (including associated communications networks) in F15 fighter and transport aircraft, weight savings of 125lb and 1500lb respectively were predicted (Seng, 1988), reducing the fuel element in the LCC. In an early consideration on the cost effects of introducing fibre optic interconnections alone (Greenwell, 1980), and excluding sensors, it was shown that fuel economies on E-3A military aircraft were equivalent to a 2.5% increase in sortie-time, a significant cost saving. Factors highlighted in this same study to offset against the benefits of installation – though equally applicable to flight control, propulsion control and health monitoring fibre sensors described above – include

- development of operations and support aspects including provision of specialist equipment and training (an example of valuation category (iii) above)

- development of manufacturing and production costs (some included in the cost of components)
- development of flight testing and qualification procedures for the new technology.

Much of this offset cost will be one-off investments, whilst the benefits from the fibres will continue to accrue over the lifetime of the aircraft.

In the commercial sector, the major objectives for competitive air transport are to meet operational reqirements of safety, punctuality, environment and comfort, whilst minimising Direct Operational Costs (DOC). DOC, as for LCC, is composed of aircraft production and aircraft operational costs. Areas where fibre optic sensor technology could contribute to cost reductions are again in performance, fuel consumption and aircraft maintenance. A reduction in aircraft production price is unlikely as a result of the introduction of fibre sensors (Schmidt and Boller, 1993). In Table 9, a typical DOC breakdown for an Airbus A320 on a 500 nautical mile trip is shown based on 1987 costs. Again, the proportion of areas in which fibre sensors impinge represents in excess of 30% of the DOC.

Component	% Cost
Aircraft Price	39.4
Crew	19.9
Fuel	19.6
Landing and Navigation	9.8
Aircraft Maintenance	6.5
Engine Maintenance	5.2

Table 9 Direct Operating Cost of An A320 Airbus Commercial Aircraft

In summary, Table 10 lists the main factors which need to be quantified for a CBA of fibre sensors for aircraft. The aerospace industry is inherently conservative with regard to new technology, rightly in view of the strict safety requirements. Now that fibre based communications and sensors are attaining technical maturity, it is clearly the cost of implementing such systems which is emerging as the key issue.

	Factor	Comment
Cost Benefit	Unit Cost Comparison	Multiplexed and Distributed Fibre Sensors Interfacing with Avionics
	Safety Improvement	
	Reliability Improvement	
	On-Board/In-Flight Health Monitoring	Maintenance Reduction Extend Operational Lifetime Improve Availability and Operational Capability
	Hardware Weight and Size Reduction	Fuel Economies Greater Payload Enhanced Manoeuverability
Cost Offset	R and D Costs	
	New Component Costs	Driven Down by Communications
	New Operation and Support Training	
	Certification/Qualification	One-Off Cost
	Specialist Equipment	One-Off Cost

Table 10 Key Factors For A CBA Of Fibre Sensors For Aircraft

8 Conclusions

An assessment has been made of the applicability of Stimulated Brillouin Scattering (SBS) in monomode optical fibres for sensing and signal processing systems. The prime motivations for the study from both commercial and technical considerations were detailed initially. This placed the work into the general context of fibre optic sensor research, principally for aerospace applications. Many specific technical merits of non-linear effects in optical fibres were then compared and assessed for sensor and signal processing purposes. SBS was identified as a suitable mechanism since it possessed a comparatively low pump power initiation threshold and the output Stokes signal from the interaction was amplified and frequency downshifted with respect to the optical pump. Further, the signal could be readily frequency modulated.

The first application of SBS in monomode fibres investigated was the demonstration of an optical heterodyning component, analogous to a Bragg cell. Using SBS, the process became all-optical - no direct electrical excitation of the fibre was necessary. By mixing the SBS signals generated simultaneously along the principal axes of high birefringent fibre and pumped at 0.5145μm, signals in the 1-10MHz region can, in principle, be produced. The use of low birefringent fibres and dual fibre topologies can extend the range down to 10kHz and up to 1GHz respectively. Using elliptical core and elliptical cladding high birefringent single fibre systems pumped at either 0.5145 or 0.532μm, carrier frequencies centred between 8 and 11MHz were produced. This was the first demonstration of an all-optical, single fibre frequency shifter system. For dual fibre systems, incorporating bow-tie birefringent fibres, frequencies up to 665MHz, dependent on the relative concentration of germania dopant between the fibre samples, were generated. An analytical approach to solving the SBS coupled wave equations was also developed and successfully applied to predict the input power requirements for, and output power levels obtained from, the fibres used in this and the later sensor work.

Two major difficulties were addressed in the frequency shifter systems. The first gave rise to frequency instabilities in the generated carrier, typically ±7.5MHz for the single fibre systems. In addition, broadband intensity modulations were produced in the system output, generally possessing a 15MHz -3dB point, but detectable up to 200MHz. Both effects were traced to non-linear dynamical processes perturbing the SBS process. The broadband bandwidth remained constant with pump power above SBS threshold for all fibre samples and pump sources. However, by introducing external feedback into the system, the magnitude of the broadband spectrum was consistently reduced by approximately 10dB across the spectrum. Significantly, the carrier modulation was also suppressed by up to 20%.

The second limitation arose through the photosensitivity exhibited by certain fibres, but particularly the bow-tie birefringent samples. After sustained pumping of the samples at 0.5145μm, their attenuation increased slowly in time, a process only partially reversed by renewed pumping at this wavelength. SBS thresholds were, therefore, significantly raised. Experiments into this mechanism showed that the photoinduced attenuation was a 3-level process, consisting of the virgin fibre, an intermediate metastable state and a third, high loss, stable state. Bleaching of the fibres from the stable to the metastable state was shown to be polarisation dependent. These results are largely in accord with the literature which has linked the photosensitive properties of the fibres to the creation and bleaching of germania related defects in the core via Two Photon Absorption in the wavelength range 0.42-0.54μm. One fibre in the study – the elliptical cladding birefringent fibre – demonstrated zero photosensitivity, despite possessing similar germania concentration levels to the bow-tie fibres. In other experiments, the polarisation properties of the photosensitive samples were modified and, hence, the ability of these to sustain SBS was severely restricted. Measurement of *direct* refractive index changes as a function of pump power was constant in all fibre samples, typically 3×10^{-8}mW^{-1}, and therefore yielded no additional information. Overall, then, in order to prevent photosensitive effects suppressing the SBS process, germania concentration in the core should be minimised and pump wavelengths in excess of 0.54μm utilised.

Fibre sensors based on frequency modulation of the output Stokes signal were investigated in both point and multiplexed systems. For temperature, Stokes frequency sensitivities of 4.3MHz°C^{-1} at 0.5145μm were measured for the fibre samples. The change in acoustic velocity with temperature was shown to be the dominant contributor to this sensitivity, an order of magnitude greater than thermo-optic effects. Output frequency instabilities, via the non-linear dynamical mechanisms, limited the effective thermal resolution of the systems to ±3°C. Post-detector averaging could improve this figure to ±2°C and the incorporation of optical feedback, as for the frequency shifter, yielded a further ±0.5°C enhancement of the resolution. From both theory and experiment, it was shown that only one Stokes signal was generated per optical input, due to the rapid depletion of the pump along the fibre length. The output frequency appeared to map the average measurand value across the interaction length. This length, typically in excess of 100m, set the system spatial resolution. The present approach was therefore not suitable for high spatial resolution measurements necessary, for example, to sense strain. A two element, dual input, multiplexed sensor was demonstrated though input power limitations prevented higher numbers of sensors from being interrogated. A full comparison was made with the two source, pump/pulsed systems proposed in the literature for fully distributed sensors that are based on instantaneous Brillouin amplification.

The frequency information present in the sustained oscillation spectrum of the Stokes signal was assessed for sensing purposes. Since no measurable perturbation to the spectrum was measured by increasing the pump power, modifying the optical path difference of the fibre through heating or introducing static mode coupling along the fibre, it was concluded that the sustained oscillations presented minimal sensing opportunities.

The systems investigated in the study were then compared with fibre ring resonators, devices which can reduce SBS threshold by two to three orders of magnitude and simultaneously restrict the active fibre length to a few metres. Extremely stable carriers are produced with no broadband spectrum and, since laser diodes may be used as pump sources, fibre photosensitivity does not occur. Ring resonators can be applied for both SBS frequency shifters and both point and multiplexed sensor systems. An overall assessment of the SBS systems completed the thesis, together with a series of possible future experiments to develop further many of the basic ideas addressed in the present study.

References

Agrawal GP Nonlinear Fibre Optics *Academic Press 1st Ed London (1989)*

Ahmed NA, Hamid S, Elder RL, Forster CP, Tatam RP and Jones JDC Fibre Optic Laser Anemometry for Turbomachinery Applications *Optics and Lasers In Engineering 16 (1992) 193-205*

Akhavan Leilabady P, Jones JDC and Jackson DA Interferometric Strain Measurement Using Optical Fibres *SPIE 586 (1985) 230-237*

Angelides D and Parsons P Optical Micromachined Pressure Sensor For Aerospace Applications *Optical Engineering 31 (1992) 1638-1641*

Aoki Y, Tajima K and Mito I Observation of Stimulated Brillouin Scattering In Single Mode Fibres With Single Frequency Laser Diode Pumping *Optics and Quantum Electronics 19 (1987) 141-143*

Ashcroft NW and Mermin ND Solid State Physics *Holt-Saunders 1st Ed Reprint Tokyo (1981)*

Askautrud JO and Engan HE Fibre Optic Frequency Shifter With No Mode Change Using Cascaded Acousto-Optic Interaction Regions *Optics Letters 15 (1990) 649-651*

Auch W, Schlemper E and Wenzel W Fibre Optic Gyroscope: An Advanced Rotation Rate Sensor *Electrical Communication 61 (1987) 372-378*

Baker GL and Gollub JP Chaotic Dynamics – An Introduction *Cambridge University Press 1st Ed Cambridge (1988)*

Bao X, Webb DJ and Jackson DA 22km Distributed Temperature Sensor Using Brillouin Gain In An Optical Fibre *Optics Letters 18 (1993a) 1038-1040*

Bao X, Webb DJ and Jackson DA 32km Distributed Temperature Sensor Based On Brillouin Loss In An Optical Fibre *Optics Letters 18 (1993b) 1561-1563*

Bao X, Webb DJ and Jackson DA Combined Distributed Temperature and Strain Sensor Based On Brillouin Loss In An Optical Fibre *Optics Letters 19 (1994) 141-143*

Bardal S and Wells PJ Intensity Dependent Shift Of Phasematched Wavelength In Second Harmonic Generation In Optical Fibres *Electronics Letters 27 (1991) 896-897*

Bardal S, Kamal A and Russell P St J Photoinduced Birefringence In Optical Fibres: A Comparative Study Of Low Birefringence and High Birefringence Fibres *Optics Letters 17 (1992) 411-413*

Bar-Joseph I, Friesem AA, Lichtman E and Waarts RG Steady and Relaxation Oscillations of Stimulated Brillouin Scattering In Single Mode Optical Fibre *JOSA B (1985) 1606-1611*

Baumbick RJ Fibre Optics For Propulsion Control Systems *J Engineering For Gas Turbines and Power 107 (1985) 851-855*

Baumbick RJ Fibre Optics For Advanced Aircraft *NASA Report TM 101294 (1988)*

Bayvel P and Radmore PM Solutions of The SBS Equations In Single Mode Optical Fibres And Implications For Fibre Transmission Systems *Electronics Letters 26 (1990) 434-436*

Bock WJ and Wolinski TR Temperature Compensated Fibre Optic Strain Sensor Based On Polarisation Rotated Reflection *SPIE 1370 (1990) 189-196*

Boller C and Dilger R In-Flight Aircraft Structure Health Monitoring Based On Smart Structures Technology *AGARD Procs 531, Paper 17, Smart Structures For Aircraft and Spacecraft (1993)*

Brooks JL, Wentworth RH, Youngquist RC, Tur M, Kim BY and Shaw HJ Coherence Multiplexing of Fibre Optic Interferometric Sensors *J Lightwave Tech 3 (1985) 1062-1072*

Bucaro JA and Dardy HD High Temperature Brillouin Scattering In Fused Quartz *J Appl Phys 45 (1974) 5324-5329*

Chaio RY, Townes CH and Stoicheff BP Stimulated Brillouin Scattering and Coherent Generation of Intense Hypersonic Waves *Phys Rev Letts 12 (1964) 592-595*

Chee JK and Lin J Polarisation Dependent Parametric and Raman Processes In A Birefringent Optical Fibre *J. Quantum Electronics 26 (1990) 541-549*

Chraplyvy AR Limitation on Lightwave Communications Imposed By Optical Fibre Nonlinearities *J. Lightwave Technology 8 (1990) 5098-5106*

Cotter D Observation of Stimulated Brillouin Scattering In Low Loss Silica Fibre At 1.3μm *Electronics Letters 18 (1982a) 495-496*

Cotter D Transient Stimulated Brillouin Scattering In Long Single Mode Fibres *Electronics Letters 18 (1982b) 504-506*

Cotter D Stimulated Brillouin Scattering In Monomode Optical Fibre *J Optical Communications 4 (1983) 10-19*

Cotter D Fibre NonLinearities In Optical Communications *Optical and Quantum Electronics 19 (1987) 1-17*

Culshaw B, Davies DEN and Kingsley SA Acoustic Sensitivity of Optical Fibre Waveguides *Electronics Letters 13 (1977) 700-701*

Culverhouse D, Farahi F, Pannell CN and Jackson DA Potential Of Stimulated Brillouin Scattering As A Sensing Mechanism For Distributed Temperature Sensors *Electronics Letters 25 (1989a) 913-915*

Culverhouse D, Farahi F, Pannell CN and Jackson DA Stimulated Brillouin Scattering: A Means To Realise Tunable Microwave Generation or A Distributed Temperature Sensor *Electronics Letters 25 (1989b) 915-916*

Dakin J Multiplexed and Distributed Optical Fibre Sensor Systems *J Phys E: Sci Instrum 20 (1987) 954-967*

Dakin J and Culshaw B Optical Fibre Sensors Vols I and II *Artech House 1st Ed London (1988)*

Dakin J, Pratt DJ, Bibby GW and Ross JN Distributed Optical Fibre Raman Temperature Sensor Using A Semiconductor Light Source and Detector *Electronics Letters 21 (1985) 569-570*

Davey ST, Williams DL, Ainslie BJ, Rothwell WJM and Wakefield B Optical Gain Spectrum Of GeO_2-SiO_2 Raman Fibre Amplifier *IEE Procs 136J (1989) 301-306*

Dynasil Corporation Data Sheet Photonics Design and Applications Handbook *Laurin Publications Nwe York (1986)*

Economou G and Davies DEN Studies of an Optical Fibre Displacement Sensor *Journal of the Institution of Electronic and Radio Engineers 57 (1987) 63-66*

Enns RH and Batra IP Saturation and Depletion In Stimulated Light Scattering *Physics Letters 28A (1969) 591-592*

Eversole W Capitalising on Defence Technologies Diversification *Texas Instruments Technology Trends Seminar, Bedford (1994)*

Farries MC and Rogers AJ Distributed Sensing Using The Stimulated Raman Interaction In a Monomode Optical Fibre *Procs Optical Fibre Sensors 2 Conference, Stuttgart, Paper 45 (1984) 121-132*

Farries MC, Fermann ME, Laming RI, Poole SB and Payne DN Distributed Temperature Sensor Using Nd^{3+} Optical Fibre *Electronics Letters 22 (1986) 418-419*

Fields JN, Asawa CK, Ramer OG and Barnowski MK Fibre Optic Pressure Sensor *J. Acoustic Society of America 67 (1980) 816-818*

Figueroa L, Hong C, Huggins RW, Miller GE, Popoff AA, Porter CR , Smith DK and Van Deventer B Fibre Optics For Military Aircraft Flight Systems *IEEE LCS Procs (1991) 52-65*

Ford HD and Tatam RP Narrow-Band Wavelength Division Multiplexers Using Birefringent Optical Fibre *Optics Communications 98 (1993) 151-158*

Friebele EJ and Griscom DL Colour Centres In Glass Optical Fibre Waveguides *Materials Research Society Symposium Procs 61 (1986) 319-331*

Fritsch K and Beheim G Wavelength Division Multiplexed Digital Optical Position Transducer *Optics Letters 11 (1986) 1-3*

Gaeta AL and Boyd RW Stochastic Dynamics of Stimulated Brillouin Scattering In An Optical Fibre *Physical Review A 44 (1991) 3205-3209*

Gardiner PT and Edwards RA Fibre Optic Sensors For Aircraft Flight Controls *Royal Aeronautical Society Colloq Procs (1987) p42-63*

Garmire E and Townes CH Stimulated Brillouin Scattering In Liquids *Applied Physics Letters 5 (1964) 84-86*

Giles IP Distributed Optical Fibre Sensors *Phys Technology 18 (1987) 153-157*

Gloge D Weakly Guiding Fibres *Applied Optics 10 (1971) 2252-2258*

Glomb WL Fibre Optic Circuits For Aircraft Engine Controls *SPIE 840 (1987) 122-127*

Glomb WL and Varshneya D Optical Multiplexing For Aircraft Sensors: Issues and Options *SPIE 989 (1988) 2-10*

Greenwell RD Economics and Key Trade-Offs of Fibre Optic Links – An Airbourne Platform Example *Procs of Int Telemetry Conference, Instrument Society of America (1980) 403-406*

Hand DP and Russell P St J Photoinduced Refractive Index Changes In Germanosilicate Fibres *Optics Letters 15 (1990) 102-104*

Harrison RG, Uppal JS, Johnstone A and Moloney JV Evidence of Chaotic Stimulated Brillouin Scattering In Optical Fibres *Phys Rev Letters 65 (1990) 167-170*

Henry WM Fibre Acoustic Modes and Stimulated Brillouin Scattering *Int J of Optoelectronics 7 (1992) 453-478*

Hill KO, Kawasaki BS Johnson DC CW Brillouin Laser *Applied Physics Letters 28 (1976a) 608-609*

Hill KO, Johnson DC, Kawasaki BS CW Generation of Multiple Stokes and Anti-Stokes Brillouin Shifted Frequencies *Applied Physics Letters 29 (1976b) 185-187*

Hill KO, Johnson DC, Kawasaki BS and MacDonald RI CW Three Wave Mixing In Single Mode Optical Fibres *J. Applied Physics 49 (1978) 5098-5106*

Horiguchi T, Kurashima T and Tateda M Tensile Strain Dependence of Brillouin Frequency Shift In Silica Optical Fibres *IEEE Photonics Technology Letters 1 (1989) 107-109*

Horiguchi T and Tateda M BOTDA – Non-Destructive Measurement of Single Mode Optical Fibre Attenuation Characteristics Using Brillouin Interaction: Theory *J Lightwave Technology 7 (1989) 1170-1176*

Ippen EP Laser Applications To Optics and Spectroscopy Volume 2 *Ch 6 Addison Wesley Massachusetts (1975)*

Ippen EP and Stolen RH Stimulated Brillouin Scattering In Optical Fibres *Applied Physics Letters 21 (1972) 539-541*

Jackson DA, Kersey AD, Corke M and Jones JDC Pseudo-Heterodyne Detection Scheme For Optical Interferometry *Electronics Letters 18 (1982) 1081-1083*

Jackson DA Monomode Fibre Optic Interferometers For Precision Measurements *J Phys E:Sci Instruments 18 (1985) 981-1001*

Jen CK, Oliveira JEB, Goto N and Abe K Role of Guided Acoustic Wave Properties In Single Mode Optical Fibre Design *Electronics Letters 24 (1988) 1419-1420*

Jen CK, Yu J, Neron C, Shang A, Saravanos C, Abe K and Bonnell L Effects of Acoustic Properties On Stimulated Backward Brillouin Scattering of Single Mode Optical Fibres *Procs of 1st International Workshop on Photonics Networks and Components World Scientific (1991) 308-314*

Johnson M Fibre Displacement Sensors For Metrology and Control *Opt Eng 24 (1985) 961-965*

Johnson RV and Marburger JH Relaxation Oscillations In Stimulated Raman and Brillouin Scattering *Physical Review A 4 91971) 1175-1182*

Johnstone A Nonlinear Dynamics of Stimulated Brillouin Scattering In Optical Fibres *PhD Thesis, Heriot-Watt University 1992*

Johnstone A, Lu W, Uppal JS and Harrison RG Sustained and Bursting Oscillations In Stimulated Brillouin Scattering With External Feedback In Optical Fibre *Optics Communications 81 (1991) 222-224*

Jones JDC and Jackson DA Fibre Optic Sensors *Optica Acta 33 (1986) 1469-1504*

Kaiser W and Maier M Laser Handbook Part E2 *North Holland Publishing Company Amsterdam 1st Ed (1972)*

Kajanto I and Friberg AT Silicon Based Fibre Optic Temperature Sensor *J Phys:E Sci Instrum 21 (1988) 555-558*

Kalli K, Culverhouse D and Jackson DA Fibre Frequency Shifter Based On Generation of SBS In High Finesse Ring Resonators *Optics Letters 16 (1991) 1538-1540*

Kalli K and Jackson DA Ring Resonator Optical Spectrum Analyzer with 20kHz Resolution *Optics Letters 17 (1992) 1090-1092*

Kaminow IP Polarisation In Optical Fibres *IEEE J. Quantum Electronics QE-17 (1981) 15-22*

Kandebo SW NASA, Navy To Evaluate Fly By Light Sensors In F/A-18 *Aviation Week and Space Technology August 2nd (1993) 55-56*

Kanellopoulos SE, Handerek VA, Jamshidi H and Rogers AJ Simultaneous Observation of Photobleaching and Photorefractive Effects In Ge-Doped Optical Fibres *IEEE Photonics Tech Letters 3 (1991) 244-246*

Kersey AD Demonstration of A Hybrid Time/Wavelength Division Multiplexed Interferometric Fibre Sensor Array *Electronics Letters 27 (1991) 554-555*

Kersey AD and Dandridge A Dual Wavelength Interferometric Sensing *SPIE 798 (1987) 176-184*

Kersey AD and Dandridge A Multiplexed Mach Zehnder Ladder Array With Ten Sensor Elements *Electronics Letters 25 (1989) 1298-1299*

Khan OS and Tatam RP Optical Frequency Shifter Based On Stimulated Brillouin Scattering In a Birefringent Optical Fibre Ring Resonator *Optics Communications 103 (1993) 161-168*

Khan OS, Mahmood S, Bowdler K and Tatam RP An Interferometric Technique For Measuring The Frequency Response of Optical Detector-Amplifier Combinations *Measurement Science Technology 4 (1993) 1232-1237*

Kim BY, Blake JN, Engan HE and Shaw HJ All Fibre Acousto-Optic Frequency Shifter *Optics Letters 11 (1986) 389-391*

Kurashima T, Horiguchi T and Tateda M Thermal Effects on the Brillouin Frequency Shift In Jacketed Optical Silica Fibres *Applied Optics 29 (1990a) 2219-2222*

Kurashima T, Horiguchi T and Tateda M Distributed Temperature

Sensor Using Stimulated Brillouin Scattering In Optical Silica Fibres *Optics Letters 15 (1990b) 1038-1040*

Kurashima T, Horiguchi T and Tateda M Thermal Effects of Brillouin Gain Spectra In Single Mode Fibres *IEEE Photonics Technology Letters 2 (1990c) 718-720*

Labudde P, Anliker P and Weber HP Transmission of Narrowband High Power Laser Radiation Through Optical Fibres *Optics Communications 32 (1980) 385-390*

Lay M Litton Poly-Scientific Awarded FOCSI II Contract *Litton Poly-Scientific Press Release (1990)*

Lin C Nonlinear Optics In Fibres For Fibre Measurements and Special Device Functions *J. Lightwave Technology LT-4 (1986) 1103-1115*

Lin C, Cohen LG, Stolen RH, Tasker GW and French WG Near Infrared Sources In The 1-1.3μm Region By Efficient Stimulated Raman Emission In Glass Fibres *Optics Communications 20 (1977) 426-428*

Lin C, Reed WA, Pearson AD and Shang H-T Phase Matching In The Minimum Chromatic Dispersion Region Of Single Mode Fibres For Stimulated Four Photon Mixing *Optics Letters 6 (1981) 493-495*

Little WR A Review of Fibre Optic Flight Experience: Past Problems, Future Directions *SPIE 989 (1989) 11-17*

Lorrain P and Corson D Electromagnetic Fields and Waves *Freeman and Co 2nd Ed San Francisco (1970)*

Lu W, Johnstone A and Harrison RG Deterministic Dynamics of Stimulated Scattering Phenomena With External Feedback *Physical Review A 46 (1992)*

Malitson IH Interspecimen Comparison of the Refractive Index of Fused Silica *JOSA 55 (1965) 1205-1210*

Marcuse D Gaussian Approximation Of The Fundamental Modes Of Graded Index Fibres *JOSA 68 (1978) 103-109*

Measures RM Fibre Optic Sensor Considerations and Developments For Smart Structures *SPIE 1588 (1991) 282-299*

Measures RM, Melle S and Liu K Wavelength Demodulated Bragg Grating Fibre Optic Sensing Systems For Addressing Smart Structure Critical Issues *Smart Materials and Structures 1 (1992) 36-44*

Melle SM, Liu K and Measures RM Practical Fibre Optic Bragg Grating Strain Gauge System *Applied Optics 32 (1993) 3601-3609*

Meltz G and Morey W Bragg Grating Formation and Germanosilicate Fibre Photosensitivity *SPIE 1516 (1991) 185-189*

Miller GE Fibre Optic Control of Jet Aircraft Engines *Procs Instrumentation Symposium 32 (1986) 269-282*

Morey WW, Dunphy JR and Meltz G Multiplexing Fibre Bragg Grating Sensors *Fibre and Integrated Optics 10 (1992) 351-360*

Morton R and Little B Fibre Optic Sensor Interface Standardisation *Fibre and Integrated Optics 11 (1993) 151-157*

Nitka EF Applications of Fibre Optic Sensors In Advanced Engine Controls *SPIE 985 (1988) 12-19*

Ouellette F, Gagnon D, Larochelle S and Poirier S Photoinduced Self-Organisation In Optical Fibre: Some Answered and Unanswered Questions *SPIE 1516 (1991) 2-13*

Pannell CN, Tatam RP, Jones JDC and Jackson DA A Fibre Optic Frequency Shifter Utilizing Travelling Flexure Waves In Birefringent Fibre *Journal of the Institution of Electronic and Radio Engineers 58(1988) S92-S98*

Parvaneh F, Valente LCG, Handerek VA and Rogers AJ Forward Scatter Frequency Derived Optical Fibre Sensing Using The Kerr Effect *Electronics Letters 28 (1992) 1080-1082*

Paton AT and Scott JC Distributed Temperature Sensing Using UV Light *Procs Optical Fibre Sensors 7 Conference, Sydney, Paper Tho4.4 (1990)*

Paton BE Optical Sensing Principles and Optical Sensor Issues *Optical Testing and Metrology II SPIE 954 (1988) 606-616*

Pelous J and Vacher R Thermal Brillouin Scattering In Crystalline and Fused Quartz From 20 To 1000°C *Solid State Communications 18 (1976) 657-661*

Pini R, Salimbeni R, Vannini M, Haider AF and Lin C High Conversion Efficiency Ultraviolet Fibre Raman Oscillator-Amplifier System *Applied Optics 25 (1986) 1048-1050*

Pitt GD Oil In Troubled Waters *Physics Bulletin 28 (1977) 459-460*

Poustie AJ Guided Acoustic Wave Brillouin Scattering with Optical Pulses *Optics Letters 17 (1992) 574-576*

Poyntz-Wright LJ, Fermann ME and Russell P St J Nonlinear Transmission and Colour Centre Dynamics In Germanosilicate Fibres At 420-540nm *Optics Letters 13 (1988) 1023-1025*

Poyntz-Wright LJ and Russell P St J Spontaneous Relaxation Processes In Irradiated Germanosilicate Optical Fibres *Electronics Letters 25 (1989) 478-480*

Rich TC and Pinnow DA Evaluation of Fibre Optical Waveguides Using Brillouin Spectroscopy *Applied Optics 13 (1974)1376-1378*

Risk WP, Kino GS and Shaw HJ Fibre Optic Frequency Shifter Using A Surface Acoustic Wave Incident At An Oblique Angle *Optics Letters 11 (1986a) 115-117*

Risk WP, Kino GS and Khuri-Yakub B Tunable Optical Filter In Fibre Optic Form *Optics Letters 11 (1986b) 389-391*

Robbins C Developments In Temperature Sensing Using Fibre Optic Techniques *Transducer Technologies June (1986) 10-15*

Rogers AJ Polarisation Optical Time Domain Reflectometry: Technique For Investigating Attenuation Characteristics *Applied Optics 20 (1981) 1060-1074*

Rogers AJ Distributed Sensors: A Review *SPIE 798 (1987) 26-35*

Rogers AJ Distributed Optical Fibre Sensors Based On Counter-Propagating Beams and NonLinear Interactions *SPIE 1011 (1988) 10-17*

Rogers AJ and Handerek VA Novel Methods For Distributed Optical Fibre Sensors *SPIE 1586 (1991) 2-12*

Rowell NL, Thomas PJ, Van Driel HM and Stegeman GI Brillouin Spectrum of Single Mode Optical Fibres *Applied Physics Letters 34 (1979) 139-141*

Ruffles P Engine Technology For The 1990s *SBAC Farnborough '90 Magazine (1990) 17-19*

Russell P St J, Culverhouse D and Farahi F Experimental Observation Of Forward Stimulated Brillouin Scattering In Dual Mode Single Core Fibres *Electronics Letters 26 (1990) 1195-1196*

Russell P St J, Culverhouse D and Farahi F Theory of Forward Stimulated Brillouin Scattering In Dual Mode Single Core Fibres *IEEE J. Quantum Electronics 27 (1991a) 836-842*

Russell P St J and Hand DP Rocking Filter Formation In Photosensitive High Birefringence Fibres *Electronics Letters 26 (1990) 1846-1848*

Russell P St J, Hand DP, Chow YT and Poyntz-Wright LJ Optically Induced Creation, Transformation and Organisation of Defects and Colour Centres In Optical Fibres *SPIE 1516 (1991b) 47-54*

Sabert H, Dong L and Russell P St J Versatile Acousto-Optic Flexural Wave Modulator, Filter And Frequency Shifter In Dual Core Fibre *J. Optoelectronics 7 (1992) 189-194*

Sakai I Frequency Division Multiplexing of Optical Fibre Sensors Using A Frequency Modulated Source *Optics and Quantum Electronics 18 (1986) 279-289*

Santos JL and Jackson DA Time Division Multiplexing of Coherence Tuned Optical Fibre Sensors Based Upon A Multimode Laser Diode *Optics Communications 83 (1991) 37-42*

Schmidt W and Boller C Smart Structures – A Technology For Next Generation Aircraft *AGARD Procs 531, Paper 1, Smart Structures For Aircraft and Spacecraft (1993)*

Seng T Overview of NASA Research In Fibre Optics For Aircraft Controls *NASA Report TM 100919 (1988)*

Senior JM Optical Fibre Communications: Principles and Practice *Prentice Hall International, London 1st Ed (1985)*

Shelby RM, Levenson MD and Bayer PW Resolved Forward Brillouin Scatter In Optical Fibres *Phys Rev Letts 54 (1985) 939-942*

Shen YR The Principles of Non-Linear Optics *John Wiley, 1st Ed New York (1984)*

Shibata N, Waarts RG and Braun RP Brillouin Gain Spectra For Single Mode Fibres Having Pure Silica, GeO_2-Doped and P_2O_5-Doped Cores *Optics Letters 12 (1987) 269-271*

Shibata N, Azuma Y, Horiguchi T and Tateda M Identification of Longitudinal Acoustic Modes Guided In The Core Region Of A Single Mode Optical Fibre By Brillouin Gain Spectra Measurements *Optics Letters 13 (1988) 595-597*

Smith RG Optical Power Handling Capacity of Low Loss Optical Fibres As Determined By Stimulated Raman and Stimulated Brillouin Scattering *Applied Optics 11 (1972) 2489-2494*

Snyder AW and Love JD Optical Waveguide Theory *Chapman and Hall 1st Ed London (1983)*

Spillman WB and MacMahon DH Frustrated Total Internal Reflection Multimode Fibre Optic Hydrophone *Applied Optics 19 (1980) 113-117*

Spillman WB and Fuhr PL Fibre Optic Rotary Displacement Sensor With Wavelength Encoding *Applied Optics 27 (1988) 3081-3084*

Stokes LF, Chodorow M and Shaw HJ All Single Mode Fibre Resonator *Optics Letters 7 (1982a) 288-290*

Stokes LF, Chodorow M and Shaw HJ All Fibre Stimulated Brillouin Ring Laser with Submilliwatt Pump Threshold *Optics Letters 7 (1982b) 509-511*

Stolen RH Phase Matched Stimulated Four Photon Mixing In Silica Fibre Waveguides *IEEE J. Quantum Electronics QE-11 (1975) 100-103*

Stolen RH NonLinear Properties of Optical Fibres *Optical Fibre Telecommunications Academic Press 1st Ed New York (1979)*

Stolen RH and Bjorkholm JE Parametric Amplification and Frequency Conversion In Optical Fibres *J. Quantum Electronics QE-18 (1982) 1062-1072*

Stolen RH and Ippen EP Raman Gain In Glass Optical Waveguides *Applied Physics Letters 22 (1973) 276-278*

Tang CL Saturation and Spectral Characteristics of the Stokes Emission In The Stimulated Brillouin Process *J Applied Physics 37 (1966) 2945-2955*

Tatam RP, Jones JDC and Jackson DA Optical Polarisation State Control Schemes Using Fibre Optics On Bragg Cells *J. Phys E:Sci Instrum 19 (1986) 711-717*

Tateda M, Horiguchi T, Kurashima T and Ishihara K First Measurement of Strain Distribution Along Field Installed Optical Fibres Using Brillouin Spectroscopy *J Lightwave Technology 8 (1990) 1269-1272*

Tkach RW, Chraplyvy AR and Derosier RM Spontaneous Brillouin Scattering For Single Mode Optical Fibre Characterisation *Electronics Letters 22 (1986) 1011-1013*

Todd JR Toward Fly-By-Light Aircraft *SPIE 989 (1988) 38-42*

Uesugi N, Ikeda M and Sasaki Y Maximum Single Frequency Input Power In A Long Optical Fibre Determined By Stimulated Brillouin Scattering *Electronics Letters 17 (1981) 379-381*

Ulrich R, Rashleigh SC and Eickhoff W Bending Induced Birefringence In Single Mode Fibres *Optics Letters 5 (1980) 273-275*

Ulrich R and Simon A Polarisation Optics of Twisted Single Mode Fibres *Applied Optics 18 (1979) 2241-2251*

Underwood FM Strain Measurement In Carbon Fibre Laminates Using A Raman Optomechanical Strain Gauge *PhD Thesis Univ. of London (1989)*

Vengsarkar AM, Michie WC, Jankovic L, Culshaw B and Claus RO Fibre Optic Sensor For Simultaneous Measurement of Strain and Temperature *SPIE 1367 (1990) 249-260*

Venkatesh S Optical Microresonator Sensor Systems *Journal of the Institution of Electronic and Radio Engineers 58 (1988) 579-584*

Walshe G and Daffern P Managing Cost Benefit Analysis *Macmillan 1st Ed London (1990)*

Wolfbeis O Fluorescence Optical Systems In Analytical Chemistry *Trends In Analytical Chemistry 4 (1985) 184-188*

Wrigley M Optical Systems For Gas Turbine Engines *SPIE 656 (1986) 231-237*

Yariv A Coupled Mode Theory For Guided Wave Optics *IEEE J Quantum Electronics QE9 (1973) 919-933*

Zarinetchi F, Smith SP and Ezekiel S Stimulated Brillouin Fibre Optic Laser Gyroscope *Optics Letters 16 (1991) 229-231*

Publications/Presentations Arising From Study

Duffy CJ and Tatam RP Optical Heterodyne Carrier Generation Using Stimulated Brillouin Scattering In Birefringent Optical Fibre *Electronics Letters 27 (1991) 2004-2006*

Duffy CJ and Tatam RP Optical Frequency Shifter Technique Based On Stimulated Brillouin Scattering In Birefringent Optical Fibre *Applied Optics 32 (1993) 5966-5972*

Duffy CJ and Tatam RP Optical Frequency Shifter Based On Stimulated Brillouin Scattering In Birefringent Optical Fibre *SPIE Vol 1511 (1991) 155-165 presented at Fibre Optic Sensors: Engineering and Applications Conference, The Hague, 1991*

Duffy CJ and Tatam RP Optical Heterodyne Carrier Generation Utilising Stimulated Brillouin Scattering In Monomode Optical Fibre *presented at European Quantum Electronics Conference, Edinburgh, Paper NDTh4, 1991*

Tatam RP and Duffy CJ A Fibre Optic Frequency Shifter Utilising Stimulated Brillouin Scattering In Birefringent Optical Fibre *presented at Optical Fibre Sensor 8 Conference, Monterey, IEEE/OSA Procs, 181-184, 1992*

Tatam RP, Ahmed NA, Atcha H, Duffy CJ and Elder RL Novel Implementations of Optical Diagnostic Techniques For Aerospace Applications *presented at Aerotech '92 Conference, Birmingham, IMechE Paper, C428/21/081, 1992*

Duffy CJ and Tatam RP Stimulated Brillouin Scattering In Monomode Optical Fibre For Sensing and Signal Processing Applications *presented at Applied Optics and Opto-Electronics Conference, Leeds, IOP Procs, 50-52, 1992*

Duffy CJ, Khan OS and Tatam RP Optical Signal Processing And Sensing Techniques Exploiting Stimulated Brillouin Scattering In High Birefringent Optical Fibre *presented at Optical Fibre Sensors 9 Conference, Florence, IEEE/OSA Procs, 7-10, 1993*

Appendices

Appendix A – Solution To Coupled Intensity Scattering Equations

We solve the equations for the *general* case of optical fibre stimulated scattering systems ie both the pump and scattered signals propagate in the forward (positive z) direction. The input air-core interface is located at $z = 0$. Under cw and steady-state (d.c.) conditions, the changes in intensity of the pump and scattered signals are given by

$$\frac{\delta I_p(z)}{\delta z} = -gI_p(z)I_s(z) - \alpha I_p(z) \tag{A1(a)}$$

$$\frac{\delta I_s(z)}{\delta z} = +gI_p(z)I_s(z) - \alpha I_s(z) \tag{A1(b)}$$

where $I_p(z)$ and $I_s(z)$ are the pump and scattered signal intensities at z, g is the gain factor of the scattering process and α is the fibre attenuation coefficient and is assumed to be constant for both I_p and I_s.

Dividing A1(a) through by $I_p(z)$ produces:

$$\frac{\delta\Big[\log\big(I_p(z)\big)\Big]}{\delta z} = -gI_s(z) - \alpha \tag{A2(a)}$$

Similarly, for A1(b) with $I_s(z)$,

$$\frac{\delta\Big[\log\big(I_s(z)\big)\Big]}{\delta z} = +gI_p(z) - \alpha \tag{A2(b)}$$

is obtained. Applying the substitutions

$$I_p(z) = \exp(-\alpha z)J_p\big(\exp(-\alpha z)\big) \text{ and } I_s(z) = \exp(-\alpha z)J_s\big(\exp(-\alpha z)\big)$$

into equations A2 yields

$$\frac{\delta}{\delta z}\Big[\log J_p\big(\exp(-\alpha z)\big)\Big] = -g\exp(-\alpha z)J_s\big(exp(-\alpha z)\big) \tag{A3(a)}$$

$$\frac{\delta}{\delta z}\Big[\log J_s\big(\exp(-\alpha z)\big)\Big] = +g\exp(-\alpha z)J_p\big(\exp(-\alpha z)\big) \tag{A3(b)}$$

where $J_{p,s}\big(\exp(-\alpha z)\big)$ are defined by the substitution. Using a second substitution,

$$Y = \exp(-\alpha z) \text{ which defines } \frac{\delta}{\delta z} = -\alpha Y\frac{\delta}{\delta Y}$$

equations A3(a) and (b) are rewritten as

$$\alpha\frac{\delta}{\delta Y}\log J_p(Y) = \alpha\frac{J_p'(Y)}{J_p(Y)} = +gJ_s(Y) \tag{A4(a)}$$

$$\alpha\frac{\delta}{\delta Y}\log J_s(Y) = \alpha\frac{J_s'(Y)}{J_s(Y)} = -gJ_p(Y) \qquad A4(b)$$

where $J_{p,s}'(Y)$ are the first order differentials of $J_{p,s}(Y)$ respectively. $J_p(Y)$ can be eliminated from equations A4 by, firstly, differentiating A4(b) with respect to Y and then dividing through by $J_p(Y)$ to produce

$$-\frac{\alpha}{J_p(Y)}\frac{\delta}{\delta Y}\Big(\frac{J_s'(Y)}{J_s(Y)}\Big) = g\frac{J_p'(Y)}{J_p(Y)} \qquad A5$$

By substituting A4(a) and then A4(b) into A5, it can be shown that

$$\frac{g}{\alpha}J_s'(Y) = \frac{\delta}{\delta Y}\Big(\frac{J_s'(Y)}{J_s(Y)}\Big) \qquad A6$$

Hence, by integration,

$$J_s'(Y) = \frac{g}{\alpha}J_s^2(Y) + KJ_s(Y) \qquad A7$$

where K is the constant of integration. An expression for K can be deduced by evoking the boundary conditions of the system. That is, for $z = 0$ (or $Y = 1$), $J_{p,s}(Y) = I_{p,s}(0)$ from the substitution definitions above. Hence,

$$K = \frac{J_s'(Y)}{J_s(Y)} - \frac{g}{\alpha}J_s(Y) = -\frac{g}{\alpha}\big(I_p(0) + I_s(0)\big) \qquad A8$$

A7 represents a first order non-linear differential equation and can be solved by substituting an expression of the form

$$J_s(Y) = \big(A + B\exp(-qY)\big)^C \qquad A9$$

into A7. Hence, by setting $C = -1$, and inserting the appropriate values of $J_s(Y)$ and $J_s'(Y)$ into A7

$$\big(A + B\exp(-qY)\big)^{-2}\Big[\tfrac{g}{\alpha} + K\big(A + B\exp(-qY)\big)\Big] = \big(+qB\exp(-qY)\big)\big(A + B\exp(-qY)\big)^{-2} \qquad A10$$

Equating coefficients of the exponential term on both sides of the equation, it is shown that $q = +K$ and similarly for the constant terms, $A = -g/\alpha K$, where K is defined in A8. To calculate B, again use the fact that $J_s(Y) = I_s(0)$ at $z = 0$ (ie $Y = 1$) in A9 which yields

$$B = \frac{\exp(+K)}{I_s(0)}\big(1 - AI_s(0)\big) = \exp(+K)\Big(\frac{\alpha K + gI_s(0)}{\alpha K I_s(0)}\Big) \qquad A11$$

By inserting the values for A, B and q into A9, and eliminating $J_s(Y)$ using the initial substitution above, we obtain

$$I_s(z) = \frac{\alpha K\exp(-\alpha z)}{\Big(\frac{\alpha K + gI_s(0)}{I_s(0)}\Big)\exp\Big[K\big(1 - \exp(-\alpha z)\big)\Big] - g} \qquad A12$$

Substituting for K and appropriate rearrangement produces

$$I_s(z) = \frac{(1+\beta)I_s(0)\exp(-\alpha z)}{\beta + \exp\Big[-\gamma(1+\beta)\Big(1 - exp(-\alpha z)\Big)\Big]} \qquad A13$$

where $\beta = I_s(0)/I_p(0)$ and $\gamma = gI_p(0)/\alpha$.

A similar argument is pursued to deduce an expression for $I_p(z)$. The term $J_s(Y)$ can be eliminated from A4 to produce a first order non-linear differential equation in $J_p(Y)$ alone,

$$J_p'(Y) = -\frac{g}{\alpha}J_p^2(Y) + K_1 J_p(Y) \qquad A14$$

where K_1 is the integration constant and related to the boundary conditions by

$$K_1 = \frac{g}{\alpha}\Big(I_p(0) + I_s(0)\Big) \qquad A15$$

The general solution given by A9 for $J_p(Y)$ with $C = -1$ again satisfies A14 with constants $q = +K_1$ and $A = g/\alpha K_1$. In this case, B takes the form

$$B = \exp(K_1)\Big(\frac{\alpha K_1 - gI_p(0)}{\alpha K_1 I_p(0)}\Big) \qquad A16$$

Inserting the appropriate values into A9 gives

$$I_p(z) = \frac{\alpha K_1 \exp(-\alpha z)}{\Big(\frac{\alpha K_1 - gI_p(0)}{I_p(0)}\Big)\exp\Big[K_1\Big(1 - exp(-\alpha z)\Big)\Big] + g} \qquad A17$$

Substitution for K_1 and simple algebraic manipulation yields

$$I_p(z) = \frac{(1+\beta)I_p(0)\exp(-\alpha z)}{1 + \beta\exp\Big[\gamma(1+\beta)\Big(1 - \exp(-\alpha z)\Big)\Big]} \qquad A18$$

where γ and β are defined as above.

Thus, in summary, if a term $G(z)$ is defined as

$$G(z) = \exp\Big[-\gamma(1+\beta)\Big(1 - \exp(-\alpha z)\Big)\Big] \qquad A19$$

then $I_s(z)$ and $I_p(z)$ can be expressed as

$$I_s(z) = \frac{(1+\beta)I_s(0)\exp(-\alpha z)}{G(z) + \beta} \qquad A20(a)$$

and

$$I_p(z) = \frac{(1+\beta)G(z)I_p(0)\exp(-\alpha z)}{G(z) + \beta} \qquad A20(b)$$

Appendix B Computer Programme for SBS Predictions

```
c     This programme calculates the output Stokes and pump powers emitted
c     from a fibre-optic SBS system for varying input pump powers. It also
c     enables calculation of both pump and Stokes signals as a function of
c     fibre length, for a given input pump power. The calculation ignores
c     2nd order SBS, FWM and other non-linear effects.
      real effa,dist,effl,gain,alpha,probe,pthr,x,y,z,pumpin1,pumpin2,pu
     +mpout,g1,g2,s,p,t,u,stokes1,stokes2,stolen,pumlen
      integer i,j
c     effa = effective core area ; alpha = loss coefficient ;dist = length;effl
c     = effective length; gain = Brillouin gain
      effa=6.53*(10.0**(-12.0))
      alpha=5.96*(10.0**(-3.0))
      dist=406.0
      gain=3.5*(10.0**(-11.0))
      effl=((1.0-exp(-(alpha*dist)))/alpha)
c     To calculate effective spontaneous Stokes probe, counterpropagating to
c     pump, 'launched' from other end. pthr = SBS threshold power.
      pthr=((21.0*effa)/(gain*effl))
      probe=pthr*(exp((alpha*dist)-21.0))
      write (6,*) effl,pthr,probe
c     This is constant for a given system. Now, we calculate the Stokes value
c     at z=0 and the pump power at z=L.
      p=0
      do 5 i=1,100
         p=p+1
         pumpin1=(0.001+((p-1)*0.001))
         stokes1=0.0
         s=0
         do 10 j=1,10000
            s=s+1
c           probe=pumpin1*(10**(-5.0))
            x=probe*(exp((1-(stokes1/pumpin1))*gain*effl*pumpin1
     +/effa))-(probe*stokes1/pumpin1)
            y=(1-(stokes1/pumpin1))*stokes1*(exp(alpha*dist))
            z=x-y
c           write(6,*) pumpin1,stokes1,z
            if (z.le.0.0) goto 11
            stokes1=(0+((s*pumpin1)/10000.0))
 10      continue
c       We now calculate the output pump power for a given input pump power.
 11      g1=exp(((1-stokes1/pumpin1))*21.0*pumpin1/pthr)
         pumpout=((1-stokes1/pumpin1)*g1*pumpin1*(exp(-alpha*dist)))/
     +(g1-(stokes1/pumpin1))
      write(6,*)pumpin1,stokes1,pumpout
      write(25,*)pumpin1,stokes1,pumpout
 5    continue
c     We now calculate the length dependence of both Stokes and pump signals.
c     We commence, again, by calculating a value for the Stokes signal at L=0
c     for a given input pump power.
      pumpin2=0.05
      t=0
      stokes2=0.0
      do 20 j=1,10000
         t=t+1.0
c        probe=pumpin2*(10**(-5.0))
         x=probe*(exp((1-(stokes2/pumpin2))*21.0*pumpin2/pthr)
     +-(stokes2/pumpin2))
         y=(1-(stokes2/pumpin2))*stokes2*(exp(alpha*dist))
         z=x-y
         if (z.le.0.0) goto 21
c        write(6,*)pumpin2,stokes2,x,y
         stokes2=(0.0+(t*pumpin2/10000))
 20   continue
 21   write(6,*)pumpin2,stokes2
c     We can now calculate the Stokes/pump length dependence.
      u=0.0
```

```
      zed=0.0
      write(26,*)zed,stokes2,pumpin2
      do 30 i=1,396
         u=u+1.0
         zed=((2.525*10**(-3.0))+((u-1)/396))*dist
         g2=exp((1-(stokes2/pumpin2))*gain*pumpin2*(1-exp(-alpha*zed))/
     +(alpha*effa))
         stolen=(1-(stokes2/pumpin2))*stokes2*exp(alpha*zed)/
     +(g2-(stokes2/pumpin2))
         pumlen=((1-(stokes2/pumpin2))*g2*pumpin2*exp(-alpha*zed)/
     +(g2-(stokes2/pumpin2)))
         write(6,*)zed,stolen,pumlen
         write(26,*)zed,stolen,pumlen
30    continue
      stop
      end
```

Appendix C Parameters Of Optical Fibres Used During The Study

York High Birefringent Argon Ion Fibre

Label In Text	HB450
Birefringence Type	Stress Inducing, 'Bow-Tie' B_2O_3-SiO_2 Doped Region In Cladding
Beat Length	1.05mm
Numerical Aperture	0.163
Core Radius, a	$1.04\mu m$
Cladding Radius	$62.5\mu m$
Cut-Off Wavelength	$0.44\mu m$
Fibre V-Number (at $0.5145\mu m$)	2.06
Mode Area (at $0.5145\mu m$)	$1.43\pi a^2$
Attenuation (at $0.5145\mu m$)	$60.8dBkm^{-1}$
Core Composition	Silica/5%wt Ge conc
Cladding (Inner)	Phosphorous-Fluorine Doped Silica

York Single Mode Argon Ion Fibre

Label In Text	SM450
Birefringence Type	Not Applicable; Circularly Symmetric Core and Cladding Regions
Beat Length	Not Applicable
Numerical Aperture	0.11
Core Radius, a	$1.67\mu m$
Cladding Radius	$62.5\mu m$
Coating Radius	$124.5\mu m$
Cut-Off Wavelength	$0.482\mu m$
Fibre V-Number (at $0.5145\mu m$)	2.25
Mode Area (at $0.5145\mu m$)	$1.22\pi a^2$
Attenuation (at $0.5145\mu m$)	$32.0dBkm^{-1}$
Core Composition	Silica/5%wt Ge conc
Cladding (Inner)	Phosphorous-Fluorine Doped Silica

3M/EOTec High Birefringent Helium Neon Fibre

Label In Text	EOTec/HB
Birefringence Type	Elliptical Cladding Stress Region
Beat Length	1.3mm
Numerical Aperture	0.16
Core Radius, a	1.44μm
Cladding Radius	40.0μm
Coating Radius	100.0μm
Cut-Off Wavelength	0.60μm
Fibre V-Number (at 0.5145μm)	2.81
Mode Area (at 0.5145μm)	0.91πa^2
Attenuation (at 0.5145μm)	27.4dBkm^{-1}
Core Composition	Silica/7.5$\pm$1.0%wt Ge conc
Cladding (Inner)	Not Specified

3M/EOTec Twisted Low Birefringence Helium Neon Fibre

Label In Text	EOTec/TW
Birefringence Type	Circularly Birefringent By Twisting Fibre About Longitudinal Axis (40 turns m^{-1})
Beat Length	0.156m
Numerical Aperture	0.12
Core Radius, a	2.0μm
Cladding Radius	40.0μm
Cut-Off Wavelength	0.61μm
Fibre V-Number (at 0.5145μm)	2.93
Mode Area (at 0.5145μm)	0.87πa^2
Attenuation (at 0.5145μm)	15.8dBkm^{-1}
Core Composition	Silica/2.6$\pm$1.0%wt Ge conc
Cladding (Inner)	Depressed Cladding (Unspecified Dopant)

Ensign-Bickford, Polarisation Maintaining Argon Ion Fibre

Label In Text	EB450
Birefringence Type	Elliptical Core Stress region
Beat Length	9.0mm
Numerical Aperture	0.16
Core Radius, a	0.75/1.25μm
Cladding Radius	62.5μm
Cut-Off Wavelength	0.45μm
Fibre V-Number (at 0.5145μm)	2.11
Mode Area (at 0.5145μm)	$1.36\pi a^2$
Attenuation (at 0.5145μm)	29.5dBkm^{-1}
Core Composition	Silica/6.0±0.5%wt Ge conc
Cladding (Inner)	Fluorine Doped, Elliptical Cladding

Fujikura Polarisation Maintaining Argon Ion Fibre

Label In Text	PANDA
Birefringence Type	Cylindrical Boron Doped Regions Either Side Of The Core
Beat Length	1mm
Numerical Aperture	0.09
Core Radius, a	1.9μm
Cladding Radius	62.5μm
Cut-Off Wavelength	0.47μm
Fibre V-Number (at 0.5145μm)	2.09
Mode Area (at 0.5145μm)	$1.39\pi a^2$
Attenuation (at 0.5145μm)	21.2dBkm^{-1}
Core Composition	Silica/1.0%wt Ge conc
Cladding (Inner)	Not Specified

Appendix D Relationship Between Absolute Index Change And Measured Index Change for Fibre Photorefractivity Experiments

The ratio between measured index change, Δn, and absolute index change, Δn_c, from the interferometric configuration of Figure 51, Chapter 4, is the ratio of the power contained within the fibre core to the total power of the mode. It is assumed that the power profile of the LP_{01} mode is a normalised Gaussian described by

$$f(x,y) = \sqrt{\frac{b}{\pi}} \exp\Big(-b(x^2+y^2)\Big) \qquad D1$$

where b is a constant.

The fibre mode radius, r_0, is defined as the $1/e^2$ point relative to the centre of the distribution and is therefore related to b by

$$b = \frac{2}{r_0^2} \qquad D2$$

giving

$$f(x,y) = \frac{1}{r_0}\sqrt{\frac{2}{\pi}} \exp -\Big(2(x^2+y^2)/r_0^2\Big) \qquad D3$$

Thus, the ratio of the power contained within the fibre radius a to the total power, $\mathcal{R}$, is the integral

$$\mathcal{R} = \frac{\int_{-a}^{+a}\int_{-a}^{+a} \exp -\Big(2(x^2+y^2)/r_0^2\Big)dxdy}{\int_{-\infty}^{+\infty}\int_{-\infty}^{+\infty} \exp -\Big(2(x^2+y^2)/r_0^2\Big)dxdy} \qquad D4$$

This is expressed in cylindrical co-ordinates (r,ϕ) as

$$\mathcal{R} = \frac{4\int_0^{\pi/2}\int_0^{a} r\exp -(2r^2/r_0^2)drd\phi}{4\int_0^{\pi/2}\int_0^{\infty} r\exp -(2r^2/r_0^2)drd\phi} \qquad D5$$

where the additional factor r is the Jacobian of the co-ordinate transformation.

Thus

$$\mathcal{R} = 1 - \exp -\Big(2(a/r_0)^2\Big) \qquad D6$$

and

$$\Delta n_c = \frac{\Delta n}{1-\exp -\Big(2(a/r_0)^2\Big)} \qquad D7$$